Investigations of Synthetic Models of Mononuclear Nonheme Iron Dioxygenases

Michael Bittner
Marquette University

INVESTIGATIONS OF SYNTHETIC MODELS OF MONONUCLEAR NONHEME IRON DIOXYGENASES

by
Michael M. Bittner, B.S.

A Dissertation submitted to the Faculty of the Graduate School,
Marquette University,
in Partial Fulfillment of the Requirements for
the Degree of Doctor of Philosophy

Milwaukee, Wisconsin

August 2014

ABSTRACT

Investigations of Synthetic Models of Mononuclear Nonheme Iron Dioxygenases

Michael M Bittner, B.S.

Marquette University, 2014

Ring cleaving dioxygenases, such as *o*-aminophenol dioxygenase (APDO) and extradiol catechol dioxygenases (CatD), play an important role in human metabolism and the degradation of aromatic pollutants, yet questions still remain concerning the enzymatic mechanisms. One area of the catalytic cycle that remains controversial is the geometric and electronic structure of the intermediate formed after O_2 binding to the Fe(II) centers. Synthetic model systems can be useful for studying enzyme active sites, as they are easier to modify and characterize than the enzymes themselves. However, synthetic models of APDOs have been relatively rare thus far.

We prepared several monoiron(II) complexes that faithfully model the enzyme-substrate intermediates of *o*-aminophenol dioxygenases (APDO) and catechol dioxygenases. The complexes use either the ^{Ph2}Tp (^{Ph2}Tp = hydrotris(3,5-diphenylpyrazol-1-yl)borate) or ^{Ph2}TIP (^{Ph2}TIP = tris(4,5-diphenyl-1-methylimidazole)phosphine) supporting ligands and one of three bidentate, redox-active ligands: 4-*tert*-butylcatecholate, 4,6-di-*tert*-butyl-2-aminophenolate, or 4-*tert*-butyl-1,2-phenylenediamine. These complexes have been extensively characterized with crystallographic, spectroscopic, and electrochemical techniques, in conjunction with computational methods (e.g, density functional theory). Each complex is reactive towards O_2, and the geometric and electronic structures of the resulting species were examined with various methods to determine whether the oxidation is iron-based, ligand-based, or a combination of both.

Treatment of the ^{Ph2}Tp / ^{Ph2}TIP monoiron(II) aminophenolate complex with a phenoxyl radical results in formation of a complex containing an iron(II) center coordinated to an iminobenzosemiquinonate radical, that to the best of our knowledge has no synthetic precedence. Further oxidation leads to a complex best described as a ferric center bound to the iminiobenzosemiquinate radical. The electronic structures of these complexes were determined with the aid of spectroscopic and computational methods.

Several monoiron(II) complexes were also prepared to model the active-site structure of β-diketone dioxygenase (Dke1). For this purpose, we employed the ^{Ph2}Tp supporting ligand and acac^X substrate ligands, where acac^X represents the anion of dialkyl malonate. Upon exposure to O_2 in toluene it was found that the complexes exhibited reactivity similar to Dke1, although at a much slower rate than the native enzyme.

ACKNOWLEDGEMENTS

Michael M Bittner, B.S.

I would like to thank Dr. Adam Fiedler for all his guidance, understanding, and patience. He has always been there for his students and provided help when they needed. My lab mates Jake Baus, Amanda Baum, Denan Wang, Xixi Hong, and Dr. Heaweon Park for their thoughtful discussions and assistance during my time at Marquettee. Most of all, my Mother, Father, and family for all their support during my graduate career.

TABLE OF CONTENTS

LIST OF TABLES

LIST OF FIGURES

LIST OF COMPLEXES

Chapter 1

Introduction: Structure and Function of Nonheme Iron Dioxygenases

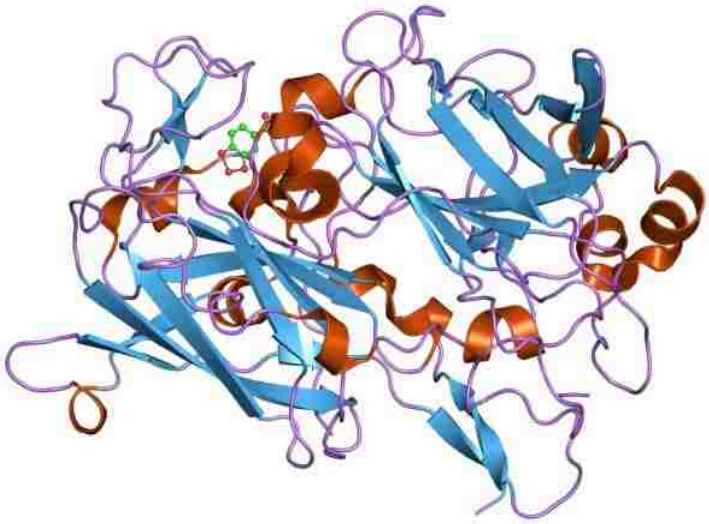

Vetting, M. W.; D'Argenio, D. A.; Ornston, L. N.; Ohlendorf, D. H. *Biochemistry* **2000**, *39*, 7943.

Abstract: Mononuclear nonheme iron dioxygenases play a central role in the biodegradation of various aromatic and aliphatic compounds. Despite their prevalence in Nature, certain aspects of the enzymatic mechanisms remain poorly understood. In the ring-cleaving dioxygenases, the catalytic cycle is thought to involve formation of substrate-based radical after binding of O_2 to the Fe(II) center, although the identity of this intermediate is controversial. We have explored fundamental questions regarding the reactivity of iron-containing dioxygenases using a biomimetic approach that combines coordination chemistry, spectroscopy, electrochemistry, and reactivity studies.

Portions of this chapter have appeared in the paper: Bittner, M. M.; Kraus, D.; Lindeman, S. V.; Popescu, C. V.; Fiedler, A. T. *Chem. Eur. J.* **2013**, 9686-9698.

1.A. Nonheme Iron Dioxygenases

A number of important metalloenzymes are found in metabolic pathways evolved by bacteria to breakdown and assimilate recalcitrant pollutants – a process referred to as *bioremediation*.[1,2] Single and multi-ring hydrocarbons are a major class of pollutants amenable to bioremediation. The aerobic degradation of these compounds is largely mediated by nonheme iron-containing dioxygenases (enzymes capable of incorporating both atoms of O_2 into substrate).[3] For example, the first step in the catabolism of naphthalene is its oxidation to the corresponding *cis*-1,2-diol (Figure 1.1) – a reaction catalyzed by naphthalene 1,2-dioxygenase (NDO).[4] After aromatization of the diol to the corresponding catechol, the aromatic ring is oxidatively opened by either an intradiol- or extradiol-cleaving catechol dioxygenase (CatD).[5] The resulting products are then further degraded to yield intermediates that can feed into the Krebs cycle, thereby allowing the organisms to utilize the pollutant as a source of energy.[1]

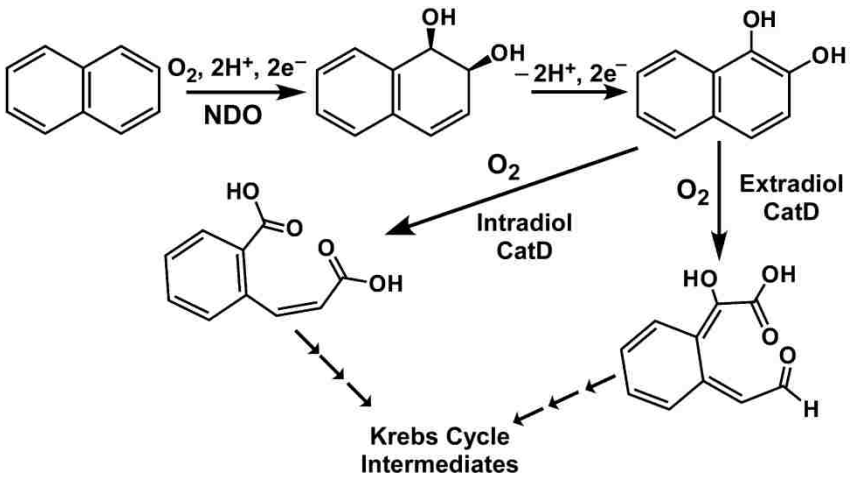

Figure 1.1. Biodegradation pathway of naphthalene.

Nonheme Fe dioxygenases have been shown to oxidatively cleave a wide variety of aromatic substrates, including catechol, protocatechuates,[6] hydroquinones[7-9], o-aminophenols[10,11], and salicylates[12-14] (Figure 1.2). With the exception of the intradiol catechol dioxygenases, these ring-cleaving dioxygenases generally share a common active-site structure: the high-spin monoiron(II) center is bound to one aspartate (or glutamate) and two histidine residues in a facial array, along with two or three H_2O ligands (Figure 1.3)[4,5,15-18]. This "2-His-1-carboxylate (2H1C) facial triad" is the dominant coordination motif found among nonheme monoiron enzymes involved in O_2 activation – other examples include the α-ketoglutarate- and pterin-dependent oxygenases and isopenicillin *N*-synthase (IPNS)[19-21]. The 2H1C structure facilitates catalysis by permitting the Fe center to bind both substrate and O_2. In the extradiol CatDs, substrate coordinates to Fe in a bidentate, monoanionic fashion with concomitant dissociation of all H_2O ligands[18,22,23]. The resulting five-coordinate Fe^{2+} center then binds O_2 in the vacant site adjacent to the bound substrate.[18,24]

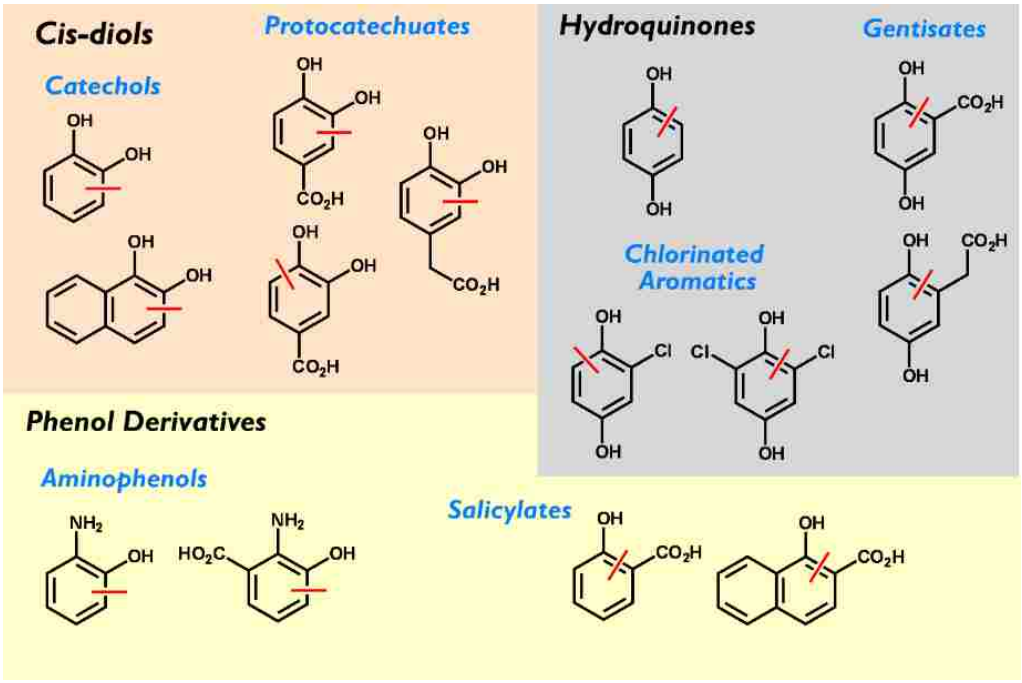

Figure 1.2. Various aromatic substrates cleaved by nonheme Fe dioxygenases.

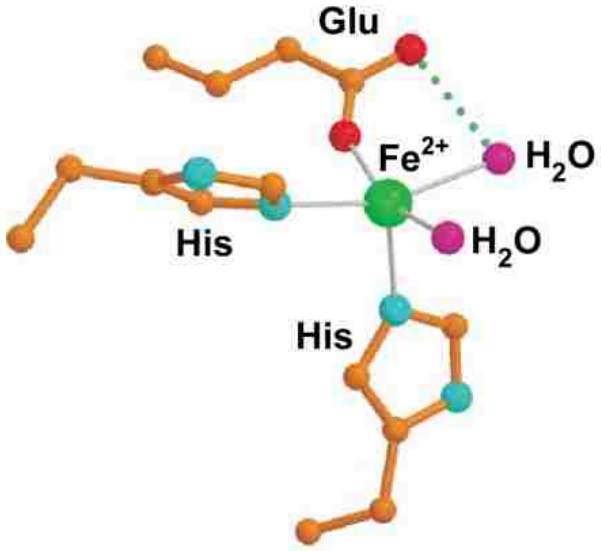

Figure 1.3. Common active-site structure of nonheme Fe dioxygenases, featuring the 2-His-1-carboxylate facial triad of protein residues.[5]

While the vast majority of nonheme iron dioxygenases are found in bacteria, a few significant examples occur in mammals (including humans). For instance, a key step in tryptophan degradation involves the O_2-mediated ring-cleavage of 3-hydroxyanthranilate (HAA) by HAA-3,4-dioxygenase (HAD; Figure 1.4)[25]. This reaction occurs as the final step in the kynurenine pathway that coverts excess tryptophan to quinolinic acid, which is then used to produce the NADH cofactor.[26] X-ray crystallographic studies revealed a nonheme Fe center coordinated by the canonical 2H1C facial triad.

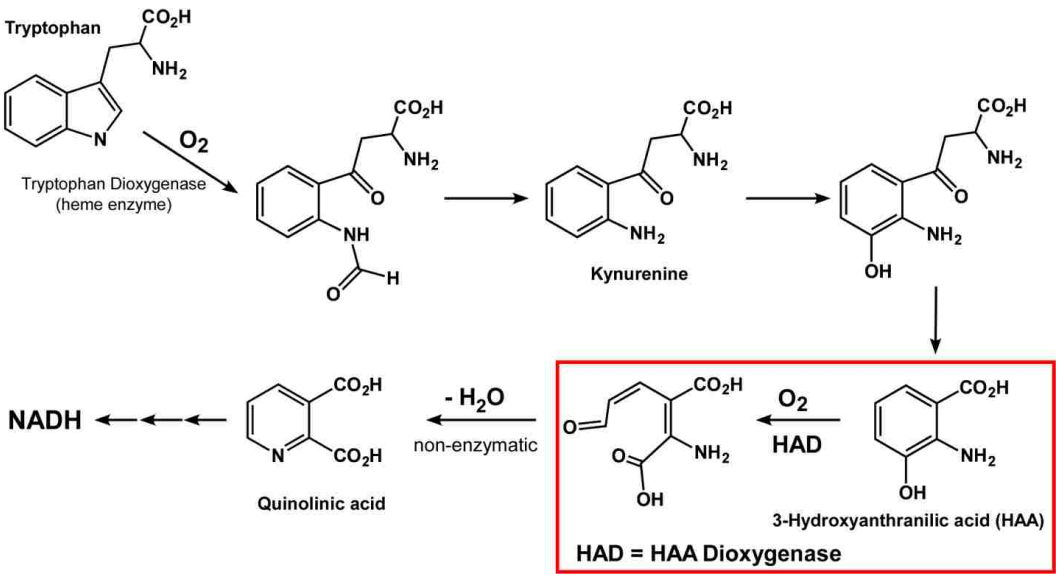

Figure 1.4. Selected reactions in the kynurenine pathway.

1.B. Catalytic Mechanism of the Nonheme Iron Dioxygenases

The catalytic mechanism of the extradiol CatDs has been studies extensively with experimental and computational methods. The first step involves bidentate coordination of substrate to Fe with loss of a proton, accompanied by displacement of the H_2O ligands[5,18,23]. The resulting five-coordinate Fe(II) center then binds O_2 in the vacant site

adjacent to the bound substrate[18,24]. Formation of a short-lived ferric-superoxo intermediate is thought to trigger the transfer of one electron from the substrate ligand to iron, resulting in a bound *o*-semiquinone radical[18]. The existence of this putative intermediate would likely require deprotonation of the distal –OH group by a second-sphere residue, although it is not clear whether these three events (O_2 coordination, electron transfer, and proton transfer) occur in a stepwise or concerted manner. The degree of semiquinone character on the substrate ligand in the O_2-bound form of the enzyme is also uncertain (*vide infra*); however, it is well-established that the next step of the catalytic cycle involves generation of an Fe(II)-alkylperoxo species, which undergoes a Criegee rearrangement and hydrolysis to eventually yield the ring-opened product. Interestingly, the general catalytic strategy employed by the ring-cleaving dioxygenases differs substantially from the O_2-activation mechanism employed by cytochrome P450s[27], methane monooxygenase[28], and α-ketoglutarate dependent dioxygenases[29]. In these enzymes, O_2 is used to generate an iron(IV)-oxo intermediate that performs the demanding hydroxylation of an aliphatic substrate. In contrast, structural, mutagenic, and radical trap experiments and also computational studies have revealed that the ring-cleaving dioxygenase mechanism does not involve high-valent Fe intermediates (Figure 1.5).[23,30-32]

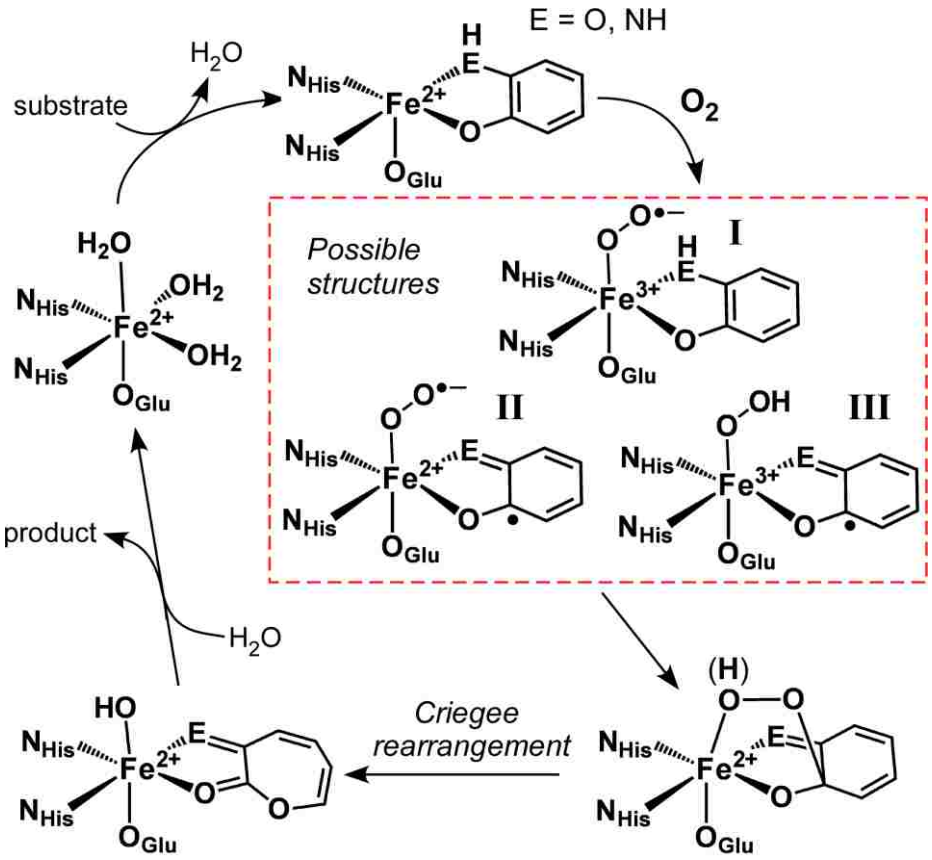

Figure 1.5. Proposed mechanism for extradiol catechol dioxygenases and *o*-aminophenol dioxygenases.

While there is broad agreement concerning the generic mechanism shown in Figure 1.5, the electronic structure of the critical Fe/O_2/substrate intermediate remains disputed. While Fe/O_2 adducts are normally described as ferric-superoxo species (such as intermediate **I** in Figure 1.5), early studies by Lipscomb[33] and Bugg[34] lead to the proposal that ring-cleaving dioxygenases proceed instead via a superoxo-Fe(II)-(imino)semiquinone species (**II**). The radical character of the substrate was presumed to facilitate reaction with the superoxo ligand, thereby overcoming the large kinetic barrier to formation of the peroxy intermediate. This hypothesis was partly inspired by model studies that had demonstrated the "non-innocent" nature of metal-bound

catecholates[35-37] and iminophenolates[38]. Subsequent experiments with a substrate analogue featuring a cyclopropyl moiety as a radical probe indicated formation of semiquinonate (SQ) radical during the catalytic cycle of MhpC, a well-studied ECDO.[39] Density functional theory (DFT) analysis by Siegbahn further supported this electronic structure description[40-42]. In addition, Emerson *et al.* demonstrated that a pair of ECDOs, Fe-HPCD and Mn-MndD, are equally active with either Fe or Mn in their active sites, despite the intrinsically different redox potential of the two metal ions.[43] This result lead to the conclusion that the Fe (or Mn) oxidation state does not change during the catalytic cycle; instead, the metal ion only serves to conduct an electron from the bound substrate ligand to O_2, thus yielding intermediate **II** directly.

Despite this large body of evidence, recent studies have challenged the prevailing notion that a substrate-based radical is generated in the catalytic cycles of ECDOs (and, by extension, other ring-cleaving dioxygenases). Firstly, Lipscomb and coworkers succeeded in isolating the Fe/O_2 adduct of a HPCD mutant (H200N) bound to the "unactivated" substrate 4-nitrocatechol. Interrogation with EPR and Mössbauer spectroscopies revealed that this species contains an Fe^{3+}–$O_2^{\bullet-}$ unit with $S = 2$ – inconsistent with the presence of a SQ ligand.[44] A follow-up study of H200N HPCD with the native substrate resulted in the isolation and spectroscopic characterization of novel intermediate best described as a hydroperoxo-Fe(III)-semiquinone species (**III** in Figure 1.5).[45] However, a recent computational study by Ye and Neese suggested that this intermediate is not catalytically viable.[46] Their calculations of the ECDO mechanism found no evidence that a SQ-containing intermediate (either **II** or **III**) is required for catalysis. Instead, they favor a mechanism in which the ferric-superoxo adduct (**I**)

converts directly to a hydroperoxo-bridged species (Figure 1.5). The kinetic barrier for this step is lowered by concomitant transfer of a proton from the second-sphere histidine residue to the nascent peroxo group.

Compared to the extensive literature that exists for the extradiol CatDs, there have been few mechanistic studies of nonheme Fe dioxygenases that oxidize non-catechol substrates, such as *o*-aminophenols and hydroquinones.[5] Proposed catalytic cycles for these dioxygenases largely follow the ordered mechanism described above for the extradiol CatDs. For instance, based on X-ray crystallographic studies, Zhang *et al.* suggested the catalytic cycle shown in Figure 1.6 for HAD.[30] As in the extradiol CatDs mechanism, the electronic structure of the key Fe/O_2/HAA adduct is uncertain.

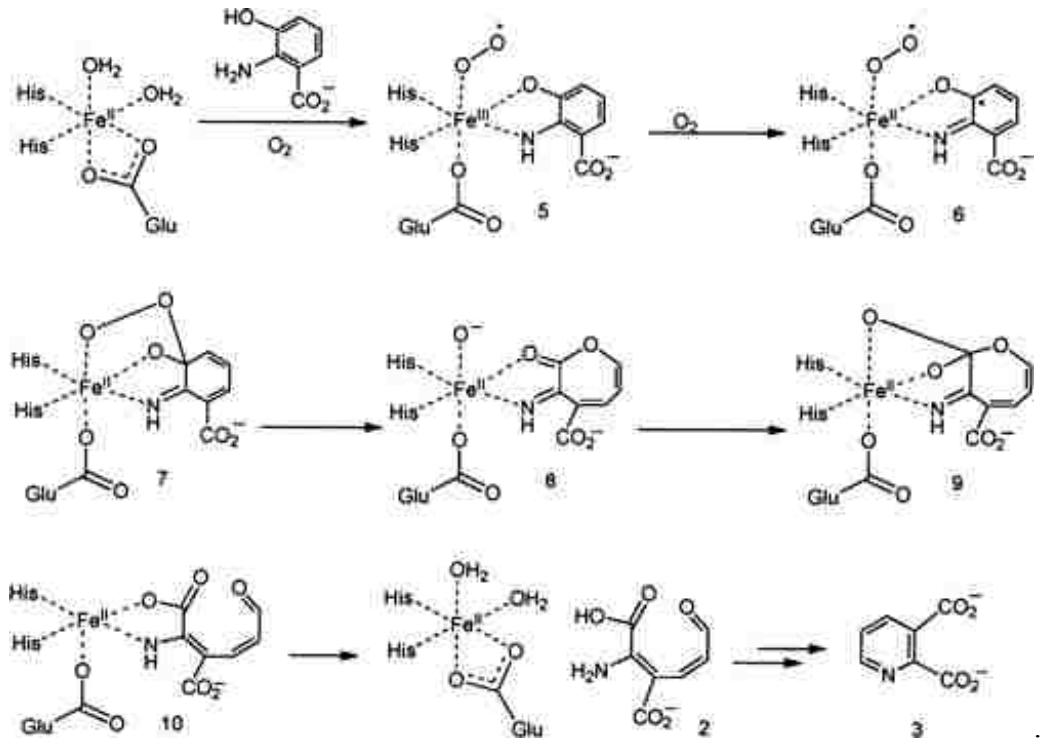

Figure 1.6. Proposed mechanism for HAD.[47]

1.C. A New Class of Nonheme Iron Dioxygenases

Despite the prevalence of the 2H1C facial triad, a new class of mononuclear nonheme Fe dioxygenases has recently emerged that employ the 3-histidine (3His) facial triad instead.[48,49] As with NDO and the extradiol CatDs, these enzymes are largely found in bacteria where they serve to degrade xenobiotic compounds (the lone exception is cysteine dioxygenase (CDO), an enzyme found in mammalian cells that initiates the catabolism of L-cysteine; see Figure 1.7).[50,51] *Members of this "3His family" catalyze novel transformations that have expanded the known boundaries of Fe dioxygenase chemistry.* For example, the enzyme β-diketone dioxygenase (Dke1) is one of the few dioxygenases capable of oxidatively cleaving aliphatic C-C bonds.[52,53] Dke1 converts acetylacetone – a toxic and prevalent pollutant – to acetic acid and 2-oxopropanal (Figure 1.7). It was first isolated from a bacterial strain (*Acinetobacter johnsonii*) that is capable of growing on acetylacetone and other β-diketones as its sole carbon source.[50] X-ray diffraction (XRD) studies confirmed that the metal center in Dke1 is facially coordinated by three His residues and presumably 2-3 H_2O molecules, although these were not resolved in the structure (Figure 1.8).[54,55] While the active site can bind several first-row transition metal ions, only Fe(II) results in catalytic activity.[52] Spectroscopic studies suggest that substrate coordinates to Fe as the deprotonated β-keto-enolate in a bidentate manner.[56]

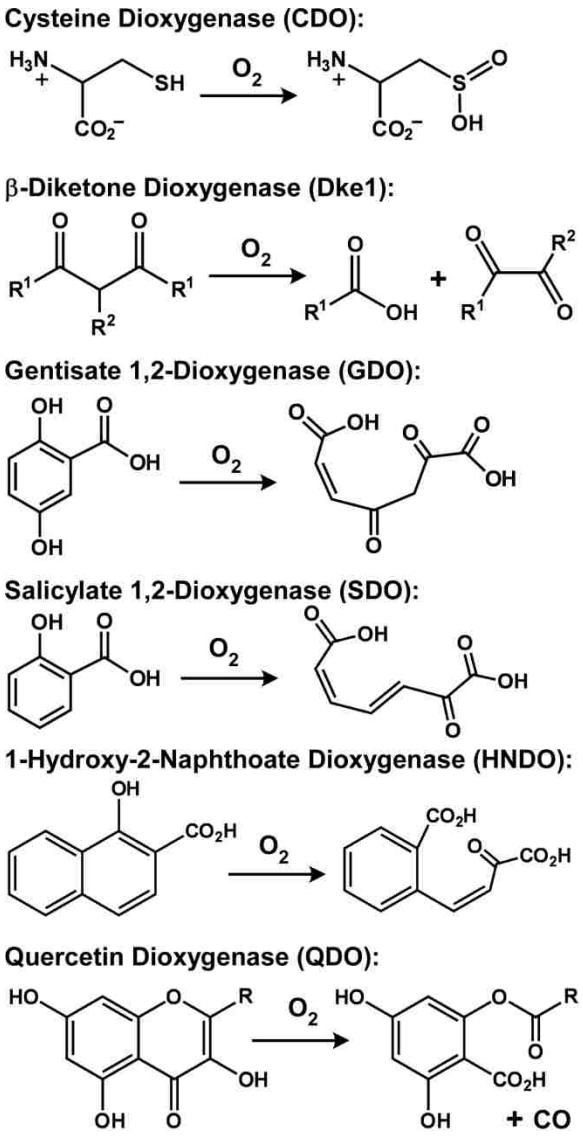

Figure 1.7. Reactions catalyzed by nonheme Fe dioxygenases with the 3His triad.

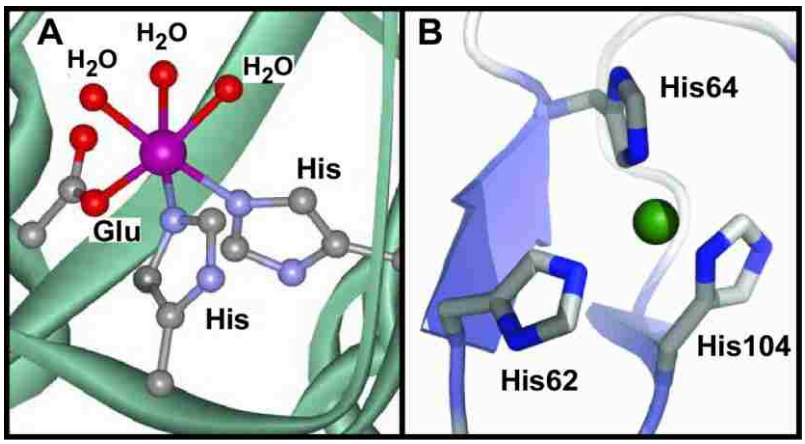

Figure 1.8. Crystallographically-derived structures of (A) the 2-His-1-carboxylate facial triad,[14] and (B) the 3His facial triad in Dke1 active site.

Other Fe dioxygenases with the 3His triad include gentisate 1,2-dioxygenase (GDO)[57] and salicylate 1,2-dioxygenase (SDO),[12,13,58] both of which oxidatively cleave aromatic C-C bonds (Figure 1.7). Sequence analysis also suggests that 1-hydroxy-2-naphthoate dioxygenase (HNDO) belongs to the 3His family of Fe dioxygenases,[13,59] although crystallographic data are currently lacking. Each of these microbial enzymes participates in the degradation pathways of polycyclic aromatic hydrocarbons.[13,57,60] The reaction catalyzed by GDO is very similar to those catalyzed by the extradiol CatDs and likely follows a similar mechanism.[57] However, the reactions of SDO and HNDO are fundamentally different due to the lack of a second hydroxyl group.[10,13,61] Only a handful of enzymes are capable of cleaving monohydroxylated aromatic compounds, and most of these examples involve aminophenol substrates in which the amino moiety assumes the role of the second hydroxyl group. *SDO and HNDO are therefore unique in performing the oxidative cleavage of aromatic rings with only one electron-donating group.*

Finally, the enzyme quercetin dioxygenase (QDO), which catalyzes the aerobic breakdown of plant flavonols by fungi and some bacteria (Figure 1.7), employs a

variation of the 3His motif.[62,63] An X-ray structure of bacterial QDO from *Bacillus subtilis* revealed two monoiron active sites per subunit.[64] Both Fe(II) centers are pentacoordinate with four protein ligands (one Glu and three facial His) and one H_2O ligand. However, in the site closest to the C-terminus, the Glu ligand is only weakly bound with an Fe-O_{Glu} distance of 2.44 Å.[64] Thus, QDO can be considered a member of the 3His family with an extra Glu residue at the interface of the first- and second-coordination spheres. While QDO from *B. subtilis* was isolated with Fe^{2+}, the enzyme exhibits equal or greater activity with other transition-metal ions.[64] Indeed, nearly all QDOs can function *in vitro* with multiple divalent metal ions, including Mn^{2+}, Fe^{2+}, Co^{2+}, Ni^{2+}, and Cu^{2+}.[64-66]

Given the prevalence and effectiveness of monoiron enzymes with the "canonical" 2H1C triad, the emergence of the 3His family of Fe dioxygenases raises an interesting question: what is the significance of this change in Fe coordination environment for catalysis? Interestingly, a mutant of Dke1 in which the His104 ligand was replaced with Glu was able to partially bind Fe^{2+} (~30% of wild type) yet exhibited no catalytic activity.[67] Similarly, a mutant of IPNS in which the Asp ligand was replaced with His was inactive although it contained approximately the same amount of Fe as the wild type enzyme.[68] Thus, *the 2H1C and 3His motifs are not functionally interchangeable, yet it remains unclear exactly how these ligand-sets tune the catalytic properties of their respective enzymes.*

Another open question concerns the mechanism of oxidative C-C bond cleavage in the 3His dioxygenases. Based on kinetic data for Dke1, Straganz has proposed that the reaction proceeds via direct addition of O_2 to the bound substrate to give an

alkylperoxidate intermediate.[69] The nucleophilic peroxidate then attacks the carbonyl group to yield a dioxetane species, which subsequently collapses to the products via concerted C-C and O-O bond cleavage (Figure 1.9A). This mechanism resembles the one proposed for the intradiol CatDs in which *the role of the Fe center is to activate substrate, not O_2.*[70,71] A more conventional *O_2-activation mechanism* has also been proposed for Dke1 that involves initial formation of an Fe-superoxo intermediate, followed by reaction with bound substrate (Figure 1.9B).[72] The mechanisms of SDO and HNDO are also unsettled. The lack of a second electron-donating group on the substrates, noted above, makes it unlikely that these enzymes follow the same catalytic cycle as the extradiol CatDs, which involves a Criegee rearrangement to form a lactone intermediate.[5,23] This step requires ketonization of the second –OH group to transfer electron-density onto the ring – an impossibility for the SDO and HNDO substrates. Thus, these 3His Fe dioxygenases require an alternative strategy for oxidative ring scission that has yet to be determined.

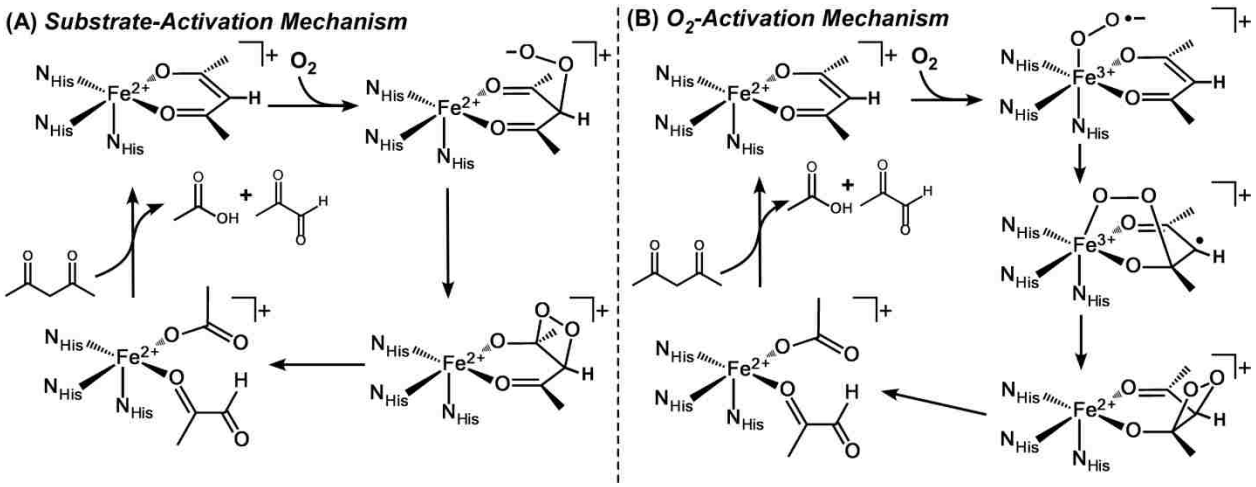

Figure 1.9. Proposed mechanism for Dke1.

1.D. Biomimetic Studies of Nonheme Iron Dioxygenases

Our knowledge of metalloenzymes has greatly benefited from the development of small-molecule analogs that replicate important structural, spectroscopic, and/or functional properties of the enzyme active sites.[73] The intra- and extradiol CatDs have been the target of numerous synthetic modeling studies, which have been extensively reviewed by Que and Gebbink.[20,74-77] By comparison, few efforts have been made to produce models of ring-cleaving dioxygenases with non-catechol substrates, such as the *o*-aminophenol or hydroquinone dioxygenases.[78,79]

To date, synthetic models of Fe dioxygenases have yielded little insight into the electronic structure of the critical Fe/O_2/substrate intermediates, which are thought (by some) to possess a coordinated substrate radical.[78,80-83] Notably, all relevant models of the extradiol CatDs feature unambiguous [Fe^{3+}–catecholate]$^+$ units. Similarly, the Fe(III)–iminosemiquinone complexes generated by Wieghardt and coworkers exclusively undergo ligand-based reductions to give the corresponding Fe(III)–imidophenolate(2-) species.[78,81,83] Thus, previous modeling studies have provided no evidence to support the existence an Fe(II)/substrate radical species in the catalytic cycles of ring-cleaving dioxygenases.

Biomimetic studies of the 3His family of Fe dioxygenases have also been lacking. A notable exception is Limberg's structural and functional model of Dke1. In 2008, Limberg *et al.* reported that the reaction of [Fe(^{Me}Tp)(Phmal)] (where Phmal = the anion of diethyl phenylmalonate; ^{Me}Tp = tris(3,5-dimethylpyrazolyl)borate) with O_2 at room temperature in MeCN results in dioxygenolytic ring cleavage of the bound ligand; yet no attempt was made to trap reactive intermediates.[72] The unique reactions performed by

the 3His family of Fe dioxygenases, as well as their relevance to bioremediation processes, make them worthy targets for biomimetic studies. Thus, one theme of our research efforts has been the design of metal complexes that serve as structural and functional models of dioxygenases with the 3His facial triad (Dke1, SDO, GDO, HNDO, and QDO).

A key advantage of the biomimetic approach is that the properties of the dioxygenase models can be modified in a *straightforward and systematic manner*, thereby allowing one to isolate those factors that play crucial roles in modulating electronic structure and catalytic activity. While similar changes can be made to protein active sites via mutagenesis, such modifications often cause widespread and ill-defined changes in structure that result in loss of activity. For instance, in the 2H1C and 3His families, many variants arising from point mutations of coordinating residues fail to bind Fe(II), and most are catalytically inactive, limiting the information that can be derived from mutagenesis studies.[49,84] In contrast, the flexible synthetic approach described here will provide a series of Fe complexes with a broad range of geometric and electronic properties. By exploring the reactivities of these various complexes with O_2, we have been able to formulate *structure-reactivity correlations* that are transferrable to the biological systems. In addition, the biomimetic approach is ideally suited for the isolation and characterization of catalytic intermediates that are difficult to observe in studies of the metalloenzymes, since it permits a great deal of control over ligand properties and reaction conditions.

1.E. Importance of Non-innocent Ligands

As shown above, redox active ligands play an important role in the mechanism of nonheme iron dioxygenases; specifically, the possible formation of a Fe^{2+}-(substrate radical) intermediate. While redox noninnocence of the substrate ligand is vital from a mechanistic standpoint; the electronic structure of compounds containing these types of ligands are often difficult to characterize, since multiple assignments of metal and ligand oxidation states are possible. This necessitates careful examination of these complexes with a variety of spectroscopic and computational methods in order to obtain an accurate description of their electronic structure.[85-89]

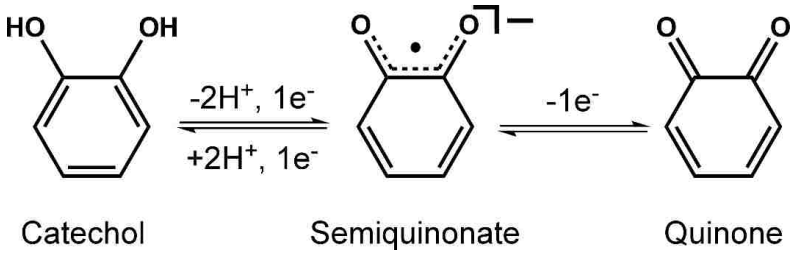

Figure 1.10. Oxidation states accessible by catechols.

Figure 1.10 shows the possible oxidation states of catechols, the prototypical example of a noninnocent redox active ligand. It is important to note that while it is possible to for these ligands to undergo electron-transfer, an area that has been studied extensively, they can also transfer two protons. This gives these ligands the ability to facilitate *proton-coupled* electron transfers (PCET)- a scenario that has received less attention. By synthesizing Fe^{2+} compounds with noninnocent ligands like aminophenols,

catechols, and phenylenediamines we hope to gain a better understanding of the possible intermediates and the role of PCET in the catalytic cycle of nonheme iron dioxygenases.

1.F. Specific Aims of this Project

Our research involves a combination of synthetic inorganic chemistry, physical characterization (crystallography, electrochemistry, and spectroscopy), computational methods, and examination of reactivities (Figure 1.11). With this integrated approach, we have addressed fundamental questions regarding the catalytic activity of nonheme Fe dioxygenases. Specifically, we have:

1. Synthesized several monoiron(II) complexes with tris(imidazolyl)phosphane (TIP) ligands in an effort to model the 3His facial triad of some Fe dioxygenases. [Chapter 2]
2. Prepared synthetic models of putative catalytic intermediates in the mechanism of aminophenol dioxygenases. Significantly, we succeed in generating the first synthetic example of an Fe(II) center coordinated a biologically-relevant iminosemiquinonate ligand. A combination of crystallographic, spectroscopic, and computational methods were used to probe the electronic structure of this unique complex. The corresponding Fe(III)-iminosemiquinone complex was also prepared and examined with similar techniques. [Chapters 3 and 4]
3. To explore the role of redox-active ligands in O_2 activation, we synthesized and structurally-characterized iron(II)-^{Ph2}TIP-based complexes with ligands derived from catechol and o-phenylenediamine. These complexes, in conjunction with the aminophenolate complex described in Chapter 4, constitute a unique series of high-

spin Fe(II) complexes with redox-active ligands. Each complex is oxidized in the presence of O_2, and the geometric and electronic structures of the resulting species were examined with spectroscopic and computational methods. The kinetics of the O_2 reactions and the identities of ring-cleavage products (if any) were also examined. [Chapter 5]

4. Examined the reactivity of Dke1 models with O_2. Building upon earlier studies performed by Drs. Heaweon Park and Jake Baus, three novel ^{Ph2}Tp-based complexes with dialkyl-malonate anions were prepared. We demonstrated that these complexes exhibit dioxygenase activity and thus serve as functional Dke1 models. [Chapter 6]

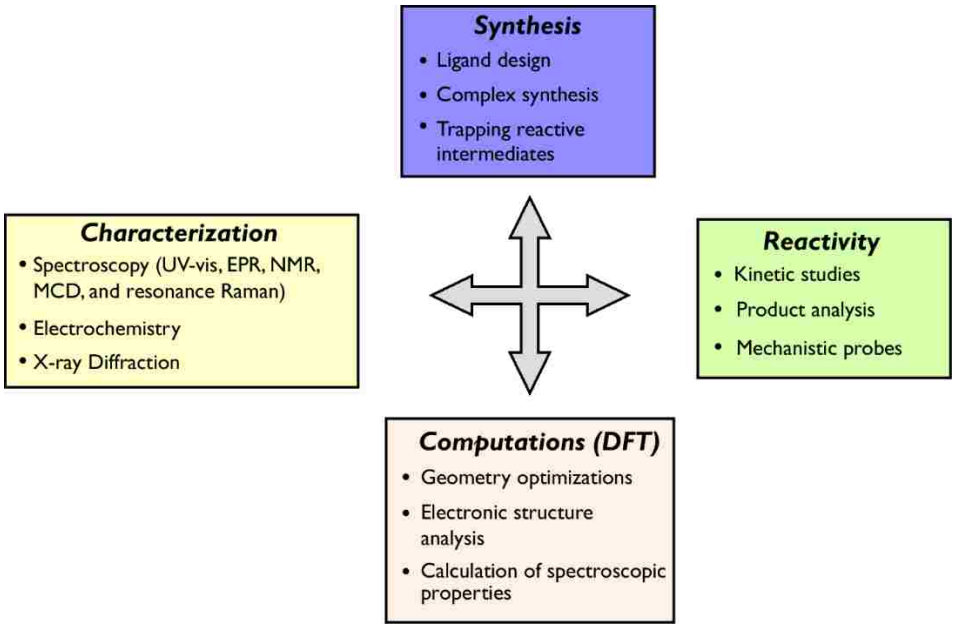

Figure 1.11. Schematic illustrating of the various methods employed in our modeling studies of nonheme Fe dioxygenases.

Chapter 2

Synthesis and Structural Characterization of Iron(II) Complexes with Tris(imidazolyl)phosphane Ligands: A Platform for Modeling the 3 Histidine Facial Triad of Nonheme Iron Dioxygenases

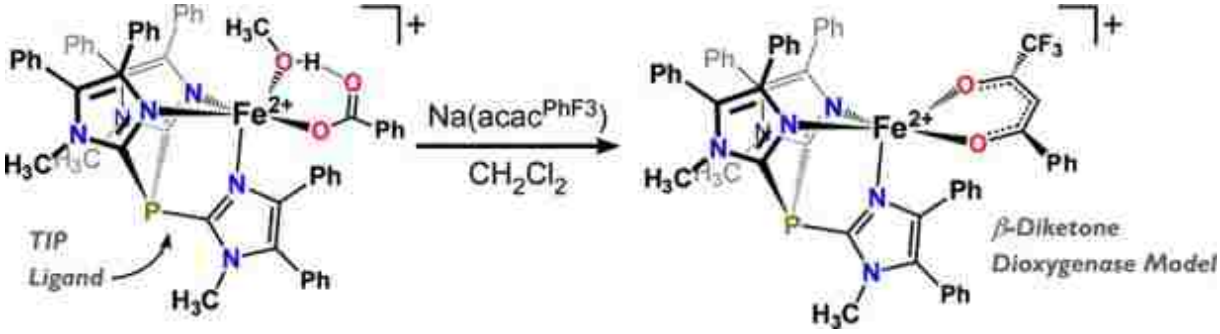

Abstract: Two monoiron(II) complexes containing the ligand tris(4,5-diphenyl-1-methylimidazole)phosphine (^{Ph2}TIP) have been prepared and structurally characterized using X-ray crystallography and NMR spectroscopy. The key feature of each of complex is the $[Fe(\kappa^3\text{-TIP})]^{2+}$ unit in which the remaining coordination sites are occupied by easily displaced ligands. The viability of these complexes was demonstrated through the synthesis of ^{Ph2}TIP-based complexes with a β-diketonate ligand that represents a faithful model of β-diketone dioxygenase (Dke1).

Portions of the following chapter have appeared in the following paper: Bittner, M. M.; Baus, J. S.; Lindeman, S. V.; Fiedler, A. T. *Eur. J. Inorg. Chem.* **2012**, *2012*, 1848.

2.A. Introduction

Mononuclear nonheme iron dioxygenases play a central role in the oxidative catabolism of a wide range of biomolecules and pollutants.[90,91,3] Members of this enzyme family include the extradiol catechol dioxygenases,[21,92,93] Rieske dioxygenases[4,17], homogentisate dioxygenase,[94,5] and (chloro)hydroquinone dioxygenases[95-98]. These enzymes feature a common active-site motif in which the ferrous center is facially ligated by one aspartate (or glutamate) and two histidine residues [the so-called 2-His-1-carboxylate (2H1C) facial triad].[19, 42] However, recent structural studies have shown that the Asp/Glu ligand in some monoiron dioxygenases is replaced with His, resulting in the 3His facial triad.[48] For example, cysteine dioxygenase (CDO)[99,50] – the first 3His enzyme to be structurally characterized – catalyzes the initial step in l-cysteine catabolism by converting the thiol into a sulfinic acid (Figure 2.1). Other 3His Fe dioxygenases include gentisate 1,2-dioxygenase (GDO)[57,100] and salicylate 1,2-dioxygenase (SDO),[58,101,102] both of which oxidatively cleave aromatic C–C bonds (Figure 2.1). Each of these microbial enzymes participates in the degradation pathways of polycyclic aromatic hydrocarbons. While the reaction catalyzed by GDO is very similar to those catalyzed by the extradiol catechol dioxygenases and likely follows a similar mechanism, SDO is unique in performing the oxidative cleavage of an aromatic ring with only one electron-donating group.

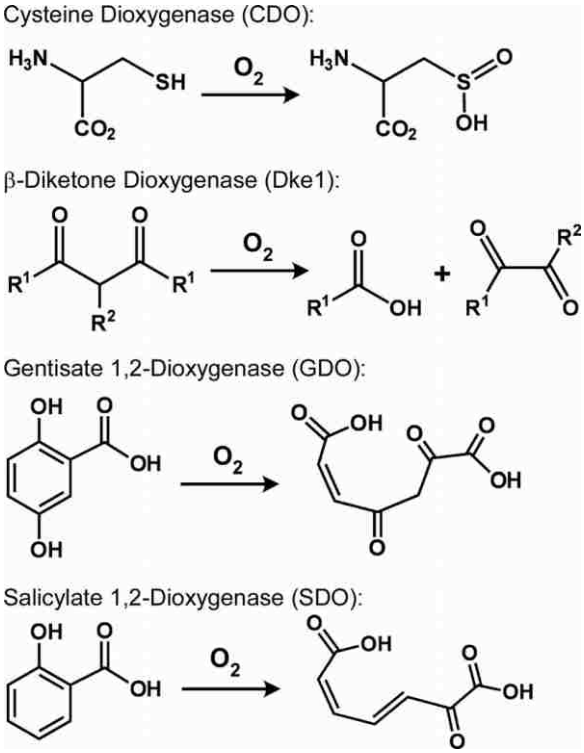

Figure 2.1. Cleavage of several different examples nonheme iron dioxygenase substrates.

In synthetic models, the 2H1C triad is typically modeled with anionic, tridentate supporting ligands such as tris(pyrazol-1-yl)borates (Tp),[103-107] bis(pyrazolyl)acetates,[108-110] and bis(1-alkylimidazol-2-yl)propionates.[111] The last two ligand sets replicate the mixed N2O donor set of the 2H1C triad by the inclusion of carboxylate arms. Given the unique and significant reactions catalyzed by the 3His family of Fe dioxygenases, it is important to develop supporting ligands with specific relevance to the 3His facial triad. To this end, we have sought to exploit the tris(imidazol-2-yl)phosphane (^{R2}TIP) framework shown in Figure 2.2, which accurately mimic the charge and donor strength of the 3 His coordination environment. These ligands were initially generated to model the 3His ligand sets found in the active sites of carbonic anhydrase (Zn^{2+}) and cytochrome c

oxidase (Cu^{2+}).[112-118] To date, the application of the TIP framework to Fe systems has been limited to homoleptic $[Fe(TIP)_2]^{2+/3+}$ complexes[119-121] and carboxylatebridged diiron(III) species.[121,73,74]

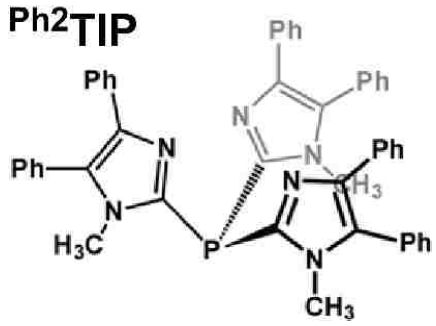

Figure 2.2. Phosphine ligand used as supporting ligand in various Fe(II) complexes synthesized.

A key advantage of the ^{R2}TIP ligand is that their steric properties can be easily modified by altering the R substituent(s). Thus far, we have primarily employed the ^{Ph2}TIP and, as the steric bulk of the phenyl rings discourages both dimerization and formation of the homoleptic $[Fe(TIP)_2]^{2+}$ complexes. The "one-pot" approach, however, is not always successful for various combinations of supporting and "substrate" ligands. Thus, as described in this chapter, we have generated several Fe^{2+} complexes with K3-TIP ligands that also contain displaceable ligands (such as solvent, triflate, and benzoate) bound to the opposite face of the octahedron. These complexes resemble the resting states of 3 His Fe dioxygenases, which feature two or three cis-labile H_2O molecules.[55,54] In addition, it is shown that these TIP-based complexes serve as excellent precursors for the formation of monoiron complexes with three facial imidazole donors and various bound substrates, including β-diketonates and salicylates (mimics of Dke1 and SDO,

respectively). Thus, the chemistry described here establishes a valuable platform for future synthetic modeling studies of nonheme Fe dioxygenases with the 3His facial triad.

2.B. Results and Discussion

The novel ^{Ph2}TIP ligand was synthesized by means of lithiation of 4,5-diphenyl-1-methylimidazole at the 2-position at –78 °C, followed by addition of PCl_3 (0.33 equiv.). Reaction of ^{Ph2}TIP with $Fe(OTf)_2$ in MeCN provided the complex [**1**]$(OTf)_2$ in 60% yield (Figure 2.3). Crystals suitable for X-ray diffraction (XRD) analysis were obtained by layering a concentrated MeCN solution with diethyl ether.

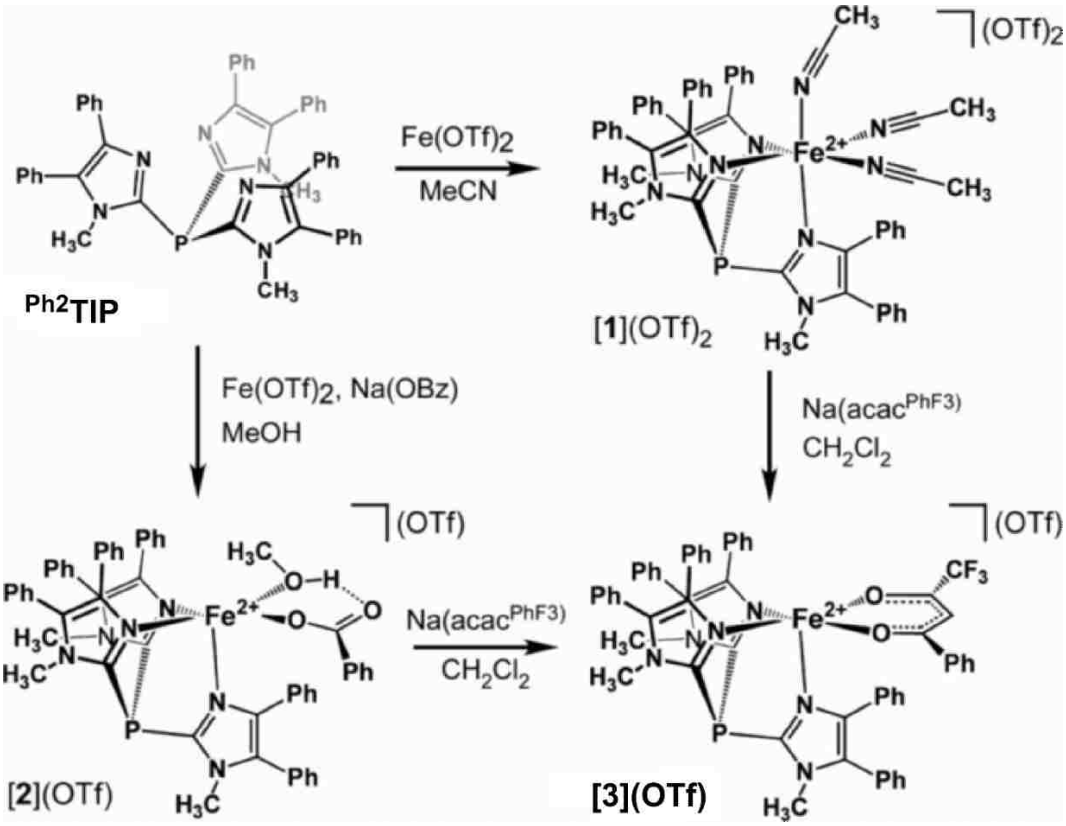

Figure 2.3. Synthesis of Fe(II) complexes with the ^{Ph2}TIP ligand.

Table 2.1. Selected metric parameters for $[Fe^{2+}(LN3)(MeCN)_3]^{2+}$ complexes. Bond lengths in Å and angles in degrees.

	[**1**](OTf)$_2$·0.5Et$_2$O[a]	[Fe(trisox^{t}Bu)(MeCN)$_3$]$^{2+}$ (ref.[122])[b]	[Fe(tpm^{Ph2})(MeCN)$_3$]$^{2+}$ (ref.[123])[c]
Fe1-N2	2.186(1)	2.257(2)	2.199(2)
Fe1-N4	2.177(1)	2.205(2)	2.196(2)
Fe1-N6	2.182(1)	2.215(2)	2.205(3)
Fe1-N7	2.196(1)	2.163(2)	2.131(3)
Fe1-N8	2.179(1)	2.131(2)	2.166(2)
Fe1-N9	2.205(1)	2.171(3)	2.156(3)
Fe-N$_{TIP}$ (av.)	2.181	2.226	2.200
Fe-Nsolv (av.)	2.193	2.155	2.151
N2-Fe1-N4	88.87(5)	84.62(6)	84.40(9)
N2-Fe1-N6	91.43(5)	82.12(6)	85.84(9)
N4-Fe1-N6	88.32(5)	86.89(7)	83.27(9)
N7-Fe1-N8	85.48(5)	90.25(8)	87.6(1)
N7-Fe1-N9	82.06(5)	91.33(8)	86.4(1)
N8-Fe1-N9	83.23(5)	86.00(8)	90.3(1)

[a] Average values for the two independent, but chemically equivalent $[1]^+$ cations. [b] trisoxtBu = 1,1,1-tris(4-tert-butyloxazolin-2-yl)-ethane. [c] tpmPh2 = tris(3,5-diphenylpyrazol-1-yl)methane.

The structure features two symmetrically independent $[\mathbf{1}]^{2+}$ units with nearly identical metric parameters (Table 2.1; details concerning the data collection and analysis of all X-ray structures are summarized in Table 2.4). As shown in Figure 2.4, the six-coordinate (6C) Fe^{2+} center is ligated by ^{Ph2}TIP and three MeCN ligands in a distorted octahedral geometry. As expected, the ^{Ph2}TIP ligand coordinates in a facial manner. The average Fe–N distance of 2.19 Å is indicative of a high-spin Fe^{2+} center (S = 2), consistent with the measured magnetic moment of 5.2 μB. The triflate counteranions are not bound to the metal centers, and the asymmetric unit also contains one equivalent of noncoordinated Et_2O.

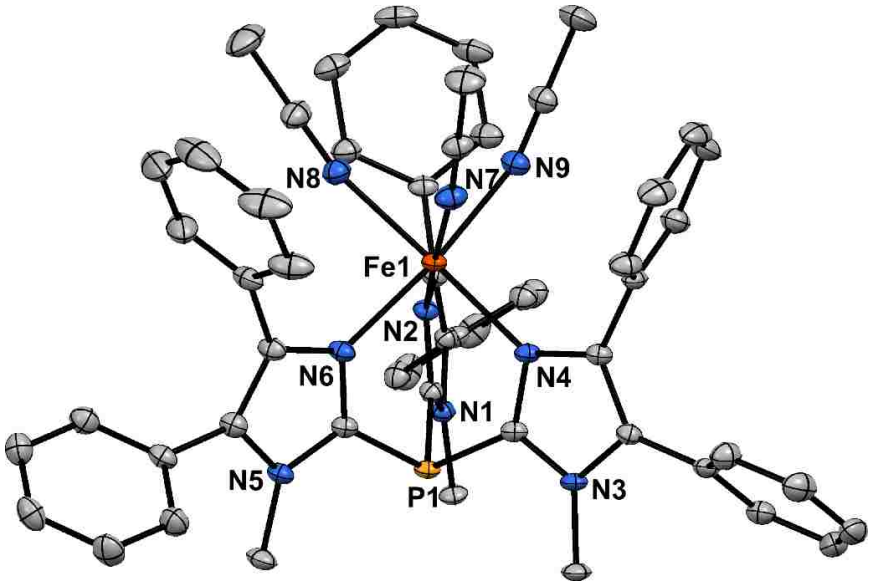

Figure 2.4. Thermal ellipsoid plot (50% probability) of [**1**](OTf)$_2$•0.5Et$_2$O. Only one of the symmetrically inequivalent [**1**](OTf)$_2$ units is shown. Hydrogen atoms, counteranions, and noncoordinating solvent molecules have been omitted for clarity.

Two related high-spin Fe^{2+} structures with $[Fe(LN3)\text{-}(MeCN)_3]^{2+}$ compositions have been reported in the literature, and their metric parameters are also provided in Table 2.1. The average Fe–N_{TIP} distance of 2.18 Å in $[\mathbf{1}]^{2+}$ is significantly shorter than the distances observed for the analogous tris(3,5-diphenylpyrazol-1-yl)methane (tpm^{Ph2})[76] and 1,1,1-tris(4-tert-butyloxazolin-2-yl)ethane ($trisox^{t}Bu$)[77] complexes, which display average Fe–N distances of 2.20 and 2.23 Å, respectively. Conversely, the average Fe–N_{MeCN} distance in $[\mathbf{1}]^{2+}$ is approximately 0.04 Å longer than those reported for the tpm^{Ph2} and $trisox^{tBu}$ complexes. Both facts suggest that ^{Ph2}TIP is a somewhat stronger donor than other neutral N3 ligands that have appeared in the literature. Elemental analysis performed with ground and dried crystals of [**1**](OTf)$_2$ indicate that at least two MeCN ligands are removed under vacuum. In addition, evidence for Fe–OTf bonding in non-coordinating solvents was obtained by using ^{19}F NMR spectroscopy (see Figure 2.5).

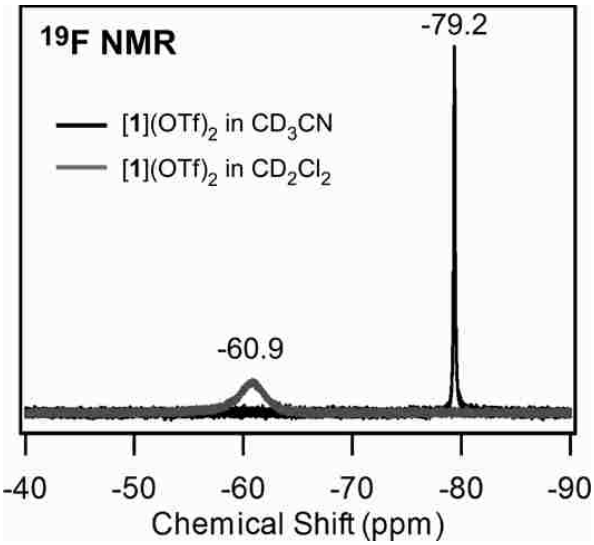

Figure 2.5. ^{19}F NMR spectra of [**1**](OTf)$_2$ in CD_3CN (black line) and CD_2Cl_2 (grey line) collected at room temperature.

For [**1**](OTf)$_2$ in CD_3CN, the triflate counteranion gives rise to a sharp peak at δ = –79.2 ppm, which is identical to the chemical shift observed for [NBu$_4$]OTf under the same conditions. The lengthy longitudinal relaxation time (T_1 value) of 128 ms measured for this feature suggests that the triflate counteranion is only weakly associated with the [Fe(^{Ph2}TIP)]$^{2+}$ unit in MeCN. In contrast, the ^{19}F NMR spectrum of [**1**](OTf)$_2$ in CD_2Cl_2 exhibits a broad feature at δ = –60.9 ppm with a short T_1 value of 14 ms which indicates that the triflate ion is directly bound to the Fe center.

Reaction of equimolar amounts of Fe(OTf)$_2$, ^{Ph2}TIP, and sodium benzoate (NaOBz) in MeOH provided the colorless complex [Fe(^{Ph2}TIP)(OBz)(MeOH)]OTf ([**2**]OTf), as shown in Figure 2.6. X-ray-quality crystals were obtained from a solution of [**2**]OTf in MeOH layered with pentane. The resulting structure reveals a pentacoordinate (5C) iron(II) center with a K3-^{Ph2}TIP ligand, monodentate benzoate ligand, and bound solvent (Figure 2.6). In addition to the second-sphere triflate anion, the asymmetric unit

also contains four MeOH molecules that do not directly interact with the [**2**]$^{+}$ cation. The complex adopts a distorted square-pyramidal geometry ($\tau = 0.25$)[124] with an O2N2 pseudobasal plane. Two phenyl rings of the ^{Ph2}TIP ligand lie across the vacant coordination site (i.e., parallel to the plane of the benzoate ligand), which prevents further solvent binding. The Fe–N_{TIP} and Fe–O distances are typical for high-spin Fe^{2+} centers (Table 2.1). The H atom of the coordinated MeOH molecule was found objectively and refined. The resulting O2···O3 distance of 2.610(2) Å and H3···O2 distance of 1.81(1) Å are indicative of an intramolecular hydrogen bond that closes a six-membered ring.

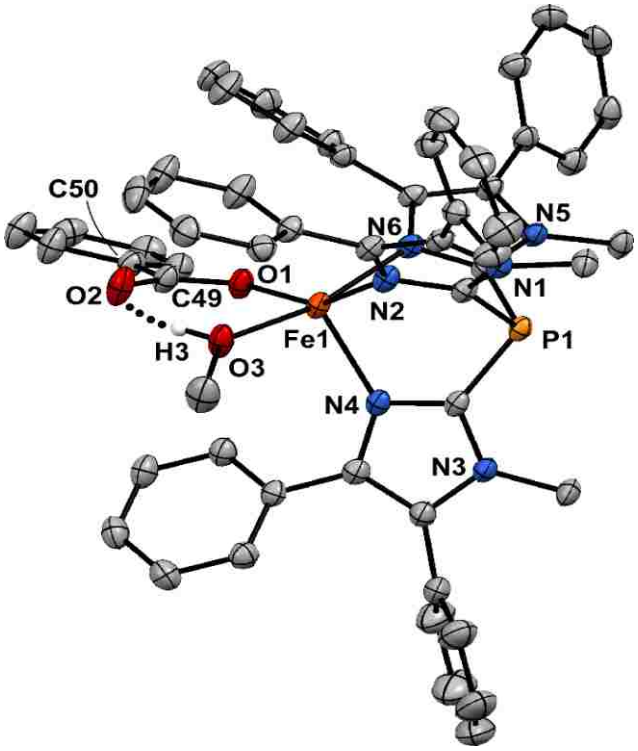

Figure 2.6. Thermal ellipsoid plot (50% probability) derived from [**2**]OTf·4MeOH. Non-coordinating solvent molecules, counter anions, and most H atoms have been omitted for clarity. The dotted line indicates the hydrogen-bonding interaction between H3 of the MeOH ligand and O2 of the benzoate anion.

Table 2.2 Selected metric parameters for ferrous carboxylate complex [**2**]OTf·4MeOH.

	[**2**]OTf·4MeOH
Fe1-N2	2.124(2)
Fe1-N4	2.127(2)
Fe1-N6	2.226(2)
Fe-N_{LN3} (av.)	2.158
Fe1-O1	2.011(1)
Fe1-O3	2.105(1)
O1-$C_{carboxyl}$	1.273(2)
O2-$C_{carboxyl}$	1.254(2)
N2-Fe1-N4	93.94(6)
N2-Fe1-N6	85.36(6)
N4-Fe1-N6	91.69(6)
O1-Fe1-N2	153.44(6)
O1-Fe1-N4	112.06(6)
O1-Fe1-N6	88.38(6)
O1-Fe1-O3	87.64(6)
N2-Fe1-O3	93.34(6)
N4-Fe1-O3	100.01(6)
N6-Fe1-O3	168.29(6)
τ value	0.25

Complex $[\mathbf{2}]^+$ resembles the structure of [Fe(^{Ph,Me}Tp)-(OBz)(^{Ph,Me}pyz)] (in which ^{Ph,Me}pyz = 3-phenyl-5-methylpyrazole) published by Fujisawa and co-workers.[125] Both complexes feature a distorted square-pyramidal geometry with a monodentate benzoate ion linked to a neutral ligand by means of an intramolecular hydrogen bond. This result is consistent with our study of $[Fe^{2+}(LN_3)(\beta\text{-diketonato})]^{+/0}$ complexes that found only slight differences (on average) between Fe–N_{TIP} and Fe–NTp bond lengths in 5C species, despite the different charges of the supporting ligands.[126]

Starting from either of these two Fe(^{Ph2}TIP) precursors – [**1**](OTf)$_2$ or [**2**]OTf – we were able to generate the complex [Fe(^{Ph2}TIP)(acac^{PhF3})]OTf ([**3**]OTf; Figure 2.7; in which acac^{PhF3} = anion of 4,4,4-trifluoro-1-phenyl-1,3-butanedione). The acac^{PhF3} ligand was selected for two reasons: (i) it is a viable Dke1 substrate, [53,56] [53,56] [57,60] [52,53] and (ii) previous studies in our laboratory found that [Fe(LN$_3$)(acac^{PhF3})]$^{+/0}$ complexes exhibit intense Fe^{2+}-acac^{PhF3} MLCT bands that serve as useful spectroscopic markers.[126] For both Fe(^{Ph2}TIP) precursors, reaction with Na(acac^{PhF3}) provides a deep purple solution that displays an absorption manifold centered at 502 nm (ε = 700 m^{-1}cm^{-1};) (Figure 2.8). Not surprisingly, the [**3**]OTf spectrum closely resembles the one published for [Fe(4-TIP^{Ph})(acac^{PhF3})]OTf, although the absorption features are blueshifted in the former by approximately 400 cm^{-1}.[126] Crystals of [**3**]OTf were obtained from the reaction of [**1**](OTf)$_2$ and Na(acac^{PhF3}) in CH_2Cl_2, followed by crystallization in CH_2Cl_2/pentane. The asymmetric unit contains two independent units with virtually identical structures. As shown in Figure 2.7, the 5C Fe^{2+} center is coordinated to the ^{Ph2}TIP and acac^{PhF3} ligands in a distorted trigonal-bipyramidal geometry (τ = 0.51) with the O atom proximal to the CF_3 group (O1) in the axial position. The metric parameters of [**3**]OTf are not significantly different from those reported for [Fe^{2+}(^{Ph2}Tp)(acac^{PhF3})] and [Fe^{2+}(4-TIP^{Ph})(acac^{PhF3})]OTf.[126]

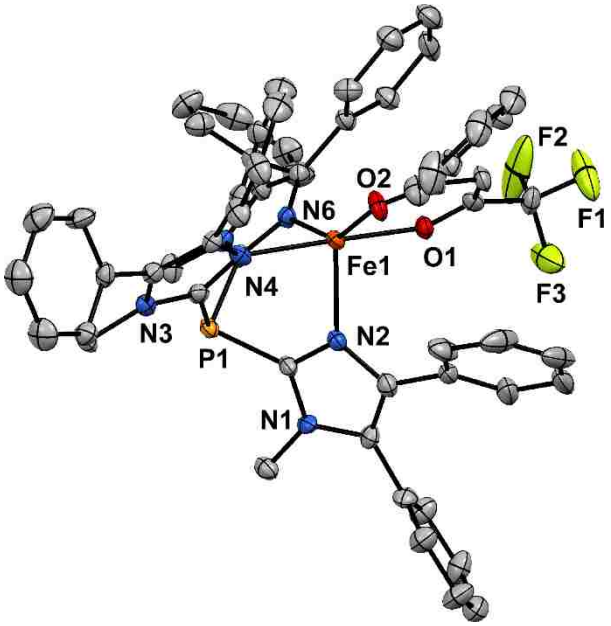

Figure 2.7. Thermal ellipsoid plot (50% probability) derived from [**3**]OTf·2CH_2Cl_2. Non-coordinating solvent molecules, counteranions, and most H atoms have been omitted for clarity. Only one of the two independent $[\mathbf{3}]^+$ units is shown. Selected bond lengths [Å] and angles [deg] for this unit: Fe1–O1 2.089(3), Fe1–O2 1.973(3), Fe1–N2 2.118(4), Fe1–N4 2.190(4), Fe1–N6 2.118(4); O1–Fe1–O2 87.2(1), O1–Fe1–N2 91.0(2), O1–Fe1–N4 176.4(2), O1–Fe1–N6 89.5(2), O2–Fe1–N2 120.4(2), O2–Fe1–N4 96.5(2), O2–Fe1–N6 146.3(2).

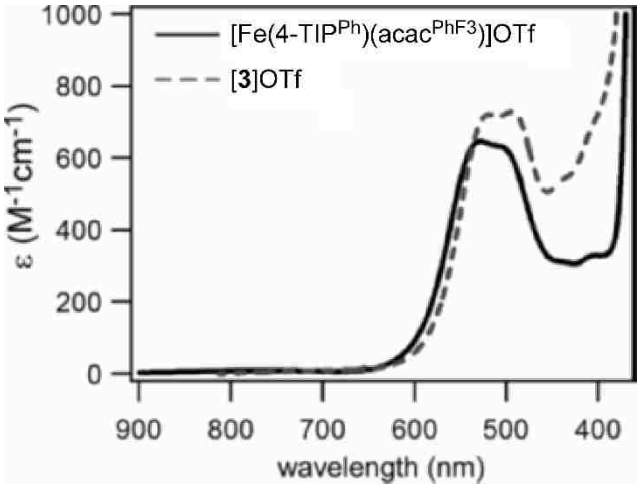

Figure 2.8. Electronic absorption spectra of the complexes [Fe(4-TIP^{Ph})($acac^{PhF3}$)]OTf (solid line) and [**3**]OTf (dashed line) measured at room temperature in MeCN.

The solution structures of [**2**]OTf and [**3**]OTf in CD_2Cl_2 were probed using ^1H NMR spectroscopy, and the observed chemical shifts, peak integrations, and T_1 values are summarized in Table 2.3. The three imidazole ligands are spectroscopically equivalent in solution due to dynamic averaging of the ligand positions on the NMR spectroscopic timescale. The ^{Ph2}TIP derived resonances were assigned with the help of peak integrations and by making two assumptions: (i) T_1 values follow the order ortho-meta-para for each phenyl ring,[105,126] and (ii) T_1 values of the 4-Ph protons are shorter than the corresponding protons on the 5-Ph ring. Thus, the fast-relaxing peaks ($T_1 \approx 1$ ms) near –20 ppm were attributed to the ortho protons of the 4-phenyl Ph2TIP substituents, which are positioned near the Fe^{2+} center. The peaks with the largest integration at (21.9) ppm were assigned to the 1-N-Me protons. The remaining resonances were then identified as the benzoate and acac^{PhF3} groups of [**2**]OTf and [**3**]OTf, respectively, by using the relative T_1 values to assign the phenyl resonances of both ligands.

Table 2.3. Summary of ^{1}H NMR spectroscopic parameters for [**2**]OTf and [**3**]OTf in CD_2Cl_2.

	[**2**]OTf			[**3**]OTf	
Resonance	δ[ppm]	T_1[ms]	Resonance	δ[ppm]	T_1[ms]
o-4-Ph	-21.0	1.1	*o-4*-Ph	-16.0	0.4
m-4-Ph	6.7	12.0	*m-4*-Ph	5.2	4.7
p-4-Ph	9.0	31.6	*p-4*-Ph	9.3	13.3
o-5-Ph	2.6	31.5	*o-5*-Ph	2.4	13.7
m-5-Ph	6.3	159	*m-5*-Ph	6.1	88.2
p-5-Ph	5.2	238	*p-5*-Ph	5.0	120
N-1-Me	21.9	15.7	N-1-Me	20.2	5.9
o-OBz	34.8	3.2	acac-*o*-Ph	22.6	1.7
m-OBz	19.0	37.0	acac-*m*-Ph	9.5	20.0
p-OBz	10.6	67.6	acac-*p*-Ph	17.3	45.5
			Acac H	39.4	0.8

This chapter has described the synthesis and X-ray structural characterization of iron(II) complexes supported by tris(imidazolyl)phosphane ligands ^{Ph2}TIP. The complexes – [**1**](OTf)$_2$, [**2**]OTf, and – feature easily displaced ligands, such as solvent molecules and/or carboxylates, in the coordination sites trans to the TIP chelate. Like the resting states of the enzymatic active sites, these "precursor" complexes are intended to serve as scaffolds that permit various substrate ligands to coordinate to the iron(II) center. The versatility of this approach was demonstrated by the formation of the Dke1 model [**3**]OTf from the reaction of Na(acac^{PhF3}) with the ^{Ph2}TIP-based complexes [**1**](OTf)$_2$ and [**2**]OTf.

2.C. Conclusions

In this chapter we have described the synthesis and X-ray structural characterization of iron(II) complexes supported the tris(imidazolyl)phosphine ligand (^{Ph2}TIP). Two of the complexes – [**1**](OTf)$_2$, and [**2**]OTf feature easily displaced ligands, such as solvent molecules and/or carboxylates, in the coordination sites *trans* to the TIP chelate. These complexes exhibit variability in their coordination numbers (5C or 6C). Intra- and intermolecular hydrogen-bonding interactions between the ligands and solvent are evident in the solid-state structures of each complex {with the exception of [**1**(OTf)$_2$]}.

Like the resting states of the enzymatic active sites, these "precursor" complexes are intended to serve as scaffolds that permit various substrate ligands to coordinate to the iron(II) center. The versatility of this approach was demonstrated by the formation of the Dke1 model [**3**]OTf from the reaction of Na(acac^{PhF3}) with the ^{Ph2}TIP-based complexes [**1**](OTf)$_2$ and [**2**]OTf. The facile formation of [**3**]OTf indicates that the TIP ligands are resistant to displacement by strong, anionic ligands. This is significant because half-sandwich ferrous complexes with neutral L_{N3} ligands, such as trispyrazolymethanes, have been shown to suffer from high lability and a tendency to decompose to the more stable bisligand species.[127] The relatively short Fe-N_{TIP} bond lengths found in our series of complexes suggest that the TIP ligands bind tightly to the iron centers. Thus, the precursor complexes described here provide a robust platform for the development of synthetic models of dioxygenases with the 3His facial triad.

2.D. Experimental

All reagents and solvents were purchased from commercial sources and used as received unless otherwise noted. MeCN and CH_2Cl_2 were purified and dried using a Vacuum Atmospheres solvent purification system. 4,5-diphenyl-1-methylimidazole[127] was prepared according to literature procedures. The synthesis and handling of air-sensitive materials were carried out under an inert atmosphere using a Vacuum Atmospheres Omni-Lab glovebox equipped with a freezer set to –30 °C. Elemental analyses were performed at Midwest Microlab, LLC in Indianapolis, IN. Infrared (IR) spectra of solid samples were measured with a Thermo Scientific Nicolet iS5 FTIR spectrometer equipped with the iD3 attenuated total reflectance accessory. UV/Vis spectra were obtained with an Agilent 8453 diode array spectrometer. NMR spectra were recorded on a Varian 400 MHz spectrometer. ^{19}F NMR spectra were referenced using the benzotrifluoride peak at –63.7 ppm. ^{31}P NMR spectra were referenced to external H_3PO_4 ($\delta = 0$ ppm). Magnetic susceptibility measurements were carried out using the Evans NMR method.

^{Ph2}TIP: 4,5-Diphenyl-1-methylimidazole (6.81 g, 29.1 mmol) was dissolved in THF (175 mL) and the solution was purged with argon for 25 min. The flask was cooled to –78 °C and nBuLi (32.0 mmol) was added dropwise. The solution was stirred for 30 min at –78 °C and then for 30 min at room temperature. The reaction was cooled again to –78 °C and PCl_3 (0.850 mL, 9.74 mmol) was added slowly. The mixture was allowed to slowly warm to room temp. over the course of several hours, and then 30% NH_4OH (75 mL) was added and stirred for 1 h. The layers were separated and the aqueous layer was extracted with THF (2-35 mL). The combined THF layers were washed with H_2O and

brine (50 mL each), dried with MgSO4, and the solvent was removed under vacuum. The orange residue was triturated with pentane and washed with methanol, thereby providing a fine white powder (1.66 g); yield 24%. $C_{48}H_{39}N_6P$ (730.8): calcd. C 78.88, H 5.38, N 11.50; found C 78.05, H 5.83, N 11.03. The disagreement indicates that small amounts of impurities are present. ^{1}H NMR (400 MHz, $CDCl_3$): δ = 7.48 (m, 12 H, Ar– H), 7.40 (m, 6 H, Ar–H), 7.17 (m, 12 H, Ar–H), 3.64 (s, 9 H, CH3) ppm. ^{13}C NMR (100 MHz, $CDCl_3$): δ = 140.5, 140.0, 139.9, 134.8, 133.6, 131.1, 131.0, 129.2, 129.0, 128.2, 126.9, 126.5, 33.4 ppm. ^{31}P NMR (162 MHz, $CDCl_3$): δ = –56.6 ppm. IR (neat cm^{-1}): ν = 3053, 2940, 2863, 1601, 1503, 1442, 1363, 1071, 1024, 961 cm^{-1}.

[Fe(^{Ph2}TIP)(MeCN)$_3$](OTf)$_2$ ([1]OTf): ^{Ph2}TIP (1.32 g, 1.81 mmol) and $Fe(OTf)_2$ (670 mg, 1.90 mmol) were mixed in CH_3CN (20 mL) and stirred until the solution had become clear (about 3h). The solution was filtered and layered with excess Et_2O; X-ray-quality crystals formed after one day. The white crystals were collected and dried under vacuum to provide 1.31 g of material; yield 60%. Elemental analysis showed that at least two of the coordinated CH_3CN ligands are removed upon drying. $C_{50}H_{39}F_6FeN_6O_6PS_2 \cdot CH_3CN$ (1125.9): calcd. C 55.47, H 3.76, N 8.71; found C 55.02, H 3.90, N 8.68. IR (neat, cm^{-1}): ν = 3048, 2932, 2283 [ν(C-N)], 1466, 1444, 1257, 1222, 1145, 1028, 983 cm^{-1}.

[Fe(^{Ph2}TIP)(OBz)(MeOH)]OTf ([2]OTf): ^{Ph2}TIP (779 mg, 1.07 mmol), NaOBz (155 mg, 1.07 mmol), and $Fe(OTf)_2$ (378 mg, 1.07 mmol) were combined in MeOH (12 mL). After stirring for several hours the precipitate was removed by filtration and the filtrate was reduced to about 5 mL in volume. Layering with pentane afforded the desired product as a white crystalline material (116 mg); yield 11%. X-ray diffraction analysis

revealed four uncoordinated MeOH molecules in the resulting structure, and elemental analysis indicated that two solvent molecules remain after drying under vacuum. $C_{57}H_{47}F_3FeN_6O_6PS \cdot 2CH_3OH$ (1152.0): calcd. C 61.51, H 4.81, N 7.30; found C 61.35, H 4.48, N 7.07. IR (neat, cm^{-1}): ν = 3043, 2953, 1598, 1551, 1443, 1370, 1258, 1153, 1029, 981 cm^{-1}.

[Fe(^{Ph2}TIP)(acac^{PhF3})]OTf ([3]OTf): A solution of 4,4,4-trifluoro-1-phenyl-1,3-butanedione (126 mg, 0.584 mmol) and $NaOCH_3$ (32 mg, 0.59 mmol) in THF was stirred for 30 min, after which the solvent was removed under vacuum to give white Na(acac^{PhF3}). Na(acac^{PhF3}) was then dissolved in CH_3CN (5 mL) and slowly added to a solution of [**1**]$(OTf)_2$ (704 mg, 0.583 mmol) in CH_2Cl_2 (5 mL). The purple solution was stirred overnight and the solvent was removed under vacuum. The residue was dissolved in CH_2Cl_2 (5 mL), filtered, and layered with pentane to yield deep red crystals suitable for X-ray crystallography (457 mg); yield 68%. The X-ray structure revealed uncoordinated CH_2Cl_2 molecules in the asymmetric units, and elemental analysis suggests that a small amount of solvent (≈0.7 equiv.) remains after vacuum drying. $C_{59}H_{45}F_6FeN_6O_5PS \cdot 0.7CH_2Cl_2$ (1210.36): calcd. C 59.24, H 3.86, N 6.94; found C 59.25, H 3.99, N 6.75. UV/Vis (MeCN): λ_{max} (ε,$m^{-1}cm^{-1}$) = 519 (720), 494 (730) nm. IR (neat, cm^{-1}): ν = 3058, 2955, 1602 [ν(C=O)], 1572, 1462, 1443, 1253, 1141, 1029, 981 cm^{-1}. ^{19}F NMR (376 MHz, CD_2Cl_2): δ = –44.9 (acac^{PhF3}), –77.7 (OTf) ppm.

Table 2.4. Summary of the X-ray crystallographic data collection and structure refinement.

	[**1**](OTf)$_2$·0.5Et$_2$O	[**2**]OTf·4MeOH	[**3**]OTf·2CH$_2$Cl$_2$[a]
Emperical formula	$C_{58}H_{53}F_6FeN_9O_{6.5}PS_2$	$C_{61}H_{64}F_3FeN_6O_{10}PS$	$C_{61}H_{49}Cl_4F_6FeN_6O_5PS$
Formula weight	1245.03	1217.06	1320.77
Crystal System	triclinic	triclinic	monoclinic
Space Group	$P\bar{1}$	$P\bar{1}$	*Pc*
a [Å]	13.3432(3)	14.9470(5)	16.0689(5)
b [Å]	15.8007(3)	15.1921(5)	20.6668(5)
c [Å]	27.8621(6)	16.4349(6)	19.6239(4)
α [°]	76.994(2)	90.642(3)	90
β [°]	88.757(2)	113.784(3)	90.088(2)
γ [°]	87.690(2)	115.873(4)	90
V [Å3]	5718.4(2)	2992.3(3)	6516.9
Z	4	2	4
*D*calcd. [g/cm^3]	1.446	1.351	1.325
λ [Å]	1.5418	1.5418	0.7107
μ [mm^{-1}]	3.749	3.205	0.489
θ range [°]	7 to 149	7 to 148	7 to 59
Reflections collected	64740	39217	56565
Independent reflections	22662	11891	28249
	(*R*int = 0.0315)	(*R*int = 0.0299)	(*R*int = 0.0339)
Data/restraints/parameters	22662/19/1591	11891/2/784	28249/12/1550
GOF (on *F*2)	1.025	1.028	1.061
*R*1/*wR*2 [$I > 2\sigma(I)$][b]	0.0332/0.0855	0.0413/0.1094	0.0608/0.1541
*R*1/*wR*2 (all data)	0.0374/0.0886	0.0449/0.1128	0.0666/0.1613

[a] One of the solvates in [4]OTf·2CH$_2$Cl$_2$ is partially occupied by a pentane molecule.
[b] $R1 = \Sigma ||F_o| - |F_c||/\Sigma|F_o|$; $wR2 = [\Sigma w(F_o^2 - F_c^2)^2/\Sigma w(F_o^2)^2]^{1/2}$.

Chapter 3

Synthetic Models of the Putative Fe(II)-Iminobenzosemiquinonate Intermediate in the Catalytic Cycle of o-Aminophenol Dioxygenases

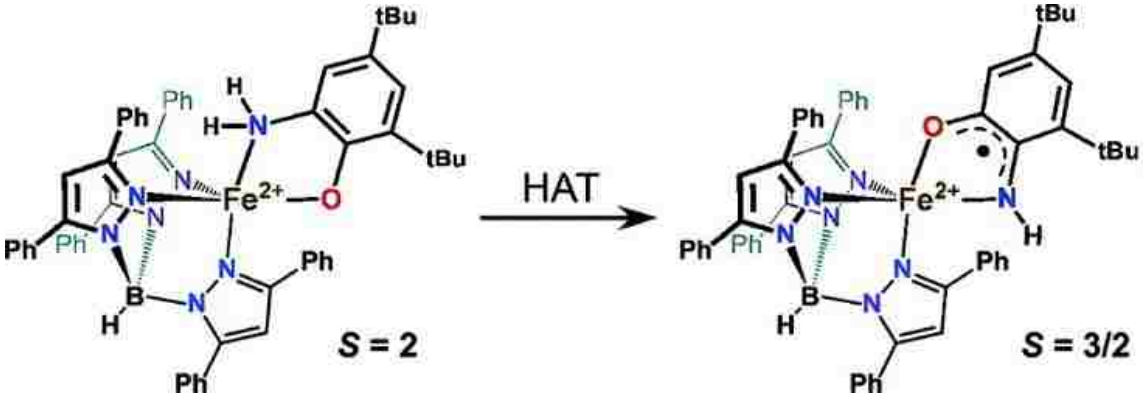

Abstract: The oxidative ring cleavage of aromatic substrates by nonheme dioxygenases is thought to involve formation of a ferrous-(substrate radical) intermediate. Here we describe the synthesis of the trigonal bipyramidal complex Fe(^{Ph2}Tp)(ISQ^{tBu}) (**5**), the first synthetic example of an iron(II) center bound to an iminobenzosemiquinonate (ISQ) radical. The unique electronic structure of this $S = 3/2$ complex and its one-electron oxidized derivative ([**6**]$^{+}$) have been established on the basis of crystallographic, spectroscopic and computational analyses. These findings further demonstrate the viability of Fe^{2+}-ISQ intermediates in the catalytic cycles of *o*-aminophenol dioxygenases.

Portions of this chapter have appeared in the paper: Bittner, M. M.; Lindeman, S. V.; Fiedler, A. T. *J. Am. Chem. Soc.* **2012**, *134*, 5460.

All DFT calculations were performed by Dr. Adam Fiedler.

3.A. Introduction

In biochemical pathways, the oxidative ring cleavage of substituted aromatic compounds, such as catechols and *o*-aminophenols, is generally performed by mononuclear nonheme iron dioxygenases.[5,23,90] While these enyzmes are usually found in bacteria, some play important roles in human metabolism: for instance, a key step in tryptonphan degradation involves the O_2-mediated ring cleavage of 3-hydroxyanthranilate (HAA) by HAA-3,4-dioxygenase (HAD; Figure 3.1).[11,30] With the exception of the intradiol catechol dioxygenases, the ring-cleaving dioxygenases share a common O_2-activation mechanism, illustrated in Figure 3.2.[5,23,90] A notable feature of this proposed mechanism is the superoxo-Fe^{2+}-(iminobenzo)-semiquinonate intermediate (**B**) that is thought to form after O_2 binding to the enzyme-substrate complex (**A**). The development of radical character on the substrate ligand presumably facilitates reaction with the bound superoxide yielding the key Fe^{2+}-alkylperoxo intermediate (**C**).[41,42] Although the electronic structure of **B** remains somewhat controversial,[128] evidence in favor of substrate radical character has been provided by radical-trap experiments[39] and DFT calculations,[41,42] as well as a remarkable X-ray structure of the Fe/O_2 adduct of an extradiol dioxygenase in which the radical character of the bound substrate was inferred from its nonplanar geometry.[18]

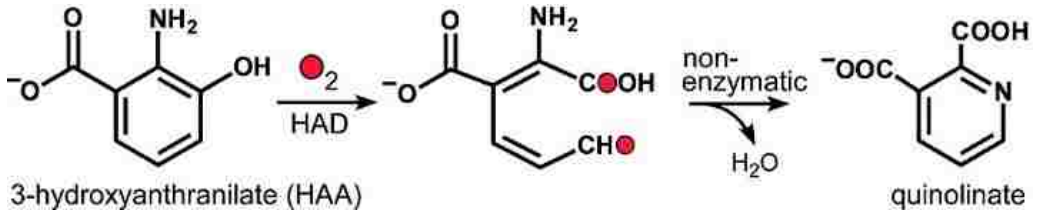

Figure 3.1 Reaction Catalyzed by HAA Dioxygenase (HAD).

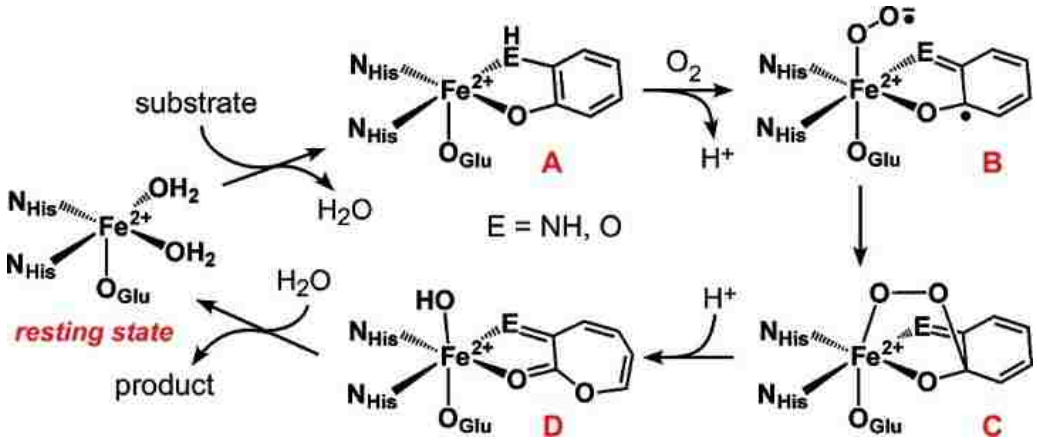

Figure 3.2 Catalytic Cycle of Ring-Cleaving Dioxygenases.

Despite these biological precedents, synthetic analogues of intermediate **B** in which a ferrous center is coordinated to an (iminobenzo)semiquinone radical, (I)SQ, have been lacking in the literature, even though numerous ferric complexes with such ligands exist.[35,36,38,78,80-83,129-131] Herein, we report the synthesis and detailed characterization of an Fe^{2+}-ISQ complex, **2a**, that represents the first synthetic model of this important type of enzyme intermediate. We also examine the geometric and electronic structures of the species $[\mathbf{3a}]^{+}$ generated via one-electron oxidation of **2a**.

3.B. Results and Discussion

In our efforts to generate synthetic models of HAD, we have used the tris(pyrazolyl)borate ligand, ^{Ph2}Tp, (where ^{Ph2}Tp = hydrotris(3,5-diphenylpyrazol-1-yl)borate(1-)) to mimic the facial His_2Glu coordination environment of the enzyme active site. The reaction of [(^{Ph2}Tp)Fe^{2+}(OBz)][105] (OBz = benzoate) with 2-amino-4,6-di-*tert*-butylphenol ($^{tBu}APH_2$) in the presence of base provided the light yellow complex [(^{Ph2}Tp)Fe^{2+}(^{tBu}APH)] (**4**) in 71% yield. The X-ray crystal structure of **4** reveals a five-coordinate (5C) Fe^{2+} center in which the $^{tBu}APH^{-}$ ligand binds in a bidentate fashion (Figure 3.3). The average Fe1-N_{Tp} bond length of 2.15 Å is typical of high-spin Fe^{2+} complexes with Tp ligands[105,126], while the short Fe1-O1 distance of 1.931(1) Å is consistent with coordination by an aminophenolate anion (Table 3.1) The complex adopts a distorted trigonal-bipyramidal geometry ($\tau = 0.61$) with the amino group of $^{tBu}APH^{-}$ in an axial position *trans* to N5. To the best of our knowledge, **4** represents the first synthetic model of an aminophenol dioxygenase.

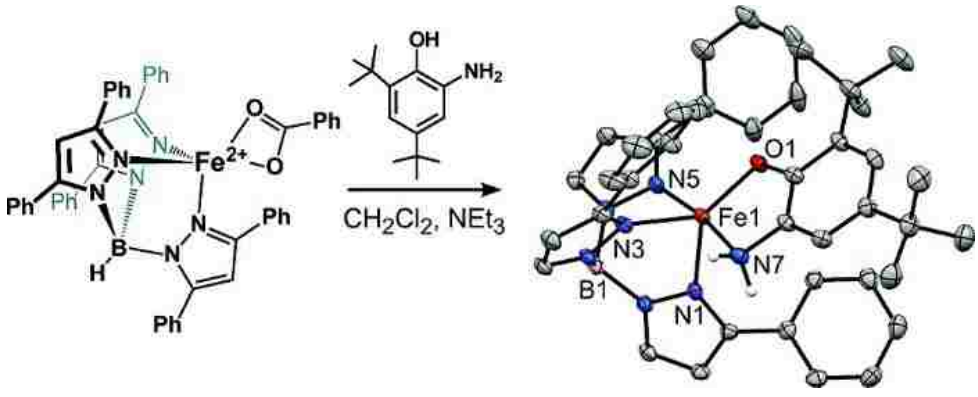

Figure 3.3. Synthesis and thermal ellipsoid diagram of complex **4**. For the sake of simplicity, the 5-Ph substituents of the ^{Ph2}Tp ligand have been omitted and only the amino hydrogens are shown. Selected bond lengths are provided in Table 3.1

Table 3.1. Selected Bond Distances (Å) for Complexes **4**-[**6**]$^+$

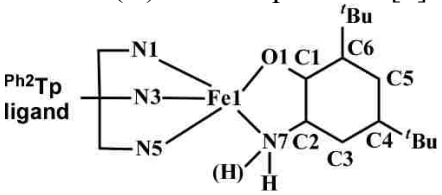

	4	5	[6]SbF$_6$[a]
Fe1-N1	2.101(1)	2.108(2)	2.071(7)
Fe1-N3	2.127(1)	2.087(2)	2.038(7)
Fe1-N5	2.223(1)	2.216(2)	2.134(6)
Fe1-O1	1.931(1)	2.095(2)	2.082(6)
Fe1-N7	2.214(1)	1.982(2)	2.017(8)
O1-C1	1.345(2)	1.285(3)	1.26(1)
N7-C2	1.451(2)	1.328(4)	1.33(1)
C1-C2	1.398(2)	1.469(5)	1.47(1)
C2-C3	1.388(2)	1.413(4)	1.42(1)
C3-C4	1.388(2)	1.363(4)	1.35(2)
C4-C5	1.403(2)	1.427(4)	1.43(2)
C5-C6	1.394(2)	1.375(4)	1.37(2)
C1-C6	1.420(2)	1.440(4)	1.44(1)

[a]The bond distances listed here represent the average distance in the two independent units of [**6**]$^+$, while the uncertainty is taken to be the larger of the two σ-values.

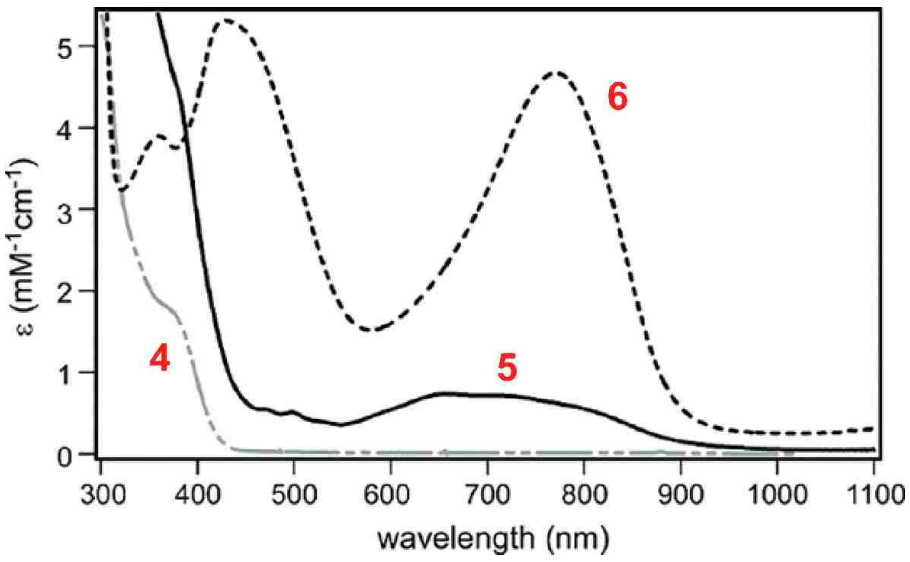

Figure 3.4. Electronic absorption spectra of **4** (— - -), **5** (—), and [**6**]SbF$_6$ (- - -) measured in CH_2Cl_2 at RT.

Reaction of **4** with 1 equiv of 2,4,6-tri-*tert*-butylphenoxy radical (TTBP$^{\bullet}$) at RT in CH_2Cl_2 gives rise to a distinct chromophore, **5**, with a broad absorption manifold centered at 715 nm (ε_{max} = 0.76 mM^{-1} cm^{-1}; see Figure 3.4). Addition of MeCN, followed by cooling to -30 °C, provides pale green crystals of **5** suitable for crystallographic analysis. As with **4**, the X-ray structure of **5** features a neutral 5C Fe complex with a distorted trigonal-bipyramidal geometry (τ = 0.58), although O1 now occupies an axial position instead of N7 (Figure 3.5). The N7 atom in **5** is monoprotonated, confirming that **5** is generated via abstraction of an H-atom from the –NH_2 group of **4**.

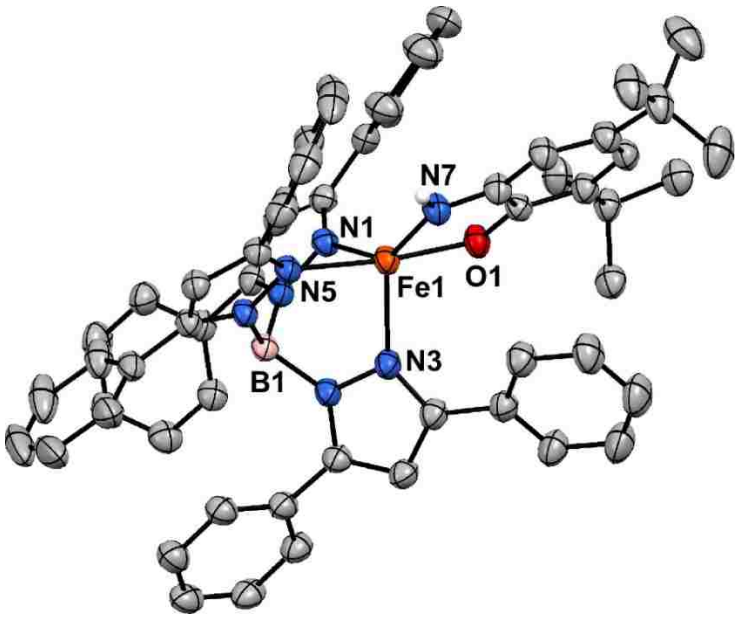

Figure 3.5. Thermal ellipsoid plot (50% probability) of **5**•2CH_2Cl_2. Noncoordinating solvent molecules and most hydrogen atoms have been omitted for clarity. The ^{tBu}ISQ ligand is disordered in a 7:1 ratio; only the high-occupancy (major) species is shown here.

Interestingly, the average Fe1-N_{Tp} bond distance observed for **5** (2.136 Å) is nearly identical to the value found for **4** (2.150 Å), suggesting minimal change in Fe charge. Metric parameters for the O,N-coordinated ligand, however, are dramatically different in the two structures. In the structure of **4**, the six C-C bonds of the $^{tBu}APH^{-}$ ring are approximately equidistant (1.40 ± 0.02 Å), reflecting its closed-shell, aromatic nature. In contrast, the corresponding C-C bond distances in **5** exhibit the "four long/two short" distortion commonly observed for quinoid moieties (Table 3.1).[35,36,38,78,80-83,129-131] The short O1-C1 and N7-C2 distance of 1.285(3) and 1.328(4) Å, respectively, are also characteristic of ISQ^{-} ligands, as amply demonstrated by Wieghardt[78,80-83,130,131] and others.[38] Thus, the X-ray crystallographic data strongly support the formulation of **5** as [(^{Ph2}Tp)Fe^{2+}(^{tBu}ISQ)]. This assignment rationalizes the absorption spectrum of **5**, which closely resembles those reported for Co^{2+} and Ni^{2+} complexes with a lone ISQ^{-} ligand.[131]

The X-band EPR spectrum of **5** displays an intense peak at g = 6.5, along with a broad derivative-shaped feature centered near g = 1.8 (Figure 3.6). Such spectra are typical of S = 3/2 systems with large and rhombic zero-field splitting parameters.[130-132] The simulated spectrum in Figure 3.6 assumed a negative D-value (with $|D| \gg h\nu$), an E/D-ratio of 0.24, and g-values of 2.36, 2.30, and 2.17. Significant E/D strain was incorporated to adequately account for the broadness of the higher-field features. The combined experimental results therefore indicate that **5** contains a high-spin Fe^{2+} center (S = 2) antiferromagnetically coupled to a ^{tBu}ISQ radical anion.

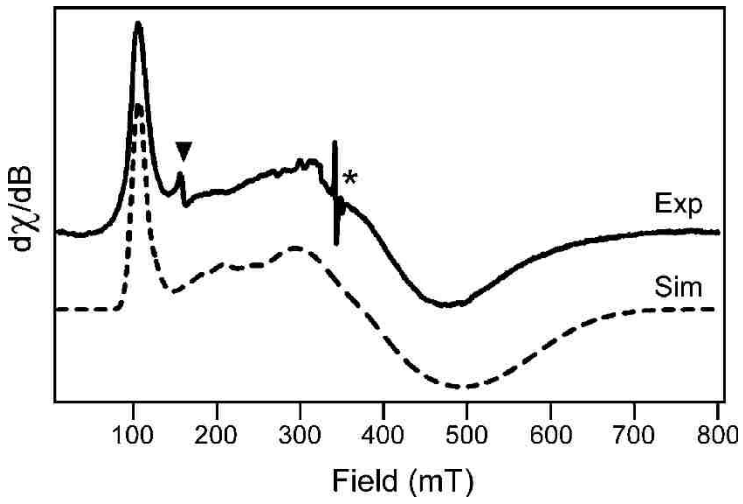

Figure 3.6. X-band EPR spectrum of **5** at 20 K. The derivative-shaped feature at g = 4.3 (▼) arises from a minor ferric impurity, while the feature at g = 2.0 (*) is due to residual TTBP radical. Parameters used to generate the simulated spectrum are provided in the text.

Further evidence in favor of a ligand-based radical was obtained from density functional theory (DFT) calculations. Two geometry-optimized models of **5** with S = 3/2 were computed that differ with respect to their electronic configurations. Analysis of the geometric and electronic structure of the first model (**5$_1$**) indicates that it contains an intermediate-spin Fe^{3+} center coordinated to a closed-shell imidophenolate ligand, $^{tBu}AP^{2-}$. The optimized structure of **5$_1$** features a square-pyramidal geometry ($\tau = 0.18$) with very short Fe-O1 and Fe-N7 distances of ~1.87 Å, in poor agreement with the experimental structure (Table 3.2). Furthermore, the computed bond distances for the $^{tBu}AP^{2-}$ ligand deviate sharply from the distances found experimentally for **5** with nearly all such differences being significantly greater than the estimated error (3σ) in the crystallographic data. The second model (**5$_2$**) was generated via a broken-symmetry calculation in order to obtain the [(^{Ph2}Tp)Fe^{2+}(^{tBu}ISQ)] electronic configuration described above. The resulting structure accurately reproduces the overall trigonal-bipyramidal

geometry of **5** and provides reasonably consistent Fe-ligand distances. Most importantly, the computed and experimental $^{tBu}ISQ^{-}$ bond distances exhibit remarkable agreement, with an rms deviation of merely 0.007 Å. (Table 3.2) Model $\mathbf{5_2}$ is also 9 kcal/mol more stable than $\mathbf{5_1}$, indicating an energetic preference for the Fe^{2+}-^{tBu}ISQ form.

To the best of our knowledge, the electronic structure of **5** has no precedent among synthetic complexes. While Fe^{2+}-SQ intermediates are often invoked in the mechanisms of catechol dioxygenases, all relevant models to date feature unambiguous $[Fe^{3+}$-catecholate$]^{+}$ units.[133-135] Similarly, the Fe^{3+}-ISQ complexes generated by Wieghardt and co-workers exclusively undergo ligand-based reductions to give the corresponding Fe^{3+}-AP species.[81,130,131] The unique Fe^{2+}-ISQ configuration of **5** is likely due to the presence of a high-spin, 5C Fe ion, whereas related complexes prepared by Wieghardt (such as $[(L)Fe^{3+}(^{R}ISQ)]^{+}$, where L = cis cyclam and R = H or ^{t}Bu) generally feature lowspin, 6C Fe centers.[81] Thus, changes in spin state and coordination geometry are capable of shifting the delicate balance between the Fe^{2+}-ISQ and Fe^{3+}-AP valence tautomers.

Reaction of **5** with 1 equiv of an acetylferrocenium salt in CH_2Cl_2 provides a dark green species, $[\mathbf{6}]^{+}$, with intense absorption features at 770 and 430 nm (Figure 3.4). Treatment of $[\mathbf{6}]^{+}$ with 1 equivalent of reductant (such as $Fe(Cp^*)_2$) fully regenerates **5**, indicating that the two species are related by a reversible one-electron process (Figure 3.7). EPR experiments with frozen solutions of $[\mathbf{6}]^{+}$ failed to detect a signal in either perpendicular or parallel mode, indicative of an integer-spin system. Indeed, the magnetic moment of $[\mathbf{6}]^{+}$ was found to be 5.0(1) μ_B at RT, close to the spin-only value for an S = 2 paramagnet.

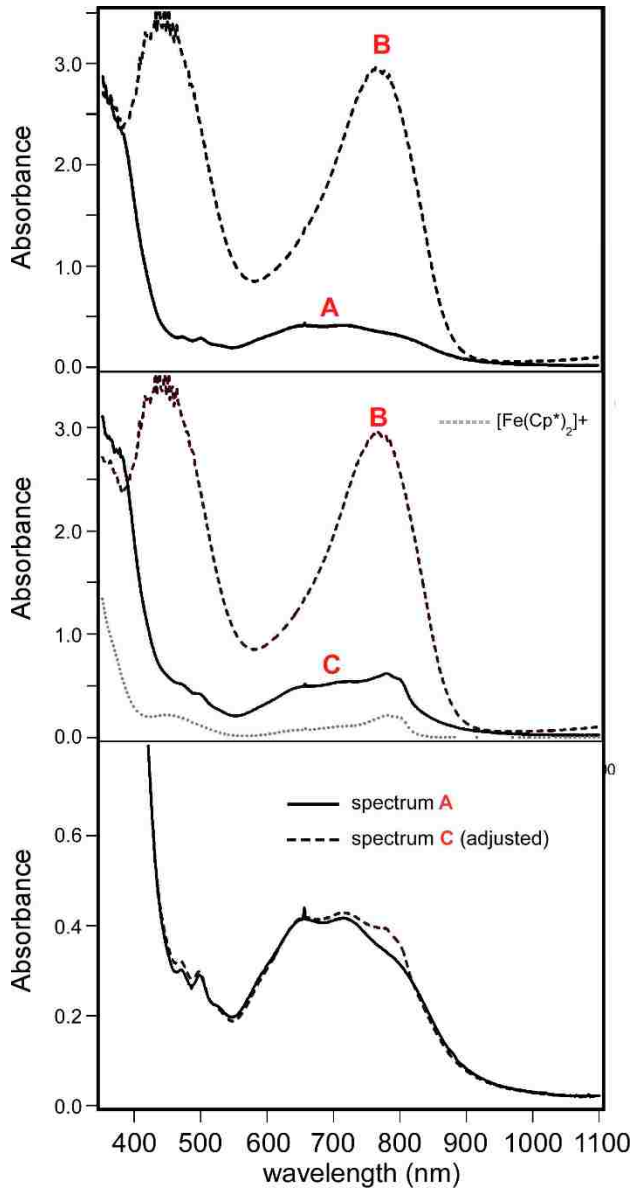

Figure 3.7. Interconversion of **5** and $[\mathbf{6}]^+$ by one-electron reactions. *Top*: Spectrum **A** = 0.55 mM solution of **5** at RT in CH_2Cl_2. Spectrum **B** = Formation of $[\mathbf{6}]^+$ after addition of 0.9 equivalents of the oxidant acetylferrocenium tetrafluoroborate to the initial solution (**A**). *Middle*: Spectrum **C** = Spectrum measured after addition of 0.95 equiv. of the reductant $Fe(Cp^*)_2$ to the **B** solution. The gray dotted line is the spectrum of 0.42 mM $[Fe(Cp^*)_2]BF_4$. *Bottom*: Spectrum **C** (adjusted) = Spectrum **C** minus the contributions from the $[Fe(Cp^*)_2]^+$ features. The adjusted spectrum is nearly identical to spectrum **A**, indicating full regeneration of **5**.

Table 3.2. Selected bond distances (Å) and bond angles (deg) for **4** and **5** obtained from X-ray diffraction (XRD) experiments, along with values computed by density functional theory (DFT) for models $\mathbf{5_1}$ and $\mathbf{5_2}$.

Bond distances	**4** (XRD)	**5**-maj (XRD)[a]	**5**-min (XRD)[a]	$\mathbf{5_1}$ (DFT)	$\mathbf{5_2}$ (DFT)
Fe1-N1	2.101(1)	2.108(2)	2.108(2)	2.057	2.129
Fe1-N3	2.127(1)	2.087(2)	2.087(2)	2.278	2.136
Fe1-N5	2.223(1)	2.216(2)	2.216(2)	2.043	2.299
Fe1-O1	1.931(1)	2.095(2)	2.13(1)	1.887	2.130
Fe1-N7	2.214(1)	1.982(2)	2.00(2)	1.887	2.029
O1-C1	1.345(2)	1.285(3)	1.284(14)	1.322	1.276
N7-C2	1.451(2)	1.328(4)	1.326(16)	1.359	1.335
C1-C2	1.398(2)	1.469(5)	1.473(18)	1.418	1.461
C2-C3	1.388(2)	1.413(4)	1.432(16)	1.404	1.420
C3-C4	1.388(2)	1.363(4)	1.356(16)	1.386	1.372
C4-C5	1.403(2)	1.427(4)	1.433(16)	1.408	1.427
C5-C6	1.394(2)	1.375(4)	1.396(14)	1.390	1.372
C1-C6	1.420(2)	1.440(4)	1.444(14)	1.405	1.432
Bond angles	**4** (XRD)	**5**-maj (XRD)[a]	**5**-min (XRD)[a]	$\mathbf{5_1}$ (DFT)	$\mathbf{5_2}$ (DFT)
N1-Fe1-N3	92.82(5)	93.44(7)	93.44(7)	89.8	94.6
N1-Fe1-N5	83.309(5)	82.76(7)	82.76(7)	87.2	83.3
N3-Fe1-N5	86.11(5)	89.80(7)	89.80(7)	89.6	86.1
O1-Fe1-N3	136.61(5)	94.16(7)	93.9(3)	91.6	97.2
O1-Fe1-N5	129.47(5)	95.62(7)	90.4(3)	97.4	97.6
N7-Fe1-N1	105.94(4)	173.93(8)	170.0(3)	173.0	176.2
N7-Fe1-N3	92.60(5)	138.99(9)	136.0(4)	163.5	138.5
N7-Fe1-N5	88.68(5)	127.37(9)	132.8(4)	106.4	126.8
N7-Fe1-N7	173.20(5)	99.36(8)	101.1(4)	95.8	98.6
O1-Fe1-N7	80.76(4)	79.52(8)	78.2(5)	83.2	78.5
T-value	0.61	0.58	0.57	0.16	0.63

[a] In the crystal structures of $5 \cdot 2CH_2Cl_2$, the ^{tBu}ISQ ligand is disordered in a 7:1 ratio. The metric parameters provided in Table 3.1 refer to the high-occupancy (major) species. Here we also provide parameters for the low-occupancy (minor) species.

Table 3.3. Selected bond distances (Å) and bond angles (deg) for [**6**]$^+$ obtained from X-ray diffraction (XRD) experiments, along with values computed by density functional theory (DFT).

Bond distances	[**6**^{1}]$^+$ (XRD)[a]	[**6**^{2}]$^+$ (XRD)[a]	[**6**$_{DFT}$]$^+$ (DFT)
Fe1-N1	2.084(6)	2.058(7)	2.078
Fe1-N3	2.037(7)	2.039(6)	2.077
Fe1-N5	2.132(7)	2.135(6)	2.137
Fe1-O1	2.088(6)	2.076(6)	2.078
Fe1-N7	2.009(8)	2.025(7)	2.047
O1-C1	1.277(11)	1.250(11)	1.256
N7-C2	1.358(11)	1.308(11)	1.311
C1-C2	1.474(11)	1.472(13)	1.482
C2-C3	1.400(12)	1.446(12)	1.425
C3-C4	1.377(13)	1.313(16)	1.364
C4-C5	1.417(13)	1.449(18)	1.451
C5-C6	1.363(13)	1.386(15)	1.361
C1-C6	1.429(11)	1.449(12)	1.442
Bond angles	[**6**^{1}]$^+$ (XRD)[a]	[**6**^{2}]$^+$ (XRD)[a]	[**6**$_{DFT}$]$^+$ (DFT)
N1-Fe1-N3	94.5(3)	93.9(3)	95.4
N1-Fe1-N5	84.6(3)	84.7(3)	88.5
N3-Fe1-N5	92.4(3)	91.6(2)	90.3
O1-Fe1-N3	86.6(2)	95.4(3)	93.3
O1-Fe1-N5	93.8(3)	96.2(2)	93.3
N7-Fe1-N1	169.6(3)	172.2(2)	175.9
N7-Fe1-N3	144.6(3)	149.3(3)	137.3
N7-Fe1-N5	117.6(3)	149.3(3)	126.0
N7-Fe1-N7	106.9(3)	99.0(3)	100.0
O1-Fe1-N7	77.4(3)	76.9(3)	76.2
T-value	0.42	0.38	0.64

[a] The crystal structure of [**6**]SbF_6•0.5DCE contains two symmetrically-independent units, here labeled [**6**^{1}]$^+$ and [**6**^{2}]$^+$.

X-ray quality crystals of [**6**]SbF_6 were prepared by vapor diffusion of pentane into a concentrated dichloroethane solution. The resulting structure (Figure 3.8) contains two symmetrically independent Fe units, each featuring a distorted square-pyramidal geometry (τ = 0.42 and 0.38). Despite the difference in charge, complexes [**6**]$^+$ and **5** have identical atomic compositions. Yet the average Fe−N_{Tp} bond distance shortens from 2.132 to 2.081 Å upon conversion of **5** to [**6**]$^+$, suggesting an increase in Fe-based charge. While the structural parameters of the bidentate O,N-donor ligand of [**6**]$^+$ are consistent

with a ^{tBu}ISQ-radical, it was not possible to rule out a neutral iminobenzoquinonate ligand (^{tBu}IBQ) due to sizable uncertainties in the bond distances.

We therefore turned to DFT calculations to further explore the electronic structure of [**6**]$^+$. The resulting geometryoptimized model, [**6$_{DFT}$**]$^+$, exhibits good agreement with the crystallographic data, although the DFT structure is more distorted toward the trigonal-bipyramidal limit (τ = 0.64; Table 3.3). The computed Fe-ligand bond distances nicely match the experimental values (rms deviation = 0.022 Å), indicating that the calculation converges to the correct S = 2 electronic configuration. Comparison of [**6$_{DFT}$**]$^+$ and **5$_2$** reveals more pronounced "quinoid" character in the O,N-donor ligand of the former. Using the experimentally derived correlations of bond distances and ligand oxidation states recently published by Brown, the O,N-donor ligand of [**6$_{DFT}$**]$^+$ has an oxidation state of −0.35(5) (i.e., partway between ISQ^{1-} and IBQ^0).[136] Moreover, the highest-occupied spin-down MO (β-HOMO) of [**6**]$^+$ contains roughly equal Fe and ligand character (47 and 42%, respectively), and the β-LUMO is evenly delocalized over the two units (Figure 3.9). Thus, the DFT results suggest that the electronic structure of [**6**]$^+$ lies between the Fe^{3+}-^{tBu}ISQ and Fe^{2+}-^{tBu}IBQ limits. Detailed spectroscopic studies of [**6**]$^+$ will be discussed in the next chapter.

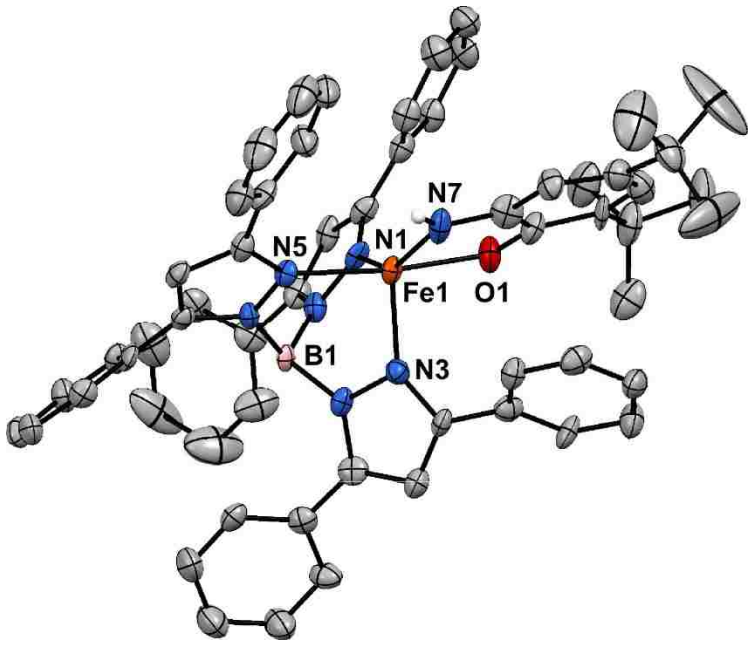

Figure 3.8. Thermal ellipsoid plot (50% probability) of **[6]SbF$_6$**•0.5DCE. Counteranions, noncoordinating solvent molecules, and most hydrogen atoms have been omitted for clarity. Only one of the two independent [**6**]$^+$ units is shown.

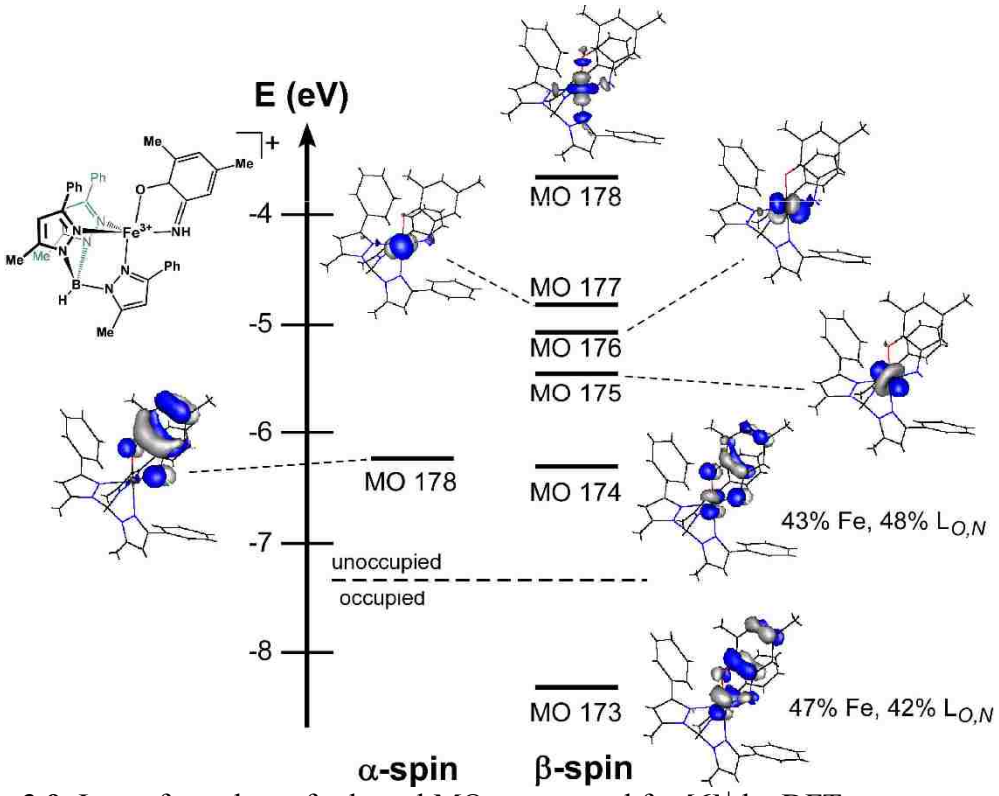

Figure 3.9. Isosurface plots of selected MOs computed for **[6]**$^+$ by DFT.

3.C. Conclusions

Complexes synthesized in this chapter model the enzyme active site structure of APDOs and are the first to do so. Complex **4** can be converted to a novel complex upon reaction with 1 equivalent of phenoxyl radical (**6**). While the structure of **6** can be described as a having an iminobenzosemiquinonate radical ligand, this is not definitive due to large uncertainties in the crystal structure bond distances. Further studies described in the following chapter will provide more evidence for the electronic structure of **5** and [**6**]SbF_6.

Complexes **4**−**6** replicate key structural and electronic aspects of the proposed *o*-aminophenol dioxygenase mechanism. In particular, the conversion of **4**→**5** mimics the transformation of the enzyme−substrate complex (**A**) into a ferrous−ISQ species (**B**) via coupled proton and electron transfers. Our results therefore provide a synthetic precedent for the existence of Fe^{2+}-ISQ intermediates in enzymatic catalysis. Of course, complex **5** is an imperfect model of intermediate B, since it lacks the coordinated superoxo ligand.

3.D. Experimental

All reagents and solvents were purchased from commercial sources and used as received unless otherwise noted. Acetonitrile and dichloromethane were purified and dried using a Vacuum Atmospheres solvent purification system. The compounds $K(^{Ph2}Tp)$,[137] $^{tBu}APH_2$,[138] and TTBP•[139] were prepared according to literature procedures. The synthesis and handling of airsensitive materials was carried out under an inert atmosphere using a Vacuum Atmospheres Omni-Lab glovebox equipped with a freezer

set to -30 °C. Elemental analyses were performed at Midwest Microlab, LLC in Indianapolis, IN. Infrared (IR) spectra of solid samples were measured with a Thermo Scientific Nicolet iS5 FTIR spectrometer equipped with the iD3 attenuated total reflectance accessory. UV-vis spectra were obtained with an Agilent 8453 diode array spectrometer. Magnetic susceptibility measurements were carried out using the Evans NMR method.

EPR experiments were performed using a Bruker ELEXSYS E600 equipped with an ER4415DM cavity resonating at 9.63 GHz., an Oxford Instruments ITC503 temperature controller and ESR-900 He flow cryostat. The spectrum shown in Figure 3.6 was obtained under the following conditions: [**5**] = 2.3 mM in CH_2Cl_2; frequency = 9.63 GHz.; power = 10.0 mW; modulation = 1 G; temperature = 20 K. The program EasySpin[140] was used to simulate the experimental spectra.

Density functional theory (DFT) calculations of complexes **5** and $[\mathbf{6}]^+$ were performed using the ORCA 2.7 software package developed by Dr. F. Neese.[141] In each case, the corresponding X-ray structure provided the starting point for geometry optimizations. In the computational models, the 5-Ph groups of the ^{Ph2}Tp ligand were replaced by -CH3 groups, and the tBu moieties at the 4- and 6-positions of the ^{tBu}ISQ ligand were also replaced with methyl groups. All calculations employed Becke's three-parameter hybrid functional for exchange along with the Lee-Yang-Parr correlation functional (B3LYP).[142,143] All atoms were equipped with Ahlrichs' valence triple-ζ basis set (TZV), in conjunction with the TZV/J auxiliary basis set.[144,145] Polarization functions were also included on all atoms. Finally, the gOpenMol program developed by Laaksonen[146] was used to generate isosurface plots of molecular orbitals.

[Fe^{2+}(^{Ph2}Tp)(^{tBu}APH)] (4). (^{Ph2}Tp)Fe^{2+}(OBz) was prepared following a published procedure. (^{Ph2}Tp)Fe^{2+}(OBz) (723 mg, 0.85 mmol) and 4,6-di-*t*-butyl-aminophenol (190 mg, 0.86 mmol) were dissolved in 12 mL of CH_2Cl_2. Following addition of 0.13 mL of NEt_3 (0.95mmol), the resulting solution was stirred for 16 hours. The solution was filtered and the solvent removed under vacuum to give a light yellow solid. The product was then dissolved in 5 mL of CH_2Cl_2, layered with excess MeCN, and placed overnight in a -30 °C freezer. The resulting crystals were dried to provide complex **4** in 71% yield (569 mg). X-ray quality crystals were obtained by vapor diffusion of MeCN into a concentrated 1,2-dichloroethane (DCE) solution of **4**. Elemental analysis calcd for $C_{59}H_{56}FeBN_7O$: C, 74.93; H, 5.97; N, 10.37%; found: C, 74.20; H, 5.86; N, 10.04%. The disagreement in the %C-value is due to the presence of small amounts of solvent impurities. UV-vis [λ_{max}, nm (ε, M^{-1} cm^{-1}) in CH_2Cl_2]: 371 (1620). IR (neat, cm^{-1}, selected bands): 3332 (NH_2), 3284 (NH_2), 2613 (BH).

[Fe^{2+} (^{Ph2}Tp)(^{tBu}ISQ)] (5). Complex **4** (301 mg, 0.32 mmol) and TTBP• (84 mg,0.32 mmol) were dissolved in 10 mL of CH_2Cl_2, and the resulting dark green solution was stirred for 45 min. The solvent was reduced to 5 mL and layered with excess CH_3CN. Thin green needles developed after standing overnight at -30 °C. The solvent was decanted and the product collected and dried to give a green powder (121 mg, 40% yield). Elemental analysis calcd. for $C_{59}H_{55}FeBN_7O$: C, 75.01; H, 5.87; N 10.38%; found: C, 74.77; H, 6.01; N 10.01%. UV-vis [λ_{max}, nm (ε, M^{-1} cm^{-1}) in CH_2Cl_2]: 335 (6950), 715 (750). IR (neat, cm^{-1}, selected bands): 3334 (NH), 2614 (BH).

[Fe^{3+}(^{Ph2}Tp)(^{tBu}ISQ)]SbF_6 ([6]SbF_6). Two distinct methods were used to generate complex [**3a**]SbF_6. **Method A:** Complex **1a** (284 mg, 0.30 mmol) and two

equivalents of $AgSbF_6$ (212 mg, 0.62 mmol) were mixed in 10 mL of CH_2Cl_2 and stirred for one hour. The solution was filtered through Celite twice and the solvent removed under vacuum. The resulting solid was washed with diethyl ether (2 x 15 mL) and dried to give 218 mg of dark green powder (62% yield).

Method B: Complex **5** (116 mg, 0.12 mmol) and one equivalent of $AgSbF_6$ (42 mg, 0.12 mmol) were mixed in 6 mL of CH_2Cl_2 and stirred for one hour. The resulting dark green solution was filtered twice through Celite and vacuumed to dryness to yield a dark green solid (75 mg, 52% yield). X-ray quality crystals of [**6**]SbF_6 were obtained by vapor diffusion of pentane into a concentrated 1,2-dichloroethane solution. UV-vis [λ_{max}, nm (ε, M^{-1} cm^{-1}) in CH_2Cl_2]: 430 (5320), 767 (4670). IR (neat, cm^{-1}, selected bands): 3266 (NH), 2646 (BH).

The sample of **[6]SbF_6** sent for elemental analysis was prepared using Method B. The results indicate that **[6]SbF_6** was only generated in 84% yield, due to incomplete oxidation of the starting material **5**. Elemental analysis calcd for $C_{59}H_{55}FeBF_6N_7OSb$: C, 60.03; H, 4.70; N, 8.31; F, 9.66%. Calculated values assuming 84% conversion of **5** to [**6**]SbF_6: C, 62.00; H, 4.85; N, 8.58; F, 8.38%. Found: C, 61.93; H, 5.25; N, 8.18; F, 8.17%.

X-ray diffraction (XRD) data were collected at 100 K with an Oxford Diffraction SuperNova Kappa-diffractometer (Agilent Technologies) equipped with dual microfocus Cu/Mo X-ray sources, X-ray mirror optics, Atlas CCD dectector, and low-temperature Cryojet device. Crystallographic data for particular compounds are shown in Table 3.4. The data were processed with CrysAlis Pro program package (Agilent Technologies, 2011) typically using a numerical Gaussian absorption correction (based on the real shape

of the crystal), followed by an empirical multi-scan correction using SCALE3 ABSPACK routine. The structures were solved using SHELXS program and refined with SHELXL program[147] within Olex2 crystallographic package.[148] B- and C-bonded hydrogen atoms were positioned geometrically and refined using appropriate geometric restrictions on the corresponding bond lengths and bond angles within a riding/rotating model (torsion angles of methyl hydrogens were optimized to better fit the residual electron density).

The structure of complex **4** contains additional MeCN and DCE (1,2-dichloroethane) solvent molecules; the latter is positioned on a crystallographic inversion center. The hydrogen atoms of the $–NH_2$ group were localized ina difference Fourier synthesis and refined isotropically.

For complex **4** the structure contains a non-stoichiometric amount of heavily disordered solvent (CH_2Cl_2) molecules. In addition, the ^{tBu}ISQ ligand is partially (13%) disordered over an internal (non-crystallographic mirror plane formed by the tripodal ^{Ph2}TP supporting ligand. The NH hydrogen atom of the minor component of the disorder was localized objectively in a difference Fourier synthesis and then refined isotropically. The corresponding –NH hydrogen of the minor component was treated geometrically.

Complex [**6**]SbF_6 has a crystal structure that represents a regular twin (with a 48:52 component ratio) grown with a 180° rotation around reciprocal x axis. It was treated using HKLF 5 refinement option (Sheldrick, 2008). The structure contains two symmetrically-independent complex ionic units along with one equivalent of DCE solvent. Because of the twinning, Fourier maps were substantially compromised and objective localization of the H atom of –NH group was not feasible.

Its presence was established by FTIR spectroscopy. Therefore, this H atom was positioned geometrically and refined using a riding model with appropriate geometric restraints.

Table 3.4. Summary of X-ray Crystallographic Data Collection and Structure Refinement[a]

	4•MeCN•0.5DCE	**5**•2CH_2Cl_2 c	[**6**]SbF_6•0.5DCE
empirical formula	$C_{62}H_{61}BClFeN_8O$	$C_{61}H_{59}BCl_4FeN_7O$	$C_{60}H_{57}BClF_6FeN_7OSb$
formula weight	1036.30	1114.64	1229.99
crystal system	monoclinic	monoclinic	monoclinic
space group	$P2_1/n$	$P2_1/c$	$P2_1/c$
a, Å	10.0304(2)	14.9365(6)	39.237(1)
b, Å	32.0673(6)	9.9321(5)	13.8346(4)
c, Å	17.1467(3)	37.6317(14)	20.7143(5)
α, deg	90	90	90
β, deg	97.680(2)	92.617(4)	97.218(3)
γ, deg	90	90	90
V, $Å^3$	5465.76(19)	5576.9(4)	11155.2(5)
Z	4	4	8
D_{calc}, g/cm^3	1.259	1.253	1.465
λ, Å	0.7107	1.5418	1.5418
μ, mm^{-1}	0.374	3.583	6.936
θ-range, deg	7 to 59	7 to 148	7 to 148
reflections collected	60411	30976	27278
independent reflections	13966	11016	27278
	[R_{int} = 0.0377]	[R_{int} = 0.0467]	[R_{int} = 0.0]
data/restraints/parameters	13966/0/682	11016/100/882	27278/0/1418
GOF (on F^2)	1.035	1.029	1.026
R1/wR2 ($I>2\sigma(I)$)[b]	0.413 / 0.0989	0.0512 / 0.1279	0.0831 / 0.2089
R1/wR2 (all data)	0.0519 / 0.1068	0.0643 / 0.1382	0.1115/0.2331

a DCE = 1,2-dichloroethane b $R1 = \sum \| F_0 \| - \| F_c \| / \sum | F_0 |$; $wR2 = [\sum w(F_0^2 - F_c^2)^2 / \sum w(F_0^2)^2]^{1/2}$ c The solvate molecules in 5•2CH_2Cl_2 are only partially populated.

Chapter 4

Spectroscopic and Computational Studies of Fe Complexes with *o*-Aminophenolate and Iminobenzosemiquinone Ligands

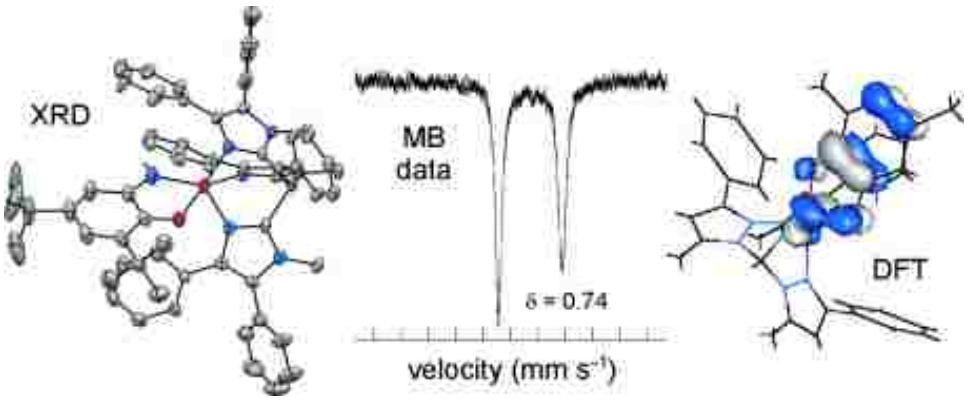

Abstract: The complexes reported in chapter 3 are examined with various spectroscopic methods, including UV-vis absorption, magnetic circular dichroism (MCD), electron paramagnetic resonance (EPR), and Mössbauer spectroscopies. In addition, an analogous series of complexes featuring the ^{Ph2}TIP supporting ligand are synthesized and characterized. The spectroscopic data are interpreted with the help of density functional theory (DFT) calculations, resulting in detailed electronic structure descriptions.

Portions of this chapter have appeared in the paper: Bittner, M. M.; Kraus, D.; Lindeman, S. V.; Popescu, C. V.; Fiedler, A. T. *Chem. Eur. J.* **2013**, 9686-9698.

All DFT calculations and resonance Raman experiments were performed by Dr. Adam Fiedler.

Mössbauer experiments were conducted by Codrina V. Popescu of Ursinus College.

4.A. Introduction

A critical step in the microbial degradation of numerous aromatic compounds involves oxidative ring scission by a mononuclear nonheme Fe dioxygenase.[90,91] Ring-cleaving dioxygenases have been shown to oxidize and impressive array of substrates, including catechols, protocatechuates,[31,149] *o*-aminophenols,[10,11] hydroquinones,[7-9,94,96,150,151] and salicylates.[58,101,102] The general catalytic strategy employed by these dioxygenase differs substantially from the "textbook" O_2-activation mechanism exemplified by the cytochrome P450s,[152] methane monooxygenase,[28] and α-ketoglutarate-dependent dioxygenases.[29] In this set of enzymes, O_2 is used to generate an iron(IV)-oxo (ferryl) intermediate that performs the demanding hydroxylation of an aliphatic substrate. By contrast, extensive experimental and computational studies have revealed that the ring-cleaving dioxygenase mechanism does not involve high-valent Fe intermediates, as illustrated for the extradiol catechol dioxygenases (ECDOs) and *o*-aminophenol dioxygenases (APDOs) in Figure 4.1[23,31,32,47] In both cases, the bidentate substrate coordinates to the Fe^{2+} center as a monoanionic ligand. Displacement of the bound H_2O molecules facilitates formation of an Fe/O_2 adduct capable of reacting directly with the bound substrate. The resulting peroxy-bridged intermediate undergoes a Criegee rearrangement to generate a lactone, which is hydrolyzed by the Fe─OH unit to provide the ring-opened product. Several of these intermediates were observed crystallographically in different subunits of the enzyme homoprotocatechuate 2,3-dioxygenase (HPCD).[18]

Despite significant progress in elucidating the catalytic cycles of ring-cleaving dioxygenases, the electronic structure of the critical Fe/O_2/substrate intermediate in

Figure 4.1 remains disputed (as described in Chapter 1). The development of suitable synthetic models can help resolve the ambiguous electronic structures of enzymatic intermediates. In the last chapter, we described the synthesis and X-ray structure of a five-coordinate Fe(II)-aminophenolate complex (**4**) (Figure 4.2). This complex was used to generate **5** – the first synthetic example of an Fe^{2+} center coordinated to a biologically relevant (imino)semiquinonate ligand (ISQ). The supporting ligand is hydrotris(3,5-di-phenylpyrazol-1-yl)borate (^{Ph2}Tp), which adequately models the facial coordination geometry and monoanionic charge of the 2-His-1-carboxylate coordination motif of most ring-cleaving dioxygenases.[19,153] A combination of crystallographic, spectroscopic (absorption, EPR), and computational methods were used to confirm the existence of the ^{tBu}ISQ ligand in **5**. The overall spin of 3/2 arises from antiferromagnetic (AF) coupling between the high-spin Fe^{3+} center (S = 5/2) and ISQ radical. Using similar techniques, we also examined the complex [**6**]SbF_6 that arises from one-electron oxidation of **5**. The X-ray structural data for [**6**]$^+$ are consistent with the presence of an Fe^{3+}—^{tBu}IBQ character (where ^{tBu}IBQ is the neutral iminobenzoquinone with *tert*-butyl substituents at the 4- and 6-positions.

Figure 4.1. Proposed catalytic cycle of ECDO and APDO.

In this chapter, we seek to develop detailed electronic-structure descriptions of **5** and $[\mathbf{6}]^{+}$ using an assortment of spectroscopic methods, including UV/Vis/NIR absorption, Mössbauer, magnetic circular dichroism (MCD), and resonance Raman (rR) spectroscopy. In addition, we have prepared a parallel series of complexes ($[\mathbf{1b}]^{+}$, $[\mathbf{2b}]^{+}$, and $[\mathbf{3b}]^{2+}$) containing the facial N_3-donor ligand tris(4,5-di-phenyl-1-methylimidazol-2-yl)phosphine (^{Ph2}TIP; Figure 4.2). X-ray structures of complexes [**1b**]BPh_4 and [**3b**]$(OTf)_2$ are presented to complement those already shown for **1a**, **2a**, and [**3a**]SbF_6. By employing this neutral supporting ligand, we are able to evaluate the role of the coordination environment in modulating the oxidation states of the Fe center and ISQ ligand. In all cases, the spectroscopic data were analyzed with the aid of DFT calculations. By elucidating the spectroscopic signatures of these synthetic complexes,

we anticipate that our results will assist in the interpretation of comparable data from the biological systems, thereby allowing researchers to determine whether Fe─(I)SQ species are viable intermediates in the catalytic cycles of ring-cleaving dioxygenases.

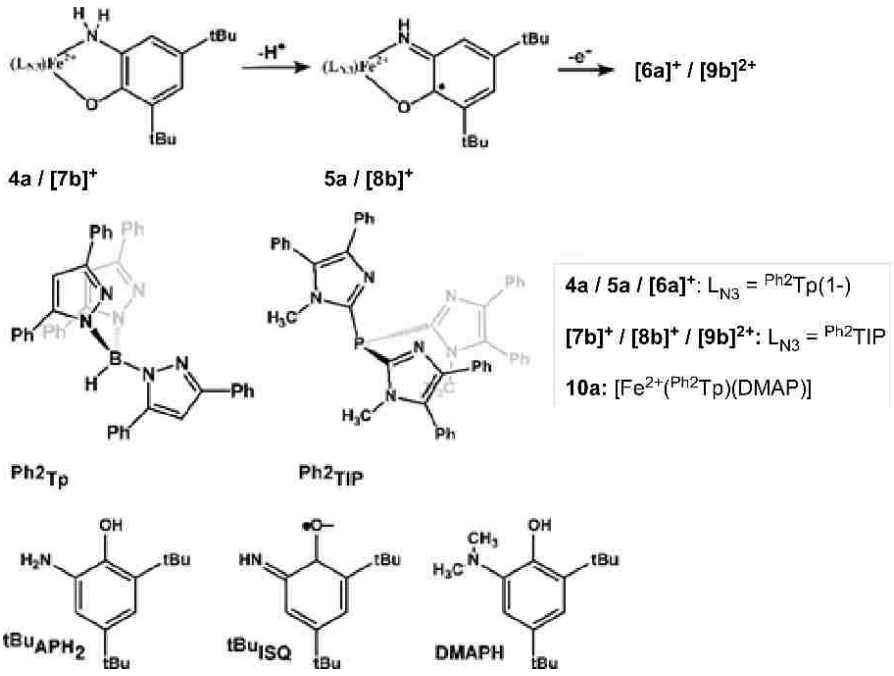

Figure 4.2. Complexes prepared and examined in this chapter.

4.B. Synthesis of Complexes [7b]$^{+}$-[9b]$^{2+}$ and 10a

The synthesis and X-ray structure of [Fe^{2+}(^{Ph2}Tp)(^{tBu}APH)] (**4a**) was reported in the previous chapter. The analogous complex [**7b**]$^{+}$ based on the neutral ^{Ph2}TIP ligand was generated by mixing [Fe^{2+}(^{Ph2}TIP)$(OTf)_2$][154] and 2-amino-4,6-di-*tert*-butylphenol ($^{tBu}APH_2$) with one equivalent of triethylamine in CH_2Cl_2; recrystallization from toluene/pentane provided [**7b**]OTf as a yellow solid. Following counteranion metathesis with $NaBPh_4$, X-ray quality crystals of [**7b**]BPh_4 were obtained by layering a

concentrated 1,2-dichloroethane (DCE) solution with MeOH. The resulting structure (Figure 4.3) contains two symmetrically independent [**7b**]$^+$ units with nearly identical geometries. Relevant structural parameters for **4a**, [**7b**]BPh_4, and **10a** are provided in Table 4.1. Similar to **4a**, complex [**7b**]$^+$ features a five-coordinate monoiron(II) center in a distorted trigonal-bipyramidal coordination environment ($\tau = 0.60$[155]). The amino and phenolate donors of the bidentate ^{tBu}APH ligand are found in axial and equatorial positions, respectively (Figure 4.1). The average Fe-N_{TIP} bond distance of 2.19 Å in [**7b**]$^+$ is ~0.04 Å longer than the average Fe-N_{Tp} distance in **4a**, reflecting the weaker donating ability of neutral ^{Ph2}TIP relative to anionic ^{Ph2}Tp. In both **4a** and [**7b**]$^+$, the Fe-N/O bond lengths are indicative of high-spin Fe(II) centers, consistent with the presence of paramagnetically-shifted peaks in their corresponding ^{1}H NMR spectra (Figure 4.4).

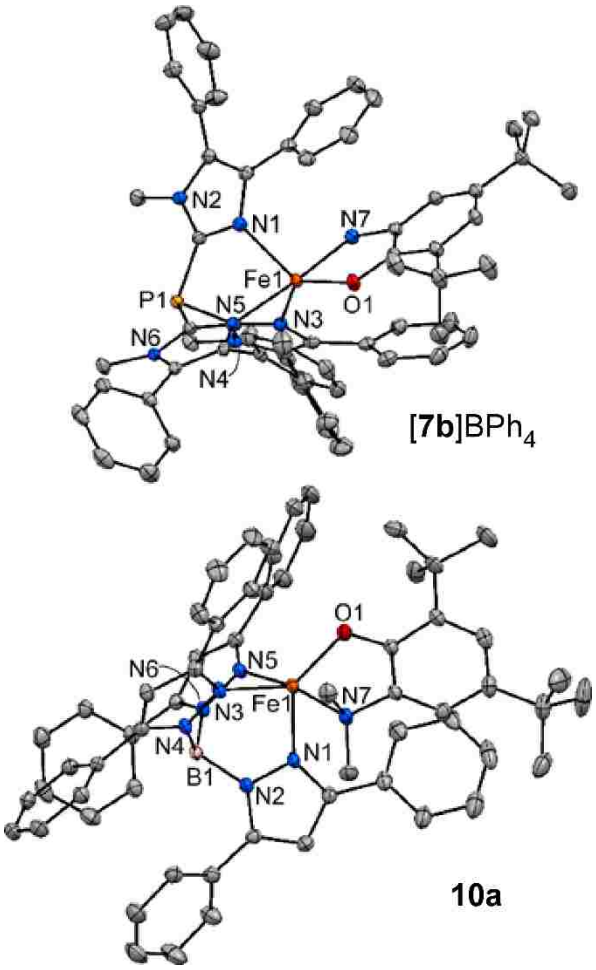

Figure 4.3. Thermal ellipsoid plot of [**7b**]BPh_4 and **10a**. Counteranions, noncoordinating solvent molecules, and most hydrogen atoms have been omitted for clarity.

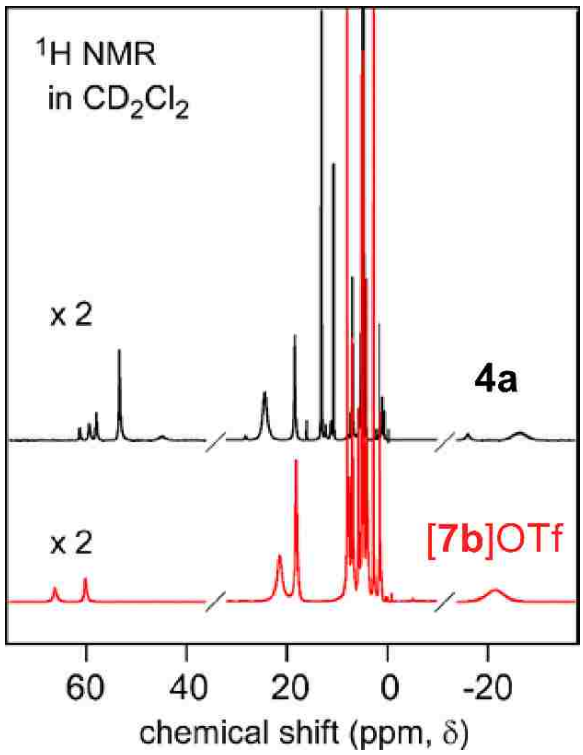

Figure 4.4. ^{1}H NMR spectra of **4a** (top) and [**7b**]OTf (bottom) in CD_2Cl_2. Note that peak intensities for the outer portions of the spectra were enlarged (x 2) for the sake of clarity.

Table 4.1. Selected bond lengths (Å) and angles (deg) for complexes **4a**, [**7b**]BPh_4, and **10a**

	4a•MeCN•0.5DCE	**7b[BPh_4]** •1.5DCE	**10a**•4CH_2Cl_2
Fe1-N1	2.101(1)	2.175(2)	2.121(2)
Fe1-N3	2.127(1)	2.175(2)	2.158(2)
Fe1-N5	2.223(1)	2.222(2)	2.236(2)
Fe1-O1	1.931(1)	1.929(2)	1.920(2)
Fe1-N7	2.214(1)	2.229(2)	2.335(2)
N1-Fe1-N3	92.82(5)	92.50(7)	100.11(9)
N1-Fe1-N5	83.30(5)	85.88(7)	80.90(9)
N3-Fe1-N5	86.11(5)	84.43(6)	81.79(9)
O1-Fe1-N1	136.61(5)	134.21(7)	131.71(9)
O1-Fe1-N3	129.47(5)	130.73(7)	127.63(9)
O1-Fe1-N5	105.94(4)	109.45(6)	109.69(9)
O1-Fe1-N7	80.76(4)	80.24(6)	78.07(8)
N1 -Fe-N7	92.60(5)	88.33(7)	100.11(9)
N3 -Fe-N7	88.68(5)	87.90(7)	98.07(9)
N5 -Fe-N7	173.20(5)	170.17(7)	170.40(9)
τ-value	0.61	0.60	0.65

The ^{Ph2}Tp-based complex **10a** contains the DMAPH ligand – the *N*,*N*-dimethylated version of ^{tBu}APH.

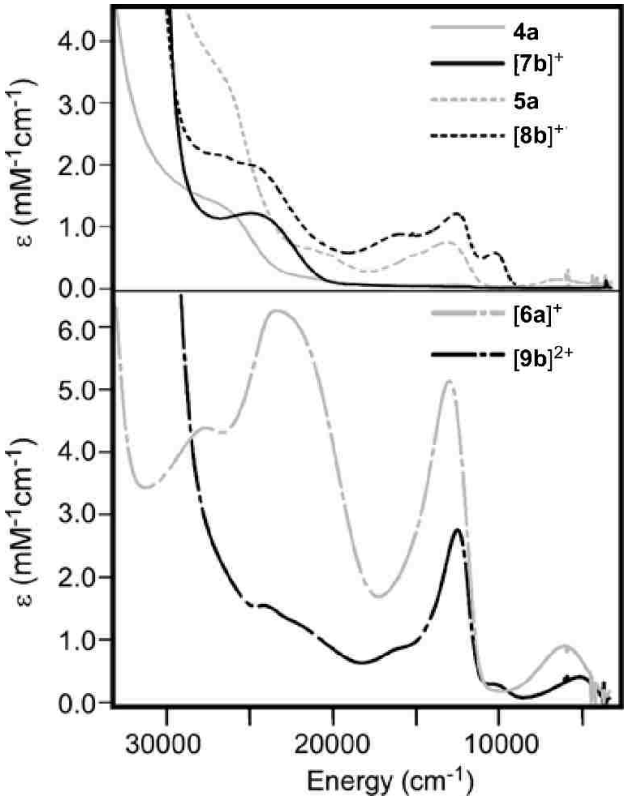

Figure 4.5. UV-vis spectra of complexes **4a-[6a]**$^+$, [**7b**]$^+$-[**9b**]$^+$, and **10a**.

This complex is intended serve as a "control", since methylation of the $-NH_2$ group hinders conversion to the ISQ state. The overall structure of **10a**, as revealed by X-ray crystallography (Figure 4.3), is quite similar to **4a**. The most prominent difference is the 0.12 Å elongation of the Fe1-N7 bond in **10a** relative to **4a** (Table 4.1), presumably due to steric repulsion between the -NMe_2 group and 3-Ph substituents of the ^{Ph2}Tp ligand. Additionally, the plane of the DMAPH ligand is bent away from the O1-Fe-N7 chelate ring by 26°, whereas the two planes are nearly colinear in **4a** and [**7b**]$^+$.

Treatment of [**7b**]OTf with TTBP$^\bullet$ in CH_2Cl_2 produces a light green chromophore [**8b**]$^+$ with an absorption spectrum similar to the one collected for **5a** (Figure 4.5). In addition, the EPR spectra of [**8b**]$^+$ and **5a** are nearly identical; both exhibit a sharp peak at $g \approx 6.5$ and broad derivative feature centered at $g < 1.8$ (Figure 4.6). Such spectra are characteristic of S = 3/2 systems with large, negative D values and moderate rhombicities (E/D = 0.24 and 0.18 for **5a** and [**8b**]$^+$, respectively). Unfortunately, despite repeated attempts, it was not possible to obtain X-ray quality crystals of [**8b**]$^+$. However, the strong resemblance between the spectroscopic features of **5a** and [**8b**]$^+$ suggests similar Fe^{2+}–ISQ electronic configurations—an assumption verified by analysis with Mössbauer spectroscopy (vide infra).

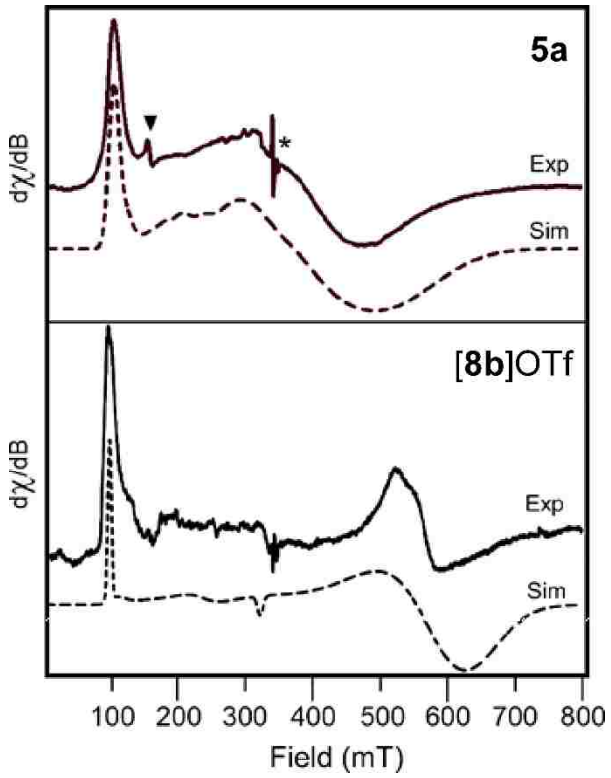

Figure 4.6. X-band EPR spectra of **5a** (top) and [**8b**]OTf collected at 20 and 10 K, respectively. The experimental spectra (solid lines) were simulated (dashed line) assuming a S = 3/2 ground state. Simulation parameters for **5a**: D = -10 cm^{-1}; E/D = 0.24; g = 2.36, 2.30, 2.17. Simulation parameters for [**8b**]OTf: D = -12 cm^{-1}; E/D = 0.18; g = 2.45, 2.35, 2.01. The program EasySpin4 was used to simulate the experimental spectra (S. Stoll and A. Schweiger, *Journal of Magnetic Resonance,* 2006, **178**, 42-55).

Oxidation of **4a** and [**7b**]OTf with two equivalents of AgX (X = SbF_6 or OTf) in CH_2Cl_2 gives rise to complexes [**6a**]SbF_6 and [**9b**]$(OTf)_2$, respectively, that each display a distinctive absorption band near 780 nm (12800 cm^{-1}; Figure 4.5). The magnetic moments of these complexes are near 5.0 μ_B, typical for S = 2 paramagnets, and the EPR spectrum of $[\mathbf{9b}]^{2+}$ exhibits a 4S signal at g = 8.7 (Figure 4.7).

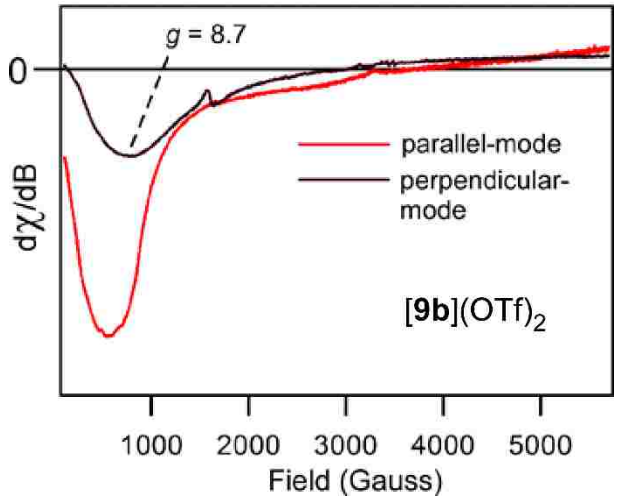

Figure 4.7. X-band EPR spectra of [**9b**](OTf)$_2$ collected at 10 K in perpendicular mode (black) and parallel mode (red).

The structural data for [**6a**]SbF_6 reported in the previous chapter suffers from large uncertainties in bond lengths ($3\sigma \approx 0.035$ Å in C─distances), which hindered evaluation of the ligand oxidation state based on geometric parameters. As noted in the introduction, DFT calculations suggested an electronic structure intermediate between Fe^{3+}─^{tBu}ISQ and Fe^{2+}─^{tBu}IBQ.

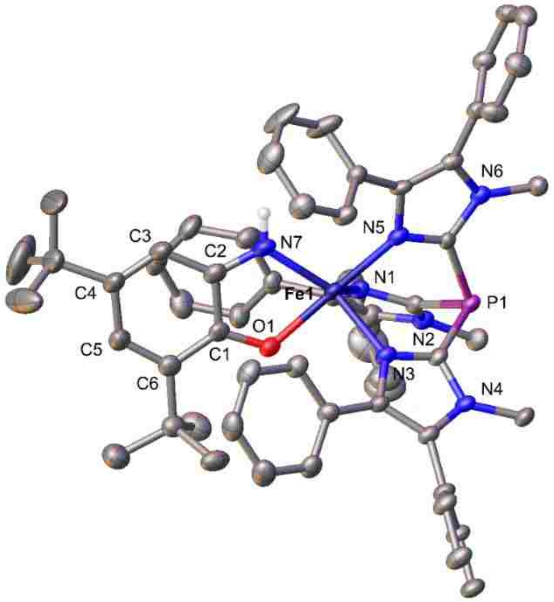

Figure 4.8. Thermal ellipsoid plot (50% probability) derived from the X-ray structure of [**9b**](OTf)$_2$•1.5 CH_2Cl_2. Non-coordinating solvent molecules, counteranions and most hydrogen atoms have been omitted for clarity. Key metric parameters are provided in Table 4.2.

Table 4.2. Selected bond lengths [Å] from the X-ray structures of [**6a**]SbF_6•0.5 DCE and [**9b**](OTf)$_2$•1.5 CH_2Cl_2.

	[**6a**]SbF_6	[**9b**](OTf)$_2$		[**6a**]SbF_6	[**9b**](OTf)$_2$
Fe1-N1	2.071(7)	2.077(3)	O1-C1	1.264(11)	1.287(5)
Fe1-N3	2.038(7)	2.089(4)	N7-C2	1.333(11)	1.314(6)
Fe1-N5	2.134(6)	2.093(4)	C1-C2	1.473(12)	1.483(6)
Fe1-O1	2.082(6)	2.037(3)	C2-C3	1.423(12)	1.429(6)
Fe1-N7	2.017(8)	2.013(4)	C3-C4	1.345(15)	1.340(7)

Crystals of [**9b**](OTf)$_2$ were obtained by layering a CH_2Cl_2 solution with pentane; the resulting X-ray structure is shown in Figure 4.8, and relevant metric parameters for [**6a**]SbF_6 and [**9b**](OTf)$_2$ are compared in Table 4.2. The σ-values for the [**9b**](OTf)$_2$ bond distances are significantly smaller than those in the [**6a**]SbF_6 structure. Like [**6a**]$^+$, complex [**9b**]$^{2+}$ features a distorted trigonal-bipyramidal coordination geometry (τ =

0.57) with O1 occupying an axial position. The O1-C1, N7-C2, and C-C bond distances of the *O*,*N*-donor ligand are fully consistent with ligand-based oxidation. Recently, Brown developed a helpful procedure for assessing the oxidation state of *o*-aminophenolate ligands based on their metric parameters.[136] Using this method, the ligands in [**6a**]$^{+}$ and [**9b**]$^{2+}$ have estimated charges of ─0.54(8) and ─0.48(10), approximately halfway between the ISQ^{-} and IBQ^{0} limits (Table 4.3). Further insights into the Fe and ligand oxidation state of [**6a**]$^{+}$ and [**9b**]$^{2+}$ are provided by spectroscopic and computational studies described below.

Table 4.3. Experimental and DFT-computed properties of selected complexes.

			4a	[**7b**]$^{+}$	**5a**	[**8b**]$^{+}$	[**6a**]$^{+[a]}$	[**9b**]$^{2+[a]}$
metric parameters	Fe-$N_{Tp/TIP}$ ave [Å]	exptl	2.150	2.191	2.137		2.081	2.086
		DFT	2.215	2.240	2.188	2.233	2.077	2.122
	O1─C1 [Å]	exptl	1.345	1.340	1.285		1.264	1.287
		DFT	1.330	1.338	1.276	1.277	1.278	1.273
	N7─C2 [Å]	exptl	1.451	1.455	1.328		1.336	1.314
		DFT	1.454	1.460	1.335	1.337	1.329	1.326
	ligand charge	exptl	-	-	─0.69		─0.54	─0.48
		DFT	-	-	─0.72	─0.73	─0.62	─0.54
Mulliken spins	Fe	DFT	+3.78	+3.76	+3.77	+3.76	+3.94	+3.93
	O,N─ligand	DFT	+0.14	+0.18	─0.86	─0.82	─0.30	─0.15
Mössbauer	δ [mms^{-1}]	exptl	1.06	1.06/1.14	0.97	0.95/0.99	0.73	0.64
		DFT	0.96	0.95	0.86	0.91	0.57	0.62
	ΔE_Q [mms^{-1}]	exptl	2.52	2.08/2.93	3.5	1.95[b]/2.5	2.33	1.94
		DFT	2.00	1.86	2.93	2.09	0.71	1.34

[a] DFT calculation employed the BP functional. [b] Average ΔE_Q value for the dominant species in the [**8b**]$^{+}$ MB spectrum.

4.C. Electrochemistry of Complexes 4a-[6a]$^{+}$

Our original intent in performing chemical oxidations of **4a** and [**7b**]OTf was to generate the corresponding ferric complexes [Fe^{3+}(^{Ph2}Tp)(^{tBu}APH)]$^{+}$ (**4a^{ox}**) and [Fe^{3+}(^{Ph2}TIP)(^{tBu}APH)]$^{2+}$ (**7b^{ox}**). However, treatment of **4a** and [**7b**]OTf with a single equivalent of one-electron oxidants (such as acetylferrocenium, [N(C_6H_4Br-4)$_3$]$^{+}$, or Ag^{+}) instead produced 0.5 equivalent of [**6a**]$^{+}$ and [**9b**]$^{2+}$, respectively. Indeed, titrations of **4a** and [**7b**]OTf with acetylferrocenium revealed a linear increase in the intensity of the [**6a**]$^{+}$/[**9b**]$^{2+}$ absorption features up to two equivalents of oxidant, indicating that the Fe(II) precursors exclusively undergo two-electron oxidations. This situation generally occurs when the product of the initial one-electron transfer undergoes a chemical change to yield a species that is more reducing than the starting complex.

To better understand this phenomenon, cyclic voltammetric studies of the ^{Ph2}Tp series were conducted in CH_2Cl_2 with 100 mM [NBu_4]PF_6 as the supporting electrolyte. All redox potentials are referenced to the ferrocenium/ferrocene couple (Fc^{+}/Fc). As shown in Figure 4.9, **4a** undergoes an irreversible oxidation at -15 mV, followed by a cathodic wave at -490 mV with half the current intensity of the anodic wave.

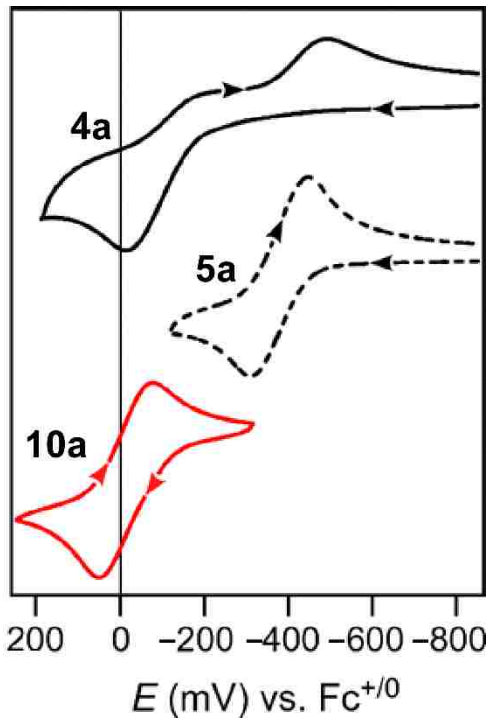

Figure 4.9. CV diagram of complexes **4a**, **5a**, and **10a**. All potentials have been referenced to the ferrocene/ferrocenium couple.

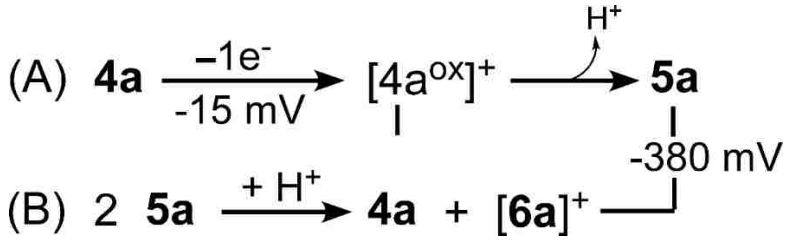

Figure 4.10. Diagram of the redox reactions/disproportionation of complexes **4a-6a**.

We therefore concluded that the oxidation at -15 mV corresponds to the two-electron process **4a** → [**6a**]$^+$ + H$^+$, while the subsequent reduction corresponds to one-electron reduction of [**6a**]$^+$ to **5a**. This conclusion was confirmed by the CV of **5a** (Figure 4.9), which shows a quasi-reversible [**6a**]$^+$/**5a** couple with $E_{1/2}$ = -380 mV (ΔE = 140 mV). Thus, **5a** is indeed more reducing than **4a**, accounting for the behavior described above.

Figure 4.10 summarizes the electrochemical properties of these complexes. One-electron oxidation of **4a** presumably yields the ferric complex **4a^{ox}**, although this transient species is never observed.

Instead, **4a^{ox}** quickly sheds a proton to the surrounding medium to give **5a**, since the change in Fe oxidation state dramatically lowers the pK_a of the coordinated –NH_2 donor. The fact that $E_{1/2}$(**4a^{ox}**/**4a**) > $E_{1/2}$([**6a**]$^+$/**5a**) ensures that **5a** is not stable in this environment; instead, it disproportionates to give 0.5 equivalent each of **4a** and [**6a**]$^+$ (Figure 4.10). Thus, the only way to convert **4a** into **5a** is to employ an H-atom abstracting agent like TTBP$^\bullet$ that is not an effective one-electron oxidant. Our results also indicate that deprotonation of the *O,N*-ligand dramatically lowers its redox potential, thus favoring ligand-based over metal-based oxidation.

The electrochemical behavior of **10a** is straightforward since the DMAPH ligand cannot easily participate in proton or electron transfers. This complex displays a quasi-reversible redox event with $E_{1/2}$ = -15 mV (ΔE = 130 mV) that corresponds to the Fe^{3+}/Fe^{2+} couple (Figure 4.9). The **10a** potential can serve as an approximate value for the irreversible **4a^{ox}**/**4a** couple. The free $^{tBu}APH_2$ and DMAPH ligands are irreversibly oxidized at more positive potentials of +280 and +450 mV, respectively, in CH_2Cl_2 (Figure 4.11).

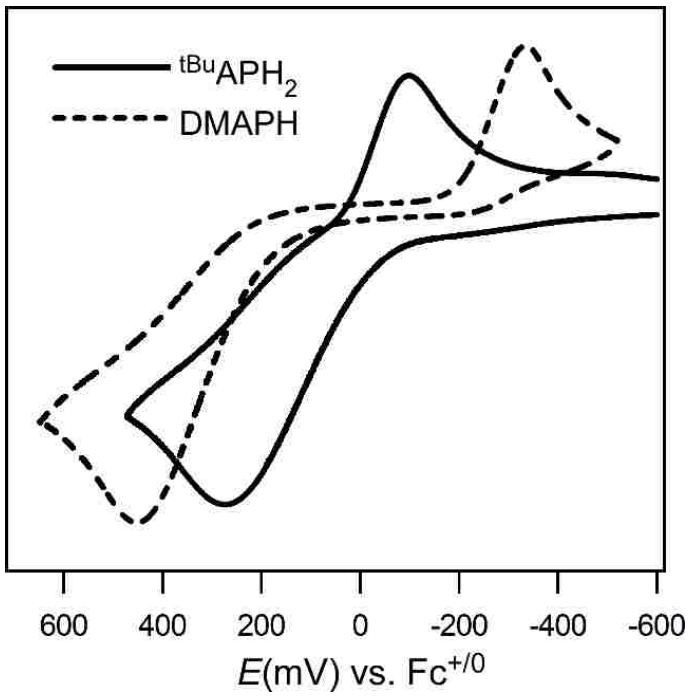

Figure 4.11. Cyclic voltammograms of ligands $^{tBu}APH_2$ and DMAPH in CH_2Cl_2 with 100 mM $(NBu_4)PF_6$ as the supporting electrolyte. The scan rate was 100 mV/s.

4.D. Geometric and Electronic Structures of DFT-Optimized Models

Since the spectroscopic data presented below are frequently interpreted with the assistance of DFT calculations, it is necessary to first describe the molecular and electronic structures of our computational models. We employed truncated versions of the complexes in which the *tert*-butyl groups of the *O*,*N*-donor were replaced with methyl groups and the phenyl substituents at the 5-positions of the pyrazole (^{Ph2}Tp) and imidazole (^{Ph2}TIP) rings were removed. Unless otherwise noted, all calculations employed the B3LYP functional. The most stable geometry-optimized structure of **5a** was obtained using the broken symmetry (BS) methodology and an overall spin of 3/2; this model provided metric parameters in excellent agreement with the crystallographic data (Table 4.4).

Table 4.4. Selected Bond Distances (Å) and Angles (deg) for Complexes **5a** and [**8b**]$^+$ Obtained by XRD and DFT.

Bond distances	**5a** (XRD)	**5a** (DFT)	[**8b**]$^+$ (DFT)
Fe1-N1	2.108(2)	2.129	2.176
Fe1-N3	2.087(2)	2.136	2.188
Fe1-N5	2.216(2)	2.299	2.335
Fe1-O1	2.095(2)	2.130	2.121
Fe1-N7	1.982(2)	2.029	2.003
O1-C1	1.285(3)	1.276	1.277
N7-C2	1.328(4)	1.335	1.337
C1-C2	1.469(5)	1.461	1.460
C2-C3	1.413(4)	1.420	1.417
C3-C4	1.363(4)	1.372	1.372
C4-C5	1.427(4)	1.427	1.430
C5-C6	1.375(4)	1.372	1.370
C1-C6	1.440(4)	1.432	1.432
Bond angles	**5a** (XRD)	**5a** (DFT)	[**8b**]$^+$ (DFT)
N1-Fe1-N3	93.44(7)	94.6	95.1
N1-Fe1-N5	82.76(7)	83.3	83.9
N3-Fe1-N5	89.80(7)	86.1	86.2
O1-Fe1-N1	94.16(7)	97.2	95.2
O1-Fe1-N3	95.62(7)	97.6	93.8
O1-Fe1-N5	173.93(8)	176.2	179.1
N7-Fe1-N1	138.99(9)	138.5	136.5
N7-Fe1-N3	127.37(9)	126.8	128.0
N7-Fe1-N5	99.36(8)	98.6	102.2
O1-Fe1-N7	79.52(8)	78.5	78.6
τ-value	0.58	0.63	0.71

The Mulliken spin populations, listed in Figure 4.3, support the view that the electronic structure of **5a** should be described as a high-spin Fe^{2+} center (3.77 α spins) AF-couple to an ISQ-based π-radical (0.86 β spins). The exchange coupling constant (J) has a computed value of -223 cm^{-1}, based on the Yamaguchi approach ($H = -2JS_A \bullet S_B$).[156] The AF coupling is mediated by a nonorthogonal pair of singly occupied

molecular orbitals (SOMOs) with opposite spins, shown in the qualitative MO diagram in Figure 4.12. The relevant magnetic orbitals for **5a** are the α-Fe(d_{xy})- and β-ISQ(π^*)-based MOs that display 33% spatial overlap, indicative of a ligand-based radical with rather weak interactions with the Fe^{2+} center. The structure and bonding scheme of [**8b**]$^+$, also computed with the BS approach, are nearly identical to the corresponding **5a** model (Table 4.3 and 4.4), consistent with the spectral similarities between **5a** and [**8b**]$^+$ (vide supra).

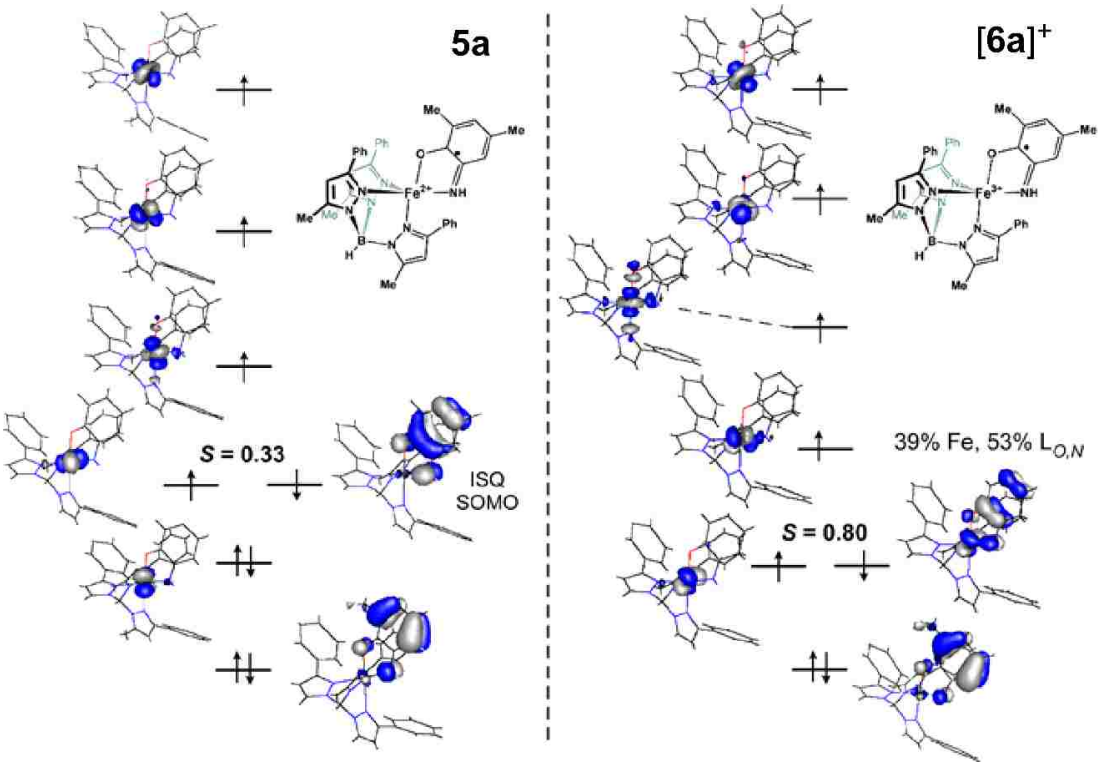

Figure 4.12. Qualitative molecular orbital diagrams for **5a** (left) and **[6a]**$^+$ (right) obtained from broken-symmetry DFT calculations. Isosurface plots for important MOs are provided, along with the overlap (s) between corresponding magnetic orbitals.

While the optimized [**6a**]$^{+}$ geometry obtained with the B3LYP functional agrees reasonably well with the crystallographic data, Fe─N/O and intraligand bond lengths in the DFT structure of [**9b**]$^{2+}$ deviate significantly from the experimental values (Table 4.5). Better agreement was obtained with the BP functional for both [**6a**]$^{+}$ and [**9b**]$^{2+}$, and therefore, our analysis of these complexes has employed the BP-derived structures.

Table 4.5. Experimental and computed bond distances (Å) and bond angles (deg) for complexes [**6a**]$^{+}$ and [**3b**]$^{2+}$ Obtained by XRD and DFT.

Bond distances	**[6a]$^{+}$** (XRD)	**[6a]$^{+}$** (B3LYP)	**[6a]$^{+}$** (BP)	**[9b]$^{2+}$** (XRD)	**[9b]$^{2+}$** (B3LYP)	**[9b]$^{2+}$** (BP)
Fe1-N1	2.071(7)	2.078	2.050	2.077(3)	2.124	2.095
Fe1-N3	2.038(7)	2.077	2.043	2.089(4)	2.135	2.091
Fe1-N5	2.134(6)	2.137	2.138	2.093(4)	2.193	2.180
Fe1-O1	2.082(6)	2.078	2.064	2.037(3)	2.180	2.057
Fe1-N7	2.017(8)	2.047	1.999	2.013(4)	2.088	2.001
O1-C1	1.264(11)	1.256	1.278	1.287(5)	1.235	1.273
N7-C2	1.333(11)	1.311	1.329	1.314(6)	1.295	1.326
C1-C2	1.473(12)	1.482	1.473	1.483(6)	1.514	1.483
C2-C3	1.423(12)	1.425	1.422	1.429(6)	1.428	1.420
C3-C4	1.345(15)	1.364	1.378	1.340(7)	1.358	1.378
C4-C5	1.433(16)	1.451	1.444	1.448(7)	1.465	1.451
C5-C6	1.375(14)	1.361	1.376	1.370(7)	1.353	1.374
C1-C6	1.439(12)	1.442	1.437	1.427(7)	1.454	1.440
RMS dev (all)		0.018	0.014		0.060	0.028
RMD dev (ligand)		0.014	0.013		0.027	0.016

Bond angles	**[3a]$^{+}$** (XRD)	**[3a]$^{+}$** (B3LYP)	**[3a]$^{+}$** (BP)	**[3b]$^{2+}$** (XRD)	**[3b]$^{2+}$** (B3LYP)	**[3b]$^{2+}$** (BP)
N1-Fe1-N3	94.5(3)	95.4	96.9	98.9(1)	95.3	98.5
N1-Fe1-N5	84.6(3)	88.5	88.3	85.5(1)	89.1	89.2
N3-Fe1-N5	92.4(3)	90.3	91.0	93.3(2)	90.7	91.4
O1-Fe1-N1	86.6(2)	93.3	93.6	91.8(1)	92.2	92.0
O1-Fe1-N3	93.8(3)	93.3	93.4	92.3(1)	92.0	91.8
O1-Fe1-N5	169.6(3)	175.9	175.0	174.1(1)	177.0	176.3
N7-Fe1-N1	144.6(3)	137.3	136.3	140.2(2)	135.7	134.4
N7-Fe1-N3	117.6(3)	126.0	126.0	119.5(2)	126.7	125.8
N7-Fe1-N5	106.9(3)	100.0	98.1	101.3(2)	102.4	99.1
O1-Fe1-N7	77.4(3)	76.2	77.4	77.6(2)	74.8	77.6
τ-value	0.42	0.64	0.65	0.57	0.69	0.70

For each complex, DFT calculations converge to the same S = 2 state irrespective of whether the BS approach is employed. The Mulliken spin populations appear to favor an Fe^{2+}—^{tBu}IBQ description, as the Fe center carries approximately four unpaired spins and the ligand-based spin density is reduced relative to **5a**/[**8b**]$^{+}$ (Table 4.3). The β-HOMO of [**6a**]$^{+}$ contains significant amounts of both Fe (39%) and O,N-ligand (53%) character (Figure 4.12), indicative of intermediate $Fe^{2+/3+}$ and IBQ/ISQ oxidation states (the corresponding values for [**9b**]$^{2+}$ are 53 and 37%). In addition, the spatial overlap between the pair of magnetic orbitals involved in the spin-coupling interaction is about 80%, which reflects a high degree of spin pairing (as opposed to the "diradical" situation of **5a**). However, these computational results should be viewed with caution, since the experimental metric parameters for [**6a**]$^{+}$/[**9b**]$^{2+}$ are not consistent with a pure IBQ description, as evident in the ligand charges shown in Table 4.3. Spectroscopic studies are therefore required to properly evaluate the electronic structures of [**6a**]$^{+}$ and [**9b**]$^{2+\cdot}$.

Finally, we generated DFT models of the hypothetical Ga^{3+} complexes, [Ga^{3+}(^{Ph2}Tp)(ISQ)]$^{+}$ (**Ga-ISQ**) and [Ga^{3+}(^{Ph2}Tp)(IBQ)]$^{2+}$ (**Ga-IBQ**). The Ga^{3+} ion has been employed in previous computational studies as a closed-shell analog of Fe^{3+} due to similarities in charge and ionic radius.[70] Since Ga^{3+} is not redox active, the **Ga-ISQ** and **Ga-IBQ** models allow us to assess the electronic and spectroscopic properties of "pure" ISQ and IBQ ligands without complications from the paramagnetic Fe center.

4.E. Mössbauer Spectroscopy

Mössbauer (MB) spectroscopy has proven capable of providing definitive assessments of Fe oxidation states in complexes with non-innocent ligands (Figure 4.13). displays low-temperature (6 K) MB spectra collected in an applied field of 0.04 T for polycrystalline samples of **4a**, **5a**, and [**6a**]SbF_6; the corresponding spectra of the ^{Ph2}TIP-based "**b** series" are provided in Figure 4.14. MB parameters are summarized in Tables 4.3 and 4.5. Complex **4a** displays a single doublet with an isomer shift (δ) of 1.06 mms^{-1} and quadrupole splitting (ΔE_Q) of 2.52 mm^{-1}, consistent with the presence of a conventional high-spin Fe^{2+} center.

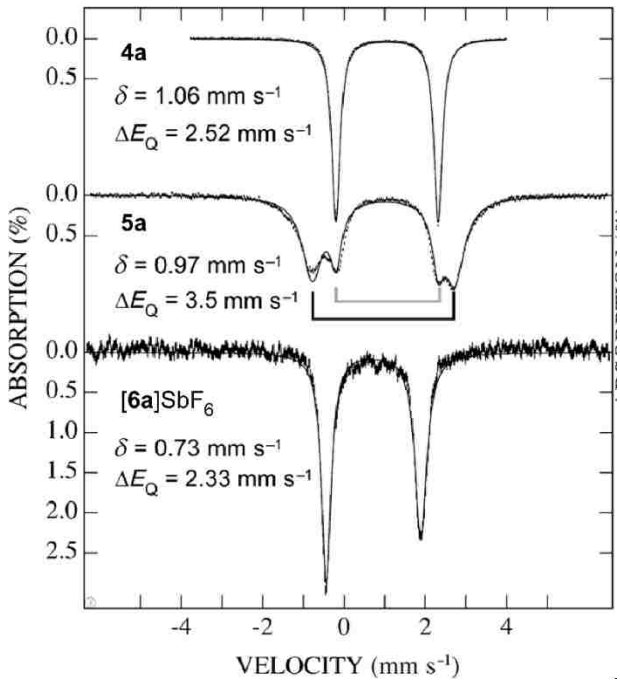

Figure 4.13. Mössbauer spectra of complexes **4a**, **5a**, and [**6a**]SbF_6 recorded at 6 K in an applied field of 0.04 T. The parameters indicated represent the principal species discussed in the text. The spectrum of sample **5a** contains a contribution from **4a**, amounting to 30% of the total Fe in the sample (inner doublet, indicated by the bracket). The spectrum of [**6a**]$^+$ shown in this figure was obtained by subtracting 20% of impurities from the raw data.

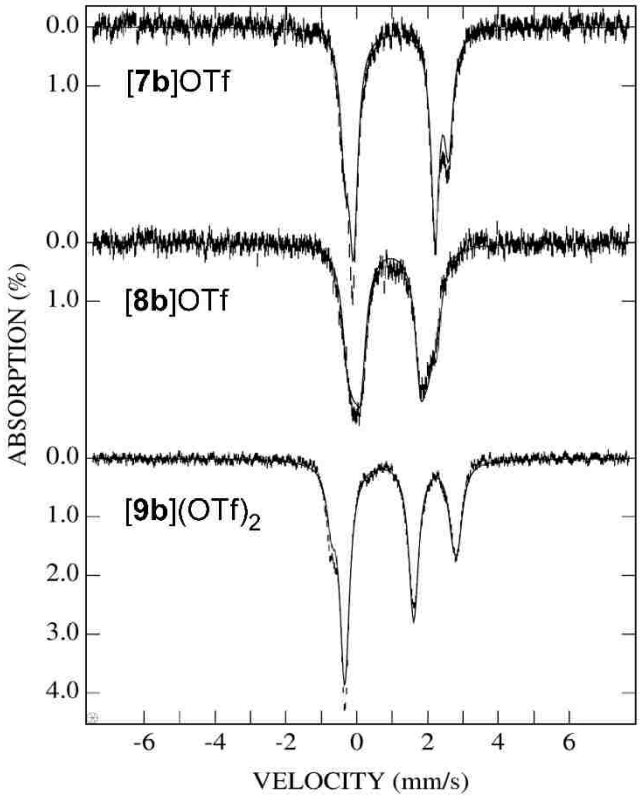

Figure 4.14. Mössbauer spectra of complexes [**7b**]OTf, [**8b**]OTf, and [**9b**](OTf)$_2$, recorded at 6 K, in an applied field of 0.04 T. The solid lines are least-square fits with parameters in Table 4.6.

Table 4.6. Experimental Mössbauer Parameters

Complex	Isomer Shift δ (mm/s)[a]	Quadrupole Splitting ΔE_Q (mm/s)	FWHM mm/s
4a	1.06	2.52	0.26
5a	0.97	3.50	0.35, 0.6
[**6a**]SbF_6	0.73 (80%)	2.33	0.4
	0.55 (15%)	0.75	0.4
	0.10 (5%)	1.0	0.28, 0.35
[**7b**]OTf	1.06 (70%)	2.08	0.29
	1.14 (30%)	2.93	
[**8b**]OTf	0.95 (26%)	2.08	0.33
	0.95 (44%)	1.68	
	0.99 (30%)	2.5	
[**9b**]$(OTf)_2$	0.64	1.94	0.35
	1.27	3.20	
	1.00	3.44	

[a]Isomer shifts are quoted at 6 K. with respect to iron metal spectra at room temperature.

In contrast, the MB spectrum of [**7b**]OTf features two doublets in a roughly 2:1 ratio; the parameters for both species are typical of high-spin Fe^{2+} complexes: $\delta = 1.06$ and 1.14 mms^{-1} and $\Delta E_Q = 2.08$ and 2.93 mms^{-1} for the major and minor components, respectively. The two observed species likely correspond to conformational isomers of $[\mathbf{7b}]^+$ that lie at different points along the continuum between square-pyramidal and trigonal-bipyramidal geometries. In support of this conclusion, the X-ray structure of

[**7b**]$^{+}$ (vide supra) features two independent complexes in the unit cell with distinct τ values of 0.60 and 0.55.

The MB spectrum of **5a** exhibits a broad doublet with a large quadrupole splitting (δ = 0.97, ΔE_Q = 3.5 mms^{-1}), although the presence of starting material (ca. 30% of Fe) is also evident (Figure 4.13). Significantly, the modest decrease of 0.09 mms^{-1} in isomer shift upon conversion of **4a** to **5a** provides unequivocal evidence that the oxidation is ligand based, in support of the Fe^{2+}─ISQ formulation for **5a**. Likewise, the MB spectrum required three doublets with δ values of (0.97 ± 0.02) mms^{-1} and ΔE_Q values between 1.7-2.5 mms^{-1} (Table 4.6). Given the nearly identical isomer shifts, these three species likely correspond to conformational isomers of [**8b**]$^{+}$, similar to the situation discussed above for [**7b**]$^{+}$. The heterogeneity observed in the [**8b**]$^{+}$ spectrum is related to the inability to prepare suitable crystals of this complex, which necessitated the use of powder samples lacking the intrinsic order of crystalline material. The broadness of the doublets for both **5a** and [**8b**]$^{+}$ is likely due to spin-spin relaxation effects.

MB spectra of [**6a**]$^{+}$ and [**9b**]$^{2+}$ each display a single doublet centered at δ = 0.73 and 0.64 mms^{-1}, respectively, with quadrupole splittings of about 2.0 mms^{-1} (Figure 4.14 and Table 4.6; the [**9b**]$^{2+}$ spectrum also contains features arising from ferrous impurities). The lower δ values suggest that one-electron oxidation of **5a** → [**6a**]$^{+}$ (or [**8b**]$^{+}$ → [**9b**]$^{2+}$) involves significant removal of electron density from the Fe ions. However, the observed isomer shifts are larger than one would expect for high-spin Fe^{3+} centers, which typically display values between 0.4 and 0.6 mms^{-1}.[157] A survey of high-spin [Fe^{3+}-$(ISQ)_n$] complexes (n = 1, 2, or 3) prepared by Wieghardt and co-workers found δ values ranging from 0.44 to 0.54 mms^{-1}.[78,80-82] The MB data are therefore consistent with our DFT

results that suggest partial IBQ character for the O,N-ligands in [**6a**]$^{+}$/[**9b**]$^{2+}$. It is also important to note that the **a**- and **b**-series of complexes yield very similar MB parameters, suggesting that the supporting ligand (^{Ph2}Tp(1─) vs ^{Ph2}TIP) has little effect on the Fe/$L_{O,N}$ unit.

As show in Table 4.3, the isomer shifts derived from DFT calculations are quite consistent with the experimental data, although DFT generally underestimates δ values by about 0.05-0.15 mms^{-1}. In particular, DFT nicely reproduces the magnitude of changes (Δδ) across the **4→5→6** (or **7→8→9)** series. The overall agreement is less satisfactory for quadrupole splittings, but it is well-known that DFT has more difficulty computing accurate ΔE_Q values.[158-160] The general agreement between calculated and experimental MB parameters indicates that our computational models faithfully represent the electronic structures of these "redox-ambiguous" complexes.

4.F. Electronic Absorption and MCD Spectroscopy

The UV/vis/NIR spectra of **5a** and [**8b**]$^{+}$ displayed in Figure 4.5 are characterized by a broad absorption manifold (ε ~ 1.0 mM^{-1}cm^{-1}) centered around 750 nm (13,300 cm^{-1}). In this region, the **5a**/[**8b**]$^{+}$ spectra closely resemble those reported for other ISQ-containing complexes with various metal ions (Co^{3+}, Ni^{2+}, and Cu^{2+}),[89,131] as well as the spectrum measured by Carter et al. for a "free" ISQ radical.[161] These spectral similarities suggest that the transitions observed for **5a** and [**8b**]$^{+}$ are primarily ligand based. This conclusion is supported by literature precedents[162,163] and our time-dependent DFT (TD-DFT) calculations. The dominant contributor to the 750 nm feature is an intraligand transition in which the acceptor orbital is the SOMO of the ^{tBu}ISQ radical. TD-DFT

calculations predict this transition to appear at 16,100 and 15,200 cm^{-1} for **5a** and $[\mathbf{8b}]^{+}$, respectively. In general, the TD-DFT methodology nicely replicates the energies and intensities of the experimental absorption features, as shown in Figure 4.15 for **5a** (electron density difference maps – EDDMs, for key transitions are provided in Figure 4.16).

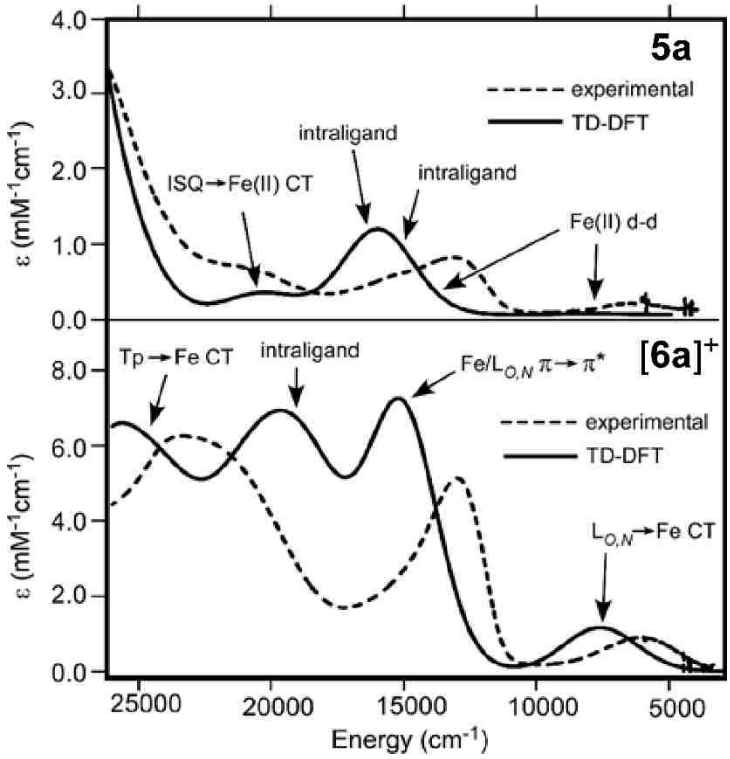

Figure 4.15. Experimental (dashed line) and TD-DFT computed (solid line) absorption spectra for **5a** (top) and $[\mathbf{6a}]^{+}$ (bottom). The arrows point to features in the computed spectra arising from the indicated type of electronic transition.

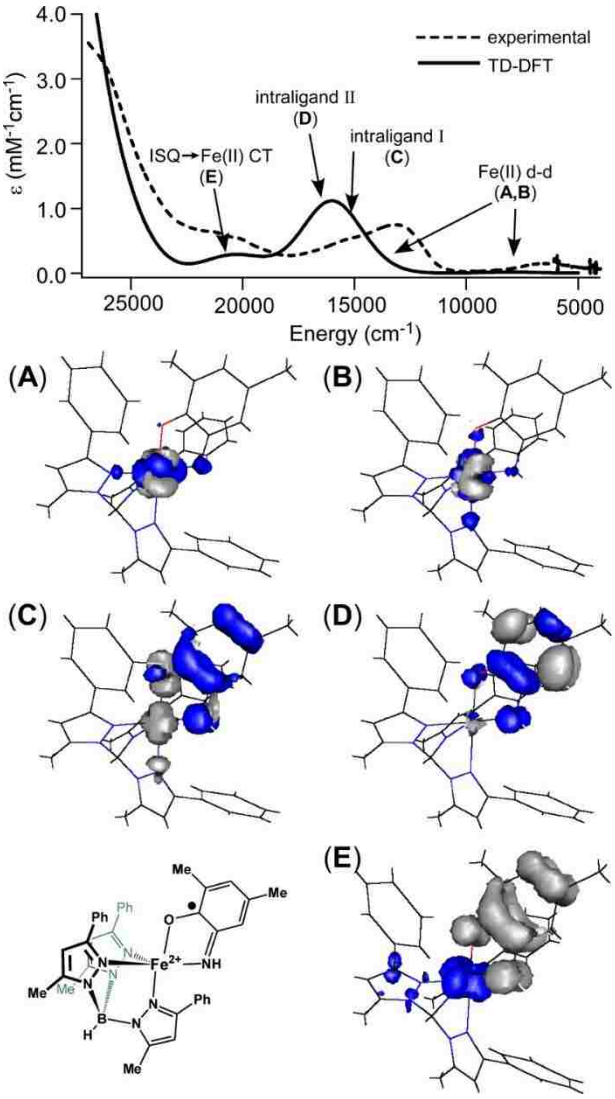

Figure 4.16. Top: Experimental (dashed line) and TD-DFT computed (solid line) absorption spectra for **5a**. Bottom: Electron density difference maps (EDDMs) for computed transitions. Blue and grey regions indicate gain and loss of electron density, respectively.

These calculations indicate that another component of the absorption manifold involves excitation to the ^{tBu}ISQ SOMO from an molecular orbital with mixed ^{tBu}ISQ/Fe(II) character; the computed energy for this transition is 15,000 cm^{-1} for **5a**. The weak near-infrared (NIR) bands evident for both complexes likely arise from Fe(II) d-d transitions, while features at higher energies (> 20,000 cm^{-1}) are attributed by TD-

DFT to ^{tBu}ISQ→Fe(II) charge transfer (CT). These latter bands are relatively weak due to poor overlap between the ^{tBu}ISQ SOMO and half-occupied Fe(II) orbitals (Figure 4.16).

Table 4.7. Comparison of Computed (TD-DFT) and Experimental Energies for Selected Electronic Transitions of Complexes **5a** and [**6a**]SbF_6.

Complex	Transition assignment	Transition energy (cm^{-1}) TD-DFT	experimental
5a	Fe(II) d-d	8000	6500
		14100	
	intraligand	15000	13200
		16100	15200
	ISQ→Fe(II) CT	20700	21400
[**6a**]SbF_6	$L_{O,N}$→Fe CT	7600	6050
	Fe/$L_{O,N}$ $\pi\rightarrow\pi^*$	14600	13050
	intraligand	19000	~20000

Analysis of the [**6a**]/[**9b**]$^{2+}$ spectra is more complex due to the large extent of mixing between Fe and ligand orbitals. For both complexes, the β-HOMO – containing approximately equal parts metal and ligand character (*vide supra*) – arises from a π-*bonding* interaction between the parent Fe 3d and $L_{O,N}$ orbitals (Figure 4.17). TD-DFT calculations, which again faithfully reproduce key features of the experimental spectrum (Figure 4.18 and Table 4.7), indicate that the intense absorption feature at about 13000 cm^{-1} involves electron transfer from the β-HOMO to its unoccupied π-antibonding counterpart; therefore, this excitation is best described as a π→ π* transition centered on the O1─Fe1─N7 unit. The broad band evident in the NIR region ($\varepsilon \approx 1.0$ mM^{-1} cm^{-1}) is then attributed to β-HOMO→Fe 3d transitions where the acceptor orbitals lack

significant $L_{O,N}$ character. Given the mixed nature of the β-HOMO, this low-energy feature possesses both Fe d-d and LMCT character, as revealed in the EDDMs in Figure 4.17.

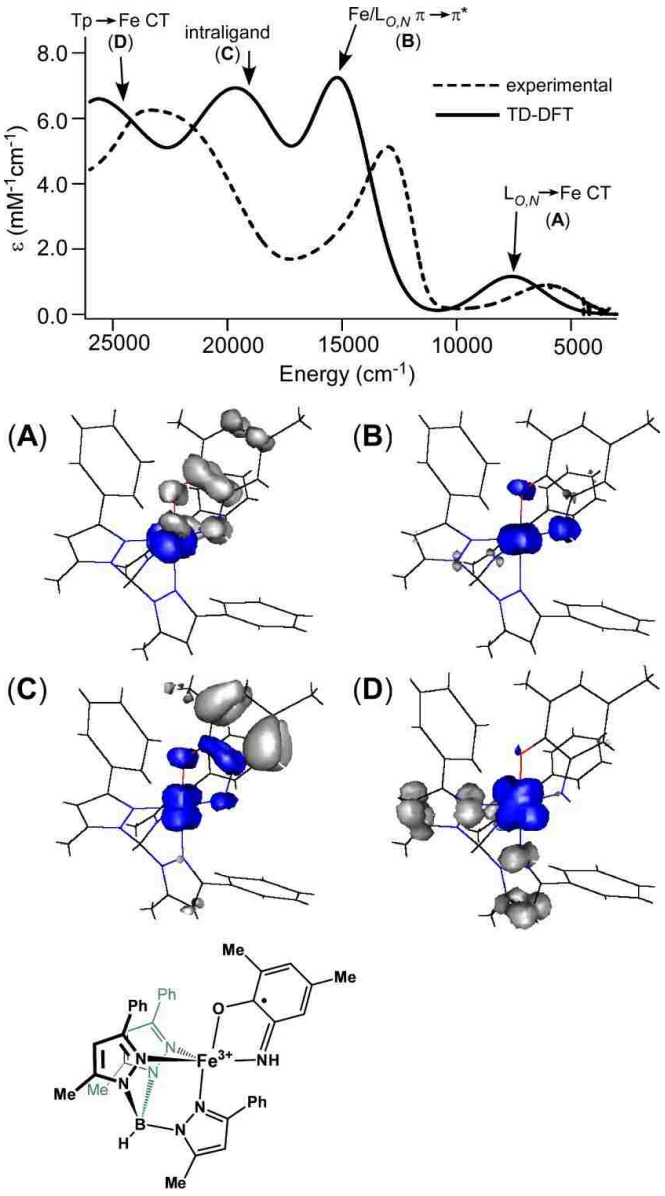

Figure 4.17. Top: Experimental (dashed line) and TD-DFT computed (solid line) absorption spectra for [**6a**]$^{+}$. Bottom: Electron density difference maps (EDDMs) for computed transitions. Blue and grey regions indicate gain and loss of electron density, respectively.

Interestingly, the intraligand transition that is prominent at about 13300 cm^{-1} in the **5a**/[**8b**]$^{+}$ spectra is calculated to appear at 18900 cm^{-1} for [**6a**]$^{+}$, although this transition now contains some LCMT character. The blueshift reflects the partial IBQ character of the O,N-coordinated ligands, since previous reports have demonstrated that the lowest-energy IBQ based transition in metal complexes occurs near 20800 cm^{-1}.[89,131] This intraligand transition is largely obscured in the [**6a**]$^{+}$ spectrum by intense $N_{Tp}\rightarrow$Fe CT transitions. However, because the ^{Ph2}TIP-based MOs are greatly stabilized relative to their ^{Ph2}TIP counterparts (on account of the difference in charge), the $N_{TIP}\rightarrow$Fe CT transitions are therefore evident in the 20000-25000 cm^{-1} region of the [**9b**]$^{2+}$ spectrum with intensities of about 1.5 mM^{-1} cm^{-1}.

The electronic transitions of [**9b**](OTf)$_2$ were further probed through the collection of solid-state MCD spectra at low temperatures (4-30 K). All bands in the visible region exhibit temperature-dependent intensities characteristic of C-term behavior (Figure 4.18, top), as expected for a paramagnetic S = 2 species. Based on our analysis of the absorption spectrum, the most intense MCD feature at 12500 cm^{-1} corresponds to the Fe/$L_{O,N}$ $\pi\rightarrow\pi^*$ transition, while the bands centered around 20000 cm^{-1} are ascribed primarily to intraligand transitions. Since MCD c-term intensity requires spin-orbit coupling between states, features that involve metal d-orbitals, such as ligand-field (d-d) and CT transitions, are relatively more intense in MCD than absorption spectra (C/D ratio).[164] Thus, the comparative weakness of the higher-energy features in the [**9b**]$^{2+}$ MCD spectrum is further confirmation of the ligand-based nature of these transitions.

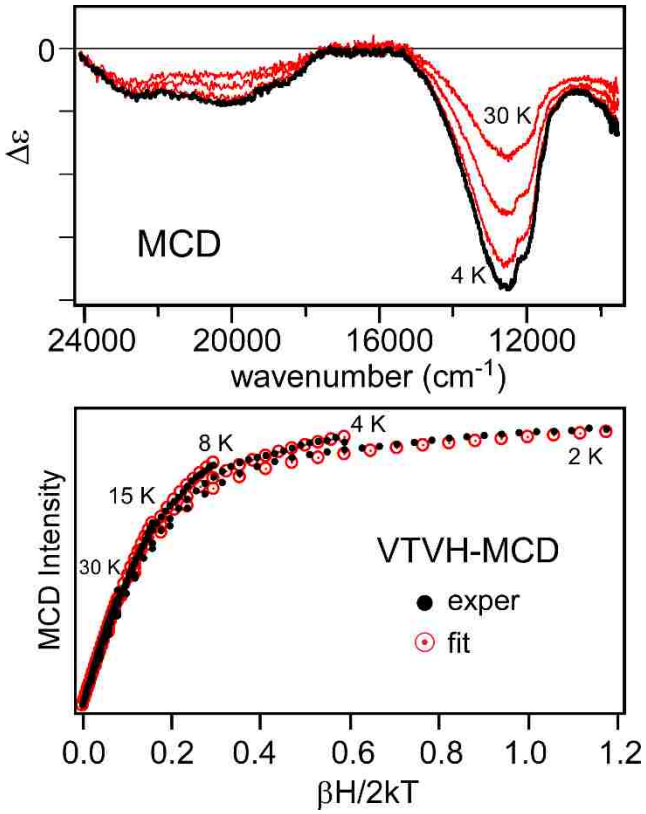

Figure 4.18. Top: Variable-temperature solid-state MCD spectra of [**9b**](OTf)$_2$. Spectra were measured at a magnetic field of 7 T and at temperatures of 4, 8, 15 and 30 K. Bottom: VTVH-MCD data collected at 790 nm for [**9b**](OTf)$_2$. Data were obtained at the indicated temperatures with magnetic fields (H) ranging from 0 to 7 T. The best fit (Θ) was obtained with the following spin Hamiltonian parameters: S = 2, D = -5 cm^{-1}, E/D = 0.20, g_{iso} = 2.0.

Variable-temperature variable-field MCD (VTVH-MCD) data were collected at 790 nm (12660 cm^{-1}) for [**9b**]$^{2+}$. In these experiments, the MCD intensity was monitored at five temperatures (2, 4, 8, 15, and 30 K) as the magnetic field (H) was varied from 0 to 7 T; by convention, the resulting magnetization curves are plotted against βH/2kT (Figure 4.18, bottom). As demonstrated by Solomon and Neese, quantitative analysis of the VTVH-MCD curves provides valuable information regarding spin-Hamiltonian parameters and transition polarizations.[165,166] The VTVH-MCD method is particularly powerful for non-Kramers systems, such as [**9b**]$^{2+}$, that are often inaccessible by EPR

spectroscopy. The magnetization curves obtained at 790 nm saturate rapidly with field and exhibit very little "nesting" (i.e., spread between curves obtained at different temperatures). Such behavior is characteristic of S =2 systems with negative zero-field splitting (ZFS).[167,168] Indeed, the best fit of the 790 nm data was obtained with D = ─5.0 cm^{-1} and E/D = 0.20 (Figure 4.18), although a broad range of negative D values (< 4 cm^{-1}) with moderate rhombicities (0.1 < E/D < 0.25) provided acceptable fits. Our analysis indicates that the corresponding transition is polarized in the *xz* direction, which requires the O,N-donor ligand to lie in the *xz* plane of the **D** tensor (Figure 4.18).

4.G. Resonance Raman Spectroscopy

Vibrational spectroscopy has proven valuable in the characterization of metal-bound phenoxyl and semiquinone radicals.[86,169-171] In the case of dioxolenecomplexes, the C─O stretching frequency is a sensitive indicator of ligand oxidation state, ranging from 1400-1500 cm^{-1} for semiquinones and 1620-1640 cm^{-1} for benzoquinones.[172] By contrast, the vibrational features of iminobenzo(semi)quinones have not been examined in detail. We therefore collected resonance Raman (rR) spectra on frozen samples of [**6a**]SbF_6 in CD_2Cl_2 (Figure 4.19). The experiments utilized 488 nm laser excitation, in resonance with the intraligand transitions that appear in this region (vide supra). To aid in peak assignments, we prepared a sample of $[\mathbf{6a}]^+$ in which the O,N-ligand was labeled with the ^{15}N isotope; the difference spectrum revealed several peaks that are sensitive to ^{15}N substitution (Figure 4.19). Interpretation of the rR data was further aided by DFT frequency calculations employing the BP functional.

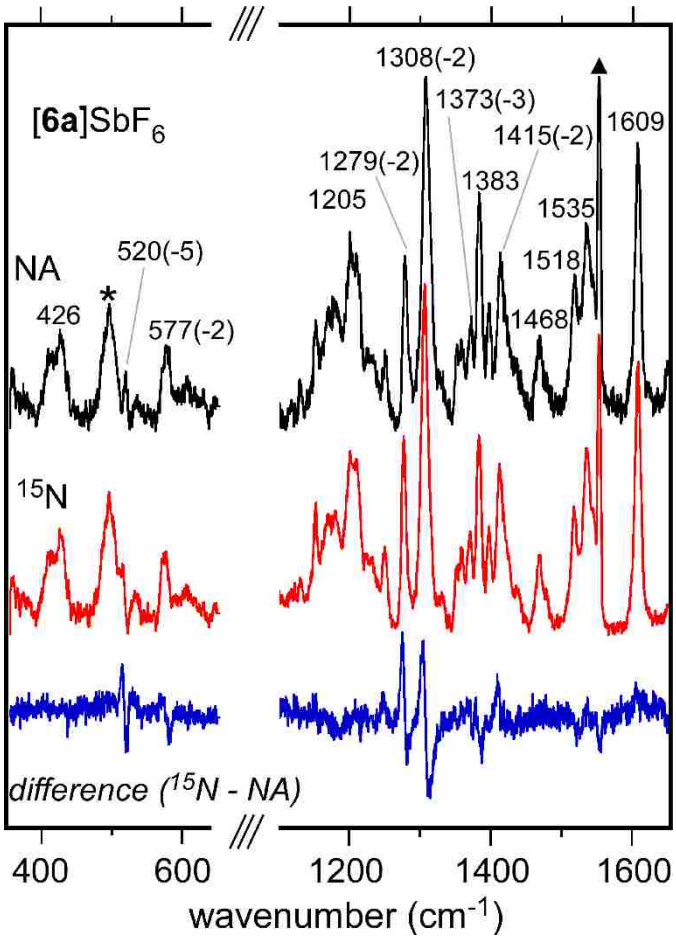

Figure 4.19. Resonance Raman spectra obtained with 488.0 nm excitation (45 mW) of frozen CD_2Cl_2 solutions of (top) natural abundance [**6a**]SbF_6 with incorporation of ^{15}N isotope in the $L_{O,N}$ ligand. The difference spectrum is shown on the bottom. Frequencies (in cm^{-1}) are provided for selected peaks, with the corresponding $^{14}N \rightarrow ^{15}N$ shifts shown in parenthesis. Peaks marked with an asterisk (*) arise from the frozen solvent, while the peak marked with a triangle arises from condensed liquid O_2.

Based on literature precedents involving metal-semiquinone complexes,[170,171] the two isotopically sensitive peaks at 520 and 577 cm^{-1} in the [**6a**]$^+$ spectrum are attributed to motions of the five-membered chelate ring formed by the Fe center and O,N-ligand. In support of this assignment, DFT predicts two modes at 532 and 588 cm^{-1} (with ^{15}N isotope shifts of 7 and 4 cm^{-1}, respectively) with large degrees of chelate stretching character. The mode at 520 cm^{-1} (calculated at 532 cm^{-1}) is best described as a chelate

breathing mode, whereas the chelate vibrations in the higher-energy mode are strongly mixed with intraligand C─C bond movements. Graphical depictions of these normal modes, along with further information concerning the computed vibrational spectrum, are provided in Figure 4.20.

Mode Diagram	Mode Description	Mode Frequency (cm^{-1}) Exp	Mode Frequency (cm^{-1}) Calc	Calculated Isotope Shifts (cm^{-1}) ^{15}N	Calculated Isotope Shifts (cm^{-1}) ^{18}O
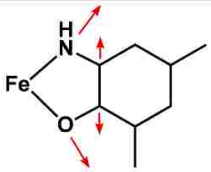	chelate breathing	520	532	-7	-7
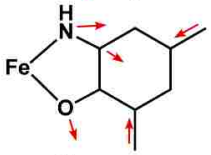	chelate + ring motion	577	588	-4	-1
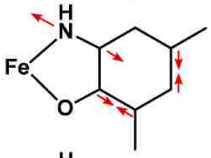	ν(N-C) + ring motion	1279	1319	-2	0
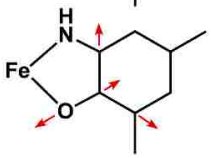	ν(O-C) + ring motion	1308	1342	-1	-9
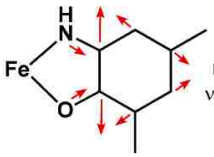	ring motions + ν(O-C) + ν(N-C)	1373	1384	-1	-3
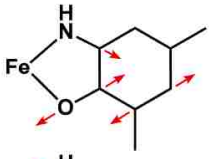	ν(O-C) + ring motion	1383	1404	-1	-6
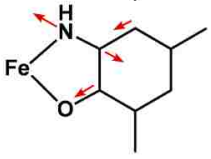	ν(N-C) + ring motion	not observed	1495	-3	-2

Figure 4.20. Normal modes, experimental and DFT-calculated frequencies, and computed isotope shifts for ^{15}N- and ^{18}O-labeled ligand.

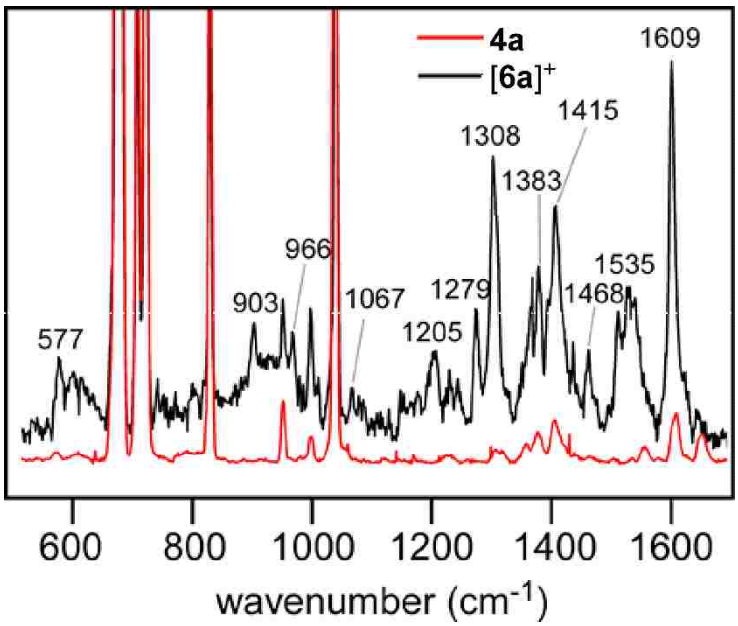

Figure 4.21. Resonance Raman spectra obtained with 488.0 nm excitation (45 mW) of frozen CD_2Cl_2 solutions of **4a** (red) and [**6a**]SbF_6 (black). Frequencies (in cm^{-1}) are provided for selected peaks.

The [**6a**]$^+$ spectrum exhibits numerous peaks in the 1000-1650 cm^{-1} region. These features are not present in the rR spectrum of **4a** (Figure 4.21); we therefore conclude that they arise from the oxidized O,N-ligand (an exception is the 1609 cm^{-1} peak, which appears in both spectra). Studies of analogous semiquinone complexes[170,171] found that the most intense peaks in this region correspond to modes that couple O─C stretching and C─C ring motions. Indeed, DFT predicts two ν(O─C)-based modes for [**6a**]$^+$ at 1342 and 1404 cm^{-1} that are slightly sensitive to ^{15}N substitution (calculated shifts of ≈ 1 cm^{-1}). These modes likely corresponding to the prominent peaks at 1308 and 1383 cm^{-1} in the experimental spectrum. Modes with significant ν(N─C) character have computed frequencies of 1319, 1384, and 1495 cm^{-1}, with ^{15}N isotope shifts of about 1-3 cm^{-1} in each case. The two lower-energy modes nicely match the experimental peaks at 1279 and 1373 cm^{-1}, while the higher-energy mode is not observed.

Vibrational frequency calculations were also performed for the **Ga-ISQ** and **Ga-IBQ** possess O,N-ligands with unambiguous oxidation states (vide supra). DFT predicts two ν(O─C) modes at 1319 and 1424 cm^{-1} for **Ga-ISQ**, while the corresponding modes for **Ga-IBQ** possess much higher frequencies of 1540 and 1584 cm^{-1}. Since the putative ν(O─C) modes of [**6a**]$^{+}$ have experimental energies of 1308 and 1383 cm^{-1}, the rR data appear to support an ISQ assignment for the ligand oxidation state.

4.H. Discussion

The results strongly support our earlier conclusion─made on the basis of XRD and EPR data─that **2a** contains a high-spin Fe^{2+} center antiferromagnetically coupled to an ^{tBu}ISQ ligand radical (overall spin of 3/2). Specifically, the presence of a ferrous ion in **5a** was verified by MB spectroscopy ($\delta = 0.97$), and the unique absorption features were shown to arise from ^{tBu}ISQ ligand-based transitions. Although we were not able to obtain a crystal structure of [**8b**]$^{+}$, similarities between the spectral properties of **5a** and [**8b**]$^{+}$ indicate that the complexes share identical electronic configurations. Analysis of the more-oxidized [**6a**]$^{+}$ and [**9b**]$^{2+}$ species is less straightforward, since a preponderance of the data indicate that actual electronic structures lie between the Fe^{3+}─ISQ and Fe^{2+}─IBQ limits. For instance, the O,N-ligand in the [**9b**]$^{2+}$ crystal structure exhibits a more pronounced quinoid distortion than expected for a typical ISQ ligand, and the isomer shifts measure for [**6a**]$^{+}$ and [**9b**]$^{2+}$ ($\delta_{ave} \approx 0.68$) are considerable outside the range expected for high-spin ferric ions. However, the ν(O─C) frequencies observed by rR spectroscopy are more consistent with an ISQ oxidation state.

The unprecedented example of an Fe^{2+} center bound to an ISQ radical in complexes **5a** and [**8b**]$^+$ is made possible by the combination of high-spin states and trigonal-bipyramidal 5C geometries, which result in Fe centers with enhanced electron affinities. Concerning the role of spin state, our DFT calculations indicate that isomers of **5a** with intermediate- or low-spin centers converge to the alternate Fe^{3+}─amidophenolate(2─) configuration. The importance of coordination number is highlighted by comparison to the six-coordinate (6C) $[(L_{N4})Fe^{3+}(ISQ)]^{2+}$ complexes prepared by Wieghardt (where L_{N4} = *cis*-cyclam or tren).[81,82] These complexes undergo only ligand-based reductions to give the corresponding Fe^{3+} species with closed-shell amidophenolate(2─) ligands, even when the Fe center is high-spin. To the best of our knowledge, Wieghardt and coworkers have not explored the reduction of their five-coordinate $[Fe^{3+}(ISQ)_2X]$ complexes (X=Cl, Br, I, N_3). However, the square pyramidal, trianionic coordination environment likely lowers the potential of the Fe^{3+} center, favoring ligand-based reduction. These insights have implications for the Fe/O_2/substrate intermediate in the catalytic cycle of APDOs. Like **5a**/[**8b**]$^+$, this species contains a high-spin center, yet it also has a 6C geometry due to the presence of the O_2 ligand. Thus, extrapolation from the synthetic models would seem to favor the closed-shell electronic structure of intermediate **1** in Figure 4.1. However, unlike Wieghardt's $[L_{N4})Fe^{3+}(ISQ)]^{2+}$ models, the sixth ligand in the enzymatic intermediate (i.e., superoxide) is redox active and electron withdrawing, and therefore capable of facilitating electron transfer from the substrate ligand to the Fe center

Finally, it is worthwhile to consider why complexes like **5a**/[**8b**]$^+$ are viable, whereas the corresponding Fe^{2+}─SQ complexes have not been reported despite extensive

efforts in modeling catechol dioxygenases. Indeed, a catecholate analogue of **5a** has already been reported and crystallographically characterized by Moro-oka, namely, [Fe^{3+}($^{tBu/Pr}$Tp)(DBC)] (where DBC = dianion of 3,5-di-*tert*-butylcatechol).[107] Like **5a**, [Fe^{3+}($^{tBu/Pr}$Tp)(DBC)] contains a trigonal bipyramidal Fe/Tp unit bound to a bidentate "substrate" ligand; however, the catecholate lacks quinoid distortion (C─O bond lengths of 1.35 and 1.38 Å), and the collective metric and spectroscopic data demand an Fe^{3+}─catecholate description. The divergent electronic structures of **5a** and [Fe^{3+}($^{tBu/Pr}$Tp)(DBC)] point to the intrinsic difference in redox potentials between catecholate and amidophenolate dianions. This difference may have mechanistic implications for APDOs and ECDOs.

4.I. Conclusions

A variety of spectroscopic and computational methods have been employed to evaluate the electronic structures of mononuclear Fe complexes bound to redox-active ligands derived from 2-amino-4,6-di-*tert*-butylphenol ($^{tBu}APH_2$). Our studies included the ^{Ph2}Tp-supported complexes **5a** and [**6a**]SbF_6, as well as a parallel "**b**-series" of complexes prepared with the neutral ^{Ph2}TIP supporting ligand (Figure 4.2). Utilizing spectroscopic and DFT methods we have provided definitive evidence that complexes **5a**/[**8b**]$^+$ can best be described as a ferrous center bound to an ISQ radical. The higher oxidized complexes [**6a**]$^+$/[**9b**]$^+$ while not as clear suggest that the oxidation state lies between an ferric-ISQ and a ferrous-IBQ.

It is assumed the ECDOs and APDOs share a common catalytic mechanism; however, our synthetic experience indicates that a species like intermediate **II** in Figure

4.1 is more feasible for APDOs than ECDOs. Thus, the two catalytic cycles may differ at this point, with the ECDOs adopting an intermediate **I** structure (as proposed by Ye and Neese[46]) and the APDOs adopting an intermediate **II** structure with considerable radical character on the substrate, exemplifying the mechanistic sophistication of the enzymes catalytic mechanism.

4.J. Experimental

All reagents and solvents were purchased from commercial sources and used as received, unless otherwise noted. Acetonitrile, dichloromethane, and tetrahydrofuran were purified and dried using a Vacuum Atmospheres solvent purification system. The synthesis and handling of air-sensitive materials were performed under inert atmosphere using a Vacuum Atmospheres Omni-Lab glovebox. The ligands K(^{Ph2}Tp),[137] ^{Ph2}TIP,[173] and ^{tBu}APH$_2$[138] were prepared according to literature procedures. ^{15}N-labeled ^{tBu}APH$_2$ was prepared using ^{15}NH$_4$OH purchased from Cambridge Isotopes. Elemental analyses were performed at Midwest Microlab, LLC in Indianapolis, IN.

Samples of [**8b**]OTf for spectroscopic studies were prepared by treating [**7b**]OTf with one equivalent of TTBP$^{\bullet}$[139] in CH_2Cl_2. After stirring for two hours, the green solution was filtered and the solvent removed under vacuum. The resulting powder exhibited the following peaks in the IR spectrum: 3342 [ν(N─H)], 3054, 1439, 1259, 1222 cm^{-1}.

UV/Vis absorption spectra were obtained with an Agilent 8453 diode array spectrometer; NIR absorption spectra were measured using an Agilent Cary 5000 spectrophotometer. Fourier-transform infrared (FTIR) spectra of solid samples were

measured with a Thermo Scientific Nicolet iS5 FTIR spectrometer equipped with the iD3 attenuated total reflectance accessory. EPR experiments were performed using a Bruker ELEXSYS E600 equipped with an ER4415DM cavity resonating at 9.63 GHz., an Oxford Instruments ITC503 temperature controller, and an ESR-900 He flow cryostat. MCD spectra were obtained using a Jasco J-715 spectropolarimeter in conjunction with an Oxford Instruments SM-4000 8T magnetocryostat. Solid-state samples of [**6a**]SbF_6 were prepared as uniform mulls in fluorolube. All MCD spectra were obtained by subtracting the -7 T spectrum from the + 7 T spectrum to eliminate potential artifacts. Resonance Raman spectra were measured using 488.0 nm excitation from a Spectra Physics Ar^+ laser (model 202505), with 45 mW at the sample point in a 180° backscattering geometry. The sample was placed in a transparent quartz Dewar cell filled with liquid nitrogen and spun at 800 rpm. Spectra were collected with the Spec-10 system (Princeton Instruments) installed on the 1269 spectrograph (SPEX Industries) equipped with a standard 1200 grove/inch grating at 80 mm slit width. Spectra were calibrated with fenchone and indene standards. Low-field (0.04 T) variable temperature (5-200 K) Mössbauer spectra were recorded on a closed-cycle refrigerator spectrometer, model CCR4K, equipped with a 0.04 T permanent magnet, maintaining temperatures between 5 and 300 K. Mössbauer spectra were analyzed using the software WMOSS (Thomas Kent, See Co., Edina, Minnesota). The samples were polycrystalline powders, suspended in nujol, placed in Delrin 1.00 mL cups and frozen in liquid nitrogen. The isomer shifts are quoted at 6 K with respect to iron metal spectra recorded at 298 K.

Cyclic voltammetric (CV) measurements were conducted in the glovebox with an epsilon EC potentiostat (iBAS) at a scan rate of 100 mVs^{-1} with 100 mM $(NBu_4)PF_6$ A

three-electrode cell containing a Ag/AgCl reference electrode, a platinum auxiliary electrode, and a glassy carbon working electrode was employed. Under these conditions, the ferrocene/ferrocenium ($Fc^{+/0}$) couple has an $E_{1/2}$ value of +0.52 V in CH_2Cl_2.

X-ray diffraction (XRD) data were collected with an Oxford Diffraction SuperNova kappa-diffractometer (Agilent Technologies) equipped with dual microfocus Cu/Mo X-ray sources, X-ray mirror optics, Atlas CCD detector, and low-temperature Cryojet device. The data were processed with CrysAlis Pro program package (Agilent Technologies, 2011) typically using a numerical Gaussian absorption correction (based on the real shape of the crystal), followed by an empirical multi-scan correction using SCALE3 ABSPACK routine. The structures were solved using SHELXS program and refined with SHELXL program[147] within Olex2 crystallographic package.[148] B- and C-bonded hydrogen atoms were positioned geometrically and refined using appropriate geometric restrictions on the corresponding bond lengths and bond angles within a riding/rotating model (torsion angles of methyl hydrogens were optimized to better fit the residual electron density).

DFT calculations were performed using the ORCA 2.8 software package developed by Dr. F. Neese.[174] Geometry optimizations employed either the Beck-Perdew (BP86) functional[175] or Becke's three-parameter hybrid functional (B3LYP).[142] Ahlrichs' valence triple-ζ basis set (TZV), in conjunction with the TZV/J auxiliary basis set,[144,145] were used for all calculations. Time-dependent DFT (TD-DFT) calculations[176-178] computed absorption energies and intensities within the Tamm-Dancoff approximation.[179] In each case, at least 60 excited states were calculated. Vibrational frequency calculations were performed with a truncated [**6a**]$^+$ model with hydrogen

atoms at the 3- and 5-positions of the Tp ligand. Calculation of the harmonic force fields proved that the optimized structure is a local minima on the approach described in Römelt et al.[180]; in these calculation, the size of the integration grid for Fe, O, and N atoms was increased. The gOpenMol program[146] developed by Laaksonen was used to generate isosurface plots of molecular orbitals.

^{Ph2}TIPFe^{2+}(^{tBu}APH)OTf ([7b]OTf): [^{Ph2}TIPFe^{2+}($CH_3CN)_3$]OTf (1.1194 g, 0.927 mMol) and 4,6-di-*t*-butyl-aminophenol (205.1 mg, 0.927 mMol) were mixed in 10 mL of CH_2Cl_2. NEt_3 (142 μL, 1.02 mMol) was added and the reaction allowed to stir over night. The next morning the reaction was filtered and the solvent removed under vacuum. The brown solid was taken up in mL toluene and the product precipitated with excess pentane. The yellow solid was collected and was further washed with pentane. The product was collected and dried to yield a bright yellow powder. % Yield 921.4mg, 86% UV-vis [λ_{max}, nm (ε, M^{-1} cm^{-1}) in CH_2Cl_2]: 399 (1163). IR (neat, cm^{-1}): 3348, 3059, 2949, 2901, 2861, 1064, 1462, 1442, 1273, 1255, 1152, 1030.

^{Ph2}TIPFe^{2+}(^{tBu}APH)BPh$_4$ ([7b]BPh$_4$): ^{Ph2}TIPFe^{2+}(^{tBu}APH)OTf (125.3 mg, 0.108 mMol) in 4 mL MeOH was combined with $NaBPh_4$ (37.6 mg, 0.110 mMol) in 3 mL MeOH. Stirred for 15 minutes. The solid was collected as a yellow paste and dried under vacuum. Crystals suitable for x-ray analysis were obtained by a 1,2-dichloroethane and MeOH layering. % Yield: 83.1 mg, 58%. Elemental Analysis cald for $C_{86}H_{81}BFeN_7OP$: C, 77.88; H, 6.16; N, 7.39%; found: C, 76.70; H, 6.13; N, 7.13%. UV-vis [λ_{max}, nm (ε, M^{-1} cm^{-1}) in CH_2Cl_2]: 815 (8.598). IR (neat, cm^{-1}): 3340, 3050, 2948, 2863, 1578, 1478, 1443, 1379, 1305, 1264, 1142, 1074, 1023.

^{Ph2}TIPFe^{3+}(^{tBu}ISQ)OTf$_2$ ([9b]OTf$_2$): ^{Ph2}TIPFe^{2+}(^{tBu}APH)OTf (184.1 mg, 0.159 mMol) and AgOTf (83 mg, .323 mMol) were stirred in 6 mL THF for 1 hour to give a dark green solution. The solution was filtered through celite and the THF removed under vacuum. The remaining dark green solid was taken up in 1,2-dichloroethane and layered with hexanes. After several days dark green crystals formed. X-ray analysis confirmed the correct structure. [λ_{max}, nm (ε, M^{-1} cm^{-1}) in CH_2Cl_2]: 798 (2506). IR (neat, cm^{-1}): 3270, 3058, 2959, 1603, 1578, 1469, 1445, 1364, 1257, 1221, 1147, 1073, 1026.

^{Ph2}TPFe^{2+}(DMAPH) (10a): 2-(N,N-Dimethylamino)-4,6-di-tert-butylphenol was prepared according to the previously published procedure.[181] The aminophenol (174.8 mg, 0.701 mMol) was taken up in 5 mL of CH_3CN while KTp^{Ph2} (496.8 mg, 0.701 mMol) and Fe(OTf)$_2$ (248.2 mg, 0.701 mMol) were taken up in 5 mL of CH_2Cl_2 and CH_3CN respectively. The aminophenol and KTp^{Ph2} solutions were mixed and NEt_3 (108 µL, 0.774 mMol) was added. The Fe(OTf)$_2$ solution was then added and the resulting brown solution stirred overnight. The solvents were removed under vacuum the next day and the solid taken up in 6 mL of CH_2Cl_2 and filtered. The solution was stored in a freezer at -30C for several days to yield bright yellow crystals. % Yield: 160 mg, 24%. Elemental Analysis cald for $C_{61}H_{60}BFeN_7O$: C, 75.23; H, 6.21; N, 10.07%; found: C, 74.97; H, 6.18; N, 10.07%. UV-vis [λ_{max}, nm (ε, M^{-1} cm^{-1}) in CH_2Cl_2]: 365 (1955). IR (neat, cm^{-1}): 3056, 2948, 2855, 2637, 1545, 1462, 1412, 1356, 1302, 1264, 1246, 1167, 1060, 1028, 1007.

Table 4.8. Summary of X-ray Crystallographic Data Collection and Structure Refinement

	[**7b**]BPh_4•1.5DCE	[**9b**]$(OTf)_2$•CH_2Cl_2	[**10a**]•4CH_2Cl_2
empirical formula	C89H87BCl3FeN7OP	C65H62Cl2F6FeN7O7PS2	C65H68BCl8FeN7O
formula weight	1474.68	1389.08	1313.56
crystal system	triclinic	monoclinic	monoclinic
space group	$P\bar{1}$	$P2_1/c$	$P2_1/c$
a, Å	17.32204(4)	20.0160(13)	17.1045(5)
b, Å	20.6267(4)	15.3008(11)	14.4938(5)
c, Å	22.0768(4)	22.2057(18)	26.5165(8)
α, deg	81.955(2)	90	90
β, deg	78.343(2)	94.320(8)	100.482(3)
γ, deg	87.958(2)	90	90
V, $Å^3$	7649.0(3)	6781.4(9)	6464.0(3)
Z	4	4	4
D_{calc}, g/cm^3	1.281	1.355	1.317
λ, Å	1.5418	0.7107	0.7107
μ, mm^{-1}	0.376	4.010	4.987
θ-range, deg	7 to 59	7 to 148	7 to 146
reflections collected	101066	35453	41153
independent reflections	37578 [R_{int} = 0.0357]	13347 [R_{int} = 0.0787]	12682 [R_{int} = 0.0356]
data/restraints/parameters	37578/0/1889	13347/0/887	12682/30/793
GOF (on F^2)	1.035	1.033	1.013
R1/wR2 (I>2σ(I))	0.0552/0.1469	0.0723/0.1786	0.0606/0.1488
R1/wR2 (all data)	0.0708/0.1608	0.1153/0.2105	0.0764/0.1588

Chapter 5

Dioxygen Reactivity of Biomimetic Fe(II) Complexes with Noninnocent Catecholate, *o*-Aminophenolate, and *o*-Phenylenediamine Ligands

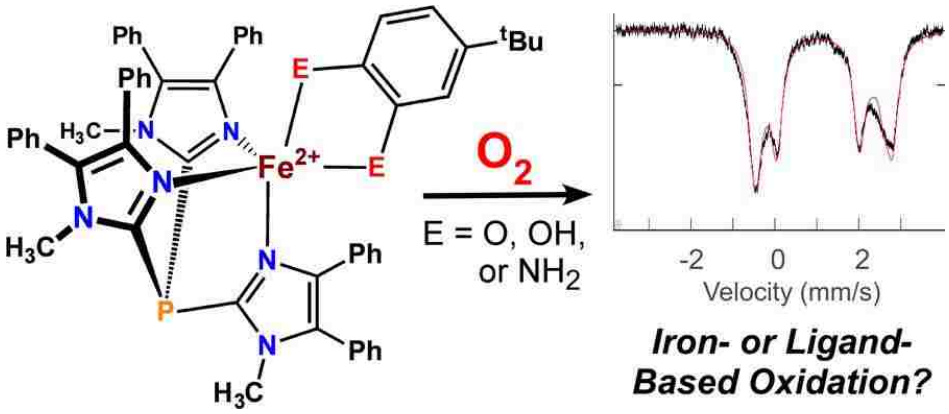

Abstract: In this chapter we describe the O_2 reactivity of a series of high-spin mononuclear Fe(II) complexes each containing the facially coordinating tris(4,5-diphenyl-1-methylimidazol-2-yl)phosphine (^{Ph2}TIP) ligand and one of the following bidentate, redox-active ligands: 4-*tert*-butylcatecholate (^{tBu}CatH$^-$), 4,6-di-*tert*-butyl-2-aminophenolate (^{tBu2}APH$^-$), or 4-*tert*-butyl-1,2-phenylenediamine (^{tBu}PDA). Each complex is oxidized in the presence of O_2, and the geometric and electronic structures of the resulting complexes were examined with spectroscopic (absorption, EPR, Mössbauer, resonance Raman) and density functional theory (DFT) methods.

Parts of the following chapter have appeared in the following paper Bittner, M. M.; Lindeman, S. V.; Popescu, C. V.; Fiedler, A. T. *Inorg. Chem.* 2014.

All DFT calculations and rR experiments were performed by Dr. Adam Fiedler. Mössbauer experiments were conducted by Codrina V. Popescu of Ursinus College.

5.A. Introduction

Catechols and their nitrogen-containing analogs (*o*-aminophenols and *o*-phenylenediamines; see Figure 5.1) are well established members of the "*o*-phenylene family" of redox noninnocent ligands.[36-38,88,136,182-194] One-electron oxidation of these bidentate ligands provides the corresponding (di)(imino)semiquinonate radicals, and two-electron oxidation yields the closed-shell (di)(imino)benzoquinones. Complexes that combine the noninnocent ligands in Figure 5.1 with redox-active metal center(s) often possess ambiguous electronic structures, since multiple assignments of ligand and metal oxidation states are possible. Thus, careful examination with a variety of experimental and computational methods is usually required to obtain accurate electronic-structure descriptions.[85-87,89,159]

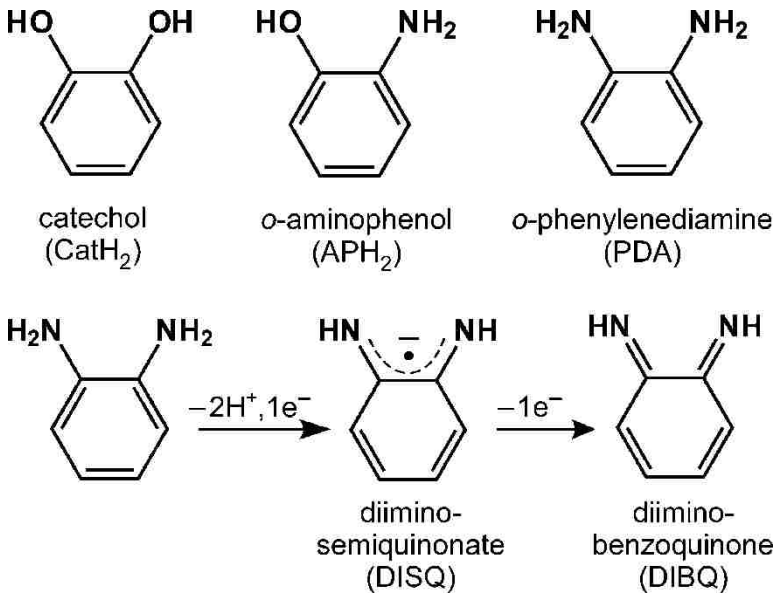

Figure 5.1 Redox active *o*-Phenylene ligands and their varying electron configurations.

While the role of *o*-phenylene ligands in electron-transfer series has been studied extensively, their ability to facilitate *proton-coupled* electron transfers (PCETs) in transition-metal complexes has received less attention. As shown in Figure 5.1, the free compounds are able to donate a total of two protons ($2H^+$) and two electrons ($2e^-$) in various combinations. Coordination to a redox-active metal center is expected to perturb the chemical and electronic properties of these ligands, resulting in complexes with rich and unpredictable PCET landscapes. Such complexes may find applications in chemical processes that require multiple proton and electron transfers, including energy-related reactions like water oxidation, hydrogen production, and nitrogen fixation.[195-200] For instance, an iron complex with *o*-phenylenediamine ligands was recently shown to undergo photochemical H_2-evolution via PCET steps.[201] Similarly, Heyduk et al. have found that zirconium(IV) complexes with noninnocent bis(2-phenolato)amide ligands react with O_2 to yield $[Zr^{4+}{}_2(\mu\text{-}OH)_2]$ species-a process that requires donation of $1H^+$ and $2e^-$ from each ligand.[202]

Our interest in noninnocent ligands stems from efforts to prepare synthetic mimics of mononuclear nonheme iron dioxygenases. These enzymes carry out the oxidative ring cleavage of aromatic substrates (catechols, aminophenols, and hydroquinones), and the catalytic cycles are thought to involve formation of a ferrous-(substrate radical) intermediate.[5,23,43,203] Earlier in this manuscript, we reported the synthesis of two mononuclear Fe(II) complexes (**4** and [**7**]OTf) that model the substrate-bound form of aminophenol dioxygenases.[173,204] The high-spin ferrous centers of **4** and $[\mathbf{7}]^+$ are bound to the 2-amino-4,6-di-*tert*-butylphenolate (^{tBu2}APH) "substrate," and the enzymatic coordination environment is replicated using a facially coordinating N3

supporting ligand: hydrotris(3,5-diphenylpyroazol-1-yl)borate (^{Ph2}TP) in the case of **4** and tris(4,5-diphenyl-1-methylimidazol-2-yl)phosphine (^{Ph2}TIP) in [**7**]OTf (see Figure 5.2).

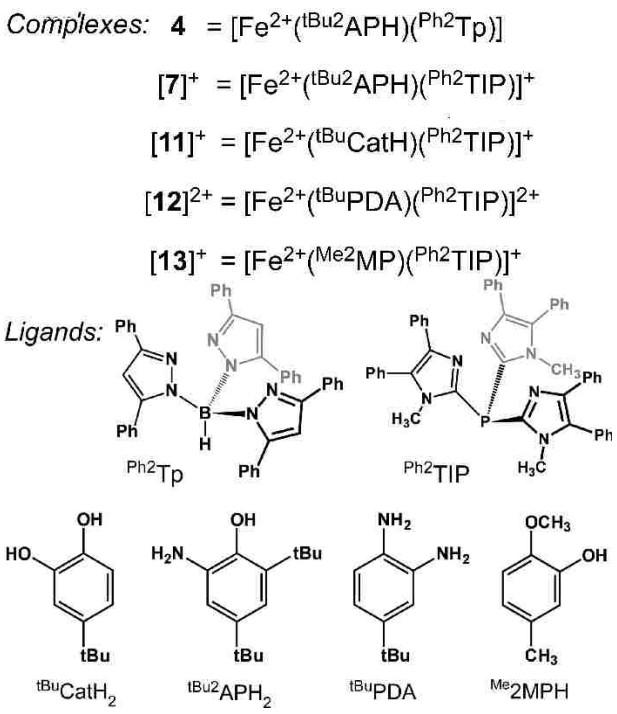

Figure 5.2 Complexes discussed in this chapter.

These complexes were shown to engage in ligand-based H-atom transfer (HAT) reactions to yield novel species containing an Fe(II) center coordinated to an iminobenzosemiquinonate (^{tBu2}ISQ) radical, thus providing synthetic precedents for the putative Fe(II)/ISQ intermediate of the enzyme. The Fe(II)/ISQ complexes can be further oxidized by one electron, although it has proven difficult to determine whether this process is ligand- or iron-based. Detailed crystallographic, spectroscopic, and computational analyses suggest that the fully oxidized species have intermediate

electronic configurations between the $Fe^{3+tBu2}ISQ$ and $Fe^{2+-tBu2}IBQ$ limits,[205] where ^{tBu2}IBQ is iminobenzoquinone with *tert*-butyl substituents at the 4- and 6- positions.

In this chapter, we expanded upon our previous studies by preparing monoiron(II) ^{Ph2}TIP-based complexes with ligands derived from catechol and *o*-phenylenediamine. Like the *o*-aminophenolate studies described earlier, we began with the synthesis and X-ray structural characterization of mononuclear, high-spin Fe(II) complexes, each containing a bidentate ligand capable of both proton and electron transfer. The catecholate complex [**11**]OTf was prepared using 4-*tert*-butylcatechol ($^{tBu}CatH_2$) and the ^{Ph2}TIP supporting ligand (Figure 5.2). The *o*-phenylenediamine complex [**12**](OTf)$_2$ has the overall formulation of [Fe(^{Ph2}TIP)(^{tBu}PDA)(OTf)$_2$, where ^{tBu}PDA is 4-*tert*-butyl-1,2-phenylenediamine. Each of the three Fe(II) complexes ([**7**]$^+$, [**11**]$^+$, and [**12**]$^{2+}$) is air-sensitive, and the products of the O_2 reactions have been characterized with spectroscopic (ultraviolet-visible (UV-vis) absorption, electron paramagnetic resonance (EPR), Mössbauer, resonance Raman) and computational (density functional theory (DFT)) methods. These studies revealed that the identity of the ligand controls whether the O_2-driven oxidation is an Fe- or ligand based process (or a combination of both). In addition, O_2 reaction rates vary by greater than 5 orders of magnitude across the series, despite the fact that the overall structures of the Fe(II) complexes are quite similar. Thus, this unique series of complexes has provided a valuable framework for exploring the relationship between ligand-based PCET chemistry and the O_2 reactivity of Fe complexes. Implications for ring-cleaving dioxygenases are also discussed.

5.B. Synthesis, Solid State Structures, and Spectroscopic Features

Reactions of [Fe(^{Ph2}TIP)(MeCN)$_3$](OTf)$_2$ with ^{tBu}CatH$_2$ or ^{tBu}PDA in THF generated the ^{Ph2}TIP-based complexes [**11**]OTf and [**12**](OTf)$_2$, respectively; the synthesis of [**11**]$^+$ also required 1 equiv. of NEt$_3$. Yellow crystals of [**11**]OTf were grown by layering a 1,2-dichloroethane (DCE) solution with hexane. Recrystallization of [**12**](OTf)$_2$ by slow diffusion of Et$_2$O into a DCE solution provided colorless and analytically pure material that was used in subsequent reactivity and spectroscopic studies. Crystals for X-ray diffraction (XRD) analysis were obtained by either (i) slow diffusion of Et$_2$O into a concentrated MeCN solution of [**12**](OTf)$_2$ or (ii) pentane layering of a DCE solution, we were able to grow well-diffracting crystals with an overall composition of [**12**](OTf)(BPh$_4$). As shown in Figure 5.3, the X-ray structure of [**11**]OTf features a five-coordinate (5C) Fe(II) complex with bidentate monoanionic catecholate and facially coordinating ^{Ph2}TIP ligands. The [**3**]OTf unit cell contains two symmetrically independent complexes, and metric parameters for both are provided in Table 5.1 The Fe(II) coordination geometry is trigonal-bypyramidal for one cation (τ = 0.70)[155] and distorted square-pyramidal (τ = 0.24) for the other.

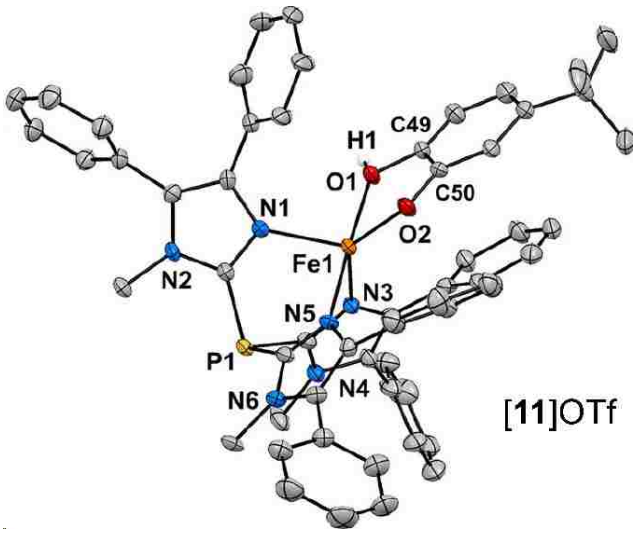

Figure 5.3. Thermal ellipsoid plot (50% probability) derived from the X-ray structure of [**11**]OTf•2DCE. Counteranions, noncoordinating solvent molecules, and most hydrogen atoms have been omitted for clarity.

The crystallographic data provide solid evidence that the catecholate ligand is monoanionic. First, there is a significant difference in the lengths of the O1-C49 and O2-C50 bonds (1.39 and 1.33 Å, respectively). Second, the ^{tBu}CatH ligand binds asymmetrically with Fe1-O1 bond distances that are ~0.30 Å longer than the corresponding Fe1─O2 distance of 2.23 ± 0.01 Å, while the anionic donor exhibits a shorter Fe1─O2 distance of 1.92 ± 0.01 Å (Table 5.1). Such bond distances are generally similar to those observed in the four previously reported Fe(II) complexes with monoanionic catecholate ligands.[206-209] The triflate counteranion forms a hydrogen bond with the hydroxyl group of the ^{tBu}CatH ligand, consistent with the O1···O3(OTf) distance of ~2.67 Å. The average Fe─N bond distance is 2.150 Å, similar to the corresponding distances measured for the ^{tBu2}APH-based complex ([**7**]$^+$) and indicative of a high-spin, pentacoordinate Fe(II) complex.[173] Consistent with this fact, the ^{1}H NMR spectrum displays paramagnetically shifted peaks ranging from 65 to -30 ppm (Figure 5.4).

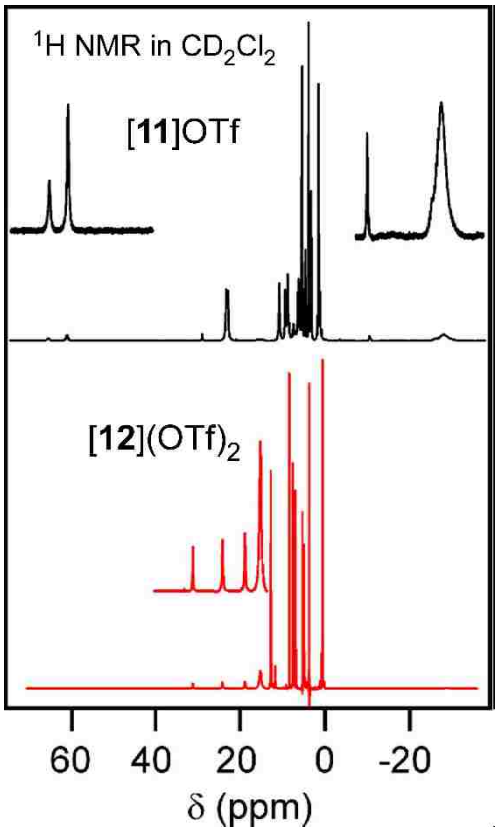

Figure 5.4. ^{1}H NMR spectra of [**11**]OTf (top) and [**12**](OTf)$_2$ (bottom) in CD_2Cl_2. Peak intensities in the insets were enlarged (× 20) for the sake of clarity.

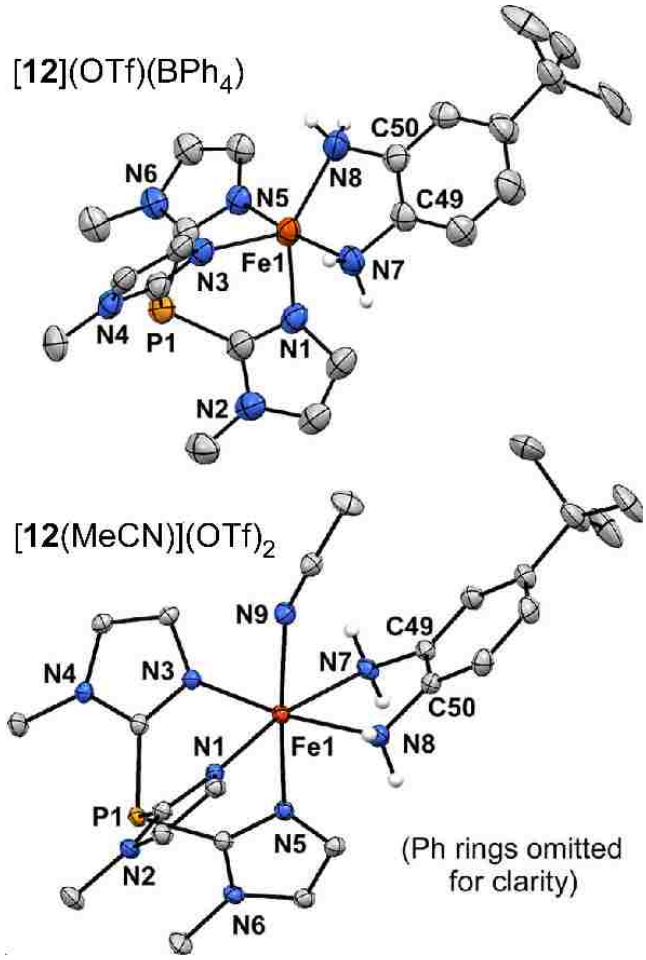

Figure 5.5. Thermal ellipsoid plots (50% probability) derived from [**12**](OTf)(BPh_4)•DCE•C_5H_{12} (top) and [**12**(MeCN)](OTf)•MeCN•Et_2O (bottom). Counteranions, noncoordinating solvent molecules, and most hydrogen atoms have been omitted for clarity. The phenyl rings of the ^{Ph2}TIP ligands have also been removed to provide a clearer view of the first coordination sphere.

Table 5.1. Selected Bond Distances (Å) and Bond Angles (deg) for [**11**]$^{+}$, [**12**]$^{2+}$, and [**13**]$^{+}$ Measured with X-ray Diffraction.

	[**11**]OTf•2DCE[a]		[**12**](OTf)(BPh_4) •DCE•C_5H_{12}	[**12**(MeCN)](OTf)•MeCN•Et_2O	[**13**](OTf)•1.5CH_2Cl_2[b]
	(A)	(B)			
Fe1-N1	2.118(3)	2.121(3)	2.089(4)	2.174(2)	2.124(2)
Fe1-N3	2.124(3)	2.155(3)	2.115(3)	2.162(2)	2.120(2)
Fe1-N5	2.192(3)	2.192(3)	2.181(3)	2.227(2)	2.142(2)
Fe1-O1/N7	2.226(3)	2.241(3)	2.224(3)	2.237(2)	2.229(2)
Fe1-O2/N8	1.922(3)	1.938(3)	2.131(4)	2.246(2)	1.919(2)
Fe1-N9				2.214(2)	
O1/N7-C49	1.390(5)	1.395(5)	1.445(5)	1.444(2)	1.390(3)
O2/N8-C50	1.323(5)	1.327(5)	1.458(5)	1.454(2)	1.336(3)
N1-Fe1-N3	93.5(1)	94.2(1)	95.3(1)	86.07(6)	94.03(7)
N1-Fe1-N5	91.3(1)	91.9(1)	84.5(1)	91.74(6)	89.20(7)
N3-Fe1-N5	85.4(1)	85.9(1)	91.1(1)	88.90(6)	85.81(7)
N1-Fe1-O1/N7	90.5(1)	102.3(1)	94.7(1)	167.47(6)	90.75(6)
N3-Fe1-O1/N7	90.7(1)	89.6(1)	96.9(1)	99.93(6)	90.21(6)
N5-Fe1-O1/N7	175.7(1)	165.4(1)	172.0(1)	89.59(6)	176.01(6)
N1-Fe1-O2/N8	130.7(1)	114.5(1)	145.3(1)	93.45(6)	124.35(7)
N3-Fe1-O2/N8	133.8(1)	1503(1)	119.2(1)	172.48(6)	139.32(7)
N5-Fe1-O2/N8	103.7(1)	100.0(1)	92.2(1)	96.87(6)	105.70(7)
O1/N7-Fe1-O2/N8	77.9(1)	77.4(1)	77.8(1)	75.38(6)	77.58(6)
τ-value[c]	0.70	0.24	0.45		0.61

[a]The [**11**]OTf•2DCE structure contains two symmetry-independent complexes per unit cell. Parameters are provided for both structures. [b]The [**13**]OTf•1.5CH_2Cl_2 structure contains two symmetry-independent complexes per unit cell. Since the structures are nearly identical, parameters are only provided for one complex. [c]See reference 39 for definition of the τ value.

The two X-ray structures of complex [**12**]$^{2+}$ shown in Figure 5.5 reflect the different conditions under which the crystals were generated (vide supra). Crystals grown in a DCE/pentane mixture contain a 5C dicationic Fe complex associated with one OTf and one BPh_4 counteranion, in addition to DCE and pentane solvent molecules (Table 5.1). The coordination environment of the Fe(II) center is intermediate between square-planer and trigonal-bipyramidal (τ = 0.45; Table 5.1). In contrast, the structure arising from crystals grown in MeCN/Et_2O features a six-coordinate (6C) Fe(II) center bound to a solvent-derived MeCN ligand in addition to ^{Ph2}TIP and ^{tBu}PDA (Figure 5.5).

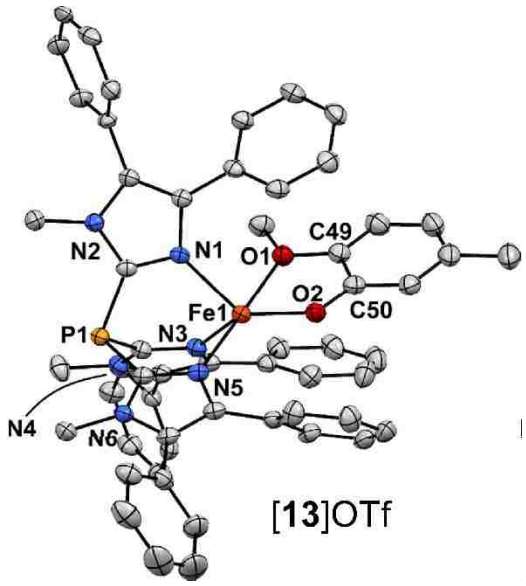

Figure 5.6. Thermal ellipsoid plot (50% probability) derived from the X-ray structure of [**13**]OTf•1.5CH_2Cl_2. Counteranions, noncoordinating solvent molecules, and hydrogen atoms have been omitted for clarity.

The increase in coordination number lengthens the average Fe-N_{TIP} bond distance from 2.13 Å in [**12**]$^{2+}$ to 2.19 Å in [**12**(MeCN)]$^{2+}$. The ^{tBu}PDA ligand binds symmetrically in the 6C structure (Fe-N_{PDA} distance of 2.24(1) Å), while the Fe1-N7/N8

distances differ by 0.093 Å in the 5C structure. The observed Fe-N bond lengths indicate that the Fe(II) centers are high-spin in both structures. This conclusion is supported by the corresponding ^{1}H NMR spectrum (Figure 5.4) and the measured magnetic moment of 5.48 μ_B in CH_2Cl_2. The neutral charge of the ^{tBu}PDA ligands is confirmed by the presence of N-C bond lengths of 1.45(1) Å, typical of aryl amines (anilide anions, in contrast, exhibit N-C bond distances of ~1.39 Å). In both structures, the ^{tBu}PDA ring tilts out of the plane formed by the N7-Fe1-N8 chelate by ~23°, and each triflate is hydrogen-bonded to an amino group of ^{tBu}PDA.

As described below, the noninnocent nature of the *o*-phenylene ligands play an important role in the reactions of the corresponding Fe(II) complexes with O_2. To highlight this phenomenon, we prepared a "control" ^{Ph2}TIP-based Fe(II) complex with a completely innocent ligand (i.e., one incapable of transferring either protons or electrons). For this purpose we selected 2-methoxy-5-methylphenolate (^{Me}2MP); this ligand is structurally similar to ^{tBu}CatH, yet the second O-donor is methylated instead of protonated. Complex [Fe^{2+}(^{Ph2}TIP)(^{Me}2MP)]OTf, was prepared in a manner similar to [**11**]OTf, and light green crystals were obtained by layering a CH_2Cl_2 solution with hexanes. The resulting structure reveals a 5C, high-spin Fe(II) center bound to ^{Ph2}TIP and ^{Me}2MP in a distorted trigonal-bypyramidal geometry Figure 5.6. Importantly, the Fe-O/N bond distances measured for [**13**]$^{+}$ are very similar to those found for [**11**]$^{+}$ Table 5.1; like ^{tBu}Cat, the ^{Me}2MP ligand binds in an asymmetric manner, with Fe-O distances of 1.92 and 2.23 Å. Thus, the overall structure of [**13**]$^{+}$ closely resembles those in the *o*-phenylene series. However, methylation of the –OH donor eliminates the possibility of

ligand-based electron transfer (ET) and proton transfer (PT), and this change causes the O_2 reactivities of [**11**]$^+$ and [**13**]$^+$ to diverge in dramatic fashion (vide infra).

Voltammetric studies of the Fe(II) complexes were conducted in CH_2Cl_2 at scan rate of 100 mV/s with 0.1 M $(NBu_4)PF_6$ as the supporting electrolyte; redox potentials were referenced to ferrocenium/ferrocene ($Fc^{+/0}$). The CV of the catecholate complex [**11**]$^+$ displays an irreversible anodic wave at +740 mV (Figure 5.7) and a quasi-reversible couple with $E_{1/2}$ = -30 mV (peak-to-peak separation, ΔE, of 120 mV). Complex [**13**]$^+$ exhibits a quasi-reversible event at nearly the same potential (-10 mV, ΔE = 145 mV), consistent with the structural similarity between [**11**]$^+$ and [**13**]$^+$ noted above. In our previous electrochemical studies of high-spin 5C Fe(II) complexes with Tp or TIP ligands, the Fe^{2+}/Fe^{3+} couple generally appears within 300 mV of the $Fc^{+/0}$ reference.[126,173,205,210] Thus, it is reasonable to assign the first oxidations of [**3**]$^+$ and [**5**]$^{2+}$ to the Fe^{2+}/Fe^{3+} couple.

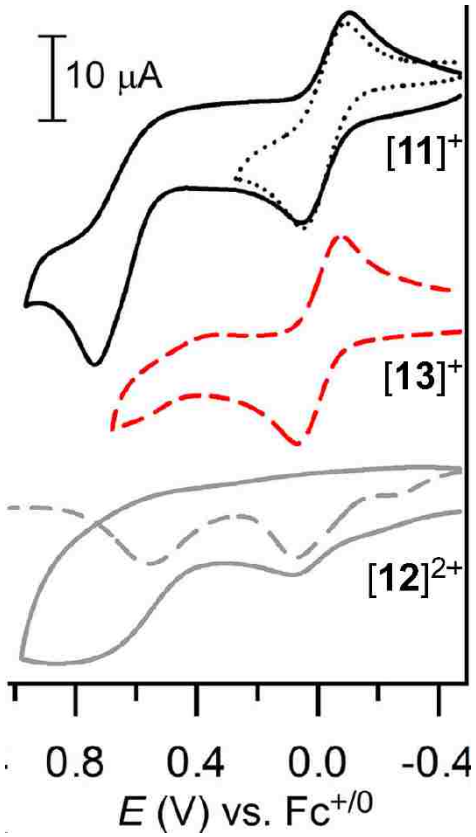

Figure 5.7. Cyclic voltammograms for [**11**]OTf (top, black), [**13**]OTf (middle, red) and [**12**](OTf)$_2$ (bottom, grey) collected in CH_2Cl_2 with 0.1 M $(NBu_4)PF_6$ as the supporting electrolyte and scan rate of 100 mV/s. The corresponding square-wave voltammogram (dashed line) is also shown for [**12**](OTf)$_2$. In all cases the voltammogram was initiated by the anodic sweep.

By comparison, the cyclic voltammogram of the phenylenediamine complex [**12**](OTf)$_2$ is less well-defined, but two events are clearly evident at +70 and 560 mV in the corresponding square-wave voltammogram (dashed line in Figure 5.7). We attribute the low-potential peak to the Fe^{2+}/Fe^{3+} couple, which appears ~100 mV higher than the corresponding potentials for [**11**]$^+$ and [**13**]$^+$. This anodic shift is likely due to the neutral charge of ^{tBu}PDA compared to the monoanionic ^{tBu}CatH and ^{Me2}MP ligands. The high-potential redox events for [**11**]$^+$ and [**12**]$^{2+}$ arise from oxidation of the catecholate or phenylenediamine ligand, respectively. This assignment is consistent with a previous

study by Lever et al., which found that the PDA ligand is oxidized at +500 mV (vs saturated calomel electrode) when bound to a Ru(II) center.[211] Both redox events are irreversible for [**12**]$^{2+}$; indeed, the electrochemical behavior of [**12**]$^{2+}$ resembles that reported previously for the *o*-aminophenolate complex **4**, which likewise exhibits an irreversible anodic wave near 0 mV, likely due to an ET-PT process.[205] For reasons that are not clear to us, complex [**7**]OTf failed to exhibit well-defined electrochemical features; however, on the basis or prior results,[126] the Fe^{2+}/Fe^{3+} potential of [**7**]OTf is likely ~150 mV more positive than the corresponding potential of **4**.

5.C. Reaction With Dioxygen

Pale yellow solutions of [**11**]OTf in CH_2Cl_2 undergo rapid color change upon exposure to air, yielding the blue-green chromophore **11^{ox}**. The corresponding electronic absorption spectrum, shown in Figure 5.8, consists of two broad bands at 700 and 905 nm with ε-values of ~1100 M^{-1} cm^{-1}. These spectral features are characteristic of ferric-catecholate(2-) complexes and arise from ^{tBu}Cat → Fe(III) ligand-to-metal charge transfer (LMCT) transitions.[206,208,209] The EPR pectrum of **11^{ox}** displays two S = 5/2 signals with E/D values of 0.14 and 0.25 (Figure 5.9), consistent with the presence of a high-spin Fe(III) center. In addition, the Mössbauer (MB) spectrum of **11^{ox}** reveals two quadrupole doublets with isomer shifts (δ) near 0.5 mm/s, typical of high-spin ferric ions (Table 5.2 and Figure 5.10). The doublets have different splittings (ΔE_Q) of 0.82 and 1.24 mm/s. The heterogeneity in E/D and ΔE_Q values likely arises from different orientations of the ^{tBu}Cat ligand in the oxidized complex, similar to the situation observed in the solid state

for [**11**]OTf. Collectively, the spectroscopic data indicate that **11**^{ox} has the formula of [Fe^{3+}(^{Ph2}TIP)(^{tBu}Cat)OTf.

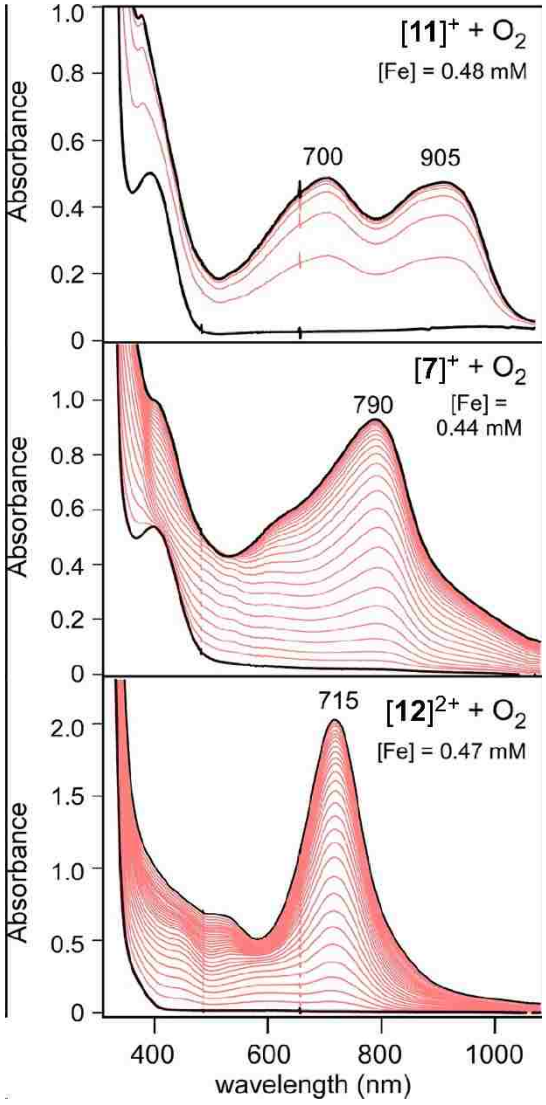

Figure 5.8. Time-resolved absorption spectra for the reaction of [**11**]OTf (top), [**7**]OTf (middle), and [**12**](OTf)$_2$ (bottom) with O_2; spectra were collected at intervals of 1, 20, and 14400 s, respectively. Each reaction was performed at room-temperature in O_2-saturated CH_2Cl_2 ([O_2] = 5.8 mM). The path length of the cuvette was 1.0 cm.

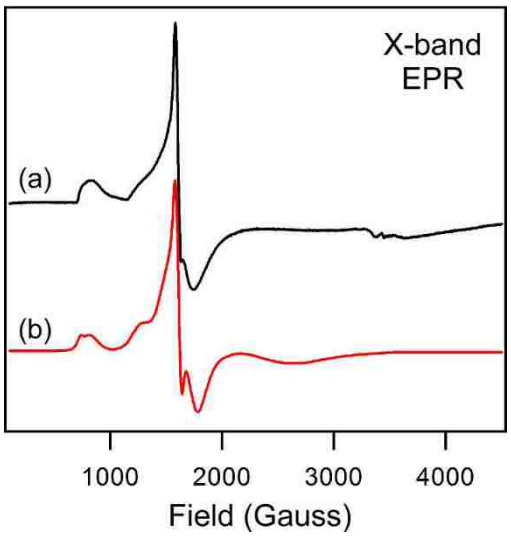

Figure 5.9. (a) Experimental X-band EPR spectrum of **11^{ox}** in CH_2Cl_2 collected at 10 K. (b) Simulated spectrum generated with the program EasySpin4. Adequate simulation required the presence of two S = 5/2 signals in a 2:1 ratio. The major and minor species have E/D−values of 0.14 and 0.25, respectively.

Table 5.2. Experimental Mössbauer Parameters

complex	isomer shift (δ) mm/s	quadrupole splitting (ΔE_Q) mm/s	reference
4	1.06	2.52	32
[**7**]OTf	1.06 (70%)/1.14(30%)	2.08/2.93	32
7^{ox}	0.64	1.94	32
[**11**]OTf	1.08	2.05	this work
11^{ox}	0.53/0.50	0.82/1.24	this work
[**12**](OTf)$_2$	1.04 (75%)/1.05 (25%)	3.13/2.53	this work
12^{ox}	1.03 (40%)/1.18 (35%)[a]	1.98/3.24	this work

[a]The remaining intensity (25%) arises from the starting material, [**12**](OTf)$_2$.

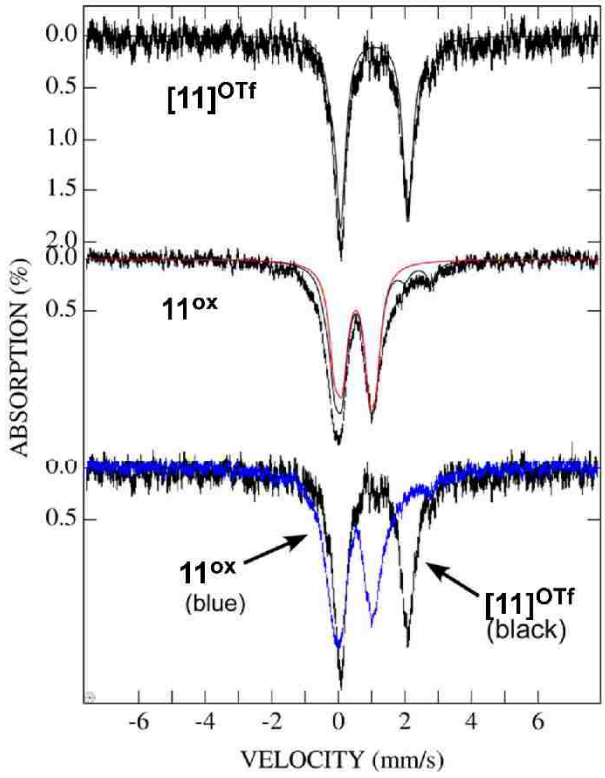

Figure 5.10. Mössbauer spectra of complexes **11** and **11^{ox}** recorded at 5 K and 77 K, respectively, in an applied field of 0.04 T. The solid lines represent spectral simulations of the most important species in the spectra. The resulting parameters are provided in Table 5.2. The lowest figure is a superposition of the **11** and **11^{ox}** spectra showing the clear conversion of the Fe(II) complex into a species with an Fe(III) center.

In the presence of air, the distinctive absorption bands of **11**^{ox} exhibit first-order decay with a half-life ($t_{1/2}$) of 6300 s, eventually yielding a nearly featureless spectrum. Previous studies of related complexes indicate that this decomposition corresponds to oxidation of the catecholate ligand via one (or more) of the pathways shown in Figure 5.11.[111,208,212]

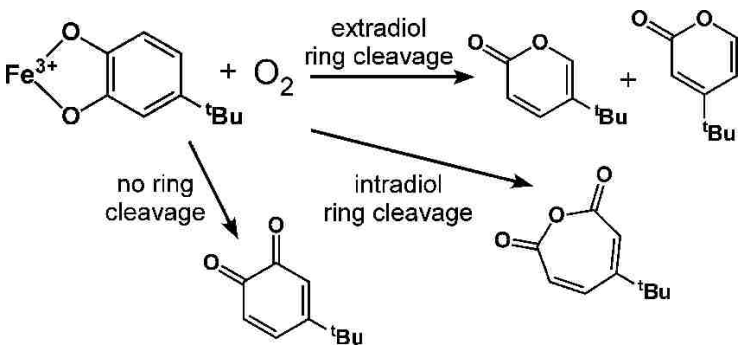

Figure 5.11. Possible decomposition pathways of Fe(III)-catecholates.

To determine reaction products, the final mixture was analyzed after treatment with acid and extraction into organic solvent ($MeCN/Et_2O$). The extradiol cleavage products, 4-*tert*-butyl-2-pyrone and 5-*tert*-butyl-2-pyrone, are generated in a 40:60 ratio with an overall yield of ~30%, as determined by ^1H NMR. These compounds were also observed using GC-MS, although the isomers are indistinguishable by this technique. When the reaction was performed with $^{18}O_2$, the ion signal arising from the extradiol products shifted upward by two mass units, providing conclusive evidence for incorporation of one O atom from O_2 (Figure 5.12). The $\mathbf{11}^{ox}$ reactivity conforms to the previously established pattern that iron(III)-catecholate complexes with facial, tridentate supporting ligands yield primarily extradiol products, while those with tetradentate ligands provide intradiol products.[107,206,213,214]

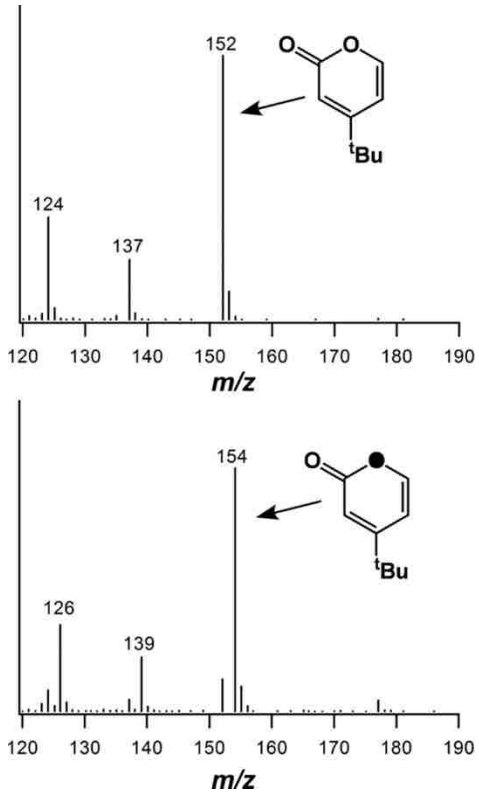

Figure 5.12. GC-MS data of the solution obtained from the reaction of [**11**]OTf with $^{16}O_2$ (top) and $^{18}O_2$ (bottom).

Interestingly, while [**11**]$^+$ converts to **11^{ox}** in a matter of seconds upon exposure to O_2, complex [**13**]$^+$ is relatively stable in the presence of air. As shown in Figure 5.13, the ^{1}H NMR spectrum of [**13**]$^+$ in CD_2Cl_2 features paramagnetically shifted peaks at 58 and -10 ppm that arise from the ^{Me2}MP ligand. These peaks display only modest decreases in intensity (relative to an internal standard) after exposure to O_2 for several days, indicating that the geometric and electronic structures of [**13**]$^+$ remain essentially intact in aerobic solution.

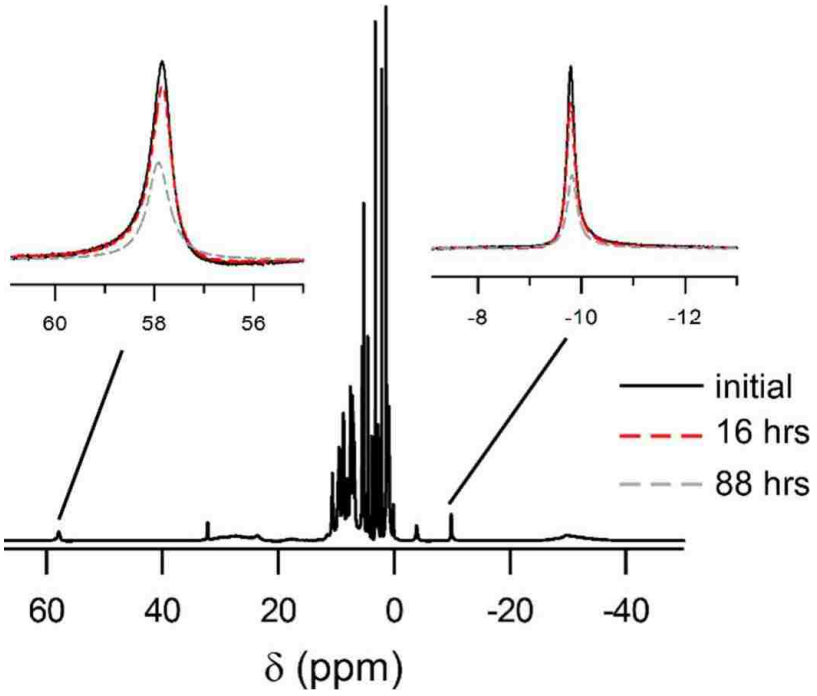

Figure 5.13. ^{1}H NMR spectra of [**13**]OTf in CD_2Cl_2. The insets display peak intensities at 58 and -10 ppm measured at t = 0, 16, and 88 hours.

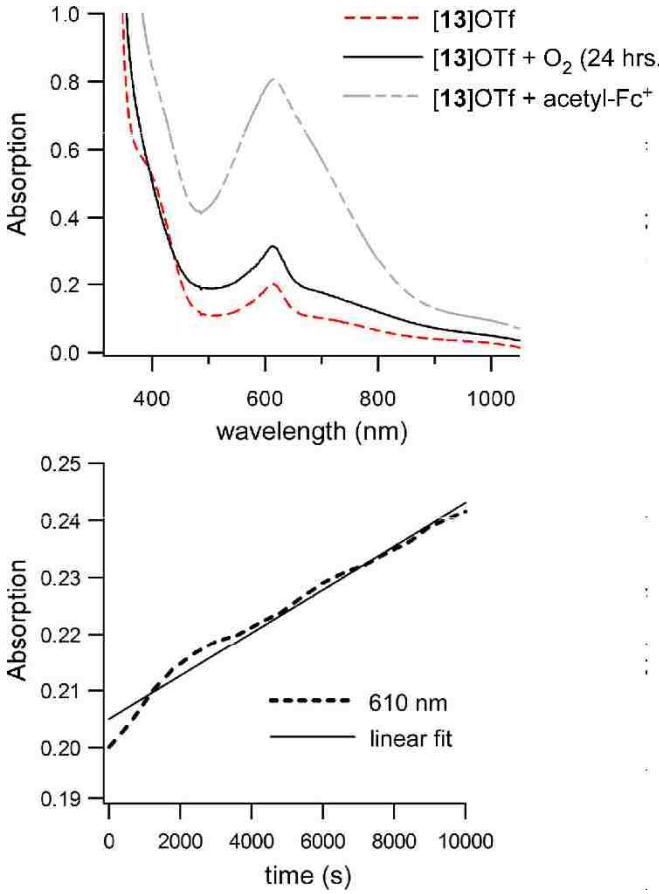

Figure 5.14. *Top*: Absorption spectrum of [**13**]OTf measured in anaerobic CH_2Cl_2 (dashed red line). The black spectrum (solid line) was collected after exposure of the same sample to O_2 for 24 hrs. The grey spectrum (dashed) was obtained after treating $[\mathbf{13}]^+$ with one equivalent of [acetyl-Fc^+]BF4, where acetyl-Fc^+ = acetylferrocenium. The concentration of $[\mathbf{13}]^+$ was 0.40 mM in each case. *Bottom*: Plot of absorption intensity at 610 nm as a function of time for the reaction of [**13**]OTf with O_2. The reaction was performed in O_2 saturated CH_2Cl_2 at room temperature ([Fe] = 0.40 mM). The solid line is a linear fit of the kinetic trace. The pathlength of the cuvettes was always 1.0 cm.

UV-vis absorption spectra of $[\mathbf{13}]^+$ in O_2 saturated CH_2Cl_2 were collected over a span of 24 hours (Figure 5.14). These data revealed a gradual increase of absorption intensity in the 500-900 nm region, which corresponds to formation of the ferric complex, $[Fe^{3+}(^{Ph2}TIP)(^{Me2}MP)]^{2+}$ ($\mathbf{13^{ox}}$). The absorption spectrum of $\mathbf{13^{ox}}$ was measured independently by treating $[\mathbf{13}]^+$ with 1 equiv. of an acetylferrocenium salt (Figure 5.14). On the basis of these results, the conversion of $[\mathbf{13}]^+ \rightarrow \mathbf{13^{ox}}$ is only 20% complete after

24 hours. The stark contrast in O_2 reactivities between [**11**]$^+$ and [**13**]$^+$ is remarkable given that the two complexes possess very similar geometric structures and Fe^{3+}/Fe^{2+} redox potentials.

As shown in Figure 5.8, reaction of the *o*-aminophenolate complex [**7**]OTf with O_2 at room temperature generates a green chromophore (**7^{ox}**) with absorption peaks at 790 and 420 nm. This spectrum is essentially identical to the one previously obtained by treating [**7**]OTf with 2 equiv. of a one-electron oxidant (e.g., AgOTf).[205] Thus, it is reasonable to assume that **7^{ox}** corresponds to [Fe(^{Ph2}TIP)($L_{O,N}$)]$^{2+}$, where the electronic structure can be described as either Fe^{3+}-^{tBu2}ISQ or Fe^{2+}-^{tBu2}IBQ (vide supra). These results indicate that O_2 is capable of extracting two electrons from [**7**]$^+$, whereas initial exposure of [**11**]$^+$ to O_2 involves only one-electron oxidation of the complex. In both reactions, the ET process is associated with loss of a proton from the bidentate ligand. Similar to **11^{ox}**, complex **7^{ox}** undergoes decomposition in the presence of O_2, albeit at a much slower rate ($t_{1/2} \approx 18$ hours).

The *o*-phenylenediamine complex [**12**](OTf)$_2$ is comparatively less reactive toward O_2, requiring days (instead of minutes or hours) for complete oxidation. The resulting complex, **12^{ox}**, displays an intense absorption band with λ_{max} = 715 nm (ε = 4300 M^{-1} cm^{-1}) and a weaker feature at ~500 nm (Figure 5.8). This deep-green species is air-stable at room temperature, allowing for crystallization from a MeCN/Et_2O mixture. Unfortunately, extensive disorder within the crystal has prevented the collection of a high-resolution structure. The crude crystallographic data indicate that **12^{ox}** carries a +2 charge, based on the number of counteranions present. The complex is 5C with the ^{tBu}PDA-derived ligand bound in a bidentate manner, although sizable uncertainties in

metric parameters preclude reliable evaluation of Fe or ligand oxidation states. Solutions of **12**^{ox} are EPR silent with room-temperature magnetic moments of 5.14 μ_B indicative of a S = 2 paramagnet. Since it was not possible to obtain a suitable X-ray crystal structure of **12**^{ox}, we employed spectroscopic and computational techniques to gain insight into its geometric and electronic structures, as described in the following section.

5.D. Spectroscopic and Computational Studies of 4^{ox}

Low-temperature (5 K) MB spectra of [**12**](OTf)$_2$ collected before and after exposure to O_2 are shown in Figure 5.14. The parameters obtained from fitting the data are provided in Table 5.2. The major component (75%) of the [**12**](OTf)$_2$ spectrum is a quadrupole doublet with an isomer shift (δ) of 1.04 mm/s and large splitting (ΔE_Q) of 3.1 mm/s. A minor feature (25%) is also evident with δ- and ΔE_Q-values of 1.05 and 2.5 mm/s, respectively. Both signals are characteristic of nonheme high-spin Fe(II) centers with N/O coordination.

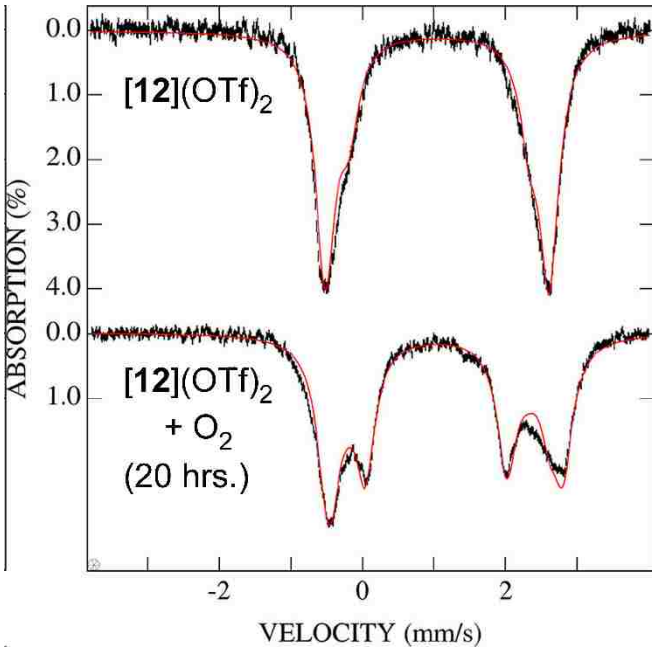

Figure 5.15. Mössbauer spectra collected before and after exposure of [**12**](OTf)$_2$ to O_2 (top and bottom spectra, respectively). Both spectra were recorded at 5 K in an applied field of 0.04 T. The solid red lines are least-squares fits to the experimental data using the parameters in Table 5.2. Both spectra were fitted assuming nested doublets. Approximately 25% of the area in the spectrum of the O_2-exposed sample (bottom) was ascribed to [**12**](OTf)$_2$ starting material.

Given the nearly identical isomer shifts, the two doublets likely correspond to conformational isomers of [**12**]$^{2+}$ that adopt different geometries along the square-pyramidal to trigonal-bipyramidal continuum; indeed, similar "τ-strain" was observed in our previous MB studies of [**7**]OTF.[205] Upon exposure to O_2 for 20 hours, new features arising from **12^{ox}** become clearly evident (Figure 5.14), although starting material remains. Adequate fitting of the new signal required two equally intense doublets with δ = 1.03 and 1.18 mm/s and ΔE_Q = 2.0 and 3.2 mm/s (Table 5.2). As with [**12**](OTf)$_2$, the observed heterogeneity is likely due to minor changes in coordination geometries. Significantly, the MB data provide conclusive proof that the conversion of [**12**]$^{2+}$ to **12^{ox}**

by O_2 does not involve oxidation of the Fe center, as the isomer shifts remain above 1.0 mm/s in the final complex.

With the MB data in hand, it is now possible to determine the oxidation state of the ^{tBu}PDA-derived ligand in **12^{ox}**. Since the overall complex has a +2 charge, the ligand itself must be neutral; thus, two possibilities exist: (diimino)benzosemiquinone radical or (diimino)benzoquinone (^{tBu}DIBQ). The former possibility is inconsistent with the EPR-silent nature of **12^{ox}** and its magnetic moment of 5.14 μ_B. Therefore, **12^{ox}** is best formulated as $[Fe^{2+}(^{Ph2}TIP)(^{tBu}DIBQ)]^{2+}$ - a conclusion further supported by the DFT and rR results described below. Similar to $[\mathbf{7}]^+$, complex $[\mathbf{12}]^{2+}$ is oxidized by two electrons upon exposure to O_2, although in the PDA system the electrons are derived exclusively from the ligand, and two protons are removed.

Table 5.2 summarizes the MB parameters reported here (and previously) for complexes **4**-$[\mathbf{12}]^{2+}$ and their **X^{ox}** counterparts. The electronic structures of the Fe(II) precursors are quite similar, with isomer shifts of $\delta = 1.09 \pm 0.05$ mm/s and ΔE_Q values between 2.05 and 3.13 mm/s. In contrast, there is considerable variation in the **X^{ox}** parameters. Isomer shifts for **11^{ox}** and **12^{ox}** are characteristic of high-spin ferric and ferrous ions, respectively, whereas the δ value of **7^{ox}** (0.64 mm/s) precludes an unambiguous assignment of oxidation state, as noted above. Significantly, the MB results reveal that the redox chemistry of these complexes spans the entire gamut from iron-based to ligand-based oxidations.

Following the experimental data, the geometry optimization of **12^{ox}** assumed a 5C geometry, S = 2 ground state, and overall charge of +2. Metric parameters for the resulting model (**12^{ox}-DFT**) are provided in Figure 5.16. The short N-C bond distances

of 1.29 Å and "four long/two short" pattern of C-C bonds in the N,N-ligand are well-established characteristics of DIBQ units.[184,201,215-218] Mulliken populations revealed that spin-density is found almost exclusively on the Fe center (3.88 α spins), while the bidentate ligand is largely devoid of unpaired spin. The most relevant molecular orbital (MO) for evaluating the **12^{ox}-DFT** electronic configuration is the highest-occupied (HO) spin-down (β) MO, shown in Figure 5.15. The character of this MO is 74% Fe and 14% N,N-ligand, with electron density from the Fe(II) center to the ^{tBu}DIBQ ligand, in agreement with the MB data presented above.

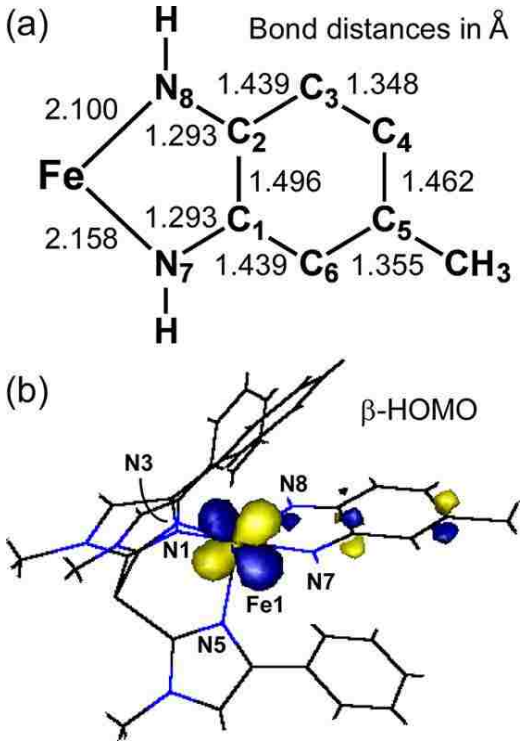

Figure 5.16. (a) Bond distances (in Å) of the $[Fe(DIBQ)]^{2+}$ unit in the **12^{ox}-DFT** model. (b) Isosurface plot of the spin-down (β) HOMO of **12^{ox}-DFT**.

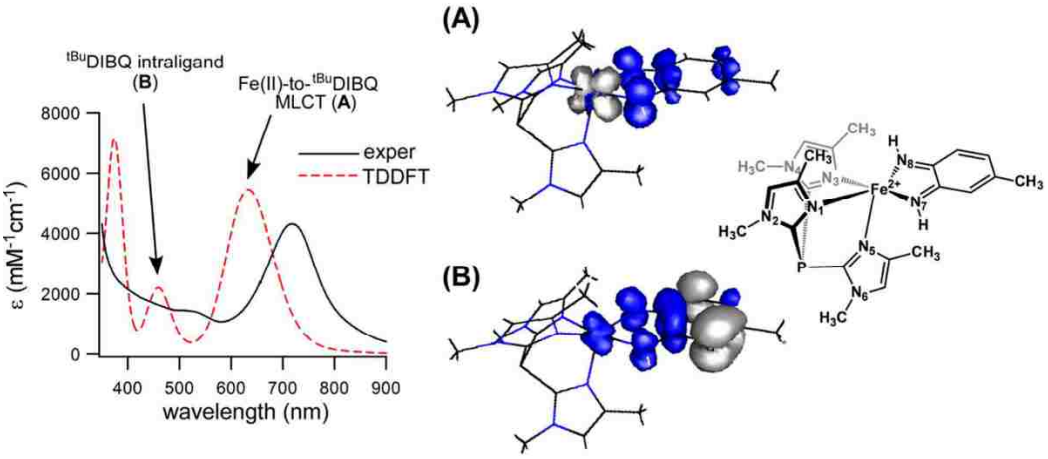

Figure 5.17. *Left*: Experimental (solid line) and TD-DFT computed (dashed line) absorption spectra for **12^{ox}**. Right: Electron density difference maps (EDDMs) for computed transitions. Blue and grey regions indicate gain and loss of electron density, respectively.

To aid in band assignments, the absorption spectrum of **12^{ox}-DFT** was calculated using TD-DFT. As shown in Figure 5.17, the computed spectrum exhibits two bands at 635 and 460 nm (ε = 5.4 and 2.2 M^{-1} cm^{-1}, respectively) that correspond to features in the experimental spectrum. The higher-energy band arises primarily from a ^{tBu}DIBQ-based π-π* transition, as revealed in the electron density difference map (EDDM; Figure 5.17). In contrast, the intense near-IR (NIR) band corresponds to an Fe(II) → ^{tBu}DIBQ MLCT transition localized on the N7-Fe1-N8 unit.

The electronic structure of the ^{tBu}PDA-derived ligand in **12^{ox}** was further examined using resonance Raman (rR) spectroscopy. Since the complex exhibits a pair of prominent absorption bands, data were collected with two wavelengths of excitation (λ_{ex}): 647.1 nm light from a Kr^+ laser was used to probe the NIR feature that arises from a MLCT transition, while 488.0 nm light from an Ar^+ laser was selected to resonate with the ^{tBu}DIBQ-based π-π* transition. The composite spectrum shown in Figure 5.18, was

obtained by irradiating frozen samples of **12^{ox}** in CD_2Cl_2. In some samples, the bidentate N,N-ligand was labeled with the ^{15}N isotope at the 2-position to aid in peak assignments.

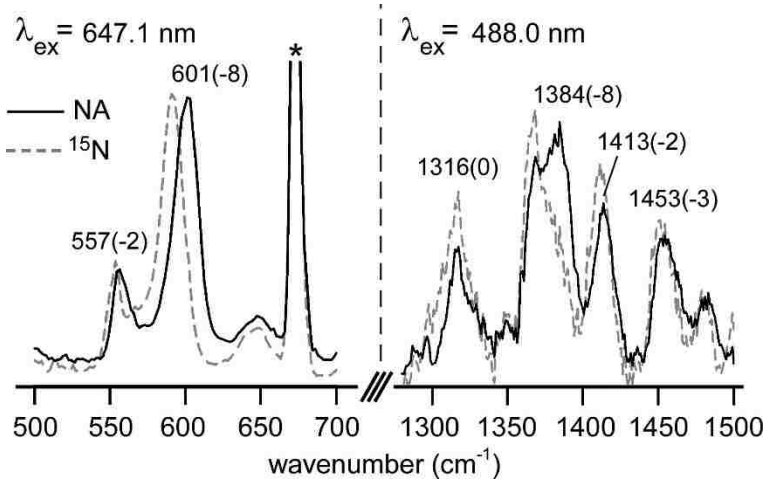

Figure 5.18. Resonance Raman spectra of **12^{ox}** in frozen CD_2Cl_2 solutions ([Fe] = 7.8 mM) collected with 647.1 nm (left) and 488.0 nm (right) laser excitation. The black (solid) spectra were obtained using natural abundance (NA) complex, while the gray (dashed) spectra were obtained using ^{15}N-substituted complex (the ^{15}N isotope was incorporated at the 2-position of the PDA ligand). Frequencies (in cm^{-1}) are provided for select peaks in the NA spectra, and the corresponding $^{14}N \rightarrow ^{15}N$ shifts are shown in parentheses. Peaks marked with an asterisk (*) arise from frozen solvent.

The low-frequency region of the **12^{ox}** spectrum features two intense peaks at 557 and 601 cm^{-1} with ^{15}N isotope shifts of 2 and 8 cm^{-1}, respectively (Figure 5.18). The 601 cm^{-1} peak is attributed to the breathing mode of the five-membered FeN_2C_2 chelate ring, based on its intensity and sizable isotope shift. This assignment is supported by literature precedents[170,171,219] and DFT frequency calculations performed with the **12^{ox}-DFT** model (computed frequencies and normal mode compositions are provided in Figure 5.19). The smaller isotope shift of the 557 cm^{-1} peak suggests that the corresponding normal mode involves substantial mixing of Fe-N stretching motions with internal C-N/C-C vibrations

of the bidentate ligand. Both modes are strongly enhanced by excitation into the NIR band at 715 nm, consistent with its assignment as an Fe(II) → ^{tBu}DIBQ MLCT transition.

Mode Diagram	Mode Description	Mode Frequency (cm^{-1}) Calc	Exp	^{15}N Isotope Shift (cm^{-1}) Calc	Exp
	chelate + ring motion	528	557	-2	-2
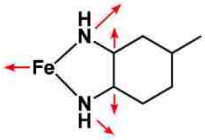	chelate breathing	535	601	-7	-8
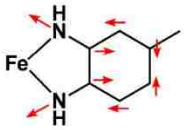	ν(N-C) + ring motion	1372	1384	-7	-8
	ring breathing + ν(N-C)	1417	1413	-4	-2
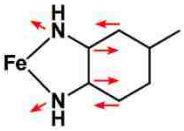	ring motion + ν(N-C)	1457	1453	-4	-3

Figure 5.19. Normal mode compositions, experimental and DFT-calculated frequencies, and computed isotope shifts for the 15N-substituted ligand.

Compared to the metallocycle-based features, peaks arising from ligand-based modes ($\nu \cong 1200\text{-}1600\ cm^{-1}$) are quite weak in the **12^{ox}** spectrum obtained with λ_{ex} = 647.1 nm. However, the higher-energy peaks gain in relative intensity when λ_{ex} is changed to 488.0 nm, providing further confirmation that the absorption manifold near 500 nm arises from ^{tBu}DIBQ-based transitions. Three isotopically sensitive peaks are apparent at 1384, 1413, and 1453 cm^{-1} (Figure 5.19). Prior rR studies of metal-dioxolene complexes indicate that these peaks correspond to modes that couple ν(N-C) and ν(C-C)

motions within the bidentate N,N-ligand.[170,171,219] On the basis of its large ^{15}N isotope shift (8 cm^{-1}), the experimental peak at 1384 cm^{-1} matches the DFT-computed mode at 1372 cm^{-1}, which has primarily ν(N-C) character (calculated ^{15}N isotope shift of 7 cm^{-1}; Figure 5.19). The peaks at 1413 and 1453 cm^{-1} then correspond to ν(C-C) motions of the ^{tBu}DIBQ ring with only minor amounts of ν(N-C) character. Similarly, Lever and co-workers recently published the crystal structure and rR spectrum of $[Ru^{3+}Cl_2(NH_3)_2(DIBQ)]^+$, where DIBQ is unsubstituted (diimino)benzoquinone.[219] This complex displays three peaks between 1400 and 1500 cm^{-1} that the authors attribute to stretching modes of the DIBQ ligand. The presence of resonance enhanced peaks at similar frequencies in the $\mathbf{12^{ox}}$ spectrum provides further evidence that his complex contains a ^{tBu}DIBQ ligand.

5.E. Kinetic Analysis of O_2 Reactivity

Kinetic studies were generally conducted in O_2-saturated CH_2Cl_2 solutions ($[O_2]$ = 5.8 mM at 20 °C[140,220]), and rates were measured by monitoring the growth of absorption features associated with $\mathbf{X^{ox}}$ species. To ensure a large excess of O_2, concentrations of the Fe(II) complexes never exceeded 1.0 mM. For the reactions of $[\mathbf{7}]^+$ and $[\mathbf{11}]^+$ with O_2, initial rates increased linearly with Fe and O_2 concentrations, indicating that the reactions are first-order in both reactants (Figure 5.20 and 5.21). Interestingly, while the $[\mathbf{12}]^{2+} + O_2$ reaction is also first-order in Fe concentration, the reaction rate displays only minor variations as $[O_2]$ increases from 0.2 to 5.4 mM (Figure 5.21). This zero-order $[O_2]$ dependence indicates that O_2 binding is not the rate-limiting step in the conversion of $[\mathbf{12}]^{2+} \rightarrow \mathbf{12^{ox}}$.

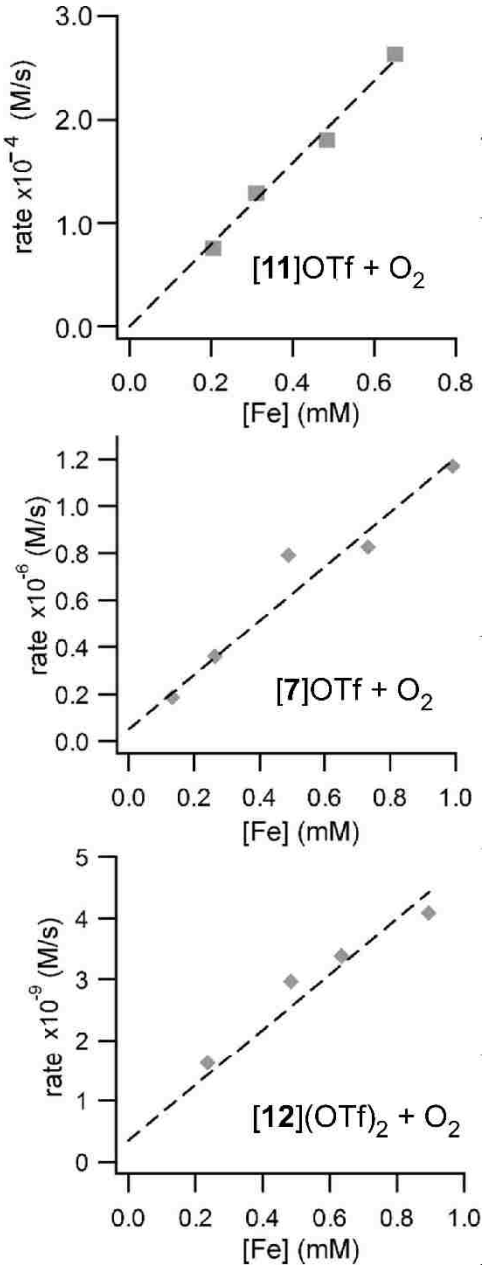

Figure 5.20. Plots of initial rates versus Fe concentration for the reactions of [**11**]OTf (top), [**7**]OTf (middle), and [**12**](OTf)$_2$ (bottom) with O_2. All reactions were performed at room temperature in O_2-saturated CH_2Cl_2. Each data point represents one reaction.

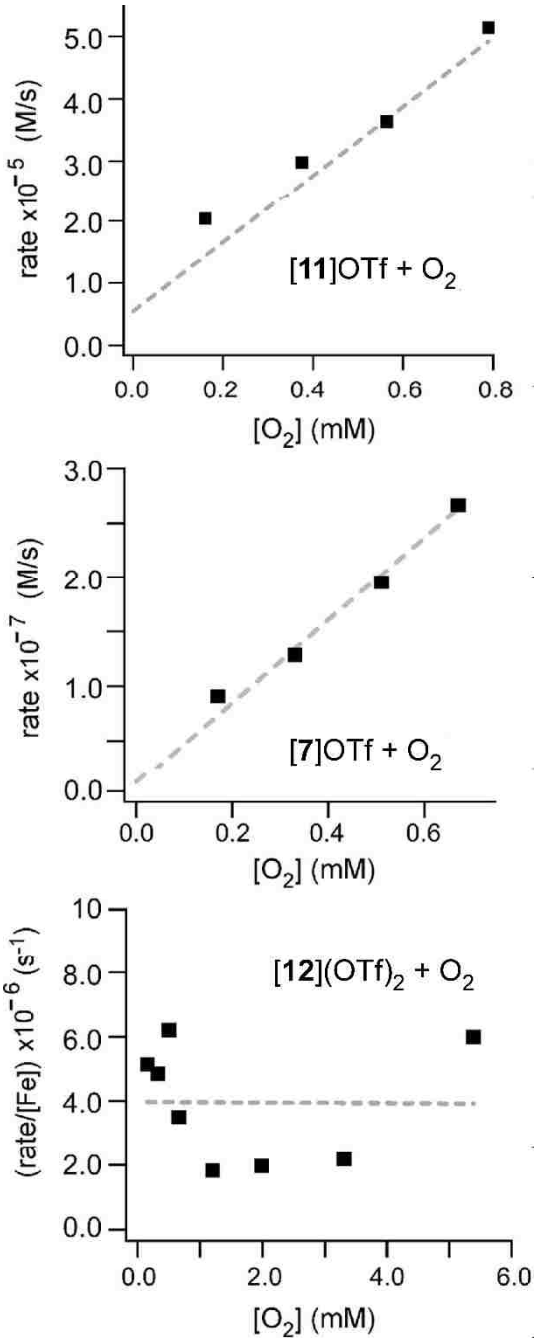

Figure 5.21. Plots of initial rates versus O_2 concentration for the reactions of [**11**]OTf (top), [**7**]OTf (middle), and [**12**](OTf)$_2$ (bottom) with O_2. All reactions were performed at room temperature in CH_2Cl_2. For reactions involving [**7**]OTf and [**11**]OTf, the Fe concentration was fixed at 0.36 mM; for [**12**](OTf)$_2$, the observed initial rate was divided by the Fe concentration. Each data point represents one reaction.

As shown in Figure 5.22, the reaction of [**11**]OTf with O_2 at ambient temperature proceeds via pseudo-first-order kinetics with a rate constant (k_1) of 0.67(5) s^{-1}. The formation of $\mathbf{7^{ox}}$ and $\mathbf{12^{ox}}$ under the same conditions is more complex, however, as indicated by the "S-shaped" kinetic traces (Figure 5.22). This behavior suggests that these species are generated via multistep mechanisms involving both ET and PT-a common occurrence for reactions that require net hydride ($\mathbf{7^{ox}}$) or H_2 transfer ($\mathbf{12^{ox}}$).[221,222] Because of this mechanistic complexity, k_1 values for the reactions of O_2 with $[\mathbf{7}]^+$ and $[\mathbf{12}]^{2+}$ were measured using the initial rates approach. Interestingly, the rates of formation span more than 5 orders of magnitude, with k_1 values of 0.67(5) ($\mathbf{11^{ox}}$), 1.3(2) $\times 10^{-3}$ ($\mathbf{7^{ox}}$), and 4(2) $\times 10^{-6}$ s^{-1} ($\mathbf{12^{ox}}$) in O_2-saturated CH_2Cl_2 at room temperature. We also measured an initial rate of 5 × 10-6 s^{-1} for the one-electron oxidation of $[\mathbf{13}]^+$ to $\mathbf{13^{ox}}$ (Figure 5.14). Thus, despite similar structures, the complexes examined here differ dramatically in their O_2 reactivities.

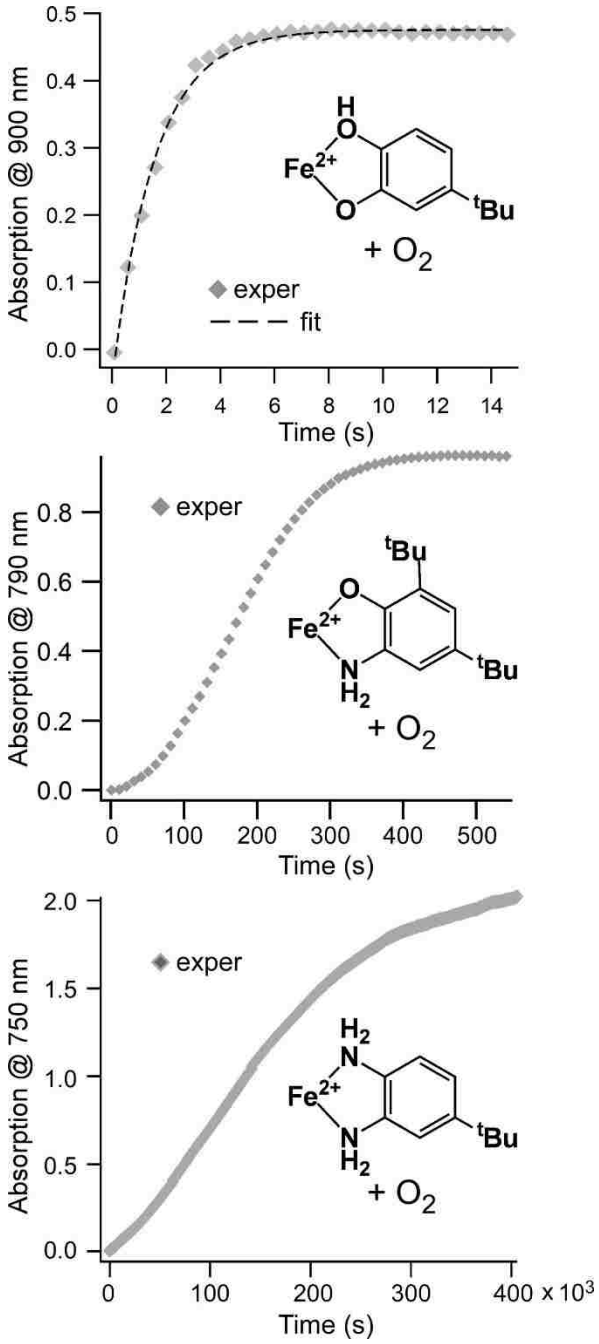

Figure 5.22. Plots of absorption intensity as a function of time for the reactions of [**11**]OTf (top), [**7**]OTf (middle), and [**12**](OTf)$_2$ (bottom) with O_2. All reactions were performed in O_2-saturated CH_2Cl_2 at room temperature ([Fe] ≈ 0.50 mM).

Activation parameters for the [**7**]OTf + O_2 reaction were determined by measuring rates at temperatures between 22 and -30 °C. The linear Eyring plot (Figure 5.23) indicates an activation enthalpy ($\Delta H^{\ddagger}$) of 12(2) kcal•mol^{-1} and a large negative activation entropy ($\Delta S^{\ddagger}$) of -22(5) kcal•mol^{-1}. Such values are similar to parameters obtained for similar Fe/O_2 adducts[223] (Because of its fast nature, it was not possible to measure accurate activation parameters for the reaction of [**11**]$^{+}$ with O_2 using conventional methods) and are consistent with an associative reaction involving O_2 binding to the Fe center as the rate-determining step.

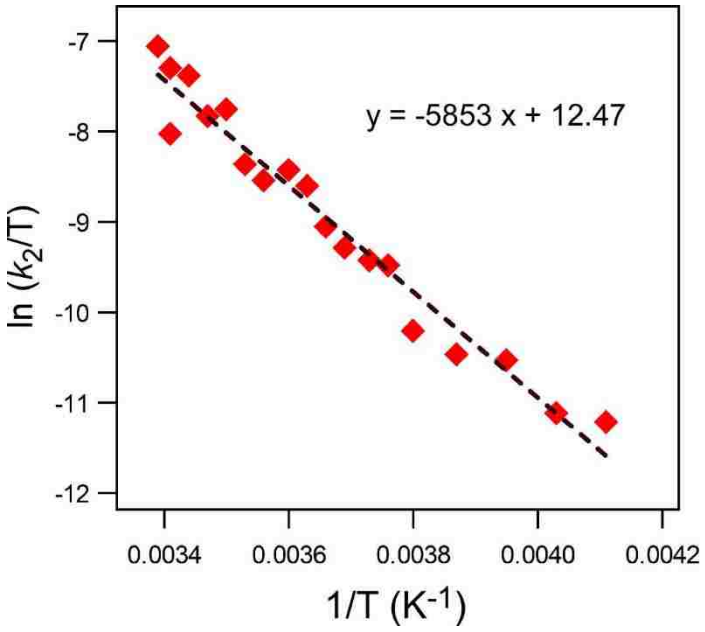

Figure 5.23. Eyring plot for the reaction of [**7**]OTf with O_2 in O_2-saturated CH_2Cl_2 over a temperature range of 22 °C to -30 °C. Second-order rate constants (*k*2) were obtained by dividing the pseudo-first order constant by [O_2] at the specified temperature. Each data point represents one reaction.

In previous sections, we demonstrated that formation of the oxidized species **7**^{ox}, **11**^{ox}, **12**^{ox} under aerobic conditions requires both electron and proton transfers from the parent complexes, although the rates of O_2 reaction vary by a factor of 10^5 across the series. Thus, it is plausible that the O_2 activation mechanisms involve a combination of electron *and* proton transfer from the complexes to either dioxygen or superoxide. We therefore examined the reactivity of the title complexes with two well-established H-atom acceptors: TEMPO$^\bullet$ and 2,4,6-tri-*tert*-butylphenoxyl radical (TTBP$^\bullet$). Both reagents exhibit a strong propensity to react via PCET mechanisms, but TTBP$^\bullet$ is a much more effective H-atom abstractor than TEMPO$^\bullet$, as indicated by the bond dissociation free energies (BDFE) of the resulting H-O bonds (BDFE = 77.1 and 66.5 kcal/mol, respectively, in MeCN).[224]

Treatment of [**11**]$^+$ with either TEMPO$^\bullet$ or TTBP$^\bullet$ yields a blue-green species with absorption features identical to those observed for **11**^{ox} (Figure 5.24). Given the formulation of **11**^{ox} as [Fe^{3+}(Cat)(^{Ph2}TIP)]$^+$, this reaction is classified as "separated PCET" because the electron and proton originate from different units of the [**11**]$^+$ complex, namely, the Fe(II) center and CatH ligand. While complexes [**7**]$^+$ and [**12**]$^{2+}$ are inert toward TEMPO$^\bullet$, both react rapidly with TTBP$^\bullet$. As described in Chapter 4 TTBP$^\bullet$ removes a hydrogen atom from the ^{tBu2}APH ligand of [**7**]$^+$ to generate the corresponding Fe(II)-^{tBu2}ISQ complex. Complex [**12**]$^{2+}$ reacts with 2 equiv. of TTBP$^\bullet$ to provide a species with spectral features that are similar to those of **12**^{ox}, although not identical (Figure 5.25). This chromophore is evident by UV-vis spectroscopy even when a single equivalent of TTBP$^\bullet$ is added; this result suggests that the species generated by removal

of one H-atom from [**12**]$^{2+}$ undergoes disproportionation to yield the starting complex and a **12**^{ox}-like species.

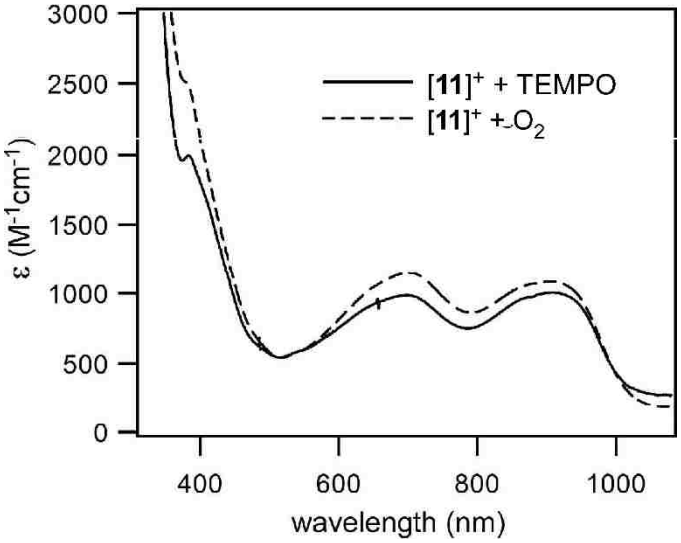

Figure 5.24. Absorption spectra obtained by treating [**11**]OTf with TEMPO• (solid line) or O_2 (dashed line) in CH_2Cl_2 at room temperature.

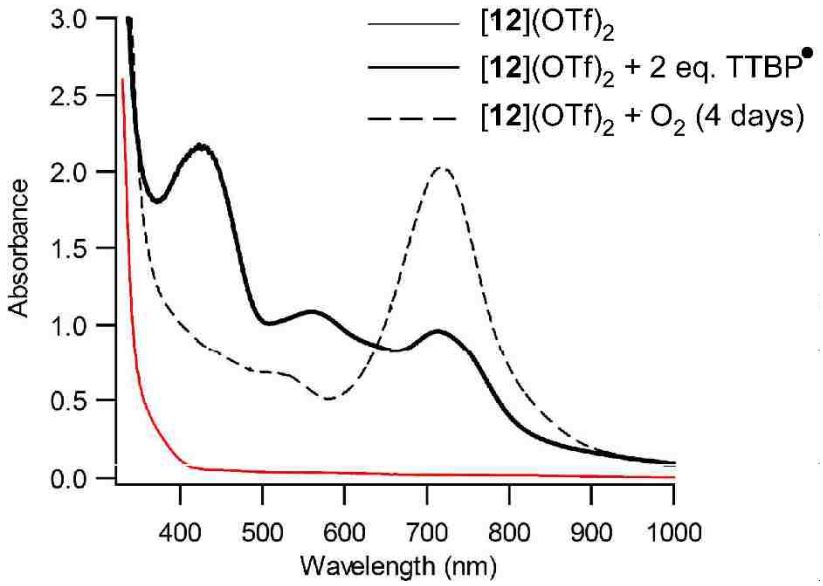

Figure 5.25. Absorption spectra of [**12**](OTf)$_2$ (solid red line) and **12^{ox}** (dashed black line) compared to the one obtained by treating [**12**](OTf)$_2$ with two equivalents of TTBP• (solid black-line). All spectra were collected in CH_2Cl_2 at room temperature ([Fe] = 0.50 mM in each case). The pathlength of the cuvette was 1.0 cm.

It is noteworthy that [**11**]$^+$ is the only complex in the series capable of donating a H-atom to TEMPO$^•$, indicating that the [**11^{ox}**-H] bond is very weak (BDFE < 66 kcal/mol). Bordwell and Mayer have demonstrated that the BDFE of the X-H bond formed in a 1H$^+$/1e$^-$ PCET reaction (i.e., X + H$^+$ + e$^-$ → X-H) is given by the following equation:

$$BDFE(X\text{-}H) = 1.37pK_a + 23.06E° + C_{G,solv}$$

where $C_{G,solv}$ is a solvent-dependent constant.[224,225] In our case, the relevant parameters are the E° values of the starting Fe(II) complexes and the pK_a values of the one-electron oxidized species. The complexes examined here exhibit greater variability in ligand acidities than in redox potentials. As described above, initial redox potentials differ by ~100 mV across the series, accounting for a modest shift of ~2.5 kcal/mol in BDFE. In

contrast, the pK_a values of aromatic amines are generally ~12 units higher than the corresponding phenols−a shift of 14 kcal/mol in BDFE.[224,226,227] Thus, while the differences in redox potential cannot be ignored, the weaker H-atom donating ability of complexes $[\mathbf{7}]^+$ and $[\mathbf{12}]^{2+}$ compared to $[\mathbf{3}]^+$ is largely due to the greater acidity of the ^{tBu}CatH ligand relative to ^{tBu2}APH and ^{tBu}PDA.

These results have mechanistic implications for the O_2 reactivity of the complexes examined here. The strength of the [$\mathbf{3}^{ox}$–H] bond is comparable to that of perhydroxyl radical ($HO_2^{\bullet}$), which is the product of HAT and O_2 (BDFE of $HO_2^{\bullet-} \cong 60$ kcal/mol).[224] Therefore, complex $[\mathbf{3}]^+$ may be able to react directly with O_2 via $1H^+/1e^-$ PCET *without prior formation of a ferric-superoxo intermediate.* By contrast, complexes $[\mathbf{7}]^+$ and $[\mathbf{12}]^{2+}$ cannot participate in HAT reactions with O_2 due to the greater strength of their N−H bonds. For these complexes, O_2 activation likely requires initial ET from Fe(II) → O_2, followed by oxidation of the ligand via concerted (or stepwise) electron and proton transfers. These mechanistic scenarios are considered further in the discussion section.

5.F. Computational Studies of O_2 Reactivity

The thermodynamics of O_2 binding were examined with DFT calculations. A previous study by Schenk et al. found that hybrid functionals with a reduced amount (~10%) of Hartree-Fock (HF) exchange are most reliable for evaluating energetics of O_2 (or NO) binding to nonheme Fe(II) centers.[228] We therefore employed the PBE functional[229] with 10% HF exchange to calculate geometries and thermodynamic parameters for O_2, the Fe(II) precursors, and the 6C [Fe/O_2] adducts. Since exchange interactions between the unpaired electrons of Fe and O_2 give rise to three possible spin

states (S_{tot} = 1, 2, 3), it was necessary to optimize three models for each [Fe/O_2] species. The resulting S = 2 [Fe/O_2] structures are shown in Figure 5.26. (Tables 5.3−5.5 provide metric parameters for each model.) The [**12**/O_2]$^{2+}$ adduct is dissociative on the S = 3 surface, with calculations invariably converging to structures with very long Fe···O distances (>3.75 Å).

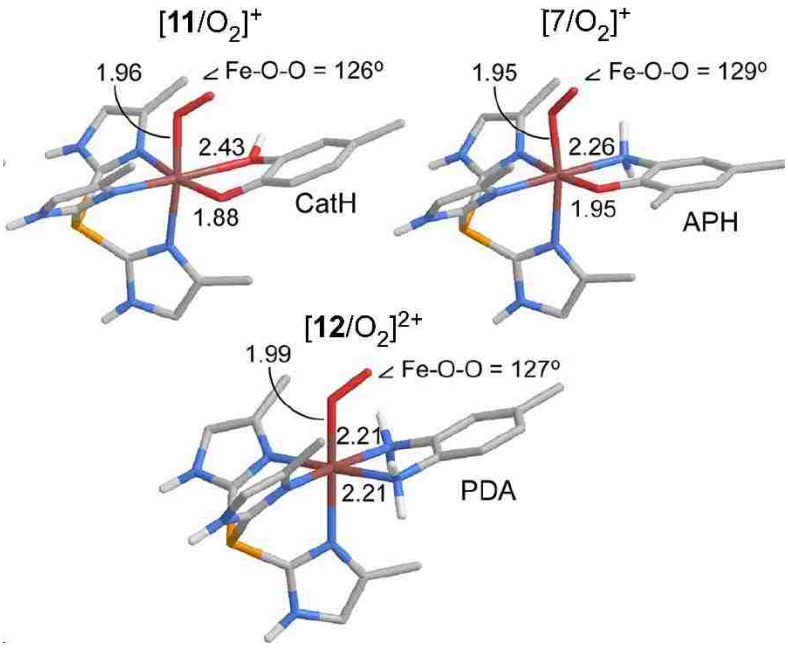

Figure 5.26. DFT-calculated structures of the Fe/O2 adducts. Selected bond distances (Å) and angles are provided (see Tables 5.3−5.5 for additional metric parameters).

Table 5.3. Selected Bond Distances (Å) and Angles (deg) for Complex $[\mathbf{7}]^+$ and the corresponding $[Fe/O_2]^+$ Species (S_{tot} = 3,2, and 1) Obtained by DFT Calculations.

		$[\mathbf{7}]^+$	$[\mathbf{7}/O_2]^+$	$[\mathbf{7}/O_2]^+$	$[\mathbf{7}/O_2]^+$
	Spin	S=2	S=3	S=2	S=1
Bond Lengths	Fe1-N1(TIP)	2.148	2.158	2.181	2.187
	Fe1-N3(TIP)	2.173	2.301	2.281	2.279
	Fe1-N5(TIP)	2.206	2.243	2.264	2.193
	Fe1-O(APH)	1.903	1.915	1.895	1.937
	Fe1-N(APH)	2.282	2.254	2.260	2.262
	Fe1-O(O_2)		2.182	1.946	2.095
	O—O		1.263	1.268	1.246
	Fe1-N(TIP) ave	2.176	2.234	2.242	2.220
	Fe1-L(all) ave	2.142	2.176	2.138	2.159
Angles	Fe—O—O		132.8	128.5	120.1

Table 5.4. Selected Bond Distances (Å) and Angles (deg) for Complex $[\mathbf{11}]^+$ and the corresponding $[Fe/O_2]^+$ Species (S_{tot} = 3,2, and 1) Obtained by DFT Calculations.

		$[\mathbf{11}]^+$	$[\mathbf{11}/O_2]^+$	$[\mathbf{11}/O_2]^+$	$[\mathbf{11}/O_2]^+$
	Spin	S=2	S=3	S=2	S=1
Bond Lengths	Fe1-N1(TIP)	2.122	2.131	2.151	2.156
	Fe1-N3(TIP)	2.138	2.214	2.223	2.177
	Fe1-N5(TIP)	2.156	2.181	2.203	2.158
	Fe1-O(CatH)	1.871	1.895	1.879	1.873
	Fe1-N(CatH)	2.482	2.606	2.435	2.727
	Fe1-O(O_2)		2.133	1.960	2.126
	O—O		1.250	1.266	1.247
	Fe1-N(TIP) ave	2.139	2.175	2.192	2.164
	Fe1-L(all) ave	2.154	2.193	2.142	2.203
Angles	Fe—O—O		139.6	125.5	121.5

Table 5.5. Selected Bond Distances (Å) and Angles (deg) for Complex $[\mathbf{12}]^{2+}$ and the corresponding $[Fe/O_2]^{+}$ Species (S_{tot} = 2, and 1) Obtained by DFT Calculations.

		$[\mathbf{12}]^{+}$	$[\mathbf{12}/O_2]^{2+}$	$[\mathbf{12}/O_2]^{2+}$
	Spin	S=2	S=2	S=1
Bond Lengths	Fe1-N1(TIP)	2.175	2.173	2.181
	Fe1-N3(TIP)	2.168	2.166	2.168
	Fe1-N5(TIP)	2.126	2.209	2.155
	Fe1-O(CatH)	2.209	2.205	2.201
	Fe1-N(CatH)	2.212	2.205	2.201
	Fe1-O(O_2)		1.994	2.128
	O—O		1.249	1.228
	Fe1-N(TIP) ave	2.156	2.183	2.168
	Fe1-L(all) ave	2.178	2.159	2.172
Angles	Fe—O—O		126.9	122.1

In all other cases, O_2 coordinates in a bent conformation with Fe−O−O angles between 120 and 140° and Fe−O distances ranging from 1.95 to 2.18 Å. The O_2 ligand can adopt two possible orientations depending on whether the O−O vector is pointed toward (T) or away (A) from the bidentate ligand. The two orientations are approximately isoenergetic with differences less than the estimated error of the calculations (±2 kcal/mol). In the remainder of this chapter, only the T isomers of the $[Fe/O_2]$ adducts are discussed, since these models are more relevant from a mechanistic standpoint.

Table 5.6 summarizes the computed thermodynamic parameters for the eight Fe(II) + O_2 → $[Fe/O_2]$ reactions considered here. While the enthalpic contributions (ΔH^{gas} + $\Delta Solv$) are slightly favorable in most instances, all of the reactions are endergonic (ΔG = +7.0−13.0 kcal/mol) due to large and unfavorable entropic effects. A

similar pattern has been observed in DFT studies of O_2 binding to nonheme Fe(II) enzymes, where the calculated ΔG values range between +8 and 12 kcal/mol.[46,230-232] To understand why the O_2 binding reactions are decidedly "uphill", it is instructive to examine the computed properties of the O−O bonds in the [Fe/O_2] intermediates. Superoxide ligands typically exhibit O−O bond distances near 1.3 Å and ν(O−O) frequencies between 1050 and 1200 cm^{-1}.[233] In contrast, our DFT-generated [Fe/O_2] models have short O−O distances of 1.25 ± 0.02 Å and ν(O−O) frequencies greater than 1250 cm^{-1} (Table 5.3), indicating that there is only partial charge transfer from Fe(II) to the O_2 ligand. The weakness of the Fe−O_2 interactions is also reflected in the low ν(Fe−O) frequencies, which range between 230 to 370 cm^{-1}.

Table 5.6. Energetics of O_2 Binding to Complexes [**7**]$^+$, [**11**]$^+$, [**12**]$^{2+}$, and Comparison of O─O Bond Distances and Stretching Frequencies in the Resulting Fe/O_2 Adducts[a]

reactants	spin (S_{tot})	ΔH^{gas}	TΔS	ΔSolv[b]	ΔG[c]	r(O─O)(Å)	ν(O─O)(cm^{-1})
[**11**]$^+$ + O_2	S =3	-0.5	-11.9	-0.1	+11.3	1.25	1287
	S = 2	-0.2	-12.2	-1.1	+10.9	1.27	1260
	S = 1	-1.6	-11.7	+0.2	+10.3	1.25	1287
[**7**]$^+$ + O_2	S = 3	-2.0	-10.0	-1.1	+6.9	1.26	1254
	S = 2	-1.4	-10.9	-1.7	+7.8	1.27	1251
	S = 1	-2.9	-11.4	-0.2	+8.3	1.25	1303
[**12**]$^{2+}$ + O_2	S = 2	+4.0	-11.3	-2.3	+13.0	1.25	1328
	S = 1	-1.8	-12.2	+0.4	+10.8	1.23	1406

[a]All energies in kcal/mol. [b]Enthalpies of solvation were calculated using COSMO.
[c]$\Delta G = \Delta H^{gas} + \Delta Solv - T\Delta S$

On the basis of the DFT calculations, complex [**7**]$^+$ has the greatest affinity for O_2, followed in the series by [**11**]$^+$ and [**12**]$^{2+}$ (Table 5.6). This trend correlates with the relative donor strengths of the bidentate ligands (APH^- > $CatH^-$ > PDA) because

formation of the Fe−O_2 bond requires transfer of electron density from an Fe d orbital to an empty O_2 π^* orbital. However, our DFT results appear to contradict the kinetic studies reported above, which found that [**11**]$^+$ is significantly more reactive than [**7**]$^+$ toward O_2. Possible explanations for this discrepancy are provided in the following section.

5.G. Discussion

In this chapter, we described the O_2 reactivity of monoiron(II) complexes bound to three types of *o*-phenylene ligands (Figures 5.1 and 5.2). The complexes resemble the substrate-bound intermediates of nonheme Fe(II) dioxygenases that catalyze the oxidative ring-cleavage of aromatic substrates.[5,23,203] The ^{Ph2}TIP supporting ligand mimics the facial triad of protein ligands in the active site and the substrate ligands each coordinate in a bidentate manner, resulting in 5C Fe(II) complexes capable of O_2 binding. In chapter 4, we demonstrated that one- and two-electron oxidation of the ^{tBu2}APH-based complex [**7**]OTf yields species containing (imino)benzosemiquinone ligands. Like aminophenolates, catecholates and phenylenediamines can serve as redox-active ligands, although the ease of oxidation of the free ligands increases across the series $CatH_2$ < APH_2 < PDA. We therefore synthesized and structurally characterized the homologous complexes [**11**]OTf and [**12**]$(OTf)_2$ to better understand the role of redox-active ligands in modulating the O_2 reactivity of Fe complexes. The ligands are capable of donating protons as well as electrons, but the acidities run counter to the redox potentials. In other words, the most acidic ligand ($^{tBu}CatH_2$) is the hardest to oxidize, while the most reducing ligand (^{tBu}PDA) is the least acidic. This interplay between ET and PT capabilities influences the rates of the O_2 reactions as well as the identities of the oxidized products.

Despite similar overall structures, the three Fe(II) complexes in this study display remarkable diversity in their O_2 reactivities, as summarized in Figure 5.27. The differences concern both the total number of electrons transferred in the reaction ($1e^-$ or $2e^-$) and the source of these electrons (iron and/or ligand). The resulting $\mathbf{X^{ox}}$ species have been characterized by various spectroscopic (UV−vis, EPR, MB, rR) and computational (DFT) methods. These results indicate that the $[\mathbf{11}]^+ \rightarrow \mathbf{11^{ox}}$ conversion is an Fe-based $1e^-$ process, while the $[\mathbf{12}]^{2+} \rightarrow \mathbf{12^{ox}}$ reaction involves $2e^-$ oxidation of the ligand only. The $[\mathbf{7}]^+ \rightarrow \mathbf{7^{ox}}$ reaction occupies an intermediate position, since substantial electron density is lost from both the Fe center and ^{tBu2}AP ligand. This continuum in electronic structures is evident in the isomer shifts (δ) of the $\mathbf{X^{ox}}$ species (Table 5.2), which range from 0.50 ($\mathbf{11^{ox}}$, Fe^{3+}) to 0.64 ($\mathbf{7^{ox}}$, $Fe^{2.5+}$) to ~1.1 ($\mathbf{12^{ox}}$, Fe^{2+}) mm/s. In addition, each of the three possible *o*-phenylene oxidation states (aromatic, semiquinone, benzoquinone; Figure 5.1) is represented in the $\mathbf{X^{ox}}$ series. Thus, the $[Fe^{2+}(^{Ph2}TIP)(o\text{-phenylene})]$ framework supports a wide spectrum of redox and O_2 chemistry.

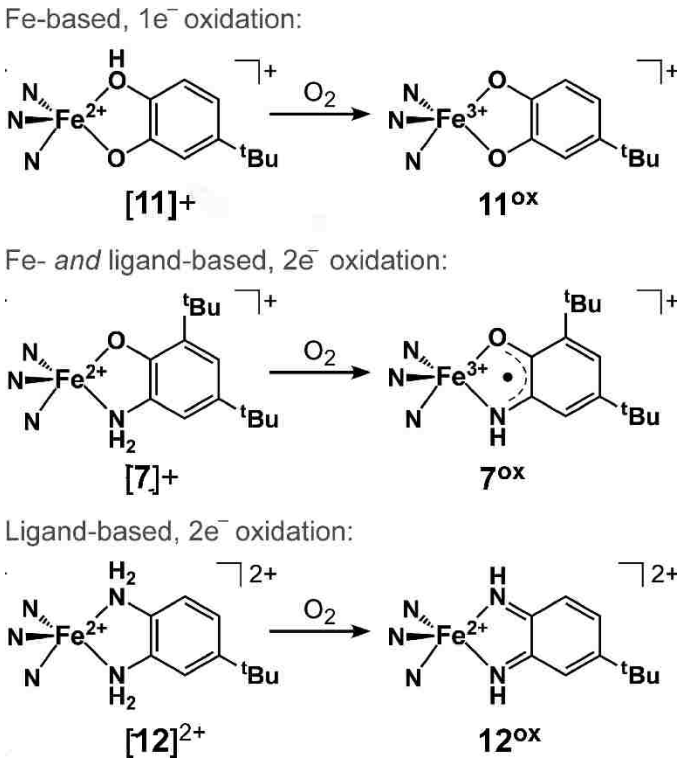

Figure 5.27. Summary of diverse O_2 reactivity displayed by our complexes.

Our kinetic analysis revealed that O_2 reaction rates vary by a factor of 10^5 across the series, following the order $[\mathbf{11}]^+ > [\mathbf{7}]^+ > [\mathbf{12}]^{2+}$. It is somewhat counterintuitive that this order is *inversely* related to the electron-donating abilities of the free ligands. Moreover, these rates fail to correlate adequately with $Fe^{2+/3+}$ redox potentials, all of which fall within a 100 mV range near 0 mV (vs $Fc^{+/0}$). Finally, if one assumes that formation of the Fe/O_2 adduct is the rate-determining step, then our DFT calculations of O_2-binding affinities indicate that $[\mathbf{7}]^+$ should be more reactive than $[\mathbf{11}]^+$, even though the kinetic data indicate that the reverse is true.

We believe these conflicting results can be reconciled by considering the role of PT in the O_2 reaction. The fact that $[\mathbf{11}]^+$ undergoes HAT with TEMPO—a very weak H-atom acceptor suggests that ET and PT processes are tightly coupled in the $[\mathbf{11}]^+ + O_2$

reaction. A likely mechanism involves concerted transfer of $1e^-$ and $1H^+$ to O_2 as it approaches the Fe center. In contrast, the intrinsically lower acidity of aromatic amines (relative to phenols) prevents PT in the initial interaction of O_2 with $[\mathbf{7}]^+$ and $[\mathbf{12}]^{2+}$. Deprotonation of these ligands in the course of the O_2 reaction likely requires complete oxidation of the Fe center to lower the pK_a of the amino group(s). Thus, these complexes cannot avoid the thermodynamically uphill ET from Fe(II) to O_2; yet once the ferric complex is generated, proton loss to superoxide or bulk solvent would be feasible, as indicated by the CV data (vide supra). Importantly, deprotonation destabilizes the redox-active MOs of the ligand, making it possible for O_2 to extract a second electron, thus generating the final $\mathbf{7^{ox}}$ and $\mathbf{12^{ox}}$ products. Thus, we propose that the $[\mathbf{7}]^+ \rightarrow \mathbf{7^{ox}}$ conversion proceeds via a stepwise ET─PT─ET mechanism, although PT may be coupled with the second ET in a HAT reaction. This mechanism follows the one established by Paine et al. for the oxidation of $[Fe^{2+}(L)(^{tBu2}APH)]$ to $[Fe^{3+}(L)(^{tBu2}ISQ)]^+$ in the presence of O_2 (where L is the tris(2-pyridylthio)methanido anion).[234]

The enormous contrast between the O_2 reactivites of $[\mathbf{11}]^+$ and $[\mathbf{13}]^+$ provides the clearest evidence for the decisive role of PT in determining reaction rates of the *o*-phenylene complexes. These two complexes have nearly identical coordination geometries and $Fe^{3+/2+}$ redox potentials; however, replacing the ─OH group of ^{tBu}CatH with the $─OCH_3$ donor of ^{Me}2MP decreases the O_2 reaction rate by 5 orders of magnitude. Indeed, complex $[\mathbf{13}]^+$ is quite stable in the presence of air, even though slow oxidation to the ferric analog ($\mathbf{13^{ox}}$) is observed over the course of days. These results provide further confirmation that the one-electron oxidation of high-spin Fe(II) centers by

O_2 is an unfavorable process, but the overall reaction barrier can be lowered substantially if the ET is coupled with PT (in either a stepwise or concerted manner).

The **11^{ox}** intermediate reacts further with O_2 to yield products arising from extradiol ring cleavage. Previous studies have proposed a mechanism that involves direct reaction of the $[Fe^{3+}(Cat)]^+$ unit with O_2 to form a ferric-alkylperoxo species, followed by rearrangement to the corresponding lactone (Figure 5.28a).[111,212] In contrast, **7^{ox}** and **12^{ox}** are relatively air-stable, since they lack the two reducing equivalents necessary to generate the critical alkylperoxo intermediate. Interestingly, Paine and co-workers recently reported a 6C complex, $[Fe^{2+}(6\text{-}Me_3\text{-}TPA)(^{tBu}APH)]^+$, that (unlike $[\mathbf{7}]^+$) reacts with O_2 to yield the ring-cleaved product (6-Me$_3$-TPA = tris(6-methyl-2-pyridylmethyl)amine).[235] The proposed mechanism is analogous to the one employed by ferric-catecholate complexes. Paine's system differs from the one described here in that the initial product of the O_2 reaction is an $[Fe^{3+}(AP)]^+$ species, whereas our studies indicate that $[\mathbf{7}]^+$ likely converts to a $[Fe^{2+}(ISQ)]$ intermediate. This difference in electronic structure apparently controls subsequent reactivity, with the latter species undergoing simple 1e$^-$ oxidation and the former direct addition of O_2.

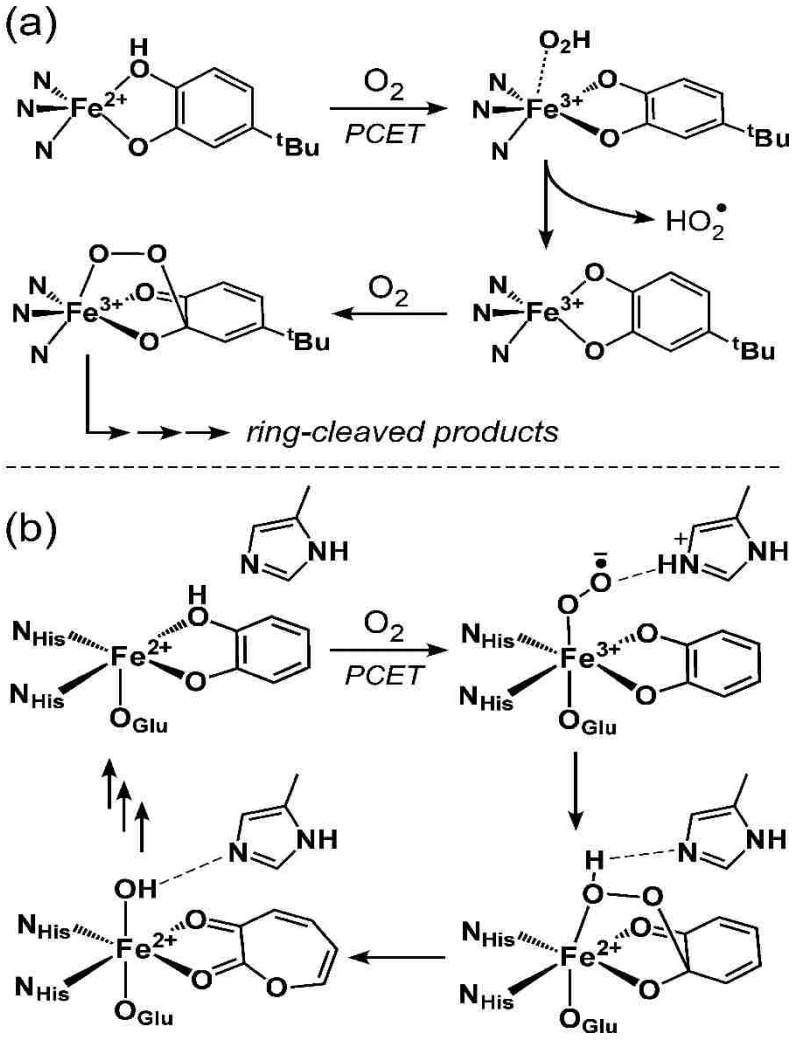

Figure 5.28. (a) Proposed mechanism for the formation of a ferric-alkylperoxo intermediate leading to ring-cleavage products. (b) Condensed mechanism utilized by ring-cleaving dioxygenases.

5.H. Conclusions

The results presented here highlight the mechanistic sophistication of the ring-cleaving dioxygenases. Figure 5.28b provides a condensed version of the canonical enzymatic mechanism. A recent DFT study by Christian et al. of extradiol catechol dioxygenases has emphasized the role of the conserved second-sphere histidine residue in the PT steps that occur after O_2 binding.[236] This residue first deprotonates the substrate ligand, resulting in an imidazolium group that stabilizes the superoxide ligand through H-bonding interactions. The proton is eventually returned to the O_2 unit *after* formation of the bridging alkylperoxo intermediate (Figure 5.28b). Thus, the enzyme carefully "manages" the PT events to promote O_2 activation and discourage the autoxidation processes observed in our models. Indeed, studies of homoprotocatechuate 2,3-dioyxgenase (HPCD) have demonstrated that if the His200 residue is mutated to Ala, the enzyme generates quinone and H_2O_2 instead of the ring-cleaved products.[44] Therefore, the critical difference between the ring-cleaving dioxygenases and the synthetic models reported here (and elsewhere) is the ability to coordinate PT with O_2 activation.

It is noteworthy that none of the synthetic dioxygenase models prepared to date follow the enzymatic mechanism in proceeding through an Fe/O_2 adduct. Even for those complexes that carry out ligand cleavage, like [**11**]OTf, the first step always involves $1e^-$ oxidation to the ferric complex followed by direct reaction of the ligand with O_2. The enzyme not only stabilizes the $[FeO_2]$ adduct through H-bonding interactions, it also prevents formation of the dead-end intermediate that arises when the substrate proton is transferred to $O_2^{\bullet-}$ instead of H200.[44,45] In this study, we have shown that PCET is an effective strategy for bypassing the unfavorable ET from Fe(II) to O_2; however, in the

case of [**11**]OTf, the PCET reaction does not lead to formation of the Fe(II)-alkyperoxo intermediate (as in the enzyme) because the resulting superoxide moiety has been deactivated through protonation, By coupling O_2 binding with PT to a second-sphere His residue, the dioxygenases reap the energetic benefits of PCET while avoiding the pitfall that has plagued synthetic models. Future modeling efforts should therefore be directed toward the generation of complexes capable of mimicking the enzyme's exquisite control of PT reactions.

5.I. Experimental

Reagents and solvents were purchased from commercial sources and were used as received, unless otherwise noted. Air-sensitive materials were synthesized and handled under inert atmosphere using a Vacuum Atmospheres Omni-Lab glovebox. The ^{Ph2}TIP[173] and ^{tBu}APH$_2$[138] ligands and the 2,4,6-tri-*tert*-butylphenoxyl radical[139] (TTBP$^{\bullet}$) were prepared according to literature procedures. Synthetic procedures for complexes [Fe(^{Ph2}TIP)(MeCN)$_3$](OTf)$_2$,[173] **4**,[204] and [**7**]OTf[205] were reported earlier in this manuscript.

Elemental analyses were performed at Midwest Microlab, LLC in Indianapolis, IN. UV─absorption spectra were measured with an Agilent 8453 diode array spectrometer equipped with a cryostat from Unisuko Scientific Instruments (Osaka, Japan). Fourier-transform infrared (FTIR) spectra of solid samples were obtained with a Thermo Scientific Nicolet iS5 FTIR spectrometer equipped with the iD3 attenuated total reflectance accessory. ^{1}H and ^{19}F NMR spectra were recorded at room temperature with a Varian 400 MHz spectrometer. ^{19}F NMR spectra were referenced to the

benzotrifluoride peak at ─63.7 ppm. Mass spectra were collected using an Agilent 6850 gas chromatography─mass spectrometer (GC-MS) with a HP-5 (5% phenylmethylpolysiloxane) column. Cyclic voltammetric (CV) measurements were conducted in the glovebox with an epsilon EC potentiostat (iBAS) at a scan rate of 100 mV/s with 100 mM $(NBu_4)PF_6$ as the supporting electrolyte. The three electrode cell contained a Ag/AgCl reference electrode, a platinum auxiliary electrode, and a glassy carbon working electrode. Potentials were referenced to the ferrocene/ferrocenium ($Fc^{+/0}$) couple, which has $E_{1/2}$ values of +0.52 V in CH_2Cl_2 under these conditions.

EPR experiments were performed using a Bruker ELEXSYS E600 featuring an ER4415DM cavity that resonates at 9.63 GHz, an Oxford Instruments ITC503 temperature controller, and an ESR-900 He flow cryostat. The program EasySpin302C was used to simulate and fit experimental spectra. Resonance Raman (rR) spectra were measured with excitation from either a Coherent I-305 Ar^+ laser (488.0 nm) or I-302C Kr^+ laser (647.1 nm) with ~50 mW of power at the sample. The scattered light was collected using a 135° backscattering arrangement, dispersed by an Action Research triple monochromator equipped with a 1200 grooves/mm grating and detected with a Princeton Instruments Spec X 100BR CCD camera. Spectra were accumulated at 77 K, and rR frequencies were referenced to the 983 cm^{-1} peak of K_2SO_4.[220] Low-field (0.04 T) variable temperature (5─200 K) Mössbauer spectra were recorded on a closed-cycle refrigerator spectrometer, model CCR4K, equipped with a 0.04 T permanent magnet, maintaining temperatures between 5 and 300 K. Mössbauer spectra were analyzed using the software WMOSS (Thomas Kent, SeeCo.us, Edina, Minnesota). The samples consisted of solid powders (or crystalline material) suspended in nujol, placed in Delrin

1.00 mL cups, and then frozen in liquid nitrogen. The [**12**](OTf)$_2$ sample was prepared from material crystallized from a mixture of 1,2-dichloroethane (DCE) and Et_2O. The air-oxidized sample **4^{ox}** was prepared by exposing a solution of [**12**](OTf)$_2$ in CH_2Cl_2 to air for 20 h, followed by removal of solvent to give a dark green powder. The isomer shifts are quoted at 5 K with respect to iron metal spectra recorded at 298 K.

X-ray diffraction (XRD) data were collected with an Oxford Diffraction SuperNova κ-diffractometer (Agilent Technologies) equipped with dual microfocus Cu/Mo X-ray sources, X-ray mirror optics, Atlas CCD detector, and low-temperature Cryojet device. The data were processed with CrysAlis Pro program package (Agilent Technologies, 2011), followed by an empirical multiscan correction using SCALE3 ABSPACK routine. Structures were solved using SHELXS program and refined with SHELXL program.[147] X-ray crystallographic parameters are provided in Table 6.4, and experimental details are available in the CIFs.

[Fe(^{Ph2}TIP)(^{tBu}CatH)(OTf) [11]OTf: Equimolar amounts of [Fe(^{Ph2}TIP)(MeCN)$_3$](OTf)$_2$ (456 mg, 0.38 mmol) and ^{tBu}CatH$_2$ (63 mg, 0.38 mmol) were dissolved in tetrahydrofuran (THF) (10 mL), followed by addition of NEt_3 (58 μL, 0.42 mmol). The dark yellow solution was stirred for 30 min, and the solvent was removed under vacuum. The crude material was taken up in DCE (5 ml) and filtered. Layering of this solution with hexane provided bright yellow crystals suitable for X-ray diffraction. Crystals were washed with hexanes and dried under vacuum (yield = 83 mg, 20%). μ_{eff} = 4.7 μ_B (Evans method). UV-vis [λ_{max}, nm (ε, M^{-1} cm^{-1}) in CH_2Cl_2]: 397 (940). IR (neat, cm^{-1}): 3058 (w), 2955 (w), 1603 (w), 1505 (m), 1460 (m), 1443 (m), 1443 (m), 1369 (m), 1241 (s), 1154 (s), 1028 (s). ^{1}H NMR (400 MHz, CD_2Cl_2): δ = -27.52, -10.44, 2.22, 4.51,

5.98, 6.94, 9.53, 10.06, 11.47, 23.88, 29.58, 61.67, 65.98. ^{19}F NMR (376 MHz, CD_2Cl_2): δ = -80.3 (OTf) ppm. Elemental analysis calcd (%) for $C_{59}H_{52}F_3FeN_6O_5PS$•2DCE: C, 58.26; H, 4.66; N, 6.47. Found: C, 58.00; H, 4.98; N, 6.46.

[Fe(^{Ph2}TIP)(^{tBu}PDA)(OTf)$_2$ [12](OTf)$_2$: Equimolar amounts of [Fe(^{Ph2}TIP)(MeCN)$_3$](OTf)$_2$ (304 mg, 0.25 mmol) and ^{tBu}PDA (42 mg, 0.25 mmol) were dissolved in tetrahydrofuran (THF) (10 mL), and the reaction was stirred for 18 h. Removal of the solvent under vacuum yielded a white solid that was dissolved in DCE (3 mL) and filtered. Vapor diffusion of ET_2O into this solution afforded the product as a colorless solid (yield = 123 mg, 39%) suitable for use in spectroscopic and kinetic studies. The complex does not exhibit absorption features in the visible region. μ_{eff} = 5.48 μ_B (Evans method). IR (neat, cm^{-1}): 3306 (w, ν(NH)), 3254 (w, ν(NH)), 3057 (w), 2960 (w), 1572 (w), 1443 (w), 1261 (s), 1147 (m), 1029 (w). ^{1}H NMR (400 MHz, CD_2Cl_2): δ = -28.8 (1H), 0.62 (9H), 4.98 (6H), 7.00 (3H), 7.32 (3H), 7.68 (6H), 8.53 (6H), 11.81 (1H), 12.89 (9H), 15.33 (6H), 19.01 (2H), 24.33 (2H), 31.36 (1H). ^{19}F NMR (376 MHz, CD_2Cl_2): δ = -79.3 (OTf) ppm. Elemental analysis revealed that a small amount of DCE solvent (0.5 equiv/Fe) remains after drying. Elemental analysis calcd (%) for $C_{60}H_{55}F_6FeN_8O_6PS_2$•2DCE: C, 56.42; H, 4.42; N, 8.63; F, 8.78. Found: C, 56.56; H, 4.51; N, 8.54; F, 8.32. X-ray quality crystals were obtained by either slow diffusion of Et_2O into a concentrated MeCN solution or pentane layering of a DCE solution containing 1 equiv. of $NaBPh_4$.

[Fe(^{Ph2}TIP)(^{Me}2MP)]OTf [13]OTf. Equimolar amounts of [Fe(^{Ph2}TIP)(MeCN)$_3$](OTf)$_2$ (143 mg, 0.12 mmol) and 2-methoxy-5-methylphenolate (^{Me}2MPH, 16.3 mg, 0.12 mmol) were dissolved in THF (10 mL), followed by addition of

NEt^3 (20 μL, 0.15 mmol). The mixture was stirred for 3 h, and the solvent was removed under vacuum. The crude solid was taken up in CH^2Cl^2 (5 mL) and layered with hexanes. After several days, light green crystals suitable for X-ray crystallography were collected (yield = 101 mg, 80%). UV-vis [λ_{max}, nm (ε, M^{-1} cm^{-1}) in CH_2Cl_2]: 390 (1400), 610 (500). IR (neat, cm^{-1}), 3048 (w), 1499 (w), 1444 (m), 1396 (w), 1260 (s), 1220 (s), 1146 (s), 1073 (w), 1028 (s), 982 (m), 790 (s), 771 (s). The crystals used for elemental analysis were prepared from a mixture of DCE/hexanes. The results suggest that some DCE solvent (~1 equiv/Fe) remains after drying consistent with the X-ray structures that found 1.5 equiv. of uncoordinated CH_2Cl_2 in the unit cell. Elemental analysis calcd (%) for C57H48F3FeN6O5PS•DCE: C, 60.47; H, 4.47; N 7.17. Found: C 59.00; H, 4.63; N, 7.55.

Synthesis of ^{tBu}PDA with ^{15}N at 2-Position. Using a published procedure,[237] acetic anhydride (2.64 g, 22.4 mmol) was added dropwise to a solution of 4-*tert*-butylaniline (3.34 g, 22.4 mmol) in CH_2Cl_2 (30 mL) at O°C. A white precipitate formed as the mixture was stirred for 30 min. After addition of 30 mL of hexanes, the solution was filtered to give 4-*tert*-butylacetanilide as a white solid. Without further purification, 680 mg (3.55 mmol) of the product was dissolved in $CHCl_3$ (15 mL). To this solution, H^2SO^4 (0.3 mL) and ^{15}N-labeled HNO_3 (1.0 g, 7.04 mmol, Aldrich, 98% ^{15}N) were added dropwise. The resulting dark orange solution was stirred for 1 h and was then washed successively with H_2O, saturated $NaHCO_3$, and brine. After drying the organic layer with $MgSO_4$ the solvent was removed to yield 4-*tert*-butyl-2-nitroacetanilide. The protecting group was then removed by refluxing in EtOH with KOH (143 mg, 2.6 mmol). The mixture was poured into ice-water, yielding a precipitate that was isolated by filtration,

washed with cold H_2O, and dried in vacuo. The resulting ^{15}N-labeld 4-*tert*-butyl-2-nitroaniline (300 mg, 1.54 mmol) was dissolved in MeOH (20 mL), and 5% Pd/C catalyst (90 mg) was added. The mixture was stirred under H_2 (46 psi) for 5 h and filtered through Celite, and the solvent was removed under vacuum to yield a dark purple solid (yield = 201 mg, 79%). ^1H and ^{13}C NMR spectra of the product were identical to those obtained with commercially available ^{tBu}PDA.

Oxygenation studies were performed by injecting anaerobic solutions of the Fe(II) complex into O_2-saturated solutions of CH_2Cl_2 at the desired temperature. Formation of the oxidized species was monitored using UV-vis spectroscopy. The concentration of O_2 in CH_2Cl_2 solutions at various temperatures (T) was estimated using the formula: $S = (LP_{O2})/TR)$, where L is the Ostwald coefficient (0.257 for CH_2Cl_2), P_{O2} is the partial pressure of O_2, and R is the gas constant.[223,238] The determination of P_{O2} accounted for the vapor pressure of CH_2Cl_2 (P_{solv}) as a function of T: $P_{O2} = 1\ atm - P_{solv}$. Following established procedures,[135,206,213,234] the decomposition products of the $\mathbf{3^{ox}} + O_2$ reaction were isolated by removing the CH_2Cl_2 solvent under vacuum, taking the residue up in MeCN, and treating the solution with ~3 mL of HCl (2 M). After extraction of the aqueous layer with Et_2O, the solvent was removed to give a residue that was analyzed with GC-MS and/or ^1H NMR spectroscopy. The ^1H data was interpreted with the aid of published spectra.[239]

DFT calculations were performed using the ORCA 2.9 software package developed by Dr. F. Neese (MPI for Chemical Energy Conversion). Calculations involving $\mathbf{4^{ox}}$ employed Becke's three-parameter hybrid functional for exchange along with the Lee-Yang-Parr correlations functional (B3LYP).[142,143] These calculations

utilized Ahlrichs' valance triple-ζ basis set (TZV) and TZV/J auxiliary basis set, in conjunction with a polarization functions on all atoms.[144,145,240] In the geometry optimized model, the ^{Ph2}TIP ligand was modified by replacing the Ph-groups at the 5-position of the imidazolyl rings with H-atom. In addition, the *tert*-butyl substituent of the ^{tBu}PDA ligand was replaced with a Me group. To avoid spurious transitions, time-dependant DFT (TD-DFT) calculations used a truncated version of the optimized **12^{ox}** model with Me groups (instead of Ph groups) at the 4-position of the imidazolyl rings. TD-DFT calculations[176-178] calculated absorption energies and intensities for 50 excited states with the Tamm-Dancoff approximation.[179,241] Isosurface plots of molecular orbitals and electron-density difference maps (EDDMs) were prepared with Laaksonen's gOpenMolprogram.[146]

Energetic parameters for the biding of O_2 to the Fe(II) complexes were computed using the Perdew-Burke-Ernzerhof (PBE) functional[229] with 10% Hartree-Fock exchange. These calculations employed modified ^{Ph2}TIP ligands containing three N-methylimidazole rings attached at the 2-position to a central P atom, and the *tert*-butyl substituents of the bidentate ligand were replaced with Me groups. Geometry optimizations were performed for the Fe(II) precursors, [Fe/O_2] adducts, and O_2 under tight convergence criteria, and the resulting models were used to obtain gas-phase vibrational and thermodynamic data. Solvent effects were calculated using the conductor-like screening model (COSMO)[242] with a dielectric constant (ε) of 9.08 for CH_2Cl_2. The "spin-flip" feature of ORCA was employed to generate [Fe/O_2] wave functions for S_{tot} = 2 and 1 states.

Table 5.7. Summary of X-ray Crystallographic Data Collection and Structure Refinement

	[**11**]OTf•2DCE	[**12**](OTf)(BPh_4)•DCE•C_5H_{12}[a]	[**12**(MeCN)]($OTf)_2$•MeCN•Et_2O	[**13**](OTf)•1.5CH_2Cl_2
empirical formula	$C_{63}H_{60}Cl_4F_3FeN_6O_5PS$	$C_{90}H_{91}BCl_2F_3FeN_8O_3PS$	$C_{68}H_{71}F_6FeN_{10}O_7PS_2$	$C_{58.5}H_{51}Cl_3F_3FeN_6O_5PS$
formula weight	1298.85	1590.34	1388.96	1200.28
crystal system	monoclinic	monoclinic	triclinic	triclinic
space group	$P2_1$	$P2_1/n$	$P\bar{1}$	P
a, Å	16.0859(2)	19.6939(4)	15.3998(3)	15.5548(2)
b, Å	21.4779(2)	18.3202(4)	15.6626(3)	17.2278(3)
c, Å	17.8488(2)	22.2057(4)	17.9588(3)	23.4768(4)
α, deg	90	90	88.191(2)	97.790(1)
β, deg	90.1428(9)	92.009(2)	64.934(2)	91.828(1)
γ, deg	90	90	61.081(2)	115.875(2)
V, $Å^3$	6166.6(1)	8006.8(3)	3351.4(1)	5578.9(2)
Z	4	4	2	4
D_{calc}, g/cm^3	1.399	1.293	1.376	1.429
λ, Å	1.5418	0.7107	0.7107	1.5418
μ, mm^{-1}	4.642	0.350	0.388	4.654
θ-range, deg	6 to 148	6 to 58	6 to 58	6 to 147
reflections collected	60871	77363	74982	71466
independent reflections	23500	19234	16362	21895
	[R_{int} = 0.0372]	[R_{int} = 0.0418]	[R_{int} = 0.0363]	[R_{int} = 0.0345]
data/restraints/parameters	23500/7/1532	19234/67/1058	16362/7/898	21895/129/1607
GOF (on F^2)	1.041	1.051	1.050	1.074
R1/wR2 ($I>2\sigma(I)$)[b]	0.0390/0.1022	0.0962/0.2182	0.0470/0.1170	0.0425/0.1169
R1/wR2 (all data)	0.0395/0.1028	0.1280/0.2375	0.0589/0.1253	0.0478/0.1215

[a]The DCE solvate is only partially (80%) populated. [b]The ethereal solvate is only partially (78%) populated.

Chapter 6

O_2 Reactivity of Fe(II) Complexes that Mimic the Active-Site Structure of Acetylacetone Dioxygenase

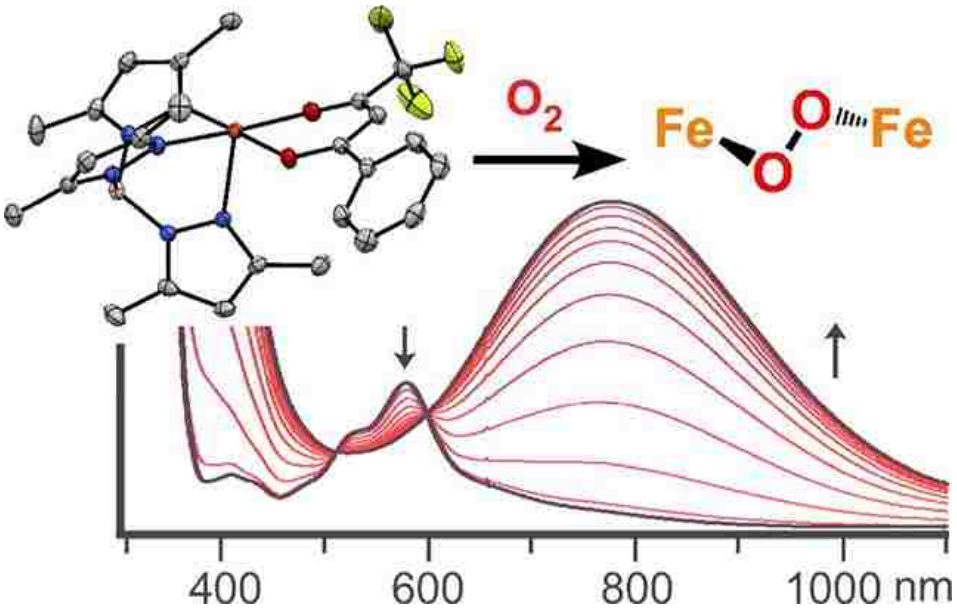

Abstract: Two complexes that exhibit Dke1 like activity have been synthesized and characterized by X-ray crystallography. Exposure of each [(^{Ph2}TpFe^{2+}(acac^{X})] (where acac^{X} is the anion of dialkyl malonate) to O_2 at room temperature in toluene results in the oxidative cleave of the substrate concomitant with degradation of the initial iron species. The reaction was monitored by ^{1}H NMR and GC-MS.

Parts of the following chapter have appeared in the following paper Park, H.; Bittner, M. M.; Baus, J. S.; Lindeman, S. V.; Fiedler, A. T. *Inorg. Chem.* **2012**, *51*, 10279-10289.

6.A. Introduction

The oxidative cleavage of carbon−carbon bonds by mononuclear nonheme iron dioxygenases is a crucial step in the microbial degradation of many organic pollutants.[2,3,203] Well studied examples include the intradiol and extradiol catechol dioxygenases,[92] (homo)gentisate dioxygenases,[243] and (chloro)-hydroquinone dioxygenases.[8,96,244] In 2003, Straganz and co-workers demonstrated that a strain of Acinetobacter johnsonii is able to use acetylacetone ─ a toxic pollutant ─ as its sole source of carbon.[52] The initial step of this process is performed by the enzyme acetylacetone dioxygenase (also known as β-diketone dioxygenase, Dke1), which uses O_2 to convert acetylacetone to acetic acid and 2-oxopropanal.[52] Biochemical and crystallographic studies revealed that the Dke1 active site contains a monoiron(II) center facially ligated by three histidine (3His) residues, a deviation from the 2-His-1-carboxylate facial triad normally employed by nonheme iron dioxygenases.[49,54,245] Dke1 is capable of oxidizing β-diketones and β-ketoesters with a variety of substituents at the 1-, 3-, and 5-positions; in each case, the substrate coordinates to Fe as the deprotonated acac-type anion.[53] Initial mechanistic studies suggested that O_2 reacts with the bound acac ligand in a concerted two-electron process, resulting in a peroxidate intermediate without direct involvement of the Fe center.[56] However, in a subsequent computational study, Solomon and Straganz have set forth an alternative mechanism that involves formation of an Fe/O_2 adduct prior to substrate oxidation.[230]

Dke1 has attracted the interest of synthetic inorganic chemists because of the presence of the unusual 3His triad in the active site, as well as the enzyme's ability to catalyze aliphatic C−C bond cleavage. Interestingly, the first relevant model system was

reported a decade before the discovery of Dke1. In 1993, Kitajima and co-workers generated the complex [Fe^{2+}(^{iPr2}Tp)(acac)(MeCN)] (where ^{R2}Tp = hydrotris- (pyrazol-1-yl)borate with R-groups at the 3- and 5-positions of the pyrazole rings).[246] Exposure to O_2 in MeCN at room temperature eventually produced crystals of the triiron(III) complex [Fe^{3+}(μ-O)(μ-OH)(μ-OAc)$_4$(^{iPr2}Tp)$_2$], where the bridging acetate ligands derive from the acac group of the ferrous precursor. Thus, this synthetic model exhibits Dke1-type reactivity, although generation of the acetate ligands may proceed via a different mechanism than the one employed by the enzyme. In 2008, Limberg and Siewer demonstrated that the related complex, [Fe^{2+}(^{Me2}Tp)(acac^{Phmal})] (acac^{Phmal} = anion of diethyl phenylmalonate), reacts with O_2 to give Dke1- type products with incorporation of oxygen atoms from O_2.[72] The activated diethyl malonate anion was used because the corresponding acac complex failed to exhibit oxidative cleavage. Significantly, the [Fe^{2+}(^{Me2}Tp)(acac^{Phmal})] system is catalytic in the presence of excess Li(acac^{Phmal}) and O_2 with a turnover frequency of 55 h^{-1}.

In our group, Dr. Heaweon Park and Jacob Baus generated three series of Dke1 models featuring Fe(II)/acac^X units (acac^X = substituted β-diketonates) bound to facially-coordinating N3 supporting ligands (L_{N3}).[247] These complexes incorporated acac^X ligands with a range of steric and electronic properties. Following the labeling scheme employed in that paper (Figure 6.1), the **1-acac^X** and **2-acac^X** complexes contain anionic ^{Me2}Tp and ^{Ph2}Tp donors, respectively. The **[3-acac^X]OTf** series utilizes the neutral tris(2-phenylimidazoly-4-yl)phosphine (^{Ph}TIP) ligand, which was shown by spectroscopic and computational analysis to faithfully reproduce the 3His coordination environment of the Dke1 active site. In this chapter, we describe the synthesis and O_2 reactivity of three

additional complexes that incorporate β-diester anions (i.e., $acac^{OMe}$ and $acac^{Phmal}$ in Figure 6.1). These complexes were prepared in order to compare our results with those previously published by Siewert and Limberg.[17] Thus, we seek to expand upon previous discoveries that have demonstrated that synthetic Fe/$acac^{X}$ complexes are capable of performing Dke1-type chemistry.

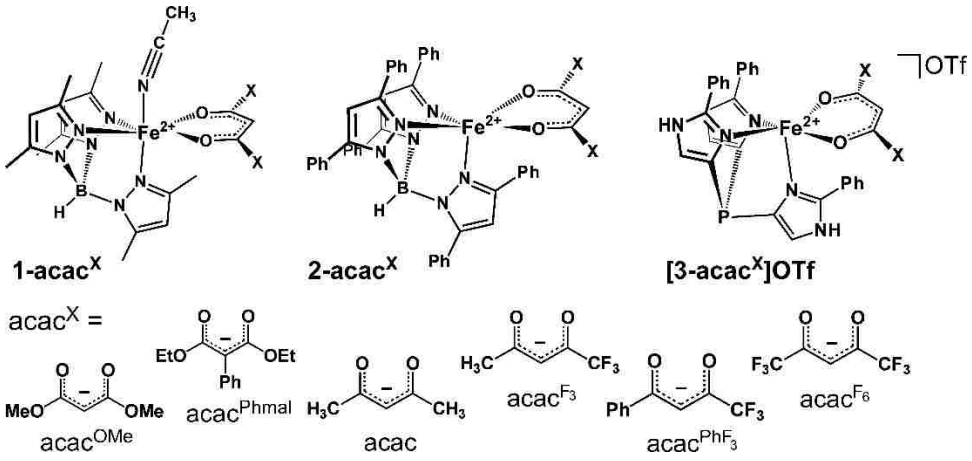

Figure 6.1. Naming scheme of compounds in this chapter.

6.B. Synthesis, Solid State Structures, and Spectroscopic Features

Following earlier procedures,[72,126] the iron(II) complexes, **2-acac^{OMe}** (**14**), and **2-acac^{Phmal}** (**15**) were prepared by reacting equimolar amounts of K(^{R2}Tp), $FeCl_2$, LDA, and dimethyl malonate or diethyl phenylmalonate. The resulting X-ray crystal structures are shown in Figure 6.1 and selected metric parameters are provided in Table 6.1. The ^{Ph2}Tp complexes **14** and **15** exhibit distorted 5C square-pyramidal geometries (τ =0.03 and 0.39, respectively[124]) with a pyrazole ligand in the axial position. The lack of bound solvent shortens the Fe−N_{Tp} and Fe−O_{acac} distances in **14** and **15** (Table 6.1). Because of

steric interactions with the 3-Ph group of the axial pyrazole, the acac^{OMe} ligand is tilted out of the N1−Fe1−N3 plane by ~30°.

Most Fe(^{R2}Tp)(acac^{X}) complexes are brightly colored because of the presence of Fe^{2+}→acac^{X} (C=O*) metal-to-ligand charge-transfer (MLCT) transitions in the visible region.[126] The acac^{OMe} and acac^{Phmal} complexes are colorless, however, as the corresponding MLCT bands appear in the UV region, reflecting the electron-rich nature of the dialkyl malonate anions. The ^{1}H NMR spectra of these complexes exhibit broad, paramagnetically shifted peaks consistent with the presence of a high-spin Fe(II) center. For complex **14**, resonances arising from the methyl groups of the acac^{OMe} moieties appear near 8 ppm in CD_2Cl_2. The remaining ^{R2}Tp-derived peaks largely follow the patterns previously described for previously published complexes.[126]

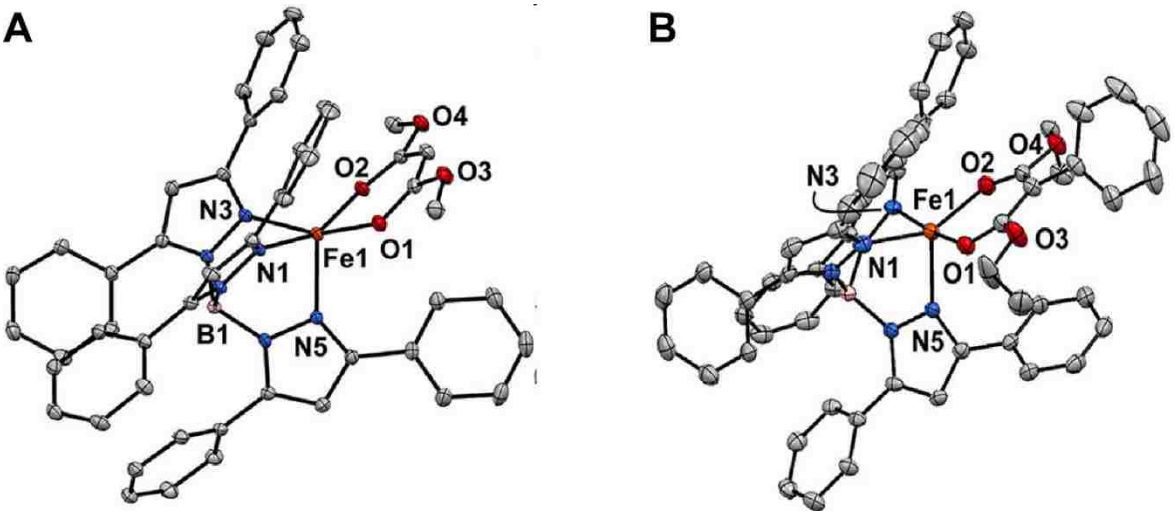

Figure 6.2. Thermal ellipsoid plots (50% probability) derived from **14** • 1.5 CH_2Cl_2 (A), and **15** • MeCN (B). Hydrogen atoms and noncoordinating solvent molecules have been omitted for clarity. Selected metric parameters are provided in Table 6.1.

Table 6.1. Selected Bond Distances (Å) and Bond Angles (deg) for **14** • 1.5 CH_2Cl_2, and **15** • MeCN

	14•1.5 CH_2Cl_2	**15** • MeCN[a]
Fe-O1	2.042(1)	1.982(2)
Fe-O2	2.046(1)	2.065(2)
Fe-N1	2.151(1)	2.214(2)
Fe-N3	2.154(1)	2.105(2)
Fe-N5	2.129(1)	2.076(2)
Fe-O_{acac} (ave)	2.044	2.024
Fe-N_{Tp} (ave)	2.144	2.132
O1-Fe-O2	87.50(4)	86.34(6)
O1-Fe-N1	92.16(4)	97.02(7)
O1-Fe-N3	159.16(4)	147.45(7)
O1-Fe-N5	108.31(4)	120.57(7)
O2-Fe-N1	157.09(4)	170.87(7)
O2-Fe-N3	88.54(4)	90.05(7)
O2-Fe-N5	109.58(4)	95.66(7)
N1-Fe-N3	83.68(4)	82.54(7)
N1-Fe-N5	92.28(4)	89.95(7)
N3-Fe-N5	92.29(4)	91.98(7)
τ-value	0.03	0.39

[a]The unit cell of **15** • MeCN contains two symmetrically independent complexes with nearly identical geometries. Only parameters for the first complex are shown.

6.C. Oxygenation of Fe(II) Complexes

Treatment of Fe(II) complexes in the **2-acac^{X}** and series with O_2 failed to generate the corresponding green intermediates or triiron complexes under any conditions. These complexes react slowly, or not at all, with O_2 in both coordinating and noncoordinating solvents. For instance, the UV−vis absorption and ^{19}F NMR spectra of **2-acac^{F3}**, and **2-acac^{PhF3}** in O_2-saturated toluene solutions exhibit no significant changes over the course of several days at room temperature. Only the β-diester complexes **14** and

15 exhibit perceptible reactivity toward O_2. Exposure of these complexes to O_2 eventually yields colorless crystals that were shown by XRD to consist of $Fe(^{Ph2}Tp)_2$ suggesting that the acac ligands are degraded in the process.[72] Monitoring the O_2 reaction with ^1H NMR spectroscopy in toluene-d_8 revealed that the paramagnetically shifted peaks of **14** and **15** slowly disappear, concomitant with the growth of peaks arising from methyl 2-oxoacetate and ethyl benzoylformate, respectively. The formation of ethyl benzoylformate was also verified by GC-MS. When the reaction with **15** was performed with ^{18}O-enriched dioxygen, GC-MS analysis indicated that one O-atom of ethyl benzoylformate is derived from O_2, proving that the observed products are due to dioxygenolytic cleavage of the ligand (the alkyl carbonate products that are also generated quickly decompose to CO_2 and the corresponding alkoxide). Thus, our ^{Ph2}Tp-based complexes are capable of performing Dke1-type chemistry on a reasonable time scale provided that the substrate ligand is sufficiently activated. The rates of the O_2 reactions in toluene were measured using UV−vis absorption spectroscopy. **15** decays relatively quickly in the presence of O_2 ($k_{O2} = 3.4 \times 10^{-4}$ s^{-1}; Figure 6.2), whereas **14** requires more than a day for complete reaction ($k_{O2} \sim 4 \times 10^{-5}$ s^{-1}).

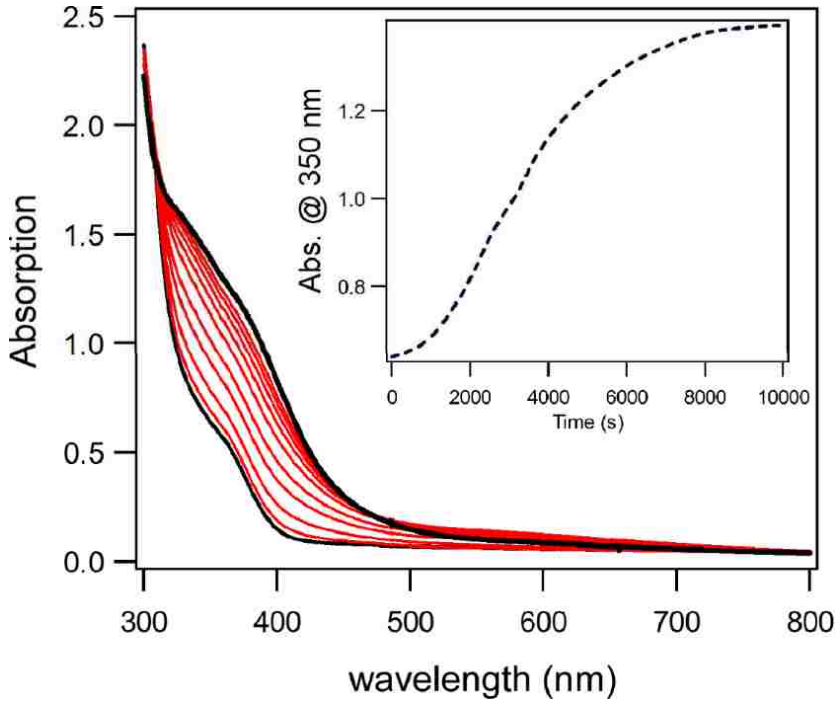

Figure 6.3. Time-dependent absorption spectra of the reaction of **15** (0.36 mM) with O_2 at room temperature in toluene. Inset: Absorption intensity at 350 nm as a function of time.

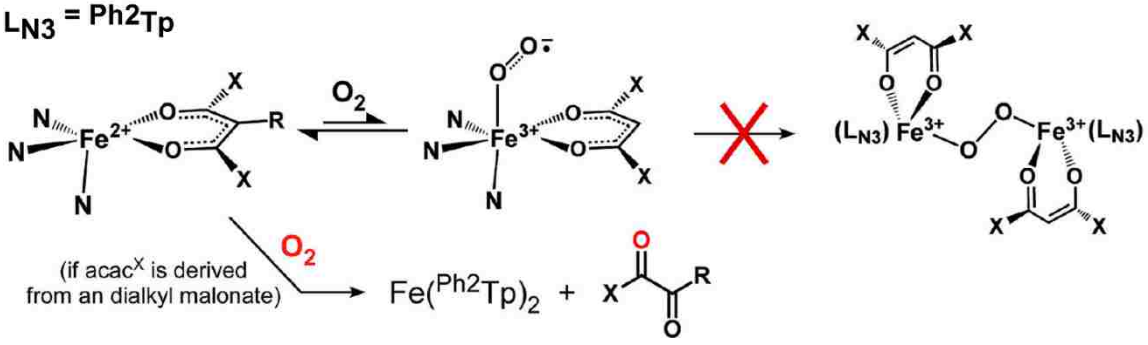

Figure 6.4. Proposed mechanistic path for the oxidative cleavage of $acac^X$ ligands utilized by our synthetic models.

Based on the work with **2-acac^X** and Dr. Parks previous work with acac-based compounds we have proposed the mechanistic framework shown in Figure 6.4 for our $[Fe^{2+}(^{Ph2}Tp)(acac^X)]$ complexes.[248] Fe(II)-$acac^X$ complexes with ^{Ph2}Tp exhibit

dramatically diminished reactivity toward O_2. Complexes with β-diketonato ligands are stable in oxygenated solutions at room temperature for several hours or days, regardless of solvent. We initially assumed that this inert behavior was due to the steric bulk of the phenyl substituents, which might be expected to block O_2 coordination the Fe center. Yet this hypothesis is not consistent with the facile formation of $FeNO^{53}$ adducts upon exposure of the **2-acac^{X}** complexes to NO, proving that formation of an Fe/O_2 species is sterically feasible for the ^{Ph2}Tp-based complexes. However, the size of the Ph groups likely prevents the formation a diiron intermediate via reaction with a second Fe(II) complex. The scenario illustrated in Figure 6.4 requires the reaction equilibrium of the first step (i.e., O_2 binding) to lie far to the side of Fe(II) + O_2, since the putative iron(III)-superoxo adduct is never observed. Indeed, a number of computational studies have indicated that the reversible transfer of one electron from a mononuclear nonheme Fe(II) center to O_2 is endergonic by approximately 5^{-10} kcal/mol.[42,230,249] In Dr.Parks ^{Me2}Tp systems, the uphill nature of this initial step is overcome by the thermodynamicly favorable second step; formation of a di- $[Fe^{3+}(^{Me2}Tp)(acac^{X})]^{+}$ intermediate, which "pulls" the entire process forward (where ^{Me2}Tp is hydrotris(3,5-diphenylpyrazol-1-yl) borate(1−) ligand. However, when this second step is hindered because of steric reasons, the ferrous complexes are rendered much less reactive toward O_2, as observed for the **2-acac^{X}** series. Obviously, the protein environment surrounding the Fe center in Dke1 prevents formation of a diiron-peroxo intermediate. Instead, the enzymatic mechanism likely involves formation of a peroxy bridge between Fe and acac following initial formation of an iron(III)-superoxo species. One would therefore expect the ^{Ph2}Tp and

^{Ph}TIP supporting ligands, which prevent dimerization, to be ideal scaffolds for reproducing the catalytic activity of Dke1.

6.D. Conclusions

We have demonstrated that complexes in the **2-acac^{X}** series with activated anions of dialkyl malonate are able to cleave the acac anion in a manner similar to the enzymatic system. Key differences a found in the rate and mechanism of oxidative cleavage. Namely, our complexes react slower and through a separate mechanism than the enzyme catalytic mechanism. We also showed that nonacctivated acac^{X} complexes do not exhibit any activity when exposed to O_2, these complexes being stable for days in air, even though ligands such as acac^{F3} are viable substrates for Dke1. The differences between our complexes and Dke1 serve to highlight the importance of second-sphere residues in the protein environment, and some of the challenges that Dke1 must overcome.

6.E. Experimental

Unless otherwise noted, all reagents and solvents were purchased from commercial sources and used as received. Acetonitrile, dichloromethane, and tetrahydrofuran were purified and dried using a Vacuum Atmospheres solvent purification system. The synthesis and handling of air-sensitive materials were performed under inert atmosphere using a Vacuum Atmospheres Omni-Lab glovebox equipped with a freezer set to −30 °C. Nitric Oxide was purified by passage through an ascarite II column followed by a cold trap at -78 °C to remove higher nitrogen impurities.

K(^{Ph2}Tp)[137] was prepared according to literature procedures. Elemental analyses were performed at Midwest Microlab, LLC in Indianapolis, IN. UV−vis absorption spectra were obtained with an Agilent 8453 diode array spectrometer equipped with a cryostat from Unisoku Scientific Instruments (Osaka, Japan) for low temperature experiments. Infrared (IR) spectra were measured in solution using a Nicolet Magna-IR 560 spectrometer. Mass spectra were recorded using an Agilent 6850 gas chromatography − mass spectrometer (GC-MS) with a HP-5 (5% phenylmethylpolysiloxane) column.

(^{Ph2}Tp)Fe(acac^{OMe}) (2-acac^{OMe}) (14): Li(acac^{OMe}) was generated by treating dimethyl malonate (0.92 mmol) with LDA (1.0 mmol) in tetrahydrofuran (THF), followed by removal of the solvent to yield the salt as a white powder. $FeCl_2$ (0.92 mmol) and K(^{Ph2}Tp) (0.92 mmol) were then combined with Li(acac^{OMe}) in 15 mL of 1:3 CH_2Cl_2/CH_3CN. The solution was stirred for 24 h, and the solvents were removed under vacuum. The white product was taken up in 5 mL of CH_2Cl_2 and filtered to remove insoluble salts. The resulting solution was layered with CH_3CN to yield colorless crystals suitable for XRD studies. Anal. Calcd for $C_{50}H_{41}BFeN_6O_4$: C, 70.11; H, 4.82; N, 9.81. Found: C, 70.02; H, 4.82; N, 9.85. UV−vis [λ_{max}, nm (ε, M^{-1} cm^{-1}) in toluene]: 330 (400). IR (KBr, cm^{-1}): 3061, 2950, 2616 [ν(BH)], 1632 [ν(CO)], 1503, 1460, 1304.

(^{Ph2}Tp)Fe(acac^{Phmal}) (2-acac^{Phmal}) (15): Diethyl phenylmalonate (Phmal) (0.712 mmol) was stirred with LDA (0.790 mmol) for 30 min in 5 mL of THF. Removal of the solvent yielded a white salt that was dissolved in a 3:2 mixture of MeCN/CH_2Cl_2. Addition of $FeCl_2$ (0.713 mmol) and K(^{Ph2}Tp) (0.712 mmol) resulted in a cloudy gray solution that was stirred overnight. The solvents were removed under vacuum to yield a pale green solid that was taken up in 5 mL of CH_2Cl_2 and layered with CH_3CN. After one

day, light green crystals suitable for XRD were obtained. Anal. Calcd for $C_{58}H_{49}BFeN_6O_4$: C, 72.51; H, 5.14; N, 8.75. Found: C, 72.39; H, 5.11; N, 8.74. UV−vis [λ_{max}, nm (ε, M^{-1} cm^{-1}) in toluene]: 350 (1806). IR (neat, cm^{-1}): 3024, 2974, 2614 [ν(BH)], 1615 [ν(CO)], 1594, 1544, 1478, 1463, 1448, 1433, 1405, 1375, 1337, 1303.

Table 6.2. Summary of X-ray Crystallographic Data Collection and Structure Refinement

	2-acac^{OMe}•CH_2Cl_2	**2-acac^{Phmal}**•MeCN
empirical formula	$C_{51.5}H_{44}BCl_3FeN_6O_4$	$C_{60}H_{52}BFeN_7O_4$
formula weight	983.94	1001.75
crystal system	triclinic	monoclinic
space group	P_1^-	$P2_1/c$
a [Å]	12.2090(3)	38.1369(8)
b [Å]	13.0283(4)	13.5597(3)
c [Å]	17.0877(5)	20.5303(4)
α [°]	95.921(3)	90
β [°]	103.201(3)	104.121(2)
γ [°]	117.095(3)	90
V [Å^3]	2287.5(1)	10295.9(4)
Z	2	8
$D_{calcd.}$ [g/cm^3]	1.429	1.293
λ [Å]	0.7107	1.5418
μ [mm^{-1}]	0.559	2.789
θ range [°]	3 to 62	7 to 148
Reflections collected	49672	72082
Independent reflections	13415 [Rint = 0.0278]	20374 [Rint = 0.0351]
Data/restraints/parameters	13415/24/609	20374/0/1321
GOF (on F^2)	1.031	1.040
R1/wR2 (I > 2σ(I))[a]	0.0364/0.0861	0.0525/0.1393
R1/wR2 (all data)[a]	0.0463/0.0925	0.0570/0.1430

[a] $R1 = \Sigma||F_o| - |F_c||/\Sigma|F_o|$; $wR2 = [\Sigma w(F_o^2 - F_c^2)^2/\Sigma w(F_o^2)^2]^{1/2}$.

BIBLIOGRAPHY

(1) Baker, K. H., D.S. In *Bioremediation*; McGraw-Hill, Inc.: New York, 1994, p 9-60.

(2) Parales, R. E.; Haddock, J. D. *Curr. Opin. Biotechnol.* **2004**, *15*, 374-379.

(3) Gibson, D. T.; Parales, R. E. *Curr. Opin. Biotechnol.* **2000**, *11*, 236-243.

(4) Kauppi, B.; Lee, K.; Carredano, E.; Parales, R. E.; Gibson, D. T.; Eklund, H.; Ramaswamy, S. *Structure* **1998**, *6*, 571-586.

(5) Vaillancourt, F. H.; Bolin, J. T.; Eltis, L. D. *Crit. Rev. Biochem. Mol. Biol.* **2006**, *41*, 241-267.

(6) Lipscomb, J. D.; Orville, A. M. *Met. Ions Biol. Syst.* **1992**, *28*, 243-298.

(7) Harpel, M. R.; Lipscomb, J. D. *J. Biol. Chem.* **1990**, *265*, 22187-22196.

(8) Machonkin, T. E.; Holland, P. L.; Smith, K. N.; Liberman, J. S.; Dinescu, A.; Cundari, T. R.; Rocks, S. S. *J. Biol. Inorg. Chem.* **2010**, *15*, 291-301.

(9) Veldhuizen, E. J. A.; Vaillancourt, F. H.; Whiting, C. J.; Hsiao, M. M. Y.; Gingras, G.; Xiao, Y. F.; Tanguay, R. M.; Boukouvalas, J.; Eltis, L. D. *Biochem. J.* **2005**, *386*, 305-314.

(10) Lendenmann, U.; Spain, J. C. *J. Bacteriol.* **1996**, *178*, 6227-6232.

(11) Li, X.; Guo, M.; Fan, J.; Tang, W.; Wang, D.; Ge, H.; Rong, H.; Teng, M.; Niu, L.; Liu, Q.; Hao, Q. *Protein Sci.* **2006**, *15*, 761-773.

(12) Matera, I.; Ferraroni, M.; Buerger, S.; Scozzafava, A.; Stolz, A.; Briganti, F. *J. Mol. Biol.* **2008**, *380*, 856-868.

(13) Hintner, J. P.; Remtsma, T.; Stolz, A. *J. Biol. Chem.* **2004**, *279*, 37250-37260.

(14) Hintner, J. P.; Lechner, C.; Riegert, U.; Kuhm, A. E.; Storm, T.; Reemtsma, T.; Stolz, A. *J. Bacteriol.* **2001**, *183*, 6936-6942.

(15) Han, S.; Eltis, L. D.; Timmis, K. N.; Muchmore, S. W.; Bolin, J. T. *Science* **1995**, *270*, 976-980.

(16) Vaillancourt, F. H.; Barbosa, C. J.; Spiro, T. G.; Bolin, J. T.; Blades, M. W.; Turner, R. F. B.; Eltis, L. D. *J. Am. Chem. Soc.* **2002**, *124*, 2485-2496.

(17) Karlsson, A.; Parales, J. V.; Parales, R. E.; Gibson, D. T.; Eklund, H.; Ramaswamy, S. *Science* **2003**, *299*, 1039-1042.

(18) Kovaleva, E. G.; Lipscomb, J. D. *Science* **2007**, *316*, 453-457.

(19) Koehntop, K. D.; Emerson, J. P.; Que, L. *J. Biol. Inorg. Chem.* **2005**, *10*, 87-93.

(20) Bruijnincx, P. C. A.; van Koten, G.; Gebbink, R. J. M. K. *Chem. Soc. Rev.* **2008**, *37*, 2716-2744.

(21) Kovaleva, E. G.; Lipscomb, J. D. *Nat. Chem. Biol.* **2008**, *4*, 186-193.

(22) Vaillancourt, F. H.; Barbosa, C. J.; Spiro, T. G.; Bolin, J. T.; Blades, M. W.; Turner, R. F. B.; Eltis, L. D. *J. Am. Chem. Soc.* **2002**, *124*, 2485-2496.

(23) Lipscomb, J. D. *Curr. Opin. Chem. Biol.* **2008**, *18*, 644-649.

(24) Sato, N.; Uragami, Y.; Nishizaki, T.; Takahashi, Y.; Sazaki, G.; Sugimoto, K.; Nonaka, T.; Masai, E.; Fukuda, M.; Senda, T. *J. Mol. Biol.* **2002**, *321*, 621-636.

(25) Li, X. W.; Guo, M.; Fan, J.; Tang, W. Y.; Wang, D. Q.; Ge, H. H.; Rong, H.; Teng, M. K.; Niu, L. W.; Liu, Q.; Hao, Q. *Protein Sci.* **2006**, *15*, 761-773.

(26) Guillemin, G. J.; Cullen, K. M.; Lim, C. K.; Smythe, G. A.; Garner, B.; Kapoor, V.; Takikawa, O.; Brew, B. J. *J. Neurosci.* **2007**, *27*, 12884-12892.

(27) Schlichting, I.; Berendzen, J.; Chu, K.; Stock, A. M.; Maves, S. A.; Benson, D. E.; Sweet, R. M.; Ringe, D.; Petsko, G. A.; Sligar, S. G. *Science* **2000**, *287*, 1615-1622.

(28) Tinberg, C. E.; Lippard, S. J. *Acc. Chem. Res.* **2011**, *44*, 280-288.

(29) Krebs, C.; Galonić Fujimori, D.; Walsh, C. T.; Bollinger, J. M. *Acc. Chem. Res.* **2007**, *40*, 484-492.

(30) Zhang, Y.; Colabroy, K. L.; Begley, T. P.; Ealick, S. E. *Biochemistry* **2005**, *44*, 7632-7643.

(31) Kovaleva, E. G.; Neibergall, M. B.; Chakrabarty, S.; Lipscomb, J. D. *Acc. Chem. Res.* **2007**, *40*, 475-483.

(32) Bugg, T. D. H.; Ramaswamy, S. *Curr. Opin. Chem. Biol.* **2008**, *12*, 134-140.

(33) Arciero, D. M.; Lipscomb, J. D. *J. Biol. Chem.* **1986**, *261*, 2170-2178.

(34) Sanvoisin, J.; Langley, G. J.; Bugg, T. D. H. *J. Am. Chem. Soc.* **1995**, *117*, 7836-7837.

(35) Koch, W. O.; Schünemann, V.; Gerdan, M.; Trautwein, A. X.; Krüger, H.-J. *Chem. Eur. J.* **1998**, *4*, 1255-1265.

(36) Pierpont, C. G. *Coord. Chem. Rev.* **2001**, *219–221*, 415-433.

(37) Pierpont, C. G. *Inorg. Chem.* **2011**, *50*, 9766-9772.

(38) Poddel'sky, A. I.; Cherkasov, V. K.; Abakumov, G. A. *Coord. Chem. Rev.* **2009**, *253*, 291-324.

(39) Spence, E. L.; Langley, G. J.; Bugg, T. D. H. *J. Am. Chem. Soc.* **1996**, *118*, 8336-8343.

(40) Georgiev, V.; Borowski, T.; Siegbahn, P. *J. Biol. Inorg. Chem.* **2006**, *11*, 571-585.

(41) Siegbahn, P. E. M.; Haeffner, F. *J. Am. Chem. Soc.* **2004**, *126*, 8919-8932.

(42) Bassan, A.; Borowski, T.; Siegbahn, P. E. M. *Dalton Trans.* **2004**, 3153-3162.

(43) Emerson, J. P.; Kovaleva, E. G.; Farquhar, E. R.; Lipscomb, J. D.; Que, L. *Proc. Natl. Acad. Sci.* **2008**, *105*, 7347-7352.

(44) Mbughuni, M. M.; Chakrabarti, M.; Hayden, J. A.; Bominaar, E. L.; Hendrich, M. P.; Münck, E.; Lipscomb, J. D. *Proc. Natl. Acad. Sci.* **2010**, *107*, 16788-16793.

(45) Mbughuni, M. M.; Chakrabarti, M.; Hayden, J. A.; Meier, K. K.; Dalluge, J. J.; Hendrich, M. P.; Münck, E.; Lipscomb, J. D. *Biochemistry* **2011**, *50*, 10262-10274.

(46) Christian, G. J.; Ye, S.; Neese, F. *Chem. Sci.* **2012**, *3*, 1600-1611.

(47) Colabroy, K. L.; Zhai, H.; Li, T.; Ge, Y.; Zhang, Y.; Liu, A.; Ealick, S. E.; McLafferty, F. W.; Begley, T. P. *Biochemistry* **2005**, *44*, 7623-7631.

(48) Straganz, G. D.; Nidetzky, B. *ChemBioChem* **2006**, *7*, 1536-1548.

(49) Leitgeb, S.; Nidetzky, B. *Biochem. Soc. Trans.* **2008**, *36*, 1180-1186.

(50) Joseph, C. A.; Maroney, M. J. *Chem. Commun.* **2007**, 3338-3349.

(51) Pierce, B. S.; Gardner, J. D.; Bailey, L. J.; Brunold, T. C.; Fox, B. G. *Biochemistry* **2007**, *46*, 8569-8578.

(52) Straganz, G. D.; Glieder, A.; Brecker, L.; Ribbons, D. W.; Steiner, W. *Biochem. J.* **2003**, *369*, 573-581.

(53) Straganz, G. D.; Hofer, H.; Steiner, W.; Nidetzky, B. *J. Am. Chem. Soc.* **2004**, *126*, 12202-12203.

(54) Leitgeb, S.; Straganz, G. D.; Nidetzky, B. *Biochem. J.* **2009**, *418*, 403-411.

(55) Straganz, G. D.; Diebold, A. R.; Egger, S.; Nidetzky, B.; Solomon, E. I. *Biochemistry* **2010**, *49*, 996-1004.

(56) Straganz, G. D.; Nidetzky, B. *J. Am. Chem. Soc.* **2005**, *127*, 12306-12314.

(57) Chen, J.; Li, W.; Wang, M.; Zhu, G.; Liu, D.; Sun, F.; Hao, N.; Li, X.; Rao, Z.; Zhang, X. C. *Protein Sci.* **2008**, *17*, 1362-1373.

(58) Hintner, J.-P.; Lechner, C.; Riegert, U.; Kuhm, A. E.; Storm, T.; Reemtsma, T.; Stolz, A. *J. Bacteriol.* **2001**, *183*, 6936-6942.

(59) Iwabuchi, T.; Harayama, S. *J. Biol. Chem.* **1998**, *273*, 8332-8336.

(60) Deveryshetty, J.; Phale, P. S. *Microbiology* **2009**, *155*, 3083-3091.

(61) Stolz, A.; Nörtemann, B.; Knackmuss, H. J. *Biochem. J.* **1992**, *282*, 675-680.

(62) Fusetti, F.; Schröter, K. H.; Steiner, R. A.; van Noort, P. I.; Pijning, T.; Rozeboom, H. J.; Kalk, K. H.; Egmond, M. R.; Dijkstra, B. W. *Structure* **2002**, *10*, 259-268.

(63) Steiner, R. A.; Kalk, K. H.; Dijkstra, B. W. *Proc. Natl. Acad. Sci. U.S.A* **2002**, *99*, 16625-16630.

(64) Gopal, B.; Madan, L. L.; Betz, S. F.; Kossiakoff, A. A. *Biochemistry* **2005**, *44*, 193-201.

(65) Steiner, R. A.; Kooter, I. M.; Dijkstra, B. W. *Biochemistry* **2002**, *41*, 7955-7962.

(66) Merkens, H.; Kappl, R.; Jakob, R. P.; Schmid, F. X.; Fetzner, S. *Biochemistry* **2008**, *47*, 12185-12196.

(67) Leitgeb, S.; Straganz, G. D.; Nidetzky, B. *Biochem. J.* **2009**, *418*, 403-411.

(68) Kreisberg-Zakarin, R.; Borovok, I.; Yanko, M.; Frolow, F.; Aharonowitz, Y.; Cohen, G. *Biophys. Chem.* **2000**, *86*, 109-118.

(69) Straganz, G. D.; Nidetzky, B. *J. Am. Chem. Soc.* **2005**, *127*, 12306-12314.

(70) Pau, M. Y. M.; Davis, M. I.; Orville, A. M.; Lipscomb, J. D.; Solomon, E. I. *J. Am. Chem. Soc.* **2007**, *129*, 1944-1958.

(71) Pau, M. Y. M.; Lipscomb, J. D.; Solomon, E. I. *Proc. Natl. Acad. Sci. U.S.A* **2007**, *104*, 18355-18362.

(72) Siewert, I.; Limberg, C. *Angew. Chem. Int. Ed.* **2008**, *47*, 7953-7956.

(73) Holm, R. H.; Solomon, E. I. *Chem. Rev.* **2004**, *104*, 347-348.

(74) Que, L., Jr. *Adv. Inorg. Biochem.* **1983**, *5*, 167-199.

(75) Que, L., Jr. *J. Chem. Soc., Dalton Trans.* **1997**, 3933-3940.

(76) Que, L., Jr. In *Bioinorganic Catalysis*; 2nd ed.; Reedijk, J., Bouwman, E., Eds.; Marcel Dekker: New York, 1999, p 269-321.

(77) Que, L., Jr. *Nat. Struct. Mol. Biol.* **2000**, *7*, 182-184.

(78) Chun, H.; Verani, C. N.; Chaudhuri, P.; Bothe, E.; Bill, E.; Weyhermüller, T.; Wieghardt, K. *Inorg. Chem.* **2001**, *40*, 4157-4166.

(79) Simándi, T. M.; Simándi, L. I.; Györ, M.; Rockenbauer, A.; Gömöry, Á. *Dalton Trans.* **2004**, 1056-1060.

(80) Chun, H.; Weyhermüller, T.; Bill, E.; Wieghardt, K. *Angew. Chem. Int. Ed.* **2001**, *40*, 2489-2492.

(81) Chun, H.; Bill, E.; Bothe, E.; Weyhermüller, T.; Wieghardt, K. *Inorg. Chem.* **2002**, *41*, 5091-5099.

(82) Chun, H.; Bill, E.; Weyhermüller, T.; Wieghardt, K. *Inorg. Chem.* **2003**, *42*, 5612-5620.

(83) Mukherjee, S.; Weyhermüller, T.; Bill, E.; Wieghardt, K.; Chaudhuri, P. *Inorg. Chem.* **2005**, *44*, 7099-7108.

(84) Grzyska, P. K.; Müller, T. A.; Campbell, M. G.; Hausinger, R. P. *J. Inorg. Biochem.* **2007**, *101*, 797-808.

(85) Chirik, P. J. *Inorg. Chem.* **2011**, *50*, 9737-9740.

(86) Verma, P.; Weir, J.; Mirica, L.; Stack, T. D. P. *Inorg. Chem.* **2011**, *50*, 9816-9825.

(87) Ray, K.; Petrenko, T.; Wieghardt, K.; Neese, F. *Dalton Trans.* **2007**, 1552-1566.

(88) Bill, E.; Bothe, E.; Chaudhuri, P.; Chlopek, K.; Herebian, D.; Kokatam, S.; Ray, K.; Weyhermüller, T.; Neese, F.; Wieghardt, K. *Chem. Eur. J.* **2005**, *11*, 204-224.

(89) Chaudhuri, P.; Verani, C. N.; Bill, E.; Bothe, E.; Weyhermüller, T.; Wieghardt, K. *J. Am. Chem. Soc.* **2001**, *123*, 2213-2223.

(90) Costas, M.; Mehn, M. P.; Jensen, M. P.; Que, L. *Chem. Rev.* **2004**, *104*, 939-986.

(91) Solomon, E. I.; Brunold, T. C.; Davis, M. I.; Kemsley, J. N.; Lee, S.-K.; Lehnert, N.; Neese, F.; Skulan, A. J.; Yang, Y.-S.; Zhou, J. *Chem. Rev.* **1999**, *100*, 235-350.

(92) Bugg, T. D. H. *Curr. Opin. Chem. Biol.* **2001**, *5*, 550-555.

(93) Bugg, T. D. H.; Lin, G. *Chem. Commun.* **2001**, 941-952.

(94) Titus, G. P.; Mueller, H. A.; Burgner, J.; Rodriguez de Cordoba, S.; Penalva, M. A.; Timm, D. E. *Nat. Struct. Mol. Biol.* **2000**, *7*, 542-546.

(95) Machonkin, T.; Holland, P.; Smith, K.; Liberman, J.; Dinescu, A.; Cundari, T.; Rocks, S. *J. Biol. Inorg. Chem.* **2010**, *15*, 291-301.

(96) Machonkin, T. E.; Doerner, A. E. *Biochemistry* **2011**, *50*, 8899-8913.

(97) Xun, L.; Bohuslavek, J.; Cai, M. *Biochem. Biophys. Res. Commun.* **1999**, *266*, 322-325.

(98) Yin, Y.; Zhou, N.-Y. *Curr Microbiol* **2010**, *61*, 471-476.

(99) Simmons, C. R.; Liu, Q.; Huang, Q.; Hao, Q.; Begley, T. P.; Karplus, P. A.; Stipanuk, M. H. *J. Biol. Chem.* **2006**, *281*, 18723-18733.

(100) Harpel, M. R.; Lipscomb, J. D. *J. Biol. Chem.* **1990**, *265*, 6301-6311.

(101) Hintner, J.-P.; Reemtsma, T.; Stolz, A. *J. Biol. Chem.* **2004**, *279*, 37250-37260.

(102) Matera, I.; Ferraroni, M.; Bürger, S.; Scozzafava, A.; Stolz, A.; Briganti, F. *J. Mol. Biol.* **2008**, *380*, 856-868.

(103) Ha, E. H.; Ho, R. Y. N.; Kisiel, J. F.; Valentine, J. S. *Inorg. Chem.* **1995**, *34*, 2265-2266.

(104) Kitajima, N.; Tamura, N.; Amagai, H.; Fukui, H.; Moro-oka, Y.; Mizutani, Y.; Kitagawa, T.; Mathur, R.; Heerwegh, K. *J. Am. Chem. Soc.* **1994**, *116*, 9071-9085.

(105) Mehn, M. P.; Fujisawa, K.; Hegg, E. L.; Que, L. *J. Am. Chem. Soc.* **2003**, *125*, 7828-7842.

(106) Mukherjee, A.; Cranswick, M. A.; Chakrabarti, M.; Paine, T. K.; Fujisawa, K.; Münck, E.; Que, L. *Inorg. Chem.* **2010**, *49*, 3618-3628.

(107) Ogihara, T.; Hikichi, S.; Akita, M.; Moro-oka, Y. *Inorg. Chem.* **1998**, *37*, 2614-2615.

(108) Beck, A.; Barth, A.; Hübner, E.; Burzlaff, N. *Inorg. Chem.* **2003**, *42*, 7182-7188.

(109) Beck, A.; Weibert, B.; Burzlaff, N. *Eur. J. Inorg. Chem.* **2001**, *2001*, 521-527.

(110) Burzlaff, N. In *Adv. Inorg. Chem.*; Rudi van, E., Ed.; Academic Press: 2008; Vol. Volume 60, p 101-165.

(111) Bruijnincx, P. C. A.; Lutz, M.; Spek, A. L.; Hagen, W. R.; Weckhuysen, B. M.; van Koten, G.; Gebbink, R. J. M. K. *J. Am. Chem. Soc.* **2007**, *129*, 2275-2286.

(112) Allen, W. E.; Sorrell, T. N. *Inorg. Chem.* **1997**, *36*, 1732-1734.

(113) Breslow, R.; Hunt, J. T.; Smiley, R.; Tarnowski, T. *J. Am. Chem. Soc.* **1983**, *105*, 5337-5342.

(114) Brown, R. S.; Huguet, J. *Can. J. Chem.* **1980**, *58*, 889-901.

(115) Kimblin, C.; Allen, W. E.; Parkin, G. *J. Chem. Soc., Chem Commun.* **1995**, 1813-1815.

(116) Kunz, Peter C.; Reiß, Guido J.; Frank, W.; Kläui, W. *Eur. J. Inorg. Chem.* **2003**, *2003*, 3945-3951.

(117) Lynch, W. E.; Kurtz, D. M.; Wang, S.; Scott, R. A. *J. Am. Chem. Soc.* **1994**, *116*, 11030-11038.

(118) Slebocka-Tilk, H.; Cocho, J. L.; Frackman, Z.; Brown, R. S. *J. Am. Chem. Soc.* **1984**, *106*, 2421-2431.

(119) Batten, M. P.; Canty, A. J.; Cavell, K. J.; Ruther, T.; Skelton, B. W.; White, A. H. *Acta Crystallogr., Sect. C: Cryst. Struct. Commun.* **2004**, *60*, m311-m313.

(120) Malkhasian, A. Y. S.; Nikolovski, B.; Kucera, B. E.; Loloee, R.; Chavez, F. A. *Z. Anorg. Allg. Chem.* **2007**, *633*, 1000-1005.

(121) Wu, F. J.; Kurtz, D. M. *J. Am. Chem. Soc.* **1989**, *111*, 6563-6572.

(122) Gade, L. H.; Marconi, G.; Dro, C.; Ward, B. D.; Poyatos, M.; Bellemin-Laponnaz, S.; Wadepohl, H.; Sorace, L.; Poneti, G. *Chem. Eur. J.* **2007**, *13*, 3058-3075.

(123) Edwards, P. G.; Harrison, A.; Newman, P. D.; Zhang, W. *Inorg. Chim. Acta* **2006**, *359*, 3549-3556.

(124) Addison, A. W.; Rao, T. N.; Reedijk, J.; van Rijn, J.; Verschoor, G. C. *J. Chem. Soc., Dalton Trans.* **1984**, 1349-1356.

(125) Fujisawa, K.; Tada, N.; Nishida, Y.; Miyashita, Y.; Okamoto, K.-i. *Inorg. Chem. Commun.* **2008**, *11*, 381-384.

(126) Park, H.; Baus, J. S.; Lindeman, S. V.; Fiedler, A. T. *Inorg. Chem.* **2011**, *50*, 11978-11989.

(127) LaRonde, F. J.; Brook, M. A. *Inorg. Chim. Acta* **1999**, *296*, 208-221.

(128) Deeth, R. J.; Bugg, T. D. H. *J. Biol. Inorg. Chem.* **2003**, *8*, 409-418.

(129) Attia; Conklin, B. J.; Lange, C. W.; Pierpont, C. G. *Inorg. Chem.* **1996**, *35*, 1033-1038.

(130) Sik Min, K.; Weyhermuller, T.; Wieghardt, K. *Dalton Trans.* **2004**, 178-186.

(131) Sik Min, K.; Weyhermuller, T.; Wieghardt, K. *Dalton Trans.* **2003**, 1126-1132.

(132) Bennett, B.; Hanson, G.; Berliner, L. In *In Metals in Biology: Applicatins of High-resolution EPR to Metalloenzymes*; Springer: New York, 2010; Vol. 29, p 345-370.

(133) Cox, D. D.; Que, L. *J. Am. Chem. Soc.* **1988**, *110*, 8085-8092.

(134) Jang, H. G.; Cox, D. D.; Que, L. *J. Am. Chem. Soc.* **1991**, *113*, 9200-9204.

(135) Bruijnincx, P. C. A.; Lutz, M.; Spek, A. L.; Hagen, W. R.; Weckhuysen, B. M.; vanKoten, G.; Gebbink, R. J. M. K. *J. Am. Chem. Soc.* **2007**, *129*, 2275-2286.

(136) Brown, S. N. *Inorg. Chem.* **2012**, *51*, 1251-1260.

(137) Kitajima, N.; Fujisawa, K.; Fujimoto, C.; Morooka, Y.; Hashimoto, S.; Kitagawa, T.; Toriumi, K.; Tatsumi, K.; Nakamura, A. *J. Am. Chem. Soc.* **1992**, *114*, 1277-1291.

(138) Khomenko, T. M.; Salomatina, O. V.; Kurbakova, S. Y.; Il'ina, I. V.; Volcho, K. P.; Komarova, N. I.; Korchagina, D. V.; Salakhutdinov, N. F.; Tolstikov, A. G. *Russ J Org Chem* **2006**, *42*, 1653-1661.

(139) Manner, V. W.; Markle, T. F.; Freudenthal, J. H.; Roth, J. P.; Mayer, J. M. *Chem. Commun.* **2008**, 256-258.

(140) Stoll, S.; Schweiger, A. *J. Magen. Reson.* **2006**, *178*, 42-55.

(141) Neese, F. *ORCA - An ab initio, Density Functional and Semi-empirical Program Package*, 2010.

(142) Becke, A. D. *J. Chem. Phys.* **1993**, *98*, 5648-5652.

(143) Lee, C.; Yang, W.; Parr, R. G. *Phys. Rev. B* **1988**, *37*, 785-789.

(144) Schafer, A.; Huber, C.; Ahlrichs, R. *J. Chem. Phys.* **1994**, *100*, 5829-5835.

(145) Schafer, A.; Horn, H.; Ahlrichs, R. *J. Chem. Phys.* **1992**, *97*, 2571-2577.

(146) Laaksonen, L. *J. Mol. Graphics* **1992**, *10*, 33-34.

(147) Sheldrick, G. M. *Acta Crystallogr., Sect. A: Found. Crystallogr.* **2008**, *64*, 112-122.

(148) Dolomanov, O. V.; Bourhis, L. J.; Gildea, R. J.; Howard, J. A. K.; Puschmann, H. *J. Appl. Crystallogr.* **2009**, *42*, 339-341.

(149) Que, L.; Ho, R. Y. N. *Chem. Rev.* **1996**, *96*, 2607-2624.

(150) Xu, L.; Resing, K.; Lawson, S. L.; Babbitt, P. C.; Copley, S. D. *Biochemistry* **1999**, *38*, 7659-7669.

(151) Yin, Y.; Zhou, N.-Y. *Curr Microbiol* **2010**, *61*, 471-476.

(152) Denisov, I. G.; Makris, T. M.; Sligar, S. G.; Schlichting, I. *Chem. Rev.* **2005**, *105*, 2253-2278.

(153) Burzlaff, N. *Angew. Chem. Int. Ed.* **2009**, *48*, 5580-5582.

(154) Bittner, M. M.; Baus, J. S.; Lindeman, S. V.; Fiedler, A. T. *Eur. J. Inorg. Chem.* **2012**, 1848-1856.

(155) Addison, A. W.; Rao, T. N.; Reedijk, J.; Vanrijn, J.; Verschoor, G. C. *J. Chem. Soc., Dalton Trans.* **1984**, 1349-1356.

(156) Soda, T.; Kitagawa, Y.; Onishi, T.; Takano, Y.; Shigeta, Y.; Nagao, H.; Yoshioka, Y.; Yamaguchi, K. *Chem. Phys. Lett.* **2000**, *319*, 223-230.

(157) E., M. In *Physical Methods in Bioinorganic Chemistry. Spectroscopy and Magnetism*; Que Jr, L., Ed.; University Science Books: Sausalito, 2000, p 287-319.

(158) Ye, S.; Price, J. C.; Barr, E. W.; Green, M. T.; Bollinger, J. M.; Krebs, C.; Neese, F. *J. Am. Chem. Soc.* **2010**, *132*, 4739-4751.

(159) Chłopek, K.; Muresan, N.; Neese, F.; Wieghardt, K. *Chem. Eur. J.* **2007**, *13*, 8390-8403.

(160) Godbout, N.; Havlin, R.; Salzmann, R.; Debrunner, P. G.; Oldfield, E. *J. Phys. Chem. A* **1998**, *102*, 2342-2350.

(161) Carter, S. M.; Sia, A.; Shaw, M. J.; Heyduk, A. F. *J. Am. Chem. Soc.* **2008**, *130*, 5838-5839.

(162) Chaudhuri, P.; Verani, C. N.; Bill, E.; Bothe, E.; Weyhermuller, T.; Wieghardt, K. *J. Am. Chem. Soc.* **2001**, *123*, 2213-2223.

(163) Min, K. S.; Weyhermuller, T.; Wieghardt, K. *Dalton Trans.* **2003**, 1126-1132.

(164) Johnson, M. K. In *Physical Methods in Bioinorganic Chemistry*; Que Jr, L., Ed.; University Science Books: Sausalito, 2000, p 233-286.

(165) Neese, F.; Solomon, E. I. *Inorg. Chem.* **1998**, *37*, 6568-6582.

(166) Neese, F.; Solomon, E. I. *Inorg. Chem.* **1999**, *38*, 1847-1865.

(167) Pavel, E. G.; Kitajima, N.; Solomon, E. I. *J. Am. Chem. Soc.* **1998**, *120*, 3949-3962.

(168) Solomon, E. I. *Inorg. Chem.* **2001**, *40*, 3656-3669.

(169) Dunn, T. J.; Ramogida, C. F.; Simmonds, C.; Paterson, A.; Wong, E. W. Y.; Chiang, L.; Shimazaki, Y.; Storr, T. *Inorg. Chem.* **2011**, *50*, 6746-6755.

(170) Op't Holt, B. T.; Vance, M. A.; Mirica, L. M.; Heppner, D. E.; Stack, T. D. P.; Solomon, E. I. *J. Am. Chem. Soc.* **2009**, *131*, 6421-6438.

(171) Hartl, F.; Stufkens, D. J.; Vlcek, A. *Inorg. Chem.* **1992**, *31*, 1687-1695.

(172) Vlček, A. *Comments Inorg. Chem.* **1994**, *16*, 207-228.

(173) Bittner, M. M.; Baus, J. S.; Lindeman, S. V.; Fiedler, A. T. *Eur. J. Inorg. Chem.* **2012**, *2012*, 1848-1856.

(174) Neese, F. University of Bonn, Bonn (Germany), 2010.

(175) Becke, A. D. *J. Chem. Phys.* **1986**, *84*, 4524-4529.

(176) Stratmann, R. E.; Scuseria, G. E.; Frisch, M. J. *J. Chem. Phys.* **1998**, *109*, 8218-8224.

(177) Casida, M. E.; Jamorski, C.; Casida, K. C.; Salahub, D. R. *J. Chem. Phys.* **1998**, *108*, 4439-4449.

(178) Bauernschmitt, R.; Ahlrichs, R. *Chem. Phys. Lett.* **1996**, *256*, 454-464.

(179) Hirata, S.; Head-Gordon, M. *Chem. Phys. Lett.* **1999**, *314*, 291-299.

(180) Römelt, M.; Ye, S.; Neese, F. *Inorg. Chem.* **2008**, *48*, 784-785.

(181) Cherkasov, V.; Druzhkov, N.; Kocherova, T.; Fukin, G.; Shavyrin, A. *Tetrahedron* **2011**, *67*, 80-84.

(182) Kaim, W. *Inorg. Chem.* **2011**, *50*, 9752-9765.

(183) Kaim, W. *Eur. J. Inorg. Chem.* **2012**, *2012*, 343-348.

(184) Agarwala, H.; Ehret, F.; Chowdhury, A. D.; Maji, S.; Mobin, S. M.; Kaim, W.; Lahiri, G. K. *Dalton Trans.* **2013**, *42*, 3721-3734.

(185) Das, D.; Sarkar, B.; Kumbhakar, D.; Mondal, T. K.; Mobin, S. M.; Fiedler, J.; Urbanos, F. A.; Jiménez-Aparicio, R.; Kaim, W.; Lahiri, G. K. *Chem. Eur. J.* **2011**, *17*, 11030-11040.

(186) Das, D.; Das, A. K.; Sarkar, B.; Mondal, T. K.; Mobin, S. M.; Fiedler, J.; Záliš, S.; Urbanos, F. A.; Jiménez-Aparicio, R.; Kaim, W.; Lahiri, G. K. *Inorg. Chem.* **2009**, *48*, 11853-11864.

(187) Das, A. K.; Sarkar, B.; Duboc, C.; Strobel, S.; Fiedler, J.; Záliš, S.; Lahiri, G. K.; Kaim, W. *Angew. Chem. Int. Ed.* **2009**, *48*, 4242-4245.

(188) Munha, R. F.; Zarkesh, R. A.; Heyduk, A. F. *Dalton Trans.* **2013**, *42*, 3751-3766.

(189) Khusniyarov, M. M.; Weyhermüller, T.; Bill, E.; Wieghardt, K. *J. Am. Chem. Soc.* **2009**, *131*, 1208-1221.

(190) Khusniyarov, M. M.; Bill, E.; Weyhermüller, T.; Bothe, E.; Harms, K.; Sundermeyer, J.; Wieghardt, K. *Chem. Eur. J.* **2008**, *14*, 7608-7622.

(191) Herebian, D.; Bothe, E.; Neese, F.; Weyhermüller, T.; Wieghardt, K. *J. Am. Chem. Soc.* **2003**, *125*, 9116-9128.

(192) Chłopek, K.; Bill, E.; Weyhermüller, T.; Wieghardt, K. *Inorg. Chem.* **2005**, *44*, 7087-7098.

(193) Gorelsky, S. I.; Lever, A. B. P.; Ebadi, M. *Coord. Chem. Rev.* **2002**, *230*, 97-105.

(194) Rajput, A.; Sharma, A. K.; Barman, S. K.; Koley, D.; Steinert, M.; Mukherjee, R. *Inorg. Chem.* **2013**, *53*, 36-48.

(195) Weinberg, D. R.; Gagliardi, C. J.; Hull, J. F.; Murphy, C. F.; Kent, C. A.; Westlake, B. C.; Paul, A.; Ess, D. H.; McCafferty, D. G.; Meyer, T. J. *Chem. Rev.* **2012**, *112*, 4016-4093.

(196) Huynh, M. H. V.; Meyer, T. J. *Chem. Rev.* **2007**, *107*, 5004-5064.

(197) DuBois, D. L.; Bullock, R. M. *Eur. J. Inorg. Chem.* **2011**, *2011*, 1017-1027.

(198) Roubelakis, M. M.; Bediako, D. K.; Dogutan, D. K.; Nocera, D. G. *Energy Environ. Sci.* **2012**, *5*, 7737-7740.

(199) Hoffman, B. M.; Lukoyanov, D.; Dean, D. R.; Seefeldt, L. C. *Acc. Chem. Res.* **2013**, *46*, 587-595.

(200) Hoffman, B. M.; Dean, D. R.; Seefeldt, L. C. *Acc. Chem. Res.* **2009**, *42*, 609-619.

(201) Matsumoto, T.; Chang, H.-C.; Wakizaka, M.; Ueno, S.; Kobayashi, A.; Nakayama, A.; Taketsugu, T.; Kato, M. *J. Am. Chem. Soc.* **2013**, *135*, 8646-8654.

(202) Lu, F.; Zarkesh, R. A.; Heyduk, A. F. *Eur. J. Inorg. Chem.* **2012**, *2012*, 467-470.

(203) Costas, M.; Mehn, M. P.; Jensen, M. P.; Que, L., Jr. *Chem. Rev.* **2004**, *104*, 939-986.

(204) Bittner, M. M.; Lindeman, S. V.; Fiedler, A. T. *J. Am. Chem. Soc.* **2012**, *134*, 5460-5463.

(205) Bittner, M. M.; Kraus, D.; Lindeman, S. V.; Popescu, C. V.; Fiedler, A. T. *Chem. Eur. J.* **2013**, 9686-9698.

(206) Jo, D.-H.; Chiou, Y.-M.; Que, L. *Inorg. Chem.* **2001**, *40*, 3181-3190.

(207) Reynolds, M.; Costas, M.; Ito, M.; Jo, D.-H.; Tipton, A.; Whiting, A.; Que, L. *J Biol Inorg Chem* **2003**, *8*, 263-272.

(208) Sayantan Paria, P. H., Biswarup Chakraborty, Tapan kanti Paine *Indian J. Chem., Sect. A* **2011**, *50A*, 420-426.

(209) Chiou, Y.-M.; Que, L. *Inorg. Chem.* **1995**, *34*, 3577-3578.

(210) Baum, A. E.; Park, H.; Wang, D.; Lindeman, S. V.; Fiedler, A. T. *Dalton Trans.* **2012**, *41*, 12244-12253.

(211) Masui, H.; Lever, A. B. P.; Auburn, P. R. *Inorg. Chem.* **1991**, *30*, 2402-2410.

(212) Comba, P.; Wadepohl, H.; Wunderlich, S. *Eur. J. Inorg. Chem.* **2011**, *2011*, 5242-5249.

(213) Lin, G.; Reid, G.; Bugg, T. D. H. *J. Am. Chem. Soc.* **2001**, *123*, 5030-5039.

(214) Jo, D.-H.; Que, J. L. *Angew. Chem. Int. Ed.* **2000**, *39*, 4284-4287.

(215) Peng, S.-M.; Chen, C.-T.; Liaw, D.-S.; Chen, C.-I.; Wang, Y. *Inorg. Chim. Acta* **1985**, *101*, L31-L33.

(216) Bugarcic, T.; Habtemariam, A.; Deeth, R. J.; Fabbiani, F. P. A.; Parsons, S.; Sadler, P. J. *Inorg. Chem.* **2009**, *48*, 9444-9453.

(217) Jüstel, T.; Bendix, J.; Metzler-Nolte, N.; Weyhermüller, T.; Nuber, B.; Wieghardt, K. *Inorg. Chem.* **1998**, *37*, 35-43.

(218) Venegas-Yazigi, D.; Mirza, H.; Lever, A. B. P.; Lough, A. J.; Costamagna, J.; Latorre, R. *Acta Crystallogr., Sect. C: Cryst. Struct. Commun.* **2000**, *56*, e281-e282.

(219) Kapovsky, M.; Dares, C.; Dodsworth, E. S.; Begum, R. A.; Raco, V.; Lever, A. B. P. *Inorg. Chem.* **2012**, *52*, 169-181.

(220) Michaud-Soret, I.; Andersson, K. K.; Que, L.; Haavik, J. *Biochemistry* **1995**, *34*, 5504-5510.

(221) Fukuzumi, S.; Kotani, H.; Prokop, K. A.; Goldberg, D. P. *J. Am. Chem. Soc.* **2011**, *133*, 1859-1869.

(222) Fukuzumi, S.; Kotani, H.; Lee, Y.-M.; Nam, W. *J. Am. Chem. Soc.* **2008**, *130*, 15134-15142.

(223) Kryatov, S. V.; Rybak-Akimova, E. V.; Schindler, S. *Chem. Rev.* **2005**, *105*, 2175-2226.

(224) Warren, J. J.; Tronic, T. A.; Mayer, J. M. *Chem. Rev.* **2010**, *110*, 6961-7001.

(225) Bordwell, F. G.; Cheng, J. P.; Harrelson, J. A. *J. Am. Chem. Soc.* **1988**, *110*, 1229-1231.

(226) Bordwell, F. G.; Zhang, X. M.; Cheng, J. P. *J. Org. Chem.* **1993**, *58*, 6410-6416.

(227) Bordwell, F. G.; Cheng, J. *J. Am. Chem. Soc.* **1991**, *113*, 1736-1743.

(228) Schenk, G.; Pau, M. Y. M.; Solomon, E. I. *J. Am. Chem. Soc.* **2003**, *126*, 505-515.

(229) Perdew, J. P.; Burke, K.; Ernzerhof, M. *Phys. Rev. Lett.* **1996**, *77*, 3865-3868.

(230) Diebold, A. R.; Straganz, G. D.; Solomon, E. I. *J. Am. Chem. Soc.* **2011**, *133*, 15979-15991.

(231) Davis, M. I.; Wasinger, E. C.; Decker, A.; Pau, M. Y. M.; Vaillancourt, F. H.; Bolin, J. T.; Eltis, L. D.; Hedman, B.; Hodgson, K. O.; Solomon, E. I. *J. Am. Chem. Soc.* **2003**, *125*, 11214-11227.

(232) Georgiev, V.; Borowski, T.; Blomberg, M. A.; Siegbahn, P. M. *J Biol Inorg Chem* **2008**, *13*, 929-940.

(233) Cramer, C. J.; Tolman, W. B.; Theopold, K. H.; Rheingold, A. L. *Proc. Natl. Acad. Sci.* **2003**, *100*, 3635-3640.

(234) Halder, P.; Paria, S.; Paine, T. K. *Chem. Eur. J.* **2012**, *18*, 11778-11787.

(235) Chakraborty, B.; Paine, T. K. *Angew. Chem.* **2013**, *125*, 954-958.

(236) Christian, G. J.; Ye, S. F.; Neese, F. *Chem. Sci.* **2012**, *3*, 1600-1611.

(237) Frantz, D. K.; Linden, A.; Baldridge, K. K.; Siegel, J. S. *J. Am. Chem. Soc.* **2012**, *134*, 1528-1535.

(238) Battino, R.; Clever, H. L. *Chem. Rev.* **1966**, *66*, 395-463.

(239) Shaikh, N.; Panja, A.; Banerjee, P.; Ali, M. *Transition Metal Chemistry* **2003**, *28*, 871-880.

(240) Weigend, F.; Ahlrichs, R. *Phys. Chem. Chem. Phys.* **2005**, *7*, 3297-3305.

(241) Hirata, S.; Head-Gordon, M. *Chem. Phys. Lett.* **1999**, *302*, 375-382.

(242) Klamt, A.; Schuurmann, G. *Journal of the Chemical Society, Perkin Transactions 2* **1993**, 799-805.

(243) Titus, G. P.; Mueller, H. A.; Burgner, J.; Córdoba, S. R. d.; Penalva, M. A.; Timm, D. E. *Nat. Struct. Mol. Biol.* **2000**, *7*, 542-546.

(244) Yin, Y.; Zhou, N. Y. *Curr Microbiol* **2010**, *61*, 471-476.

(245) Diebold, A. R.; Neidig, M. L.; Moran, G. R.; Straganz, G. D.; Solomon, E. I. *Biochemistry* **2010**, *49*, 6945-6952.

(246) Kitajima, N.; Amagai, H.; Tamura, N.; Ito, M.; Morooka, Y.; Heerwegh, K.; Penicaud, A.; Mathur, R.; Reed, C. A.; Boyd, P. D. W. *Inorg. Chem.* **1993**, *32*, 3583-3584.

(247) Park, H.; Baus, J. S.; Lindeman, S. V.; Fiedler, A. T. *Inorg. Chem.* **2011**, *50*, 11978-11989.

(248) Park, H.; Bittner, M. M.; Baus, J. S.; Lindeman, S. V.; Fiedler, A. T. *Inorg. Chem.* **2012**, *51*, 10279-10289.

(249) Davis, M. I.; Wasinger, E. C.; Decker, A.; Pau, M. Y. M.; Vaillancourt, F. H.; Bolin, J. T.; Eltis, L. D.; Hedman, B.; Hodgson, K. O.; Solomon, E. I. *J. Am. Chem. Soc.* **2003**, *125*, 11214-11227.